UNIVERSITÉ DE STRASBOURG

ÉCOLE DOCTORALE DE PHYSIQUE ET CHIMIE-PHYSIQUE (ED182)

Institut de Physique et Chimie des Matériaux de Strasbourg (IPCMS)

(UMR 7504 CNRS-Unistra)

THÈSE

présentée par :

Alexandre ADAM

soutenue le : **23 février 2022**

pour obtenir le grade de : **Docteur de l'université de Strasbourg**

Discipline/ Spécialité : Chimie-Physique des Matériaux

Nanoplateformes à base de silices mésoporeuses pour l'hyperthermie magnétique, la photothermie et la délivrance d'agents thérapeutiques

THÈSE dirigée par :

M. MERTZ Damien	Chargé de recherches, IPCMS (UMR 7504 CNRS-Université de Strasbourg)

RAPPORTEURS :

M. WONG CHI MAN Michel	Directeur de recherches, ICG (UMR 5253 CNRS-Université de Montpellier)
M. HERZOG Grégoire	Chargé de recherches, LCPME (UMR 7564 CNRS-Université de Lorraine)

EXAMINATEURS :

Mme LEBEAU Bénédicte	Directeur de recherches, IS2M (UMR 7361 CNRS-Université de Haute-Alsace)
Mme GAZEAU Florence	Directeur de recherches, MSC (UMR 7057 CNRS-Université Paris Diderot)

INVITÉS :

M. HARLEPP Sébastien	Maître de conférences, INSERM (UMR_S 1109, Université de Strasbourg)
Mme BEGIN-COLIN Sylvie	Professeur, ECPM, IPCMS (UMR 7504 CNRS, Université de Strasbourg)

Remerciements

Les travaux présentés dans ce manuscrit n'auraient pas la même allure et n'auraient certainement pas pu voir le jour sans les nombreuses personnes qui m'ont permis de bénéficier d'un environnement de travail idéal à la fois stimulant et apaisé et qui pousse à donner le meilleur de soi-même. C'est pourquoi je tiens à écrire ces quelques lignes pour remercier toutes les personnes passionnées qui m'ont apportées leur expérience si précieuse et tous ceux qui ont contribué de près ou de loin à ce projet.

Tout d'abord, je tiens à remercier M. Pierre Rabu, directeur de l'IPCMS et Mme Nathalie Viart pour leurs accueils chaleureux au sein de l'institut et du Département de Chimie des Matériaux Inorganiques.

Je remercie tous les membres de mon jury de thèse pour avoir examiné ces travaux, M. Michel Wong Chi Man, directeur de recherches à l'université de Montpellier, M. Grégoire Herzog, chargé de recherches à l'université de Lorraine ainsi que Mme Bénédicte Lebeau, directrice de recherches à l'université de Haute-Alsace et Mme Florence Gazeau, directrice de recherches à l'université Paris Diderot.

Tout naturellement, je tiens à remercier très chaleureusement mon directeur de thèse, Damien Mertz. Ces trois années furent très riches et parfois mouvementées. Tu as toujours su te rendre disponible quand il y en avait besoin et je t'en remercie. Je suis fier d'avoir été ton « premier » doctorant officiel et je pense qu'ensemble nous avons appris pas mal de choses. Merci aussi pour toutes ces discussions plus ou moins formelles qui font de la thèse aussi une expérience humaine.

Je veux aussi remercier tout particulièrement Sylvie Bégin-Colin qui m'a suivi quasiment tout au long de mes études supérieures de plus ou moins loin. En plus de Damien, tu as su me convaincre de rejoindre le monde des (nano)matériaux et ce fut un immense plaisir de travailler avec toi dans l'équipe CEFUN. Tu es une scientifique passionnée et les discussions sont toujours pertinentes et enrichissantes. Tu es aussi une super cheffe d'équipe qui nous a permis de vivre plein d'expériences et de moments conviviaux extra-thèse mais tellement importants, notamment autour des traditionnels barbecue et volley ; mais aussi de nombreux restaurants. Merci pour tout.

En trois années de thèse en chimie, on apprend beaucoup au laboratoire. Un merci tout particulier à Céline Kiefer qui, en plus d'être une personne authentique que j'apprécie beaucoup, est une technicienne hors-pair. Merci pour ta disponibilité ; on sait qu'on peut toujours compter sur toi si on a une question et c'est essentiel avec tous ces jeunes doctorants. Je tiens aussi à remercier Marie-Noëlle Lalloz, Cédric Leuvrey et Didier Burger qui m'ont aidé sur de nombreux aspects au laboratoire mais aussi pour caractériser mes échantillons par RMN, MEB et ATG.

Merci aussi à Sébastien Harlepp qui m'a fait découvrir l'INSERM et le monde de la biologie, méconnu des chimistes et pas toujours facile à saisir. Ce fut pour moi très enrichissant et j'ai beaucoup aimé travailler à l'interface de ces deux disciplines.

En côtoyant si longtemps les mêmes personnes, il arrive qu'on s'en fasse des amis. Ainsi je tiens à remercier tout spécialement Pier Berling et Frédéric Payet. On termine chacun notre thèse comme on l'a commencée, c'est-à-dire ensemble. Au fil du temps, nous avons formé une super équipe, un trio de choc soudé. Sans vous, cela aurait été beaucoup moins drôle et j'espère que nos chemins ne s'éloigneront pas trop. Puis une nouvelle génération de doctorants est arrivée, avec, en particulier, Barbara Freis et Guillaume Krieger qui ont agrandis le cercle. Votre bonne humeur et joie de vivre ont beaucoup contribué à faire de cette période un super moment. Merci aussi à mes autres collègues de bureau actuels ou qui ont déjà terminés leur thèse, Joana Vazramos, Nesrine Benamara, Francis Perton, Paula Duenas-Ramirez, Kévin Sartori qui m'ont beaucoup appris sur le laboratoire, les synthèses et transmis leurs trucs et astuces. Je n'oublie pas mon binôme de laboratoire, Joëlle Bizeau à qui je transmets le flambeau de Chimie 3, prends en soin ! Merci d'avoir su être patiente et d'avoir subi mon organisation dans le labo.

J'adresse aussi un très chaleureux remerciement à tous les membres du DCMI pour la bonne humeur, la bonne ambiance et les nombreux conseils et aides que j'ai pu recevoir. J'ai pu apprécié les supers moments de convivialité et divers repas d'avant-Covid et j'espère que les prochains doctorants pourront connaitre ses instants si importants.

Un grand merci à toute ma famille, mes parents, mon frère, mes grands-parents, oncles, tantes et cousins qui m'ont toujours suivi et soutenu toutes ces années même si je n'ai pas toujours bien su vous expliquer ce que je faisais. Merci à mes amis de (presque) toujours Adrien, Quentin, Louis, Marco, mes chers alsaciens que je connais depuis plus de 15 ans. Et bien-sûr merci à la fine équipe de prépa et de l'ECPM, Emilie, Camille, Garance, Alicia et les Marion[2] de si bons amis qui ont toujours été là dans tous les moments et dont la bonne humeur et le sens de l'amitié comptent tant pour moi. Enfin merci à Pierrick pour son soutien indéfectible et ses encouragements à tout épreuve notamment au moment de la rédaction qui ont beaucoup comptés.

Table of content

Table of abbreviations

AHMPD	2-amino-2-(hydroxymethyl)-1,3-propanediol
AMF	Alternating magnetic field
AP	alkaline phosphate
APTES	3-(aminopropyl)triethoxy silane
BCA	Bicinchoninic acid
BET	Brunauer-Emmet-Teller
BJH	Barrett-Joyer-Halenda
CMC	Critical micelle concentration
CNT	Carbon nanotubes
CTAB	Cetyltrimethylammonium bromide
CTATos	Cetyltrimethylammonium tosylate
DLC	Drug loading capacity
DLE	Drug loading efficiency
DLS	Dynamic light scattering
DMF	Dimethylformamide
DNA	Desoxyribonucleic acid
DOX	Doxorubicine
EDC	1-Ethyl-3-(3-dimethylaminopropyl)carbodiimide
Et_3N	Triethylamine
EtOH	Ethanol
FITC	Fluorescein isothiocyanate
Fmoc-FFpY	Fmoc: fluorenylmethyloxycarbonyl; F: phenylalanine; Y: tyrosine; p: phosphate
Fwr	feed weight ratio
HEPES	4-(2-hydroxyethyl)-1-piperazineethanesulfonic acid
HSA	Human serum albumin
IBAM	Isobutyramide
IO	Iron oxide
LCST	lower critical solution temperature
LPMS	large pore mesoporous silica
MD	Molecular dynamics
MHT	Magnetic hyperthermia
MRI	Magnetic resonance imaging
MS	Mesoporous silica
MTT	3-(4,5-dimethylthiazol-2-yl)-2,5-diphenyltetrazolium bromide

MW	Molecular weight
NHS	*N*-Hydroxysuccinimide
NIR	Near Infrared
NPs	Nanoparticles
PEG	Polyethylene glycol
PEI	Polyethylenimine
PNIPAM	Poly(N-isopropylacrylamide)
pNP	para-nitrophenol
pNPP-Na	para-nitrophenyl phosphate disodium hexahydrate
PTT	Photothermal therapy
QDs	Quantum dots
RNA	Ribonucleic acid
RT	Room temperature
SAR	Specific absorption rate
SEM	Scanning electron microscopy
siRNA	small interfering ribonucleic acid
SPMS	Small pore mesoporous silica
STMS	Stellate mesoporous silica
TEM	Transmission electron microscopy
TEOS	Tetraethyl orthosilicate
TGA	Thermogravimetric analysis
TIB	1,3,5-triisopropylbenzene
ZF	Zebra fish
ZMEL	Zebrafish melanoma cells
ZP	Zeta potential

Résumé en français

Introduction

En 2020, le cancer était responsable de la mort de 10 millions de personnes à travers le monde et près de 28.4 millions de cas de cancer sont attendus en 2040, d'après l'Agence International pour la Recherche sur le Cancer.[1] Les cancers surviennent quand des cellules normales se transforment en cellules néoplasiques, ce qui induit chez elles une croissance incontrôlée et la formation de tumeur. Tous les mécanismes de formation et propagation d'un cancer ne sont pas élucidés à l'heure actuelle. Cependant, il a été montré que facteurs à la fois externe comme une exposition aux radiations ou aux produits toxiques, des infections, le tabagisme mais aussi des facteurs internes comme des mutations génétiques ou un système immunitaire défaillant peuvent agir ensemble ou indépendamment pour induire un cancer.[2]

La nanomédecine a pour but d'utiliser les nanotechnologies aux interfaces de différents domaines (biologie, chimie, physique) pour développer de nouveaux traitements contre des maladies telles que le cancer. Un des challenges majeurs est de produire des nanoplateformes capable de combiner en un seul objet des fonctions de diagnostic et de thérapies (théranostique) et qui soit adapté à chaque patient et chaque maladie. Avec les progrès actuels dans la synthèse de nanoplateformes complexes, la production de nanoparticules (NPs) multifonctionnelles ouvre la voie à de nouvelles perspectives pour l'oncologie. Pour cela, une grande variété de nanomatériaux a été développé tels que des NPs à base de liposomes, lipides, polymères ou particules virales mais aussi des NPs inorganiques fait d'oxyde d'hafnium, d'or, d'argent, de silice ou basés sur le carbone comme les nanotubes de carbone ou fullerènes.[3,4]

Parmi les nano-objets prometteurs, les nanomatériaux à base de ferrites sont particulièrement intéressants car leurs propriétés leurs permettent de servir à la fois d'agents de contraste en imagerie par résonance magnétique (IRM) et d'agents thérapeutiques par effet magnétothermique sous champ magnétique alternatif (AMF) et par effet photothermique sous lumière proche infrarouge (NIR). Dans ce cadre, les oxydes de fer (IO) et en particulier la magnétite sont très adaptés car ils sont peu onéreux, biodégradables et biocompatibles. Les NPs d'oxydes de fer (IO NPs) sont déjà utilisés en clinique comme agents de contraste T_2 pour l'IRM. Les IO NPs sont fonctionnalisées avec des ligands organiques pour assurer la stabilité colloïdale, l'état d'agrégation et une bonne biodistribution. Ces IO NPs peuvent aussi être utilisées pour du traitement par hyperthermie magnétique (MHT) sous AMF. Par leur mouvement et par relaxation du moment magnétique, les NPs génèrent de la chaleur localement qui se propage ensuite au milieu environnant. Cela a pour effet de tuer ou d'affaiblir les cellules cancéreuses qui sont généralement plus sensibles aux élévations de température que les cellules saines. Cela

augmente aussi l'efficacité des traitements associés tels que la chimiothérapie ou la radiothérapie. Nanotherm®, développé par une entreprise allemande, MagForce Nanotech AG, est le premier produit thérapeutique basé sur cet effet en utilisant des IO NPs à être autorisé en Europe (en 2011) pour le traitement des tumeurs du cerveau, mais d'autres produits sont en cours d'essais cliniques. Un large éventail de perspectives s'ouvre donc pour les nanoformulations à base de IO NPs. Actuellement, une des principales limitations du traitement par hyperthermie magnétique vient de la relative faible puissance de chauffe des produits existants, ce qui requiert une injection intratumorale de NPs en grande quantité (environ 20-30 mg d'oxyde de fer par cm^3 de tumeur en moyenne).[5,6] Un des challenges est donc de produire des NPs très efficaces pour réduire significativement les doses administrées et donc les potentiels effets secondaires.

Outre les IO NPs, les nanotubes de carbone (CNTs) sont aussi particulièrement attractifs pour des applications biomédicales et en particulier dans le domaine des matériaux composites adaptatifs. En effet ceux-ci présentent une fluorescence intrinsèque dans la seconde fenêtre biologique (NIR-II) et ils libèrent aussi très efficacement de la chaleur par irradiation avec de la lumière NIR. Ils sont donc très prometteurs comme outils d'imagerie et de thérapie photothermique du cancer. De plus, les CNTs ont d'excellentes propriétés mécaniques : résistance à la traction et module d'Young élevés, ce qui en fait un matériau idéal à incorporer dans des structures polymères tels que des hydrogels ou des fibres électrofilées.

Cependant, ce domaine de recherche doit encore relever plusieurs défis comme limiter la toxicité des NPs, améliorer la stabilité colloïdale et la fonctionnalisation de surface, assurer un chargement adapté en médicament et une libération contrôlée etc… C'est pourquoi, pour développer une nouvelle génération de matériaux théranostiques, il semble prometteur de combiner les propriétés des IO et CNTs avec d'autres matériaux leur apportant de nouvelles fonctionnalités capables de surmonter ces défis.

En association avec d'autres matériaux, en particulier les IO ou CNTs, l'utilisation de la silice dans les systèmes magnéto- et photorépondants a été peu étudiée. L'ajout de silice aux matériaux IO et NTC offre la possibilité de concevoir de nouvelles NPs cœur-coquille mésoporeuses intelligentes. En effet, la porosité et la surface spécifique élevée de la silice peuvent être avantageusement utilisées pour un chargement efficace d'une large gamme de molécules. Les pores peuvent être conçus pour charger des médicaments, peptides ou protéines. Un revêtement de silice améliorerait également considérablement la biocompatibilité de la NP cœur-coquille, rendant ainsi possible l'utilisation de nombreux matériaux pour des applications biomédicales. Enfin, sa chimie de surface est très polyvalente et peut être modifiée pour un ciblage efficace et une libération « sur demande » de médicaments. À ce jour, une seule formulation nanocomposite est impliquée dans des essais cliniques et est basée sur des nanoparticules d'or recouvertes de silice pour des applications d'ablation photothermique, Aurolase® par Nanospectra Biosciences. Ainsi, la synthèse de nanocomposites ayant une couche de silice recouvrant un noyau inorganique (NPs cœur-coquille) ouvrirait la voie à une classe novatrice de

matériaux biomédicaux qui combineraient les propriétés des deux matériaux, créant ainsi des nanoplateformes multimodales commercialisables.

Ainsi, le but de ma thèse de doctorat est la conception de NP avec une enveloppe de silice et un matériau de cœur pouvant être activées en générant de la chaleur lorsqu'un stimulus externe est appliqué (AMF ou lumière NIR). Ces nanoplateformes ont été conçues avec une enveloppe de silice poreuse conçue pour stabiliser, fonctionnaliser et charger les médicaments dans une unique nanoplateforme stimulable par un champ externe. Évidemment, le revêtement de silice n'est pas sans conséquence et devrait avoir une influence sur les propriétés du cœur et en particulier sur le comportement de chauffage sous stimuli. Cette caractérisation fondamentale est encore très peu rapportée. Ainsi, il est nécessaire de comprendre l'impact qu'a la coquille de silice autour du cœur lorsque ses propriétés physiques telles que l'épaisseur et la porosité sont modulées.

Dans une première étude (chapitre 2), nous avons cherché à contrôler les paramètres de synthèse des coquilles de silice mésoporeuse (MS) autour des cœur d'IO et l'influence du type de silice mésoporeuse sur les propriétés magnétothermales nanocomposites a été étudié. Par un contrôle fin des paramètres de synthèse, nous verrons comment il est possible de produire différentes morphologies et épaisseurs de silice. En particulier, dans ce chapitre, l'impact de l'ingénierie de la coquille de silice sur le propriétés d'agents de contraste IRM et les propriétés magnétothermales de l'IO a été étudié.

En plus de stabiliser et de protéger le cœur, le revêtement de silice lui-même a de nombreux avantages. En effet, en augmentant considérablement la surface spécifique, les NP enrobées de silice mésoporeuse sont très adaptés pour transporter des médicaments. **Dans une deuxième étude** (chapitre 3), nous nous sommes concentrés sur le développement d'un vecteur d'administration de médicaments associant des propriétés photothermiques. Cependant, un défi important, en plus d'avoir une charge de médicaments élevée, est de pouvoir retenir les médicaments dans les porosités de la silice et de pouvoir libérer ce médicament sur demande. Cela implique de créer des interactions/liaisons entre le médicament et la surface de silice assez fortes pour maintenir le médicament tout en étant assez faibles pour une libération efficace lors du chauffage. C'est pourquoi la conception d'une chimie de surface intelligente est cruciale pour contrôler le comportement de chargement et de libération des médicaments. Ainsi, dans ce travail, nous avons examiné la capacité de chargement de NPs IO@MS en fonction de la chimie de surface et du pH de la solution de chargement. Dans cette étude, par irradiation avec un laser NIR, les propriétés photothermiques de ces systèmes IO@MS ont été étudiées et le comportement associé à la libération du médicament a été quantifié. L'utilisation d'IO et de MS comme agents photothermiques est un domaine très innovant[7,8] et nous proposons ici une formulation capable d'associer ce mode de thérapie non invasif à de la délivrance de médicaments pour ainsi avoir un objet de bithérapie efficace dans le traitement du cancer.

Les NPs pour applications biomédicales peuvent être conçues pour des formulations circulantes, c'est-à-dire que le traitement est injecté au patient et transite par la circulation sanguine jusqu'à sa cible. Mais un autre niveau d'organisation peut être ajouté à la formulation en incorporant les NP dans des matrices implantables telles que les hydrogels. Cela a l'avantage d'empêcher toute dissémination des NP dans le corps, ce qui peut constituer un problème de santé, et de fournir une administration prolongée du médicament sans injection répétée. Cependant, les hydrogels ont généralement des propriétés de résistance mécanique très limitées. **Dans une troisième étude (chapitre 4)**, avec pour but de concevoir des structures implantables adaptées, nous avons étendu notre concept de NP mésoporeuses à un autre matériau : les CNTs, dont les propriétés ont été décrites au-dessus. De par leur forme et rigidité, les CNTs montre une certaine cytotoxicité. C'est pourquoi, les CNT@MS ont été formulés afin d'étendre leur utilisation aux systèmes implantables biocompatibles. Pour cela, ils ont été conçus pour servir de support d'immobilisation d'une enzyme capable de déclencher l'auto-assemblage d'un peptide en un hydrogel supramoléculaire. Ce gel a été étudié comme une structure originale et chargée de médicaments dont la libération peut être activée avec la lumière NIR.

I. Ingénierie de la coquille de silice autour de nanoparticules d'oxyde de fer pour moduler les propriétés magnétothermiques de ces composites

Les NP d'IO ont des propriétés prometteuses pour les applications biomédicales et théranostiques, comme il a été détaillé au chapitre 1. Elles peuvent être utilisés comme agents de contraste pour l'IRM et agents magnétothermiques pour la MHT. Cependant, leur revêtement par une coquille de silice n'est pas sans conséquence sur les propriétés de ces cœurs d'IO et il est donc important de réfléchir au meilleur design de la coquille de silice afin de produire des NPs cœur-coquille IO@SiO_2 performantes. L'évaluation de leurs propriétés IRM et MHT devrait alors nous aider à choisir le système le plus approprié pour des thérapies efficaces. Ainsi, dans ce chapitre, nous allons mettre en œuvre la synthèse de la coquille de silice et modifier les paramètres de la réaction qui permettent de moduler la morphologie des pores et l'épaisseur de la coquille (**Figure 1**). Ensuite, l'influence de cette coquille de silice sur la capacité de chauffage sous AMF et lumière NIR sera étudiée. Bien que des systèmes IO@MS aient déjà été reportés en particulier pour leurs propriétés en IRM, l'influence de la conception de la coquille de silice et la façon dont sa structure poreuse peut modifier le transfert de chaleur du cœur central vers l'environnement ont été peu étudiées.

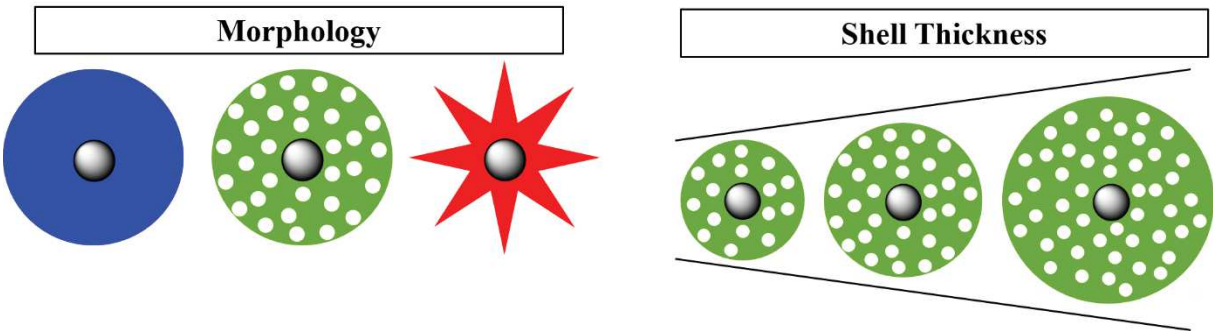

Figure 1. Schéma de la modulation de la morphologie des pores et de l'épaisseur de la coquille de silica autour des noyaux d'IO.

Ce chapitre est divisé en trois parties principales :

i) Dans une première section (II.2), nous nous concentrons sur des systèmes spécifiques produisant des coquilles de silice mésoporeuse avec une morphologie de type « stellaire » ou bien « worm-like ». Nous montrons que la température de réaction sol-gel est un paramètre fondamental pour contrôler l'auto-assemblage des micelles de surfactants et ensuite la condensation de la silice autour de ces structures. Des transformations profondes de la morphologie des pores (largeur et orientation des pores) sont observées, ce qui affecte les caractéristiques de l'IRM et le transfert de chaleur vers l'environnement lors de l'application de l'AMF.

ii) Ensuite, dans une deuxième section (II.3), la synthèse de coquille de silice poreuse autour de cœur d'IO est étendue à d'autres formes de pores, largeurs et épaisseurs de silice, afin d'étudier plus en détails l'influence des propriétés de la silice sur les propriétés magnétothermiques, en particulier sur les valeurs de SAR (specific absorption rate).

iii) Enfin, un concept prometteur pour détecter la température locale à la surface des NPs est proposé (II.4). Nous avons essayé d'utiliser avantageusement la luminescence de boîtes quantiques (quantum dots) greffés sur les NPs cœur-coquille IO@MS pour évaluer la température locale en surface des NPs. Cette méthode est appelée nanothermométrie et devrait nous permettre de suivre la température locale lors de l'application d'un AMF.

I.1. Influence de la température de réaction sur la morphologie des pores

Pour permettre d'ajuster la structure du réseau de pores, diverses méthodes ont été développées dans le but de changer la morphologie et la taille des pores, en jouant sur divers paramètres de synthèse. Ainsi, l'augmentation de la concentration en surfactant[9] ou du rapport surfactant/silice permet de modifier l'auto-assemblage des micelles et donc la structure des pores.[10] Le diamètre des pores peut aussi être modulé en faisant varier la longueur de la chaîne carbonée du surfactant ou en utilisant un

agent de gonflement des micelles, tel que triméthylbenzène.[11–13] Récemment, Zhang, Bonneviot *et al.* ont décrit une méthode pour contrôler finement, de manière robuste et reproductible, la morphologie des pores des MS NPs ayant un diamètre de l'ordre de 100 nm.[14] Dans cette étude, les auteurs ont utilisé de petites amines organiques (SOA) pour contrôler la croissance de la silice et permettant d'atteindre une bonne monodispersité des NPs. De plus, ils ont montré que lorsque la synthèse des MS NPs est effectuée en milieu basique doux (pH proche de 7 en raison de la faible quantité de SOA), la nature du contre-ion du surfactant utilisé détermine la structure des pores des MS NPs.

Ici, l'influence de la température comme simple paramètre de synthèse a été étudiée dans le but de moduler la morphologie des pores des MS NPs et aussi de la coquille de MS autour de cœurs d'IO. Ainsi nous avons montré que lorsque la température de réaction sol-gel (T_{sg}) dépasse un certain seuil, mesuré à environ 80 °C, la structure des pores passe d'une morphologie stellaire (ST) à une morphologie « worm-like » (WL) (**Figure 2**).

Une étude approfondie des isothermes d'adsorption-désorption de N_2 ont été réalisés pour caractériser ces changements de morphologie. Les caractéristiques relaxométriques (pour l'IRM) et magnétothermiques des NPs cœur-coquilles IO@STMS ou IO@WLMS ayant respectivement des morphologies stellaires ou de type WL ont été évaluées. Elles présentent des puissance magnétothermiques SAR dans la gamme 500 W/g (H=300 G, f=536 kHz) et des grandes relaxivités transversales des protons de l'eau r_2 (respectivement 307 vs. 156 $mM^{-1}.s^{-1}$ pour ST et WL) ce qui démontre que leurs propriétés sont parfaitement adaptées pour les applications en IRM et en hyperthermie magnétique (**Figure 3**). Par des mesures de relaxométrie et des images phantoms les propriétés d'imagerie IRM de ces objets en fonction de la porosité de la silice ont été montrées. Ces travaux ont donné lieu à la publication d'un article paru en 2021: Adam, A. *et al.* Orienting the Pore Morphology of Core-Shell Magnetic Mesoporous Silica with the Sol-Gel Temperature. Influence on MRI and Magnetic Hyperthermia Properties. *Molecules* **26**, 971 (2021).

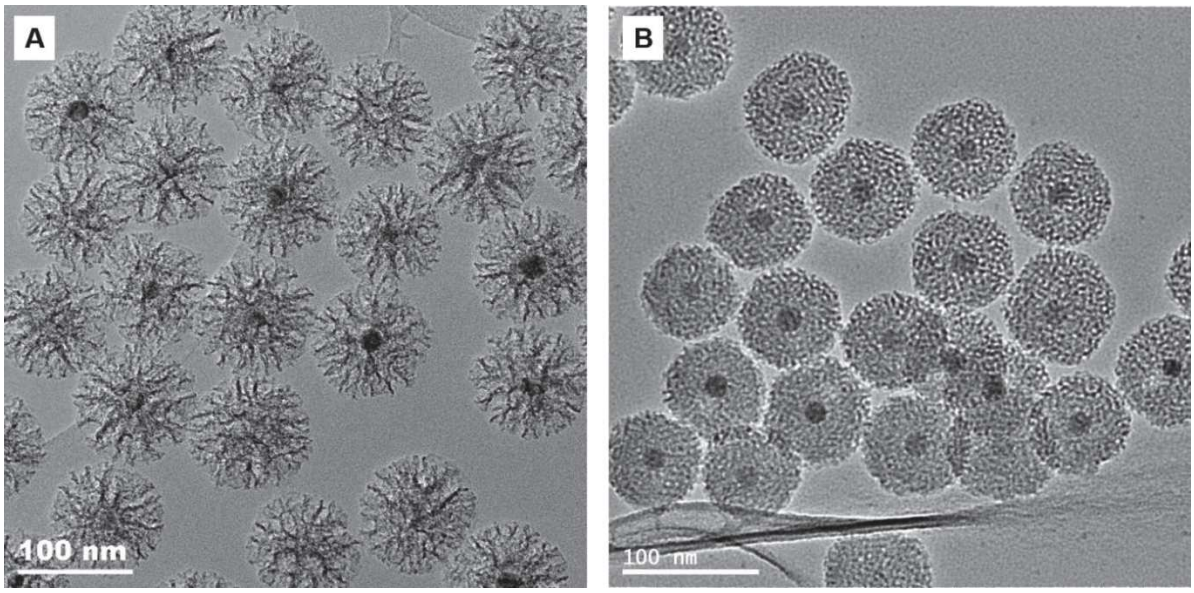

Figure 2. IO@STMS synthétisés à 70 °C (A) et IO@WLMS synthétisés à 80 °C (B).

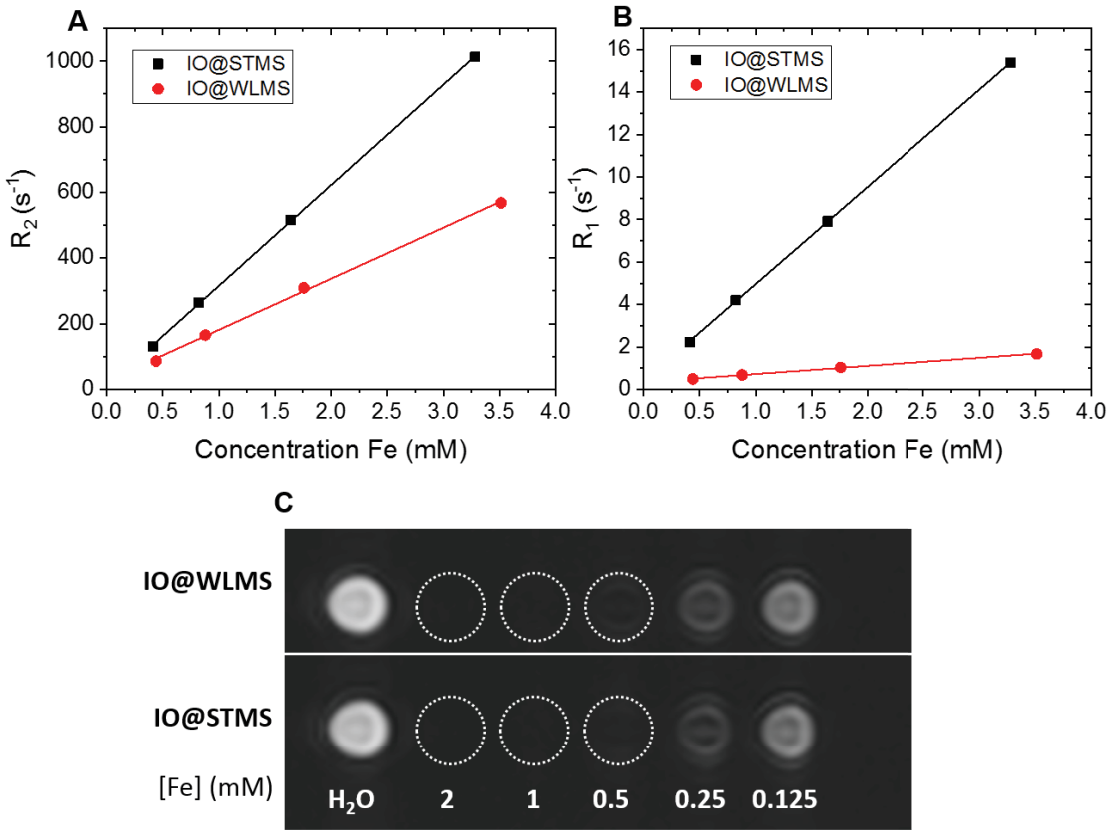

Figure 3. Vitesses de relaxation transervales $R_2 = 1/T_2$ (s^{-1}) (A) et longitudinales $R_1 = 1/T_1$ (s^{-1}) (B) en fonction de [Fe] (mM) pour IO@STMS et IO@WLMS dans l'eau à 37 °C et 1.41 T; images IRM pondérées en T_2 des IO@WLMS et IO@STMS, les cercles en pointillés blancs indiquent les positions de l'échantillon (C).

I.2. Influence des conditions de synthèses sur la morphologie de la silice et des propriétés magnétothermiques

Dans cette partie, nous avons ensuite synthétiser encore d'autres morphologies de silice en changeant cette fois-ci sur les réactifs en jeu lors de la réaction de formation de la silice. D'une part, par microémulsion inverse, il a été possible de synthétiser une coquille de silice qui ne présente pas de mésopores. D'une part, la morphologie des pores peut être modifiée en changeant la nature du surfactant. En effet, ceux-ci forment en solution des micelles de taille et de stabilité différentes. Ainsi la condensation du TEOS autour de ces structures conduit à différentes morphologies de la silice autour du cœur d'oxyde de fer (**Figure 4**). En utilisant le CTAB, les pores ont un diamètre d'environ 2-3 nm alors qu'avec le CTATos les pores sont plus élargis. En modulant T_{sg}, nous avons montré que la morphologie des pores de la coquille de silice MS peut être facilement orientée avec T_{sg}, soit vers la morphologie stellaire (ST) (grands pores radiaux d'environ 10 nm) pour $T_{sg} \leq 80$ °C ou vers une morphologie de type « worm-like » (WL) (canaux à pores aléatoires, de 3–4 nm de taille de pore) pour $T_{sg} \geq 80$ °C. Enfin, il est possible de faire varier l'épaisseur de la silice en variant le rapport [CTAB]/[Fe].

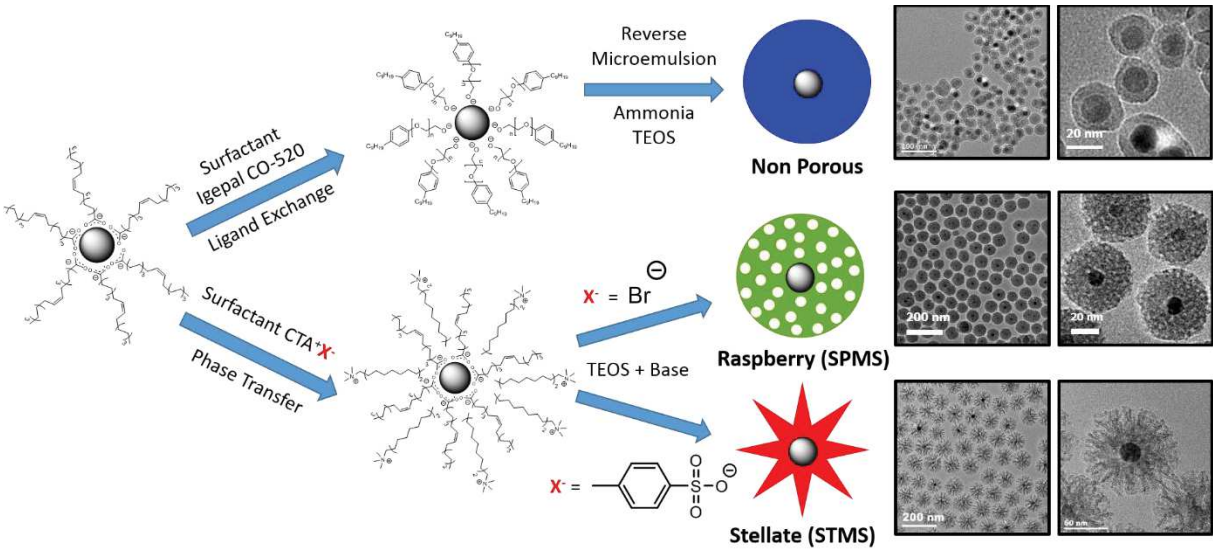

Figure 4. Résumé des différentes voies de synthèse résultant en différentes morphologies de pores.

L'évaluation des performances des nanomatériaux se fait en suivant des profils de température sous stimulus. Ceux-ci permettent ensuite de calculer les SAR. On constate que la morphologie de la silice a une influence significative sur les performances. En effet, à épaisseur constante, plus la silice est dense plus la SAR est faible. Le front de chaleur se dissipant depuis les cœurs d'oxyde de fer jusqu'à l'eau environnante est beaucoup plus atténué lorsque les pores de la silice sont resserrés et la coquille épaisse. Les molécules d'eau jouent probablement un rôle important dans le transport de la chaleur; une couche solide dense peut inhiber le transfert de chaleur par convection, qui est connu pour être beaucoup plus efficace que la conduction pure.

I.3. Nanothermométrie

La nanothermométrie est une technique développée pour mesurer la température à l'échelle nanométrique en utilisant des phénomènes physiques capables de sonder la température localement, au contact d'une NP par exemple. Les nanothermomètres luminescents sont certainement les plus prometteurs, mais très peu sont facilement disponibles.[15] Dans notre équipe, Perton *et al.*[16] ont montré qu'il était possible de greffer des QDs CdSeS/ZnS à la surface des NPs STMS. Nous avons donc étudié l'utilisation de ces QDs comme nanothermomètres pour les NP cœur-coquille IO@MS.

La première étude a visée à établir des courbes d'étalonnage par spectrofluorimétrie pour corréler les spectres d'émission des QDs à la température pour vérifier leur utilisation en tant que nanothermomètres. Pour cela, ces spectres d'émission d'une dispersion de QDs ont ensuite été enregistrés en fonction de la température (**Figure 5 A et B**). L'étape suivante a consisté à greffer ces QDs sur les NPs IO@MS afin d'étudier de mesurer la température locale à la surface des QDs. Il est clairement apparu que l'émission de QDs est restée sensible à la température et que le greffage n'a pas dégradé sa fluorescence. Lorsqu'on compare les variations linéaires de λ_{max} et d'I_{max} avec la température, on note que la pente de la variation de λ_{max} reste constante pour les deux systèmes (QDs greffés et non-greffés) (environ 0,1 nm/°C) (**Figure 5**).

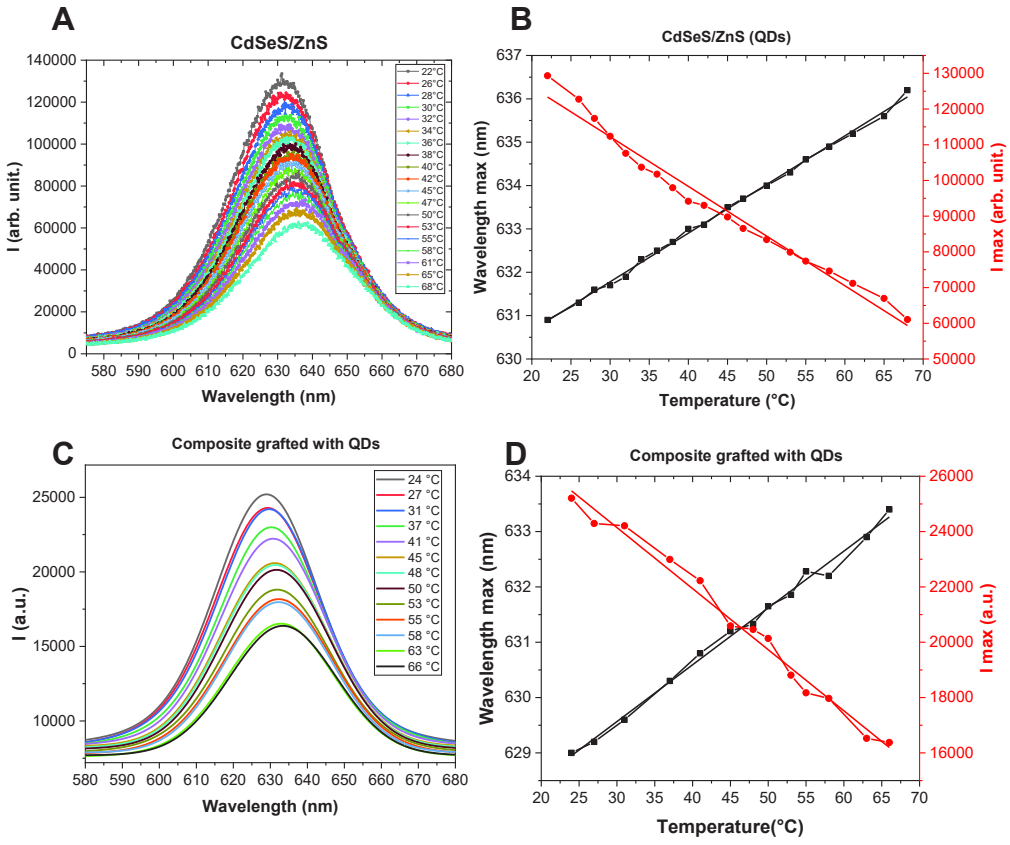

Figure 5. Fluorescence de QDs CdSeS/ZnS QDs en fonction de la température; **(A)** données brutes, **(B)** données ajustées avec un modèle de Voigt et **(C)** λ_{max} and I_{max} en fonction de la température.

Malheureusement, à la suite de différents essais, aucun effet clair de l'AMF n'a pu être constaté. Par conséquent, il est difficile de conclure si une température locale (hot spot) a été détectée ou non en raison de phénomène tels que la sédimentation des NPs et l'interaction du champ magnétique avec la sonde de température qui masquait le signal.

En résumé, il s'agit d'une expérience prometteuse qui pourrait nous aider à mieux comprendre la dissipation de la chaleur depuis le cœur d'oxyde de fer vers l'environnement. Cependant, le montage, le greffage des QDs et le traitement des données doivent être améliorés. De nouvelles sessions d'expériences ont été programmées et devraient contribuer à perfectionner le système. Plusieurs options sont à l'étude; en particulier, immobiliser les NPs dans un gel ou les déposer sur un substrat, pour s'affranchir des effets de sédimentation.

II. Nanoparticules coeur-coquille oxyde de fer-silice pour un traitement combiné par photothermie et délivrance de médicaments : influence du pH et de la chimie de surface

Outre l'utilisation d'un champ magnétique alternatif comme stimulus externe, l'application d'un laser à lumière proche infrarouge (NIR) est également très prometteur. En effet, grâce à sa simplicité d'utilisation et son faible coût, la lumière NIR peut être facilement appliquée par toute une gamme de lasers avec des puissances et des longueur d'onde variables. Par rapport à la lumière visible, la lumière NIR a une meilleure pénétration des tissus biologiques, dans la plage de 800 - 1300 nm, allant jusqu'à 3 cm.[17,18] L'hyperthermie induite par laser NIR (photothermie) est actuellement développée comme un traitement très peu invasif où des sensibilisateurs photothermiques organiques ou inorganiques transforment cette lumière absorbée en chauffage localisé dans l'environnement des nanoparticules.

II.1. Conception de la nanoplateforme et étude du chargement et de la libération de médicaments

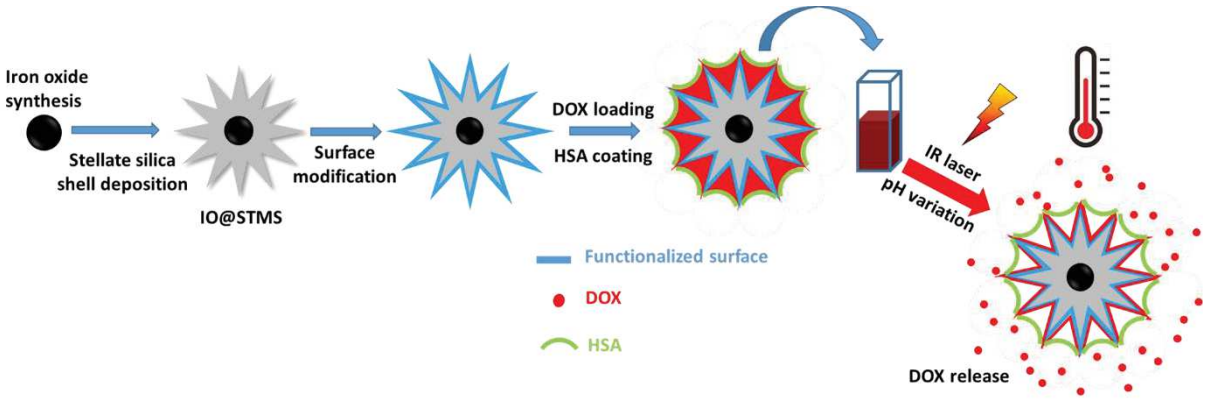

Figure 6. Représentation schématique illustrant la préparation étape par étape de nanocomposites cœur-coquille chargés de médicaments et les propriétés combinées de photothermie induite par la lumière NIR et la libération de médicaments déclenchée par le pH.

Dans cette deuxième partie, nous étudions l'utilisation de NPs cœur-coquille IO@STMS comme système original combinant des propriétés photothermiques et de libération de médicament pour une bithérapie du cancer (**Figure 6**). Tout d'abord, les propriétés photothermiques de ces NP cœur-coquille ont été étudiées sous stimulation par lumière NIR. Pour cela, les profils de température ont été tracés et les taux d'absorption spécifiques (*specific absorption rate* (SAR)) ont été calculés en fonction de la puissance du laser et de la concentration des NPs. Les données indiquent que les suspensions s'échauffent rapidement sous l'effet de la lumière NIR. En fonction de la concentration en NPs et de la puissance du laser, les propriétés photothermiques peuvent être finement ajustées, ce qui en fait des systèmes performants pour des applications biomédicales (**Figure 7**).

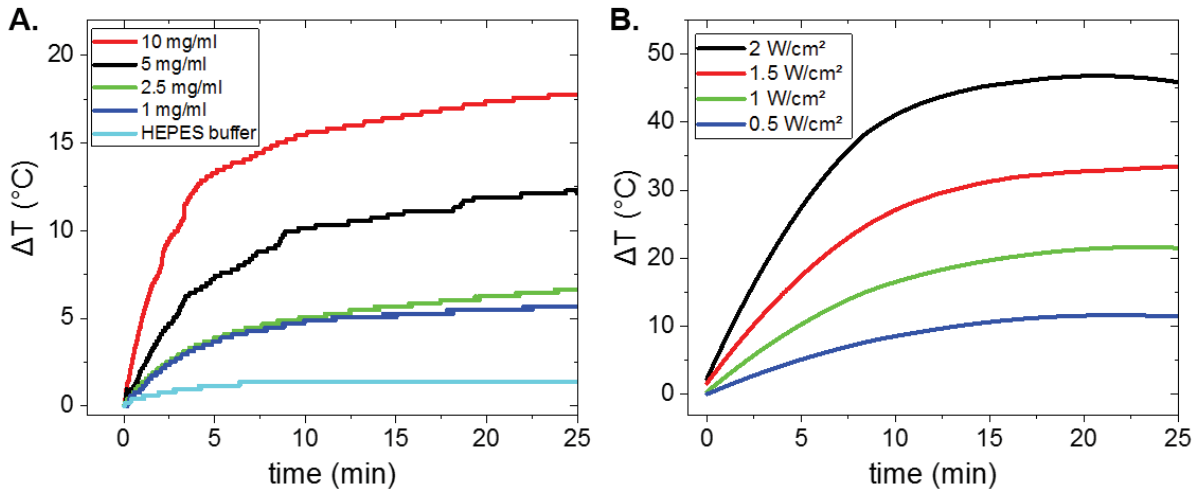

Figure 7. (A) Elévations de température sous laser NIR laser à 1 W.cm^{-2} pour différentes concentrations en NPs et **(B)** pour différentes puissances de laser, à une concentration en NPs concentration de 5 mg.mL^{-1}.

Deuxièmement, l'effet de paramètres clés, tels que le pH de la solution d'imprégnation du médicament, la chimie de surface des NPs ou la présence d'un cœur d'oxyde de fer (STMS vs. IO@STMS) sur la capacité de charge du médicament a été étudié. Un moyen très classique d'améliorer la charge en médicaments sur les nanoparticules de silice par rapport à la surface non-modifiées est la modification par un aminosilane et particulièrement par APTES (3-aminopropyltriethoxysilane) qui est testé ici avec IO@STMS. De manière plus originale, les groupes amines sont ensuite modifiés par des fonctions isobutyramide (IBAM). L'objectif de ce traitement de surface est de pouvoir à la fois charger la DOX en grande quantité et de pouvoir revêtir la surface de HSA pour assurer une bonne stabilité colloïdale, ainsi qu'une bonne biocompatibilité en limitant par exemple l'opsonisation ou l'immunogenicité des NPs. En ce qui concerne le chargement en DOX de ces nanocomposites, le pH de la solution d'imprégnation s'est avéré être le paramètre critique déterminant le chargement en médicaments alors que la chimie de surface : non-modifié, APTES ou IBAM a un impact limité. Par exemple, avec IO@STMS@IBAM nous avons montré qu'un chargement à pH = 7,5, permettait d'atteindre une DLC jusqu'à 73%, un chargement élevé par rapport à la littérature, alors qu'à pH = 5,5, la DLC atteignait seulement 7% (**Figure 8**).

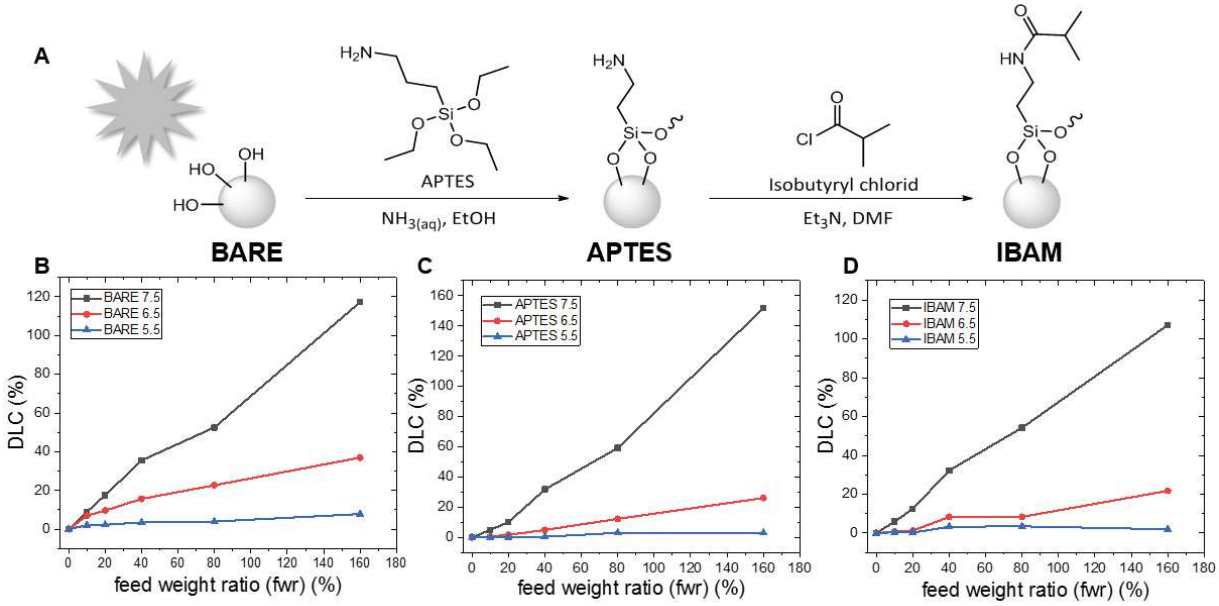

Figure 8. Voie chimique utilisée pour obtenir les différentes chimies de surface (A) et les DLC correspondantes des surfaces BARE (B), APTES (C) et IBAM (D) aux trois pHs évalués.

Enfin, pour évaluer à la fois la possibilité d'un traitement par hyperthermie induite par la lumière NIR et combiné à la libération de médicaments à partir de ces systèmes IO@STMS@DOX@HSA, une étude de libération cumulative a été réalisée pendant 4 jours en présence ou en l'absence de lumière NIR. Ains, l'irradiation NIR ne semble pas déclencher la libération du médicament ; mais une baisse du pH est très efficace pour libérer la DOX en solution et la quantité libérée dépend beaucoup de la chimie de surface. Cette libération de médicaments à faible pH (pH 5,5) peut être bénéfique pour une

administration intracellulaire dans les compartiments lysosomaux ou dans les tissus cancéreux qui sont connus pour être des environnements acides. Dans les travaux suivants, une étude biologique sur des cellules cancéreuses devra évaluer les interactions des NPs avec les cellules et l'effet synergique de la photothermie et de la libération de médicaments dans le but de produire des traitements antitumoraux.

II.2. Etudes biologiques

L'étape suivante consiste à évaluer et à valider cette nanoplateforme en tant que système efficace pour la PTT et la libération localisée de médicaments. Pour cela, nous avons collaboré avec des biologistes de l'INSERM (équipe U1109 Tumor Biomechanics) pour évaluer l'efficacité antitumorale et la biocompatibilité de ces nanoplateformes. Des études préliminaires *in vitro* et *in vivo* ont été effectuées. Des cellules du mélanome du poisson-zèbre (ZMEL-1) ont été choisies comme modèle de la lignée cellulaire de référence. A la lumière des résultats de la section précédente (III.1) où nous avons étudié trois chimies de surface différentes, nous avons pu choisir le système plus approprié, IO@STMS@IBAM@DOX@HSA. Ainsi, l'efficacité de nos nanoplateformes sur ces cellules cancéreuses *in vitro* a été étudiée et les conditions les plus appropriées (concentration des NP, puissance laser et durée) ont été définies. Ensuite, la même lignée cellulaire peut être étudiée *in vivo* après une transplantation intraveineuse chez le poisson zèbre pour imiter des tumeurs métastatiques. Les embryons de poisson zèbre (ZF) sont des modèles particulièrement adaptés aux études *in vivo*. Ils présentent les avantages de se reproduire rapidement, d'avoir un développement rapide et d'être optiquement transparents. Ce dernier point permet de suivre les NPs fluorescentes par microscopie confocale.

Une première expérience a consisté à observer par microscopie optique (transmission) et confocale, l'effet de l'irradiation lumineuse NIR sur les cellules tumorales ZMEL-1 incubées avec des NP IO@STMS@IBAM@DOX@HSA-FITC. Ici, la couche externe de protéine du nanocomposite a été remplacée par une HSA marquée avec de l'isothiocyanate de fluorescéine (HSA-FITC) pour avoir une couleur de fluorescence supplémentaire. La FITC permet un marquage vert alors que la DOX fluoresce naturellement dans le rouge.

Les intensités de fluorescence intracellulaire ont été mesurées en fonction du temps afin d'étudier l'accumulation et la diffusion de DOX à l'intérieur des cellules sur de larges clichés contenant des dizaines de cellules. Lors de l'irradiation NIR, le niveau de fluorescence DOX est très élevé par rapport aux systèmes non irradiés qui n'ont montré qu'un niveau relativement très faible de fuite. Ainsi, l'irradiation NIR semble déclencher la libération de DOX. Ce résultat est très prometteur et tend à montrer que le système peut être activé par la lumière dans les cultures cellulaires, ce qui n'était pas le cas lorsqu'il a été testé comme dispersion dans des cuvettes dans la section précédente (III.1).

Sur les photos, l'accumulation des NP sur les parois cellulaires et à l'intérieur du cytoplasme peut être observée (taches fluorescentes plus intenses). La DOX qui se dégage des NP se diffuse et s'accumule progressivement à l'intérieur des noyaux cellulaires, ce qui correspond au mode d'action de la DOX (**Figure 9**).

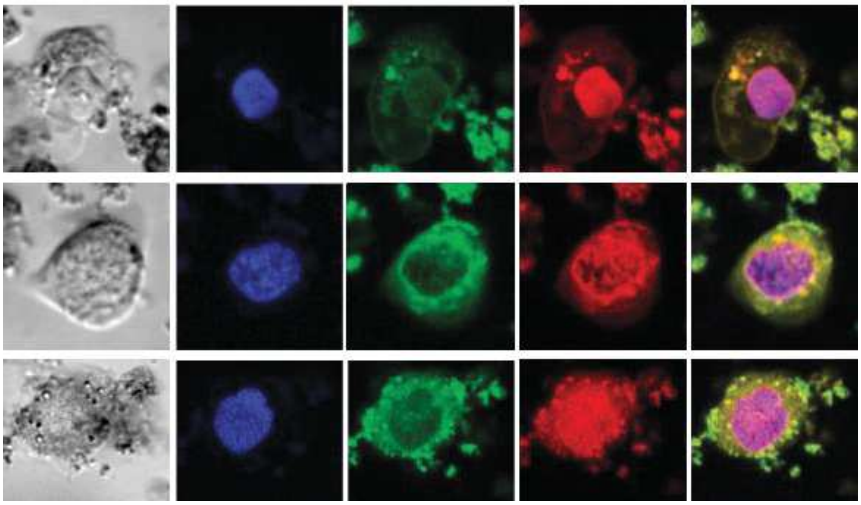

Figure 9. Première colonne : microscopie optique en transmission de cellules individuelles après incubation avec IO@STMS@IBAM@DOX@HSA-FITC. De la deuxième à la dernière colonne, les mêmes cellules en microscopie par fluorescence : bleu (noyau), vert (HSA-FITC), rouge (DOX) et les images fusionnées sur la dernière ligne.

Des tests de cytotoxicité cellulaires ont ensuite été réalisés sur ces mêmes cellules Zmel. Nous avons étudié l'effet de la concentration en NPs (chargées en DOX vs non chargées) et nous avons comparé l'effet antitumoral sous lumière NIR par rapport à l'absence de lumière IR (**Figure 10 et 12).** Tout d'abord, les résultats montrent qu'en l'absence de la lumière IR, la toxicité cellulaire est modérée, indépendamment de la concentration en NPs et de la charge en DOX (cf barres noires, **Figure 10**). Ensuite, en ce qui concerne l'action de la lumière IR, les données montrent qu'en l'absence de DOX, l'action photothermique a un effet très important sur la toxicité cellulaire qui est dose-dépendante (cf barres rouges, No DOX). Enfin, pour les NPs chargées en DOX, le plus fort effet cytotoxique est observé sous l'action de la lumière IR (cf barres rouges, DOX) ; ce qui démontre un effet synergique important de l'action photothermique et de la libération de DOX.

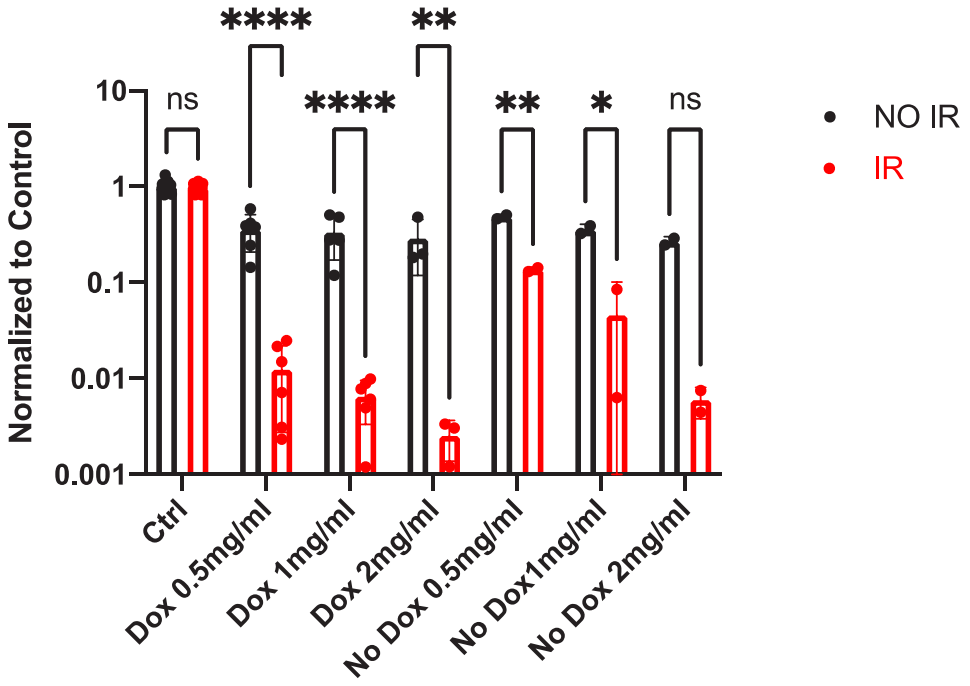

Figure 10. Tests de cytotoxicité avec (barres rouges) and sans (barres noires) irradiation NIR. Des NPs charges en DOX (Dox) and non-chargées (No Dox) ont été testées à trois concentrations différentes.

Enfin, une étude préliminaire *in vivo* sur des embryons de poissons zèbre injectés avec des NPs cœur-coquilles a été réalisée dans le but d'évaluer l'effet de ces NPs sur le développement des embryons sur plusieurs jours, la biocompatibilité et la biodistribution de ces NPs. Les NPs ont été injectées dans le yolk des poissons zèbre. La mesure de la taille des embryons montre que l'injection des nanoparticules n'affectent pas leur croissance sur les 4 jours de l'étude par rapport à l'expérience contrôle sans NPs. Une expérience complémentaire mesurant le nombre de battements de cœur par seconde dans les poissons n'a pas montré de différence entre les poissons injectés avec les NPs et les poisson non injectés.

Pour observer la biodistribution à l'intérieur des embryons ZF, ils ont été injectés avec des core-shell marqués à la fluorescéine IO@STMS@IBAM@DOX@HSA-FITC. Une distribution homogène de NP dans le corps entier du poisson peut être observée par un marquage fort de la vascularisation. Ces données mettent en évidence la bonne circulation des NPs. La colocalisation de la fluorescence rouge de la DOX et de la fluorescence verte de la HSA-FITC suggère que ces deux molécules sont toujours sur les NPs lorsque les images ont été prises, ce qui indique une bonne stabilité de la formulation (**Figure 11**). D'autres expériences de colocalisation des NPs avec la DOX et la HSA seront menées. Plusieurs méthodes peuvent être utilisées pour localiser les NPs à base d'IO comme l'IRM *in vivo*, le TEM sur de minces sections de tissu, la spectroscopie de particules magnétiques (MPS)[19] ou la coloration par bleu de Prusse[20].

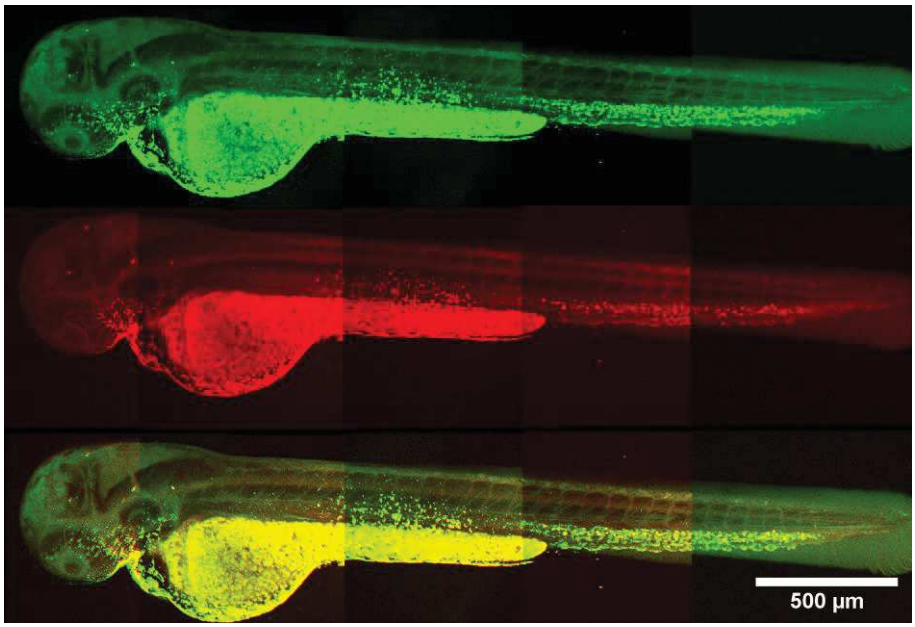

Figure 11. Microscopie par fluorescence d'embryons ZF 3 h après injection avec des NP chargées en DOX ; de haut en bas, vert de la FITC, rouge de la DOX et images fusionnées.

III. Hydrogels de peptides auto-assemblés comme modèle de matrice implantable thérapeutique

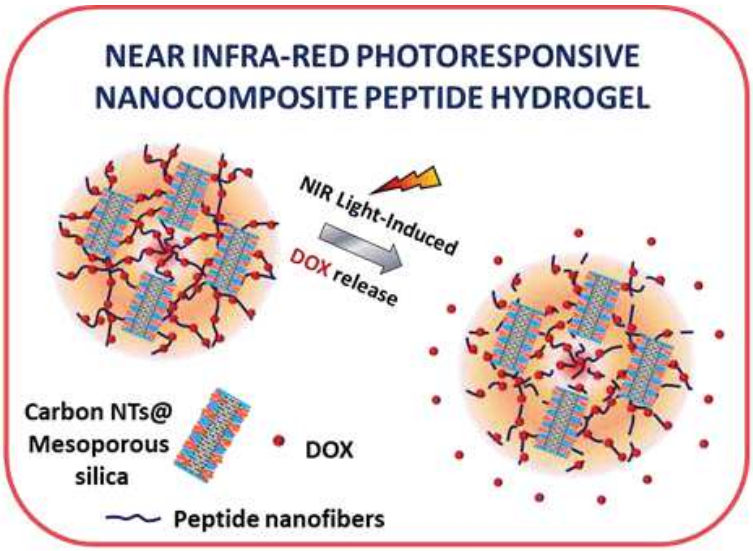

Dans le chapitre précédent, nous avons démontré que les NPs IO@STMS peuvent être des systèmes adaptés pour de nouvelles applications combinant la PTT et la délivrance de médicaments. Cependant, dans certains cas de cancer, il peut être très difficile de cibler les sites tumoraux en utilisant des NP circulantes ou des médicaments injectés dans la circulation sanguine. Soit par la clairance rénale ou par absorption par les macrophages, le médicament peut être éliminé rendant le traitement inefficace.

Mais le médicament peut également s'accumuler dans les tissus sains, généralement les organes filtrants tels que le foie, les reins, la vessie, la rate et causant une cytotoxicité indésirable.

Des systèmes de délivrance de médicaments implantables sont maintenant conçus pour tenter de combler ces lacunes. En étant implantés autour ou à l'intérieur de la tumeur, ils devraient permettre de délivrer des médicaments localement, présenter un profil de libération contrôlée du médicament pour maintenir une concentration thérapeutique sur des temps longs et prévenir l'élimination du médicament. Des implants intelligents qui pourraient être activés à distance par des champs externes comme la lumière NIR sont donc particulièrement nécessaires. Ceux-ci pourraient être obtenus par la combinaison de NPs activables comme nous l'avons décrit ci-dessus et d'une matrice implantable biocompatible comme des hydrogels qui émergent comme outils pour concevoir cette nouvelle génération de matériaux. L'incorporation de NPs a également l'avantage d'augmenter la stabilité mécanique de l'hydrogel.

Ainsi, dans ce dernier chapitre de thèse, nous décrivons une approche originale pour déclencher l'auto-assemblage d'un tripeptide en un hydrogel à partir d'un nanocomposite (CNT@LPMS) recouvert d'enzymes. Les CNTs, qui ont été choisis pour leur propriétés photothermiques sous lumière NIR, ont été recouvert d'une couche de silice mésoporeuse à large pores (> 10 nm) (CNT@LPMS), ce qui les rend particulièrement adaptés au chargement de biomacromolécules comme des enzymes (**Figure 12**). En chargeant ces hydrogels de médicaments, le but est d'induire une libération contrôlée de celui-ci par irradiation NIR et photothermie.

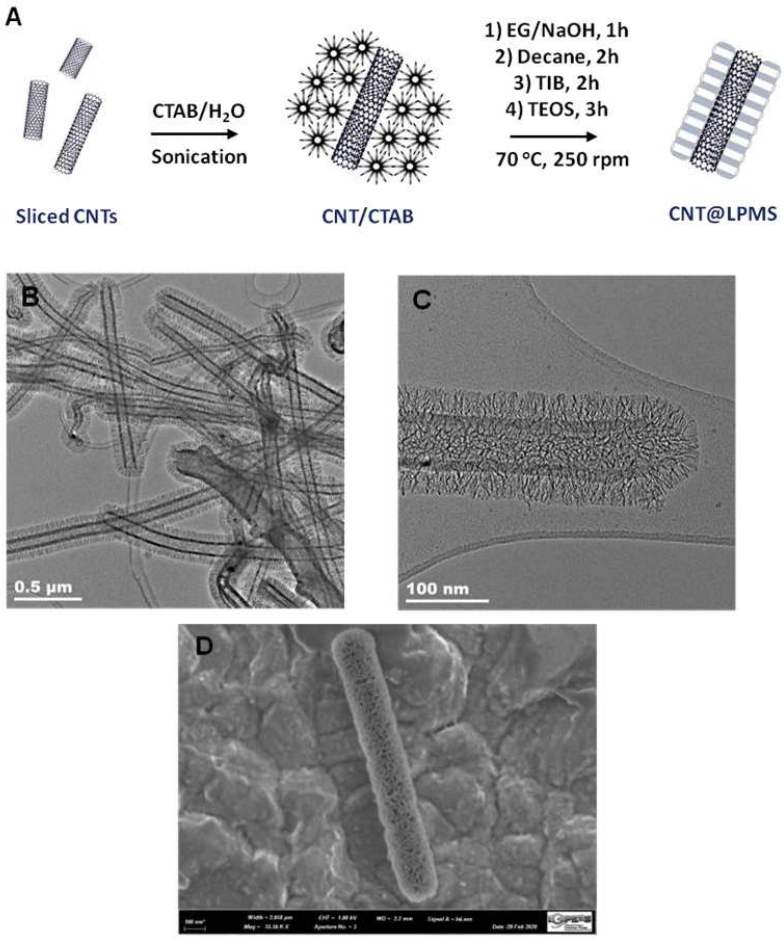

Figure 12. (A) Représentation schématique de la synthèse de CNT@LPMS. (B, C) images MET et (D) images MEB des CNT@LPMS.

Grâce à une modification de la surface de la silice par des groupements IBAM, une grande quantité d'enzymes, la phosphatase alcaline (AP), a pu être immobilisée dans les pores larges de la silice. Pour régir avec cette enzyme, un tripeptide phosphaté, le Fmoc-FFpY, a été choisi. Par réaction avec AP dans des conditions alcalines, le groupement phosphate est retiré. Dans des conditions optimales, ce peptide déphosphaté est connu pour s'auto-assembler. L'excellente capacité de charge en AP des composites CNT@LPMS@IBAM leur permet d'agir comme points d'activation de l'auto-assemblage du peptide et de points de réticulation de l'hydrogel supramoléculaire, ce qui permet une croissance localisée des nanofibres à partir de la surface de silice.

L'incorporation de doxorubicine (DOX) pendant le processus d'hydrogélation conduit à un matériau réservoir d'agents anticancéreux. Par la combinaison d'études rhéologiques et de simulations moléculaires, un mécanisme original d'interactions de la DOX avec le gel est mis en évidence : la DOX n'est pas juste dans des poches de solvant entres les fibres mais s'inclut dans les fibres de peptides. De plus, une libération importante de DOX à partir de ces hydrogels est obtenue lorsque les hydrogels chargés de DOX ont été stimulés par chauffage : environ trois fois plus de DOX se libère à 42 °C qu'à 25 °C.

Ensuite, la capacité de ces hydrogels à chauffer sous stimulation par lumière NIR a été évaluée. Pour cela, les gels sont placés dans 1 mL d'eau ultra pure. Comme le montre la **Figure 13**, un effet photothermique évident dépendant la concentration en CNT@LPMS est observé. La température de la solution autour des gels de CNT@LPMS augmente rapidement au début puis se stabilise en prolongeant la stimulation lumineuse NIR. Avec une masse de CNT@LPMS de 200 µg, l'augmentation de T peut atteindre environ 11 °C. Ces performances photothermiques de CNT@LPMS sont remarquables et en font un agent photothermique efficace pour stimuler la libération de médicaments.

Puis, on a étudié la libération de la DOX par effet photothermique sous lumière NIR à partir d'hydrogels de ces nanocomposites en exposant des hydrogels contenant différentes masses de CNT (9 à 94 µg) au laser NIR pendant 2 h (**Figure 13.C**). Pour mesurer la fuite spontanée de médicaments, on mesure aussi la quantité de DOX libérée par des échantillons témoins contenant la même masse de CNT sans stimulation NIR (barres bleues). Les résultats (barres rouges) indiquent que l'augmentation de la masse de CNT dans l'hydrogel conduit à des niveaux similaires de libération de DOX sous la stimulation de la lumière NIR. Environ 6 % de la DOX a été libérée sur deux heures par l'hydrogel sous stimulation laser NIR, ce qui était presque quatre fois celui de l'échantillon témoin (environ 1,5 %).

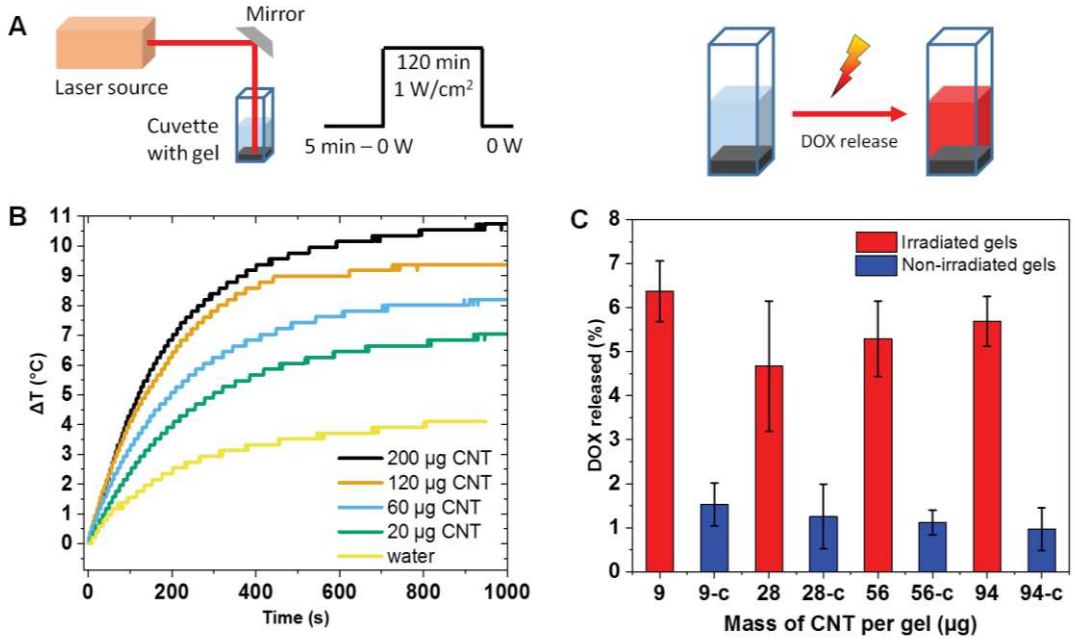

Figure 13. (A) Schéma du dispositif et de la séquence utilisés pour réaliser l'irradiation par lumière NIR. **(B)** Profils de température en fonction de la masse de composites CNT@LPMS. **(C)** Taux de libération de DOX (% par rapport au chargement initial) sous irradiation NIR pendant 2 h à 1W/cm^2.

Dans l'ensemble, ces résultats indiquent que ces hydrogels supramoléculaires nanocomposites assemblés à partir de matériaux mésoporeux à larges pores et enrobés d'enzymes peuvent être utilisés comme nanoplateformes de libération contrôlée de médicaments par stimulation infrarouge. L'association des nanocomposites CNT@LPMS et de l'hydrogel supramoléculaire est une stratégie

innovante qui peut être utilisée pour développer une nouvelle génération de systèmes de délivrance de médicaments activables par des stimuli adaptés aux applications biomédicales.

Conclusion

Les objectifs de ma thèse de doctorat étaient de combiner des silices mésoporeuses avec des matériaux répondants au champ magnétique et à la lumière infrarouge dans le but de produire des nanoplateformes cœur-coquille intelligentes pour une thérapie multimodale du cancer. Après avoir examiné les systèmes existants à partir de la littérature, un ensemble de spécifications que ces nanoplateformes devaient respecter a été établi :

i) Par un choix approprié du matériau de cœur, les nanomatériaux devraient produire de la chaleur par application d'un AMF, de lumière NIR ou des deux.

ii) Par à un design optimisé de la coque de silice, les nanocomposites devraient pouvoir transporter et libérer une grande quantité de médicaments antitumoraux.

iii) Par une formulation appropriée, les nanoplateformes développées devraient être utilisables comme traitement injectable ou implantable.

Pour ce faire, nous nous sommes d'abord concentrés sur la synthèse de NP silice@oxyde de fer (**chapitre 2**). A partir des NP d'IO, nous avons réussi à produire des coquilles de silice de différentes épaisseurs et morphologies en ajustant la température de la réaction sol-gel ou en modulant les réactifs et les méthodes de synthèse. Avec une coquille de silice plus épaisse et plus dense autour des cœurs d'IO, le transfert de chaleur est plus réduit et donc l'élévation de température sous AMF est atténuée. Pour un transfert de chaleur optimal, les pores de la silice doivent être très ouvert et la coquille relativement mince. Afin d'évaluer la variation du transfert de chaleur en fonction de la coquille de silice, des expériences de nanothermométrie ont été mises en œuvre. Celles-ci sont toujours en cours car certaines optimisations du dispositif sont nécessaires.

Ensuite, nous sommes allés plus loin dans l'évaluation de ces NPs IO@STMS pour le traitement par hyperthermie. Comme alternative originale au traitement par hyperthermie magnétique, l'accent a été mis sur leurs caractéristiques en tant qu'agents de photothérapie (**Chapitre 3**). En effet, ces NPs cœur-coquille ont montré une très bonne conversion de la lumière NIR en chaleur, ce qui les rend adaptés au PTT. Par la suite, le chargement et la libération de médicaments (doxorubicine) depuis ce système a été étudié. Nous avons montré que le pH est crucial lorsque la DOX est utilisée comme anticancéreux. Un pH légèrement supérieur à 7 permet d'améliorer considérablement la quantité de médicament chargée grâce à des interactions DOX-silice et DOX-DOX favorables. En ce qui concerne la libération du médicament, la chimie de surface et le pH semblent importants à la fois pour minimiser la fuite

indésirable du médicament et pour maximiser la libération du médicament au moment opportun. Pour cela, la fonctionnalisation par des groupes IBAM a montré les meilleurs résultats. Ainsi, nous avons synthétisé un système à base de NP cœur-coquille qui peut être utilisé pour une double thérapie du cancer. Des tests biologiques préliminaires a été effectuée pour démontrer le potentiel de cette formulation : IO@STMS@IBAM@DOX@HSA. Les tests *in vitro* ont montré que la libération de DOX pouvait être déclenchée par l'irradiation infrarouge. De plus, les tests de cytotoxicité sur des cellules du mélanome, ont montré une action antitumorale synergique de l'exposition à la lumière NIR et à la DOX. Ces résultats sont très encourageants pour comprendre l'efficacité des nanoformulations développées comme traitements antitumoraux par double thérapie : photothermie et délivrance de médicaments.

Dans un dernier chapitre, nous avons ajouté un niveau d'organisation supplémentaire aux nanocomposites en les incorporant dans un hydrogel (**chapitre 4**). L'une des principales limites à l'utilisation d'hydrogels pour les applications biomédicales est leur résistance mécanique qui peut être très faible par rapport à d'autres matrices implantables. Ainsi, la nanoparticule a été conçue de manière à ce que son incorporation dans un gel apporte une meilleure stabilité mécanique, tout en pouvant être activée à distance pour la thérapie. C'est pourquoi les NTC ont été choisis comme matériau de base. Ensuite, une coquille de silice à larges pores a été synthétisée autour pour construire le composite NTC@LPMS. Puis, nous avons utilisés la porosité et la capacité d'immobilisation de la silice modifiée par des groupes IBAM pour y charger une enzyme capable de déclencher l'auto-assemblage d'un tripeptide en un hydrogel. Par conséquent, CNTs@LPMS a agi comme des points de réticulation pour l'assemblage de l'hydrogel permettant d'augmenter la stabilité du gel et d'empêcher toute diffusion de nanoparticules à l'extérieur. De plus, le gel a été chargé de DOX et nous avons démontré que la libération de DOX à partir du gel pouvait être déclenchée par stimulation sous laser NIR. Cette stratégie novatrice devrait déboucher sur la mise au point d'une nouvelle génération de systèmes activables de délivrance de médicaments.

Références

(1) Sung, H.; Ferlay, J.; Siegel, R. L.; Laversanne, M.; Soerjomataram, I.; Jemal, A.; Bray, F. Global Cancer Statistics 2020: GLOBOCAN Estimates of Incidence and Mortality Worldwide for 36 Cancers in 185 Countries. *CA. Cancer J. Clin.* **2021**, *71* (3), 209–249.

(2) Feng, S.-S.; Chien, S. Chemotherapeutic Engineering: Application and Further Development of Chemical Engineering Principles for Chemotherapy of Cancer and Other Diseases. *Chem. Eng. Sci.* **2003**, *58* (18), 4087–4114.

(3) Anselmo, A. C.; Mitragotri, S. Nanoparticles in the Clinic: An Update. *Bioeng. Transl. Med.* **2019**, *4* (3), e10143.

(4) Huang, H.; Feng, W.; Chen, Y.; Shi, J. Inorganic Nanoparticles in Clinical Trials and Translations. *Nano Today* **2020**, *35*, 100972.

(5) van der Zee, J. Heating the Patient: A Promising Approach? *Ann. Oncol.* **2002**, *13* (8), 1173–1184.

(6) Overgaard, J. Effect of Hyperthermia on Malignant Cells in Vivo: A Review and a Hypothesis. *Cancer* **1977**, *39* (6), 2637–2646.
(7) Kolosnjaj-Tabi, J.; Kralj, S.; Griseti, E.; Nemec, S.; Wilhelm, C.; Plan Sangnier, A.; Bellard, E.; Fourquaux, I.; Golzio, M.; Rols, M.-P. Magnetic Silica-Coated Iron Oxide Nanochains as Photothermal Agents, Disrupting the Extracellular Matrix, and Eradicating Cancer Cells. *Cancers* **2019**, *11* (12), 2040.
(8) Nemec, S.; Kralj, S.; Wilhelm, C.; Abou-Hassan, A.; Rols, M.-P.; Kolosnjaj-Tabi, J. Comparison of Iron Oxide Nanoparticles in Photothermia and Magnetic Hyperthermia: Effects of Clustering and Silica Encapsulation on Nanoparticles' Heating Yield. *Appl. Sci.* **2020**, *10* (20), 7322.
(9) Du, X.; He, J. Fine-Tuning of Silica Nanosphere Structure by Simple Regulation of the Volume Ratio of Cosolvents. *Langmuir* **2010**, *26* (12), 10057–10062.
(10) Wang, S.-G.; Wu, C.-W.; Chen, K.; Lin, V. S.-Y. Fine-Tuning Mesochannel Orientation of Organically Functionalized Mesoporous Silica Nanoparticles. *Chem. – Asian J.* **2009**, *4* (5), 658–661.
(11) Cho, Y.; Shi, R.; Ivanisevic, A.; Borgens, R. B. A Mesoporous Silica Nanosphere-Based Drug Delivery System Using an Electrically Conducting Polymer. *Nanotechnology* **2009**, *20* (27), 275102.
(12) Wu, L.; Jiao, Z.; Wu, M.; Song, T.; Zhang, H. Formation of Mesoporous Silica Nanoparticles with Tunable Pore Structure as Promising Nanoreactor and Drug Delivery Vehicle. *RSC Adv.* **2016**, *6* (16), 13303–13311.
(13) Zhao, D.; Huo, Q.; Feng, J.; Chmelka, B. F.; Stucky, G. D. Nonionic Triblock and Star Diblock Copolymer and Oligomeric Surfactant Syntheses of Highly Ordered, Hydrothermally Stable, Mesoporous Silica Structures. *J. Am. Chem. Soc.* **1998**, *120* (24), 6024–6036.
(14) Zhang, K.; Xu, L.-L.; Jiang, J.-G.; Calin, N.; Lam, K.-F.; Zhang, S.-J.; Wu, H.-H.; Wu, G.-D.; Albela, B.; Bonneviot, L.; Wu, P. Facile Large-Scale Synthesis of Monodisperse Mesoporous Silica Nanospheres with Tunable Pore Structure. *J. Am. Chem. Soc.* **2013**, *135* (7), 2427–2430.
(15) Brites, C. D. S.; Lima, P. P.; Silva, N. J. O.; Millán, A.; Amaral, V. S.; Palacio, F.; Carlos, L. D. Thermometry at the Nanoscale. *Nanoscale* **2012**, *4* (16), 4799.
(16) Perton, F.; Tasso, M.; Muñoz Medina, G. A.; Ménard, M.; Blanco-Andujar, C.; Portiansky, E.; van Raap, M. B. F.; Bégin, D.; Meyer, F.; Begin-Colin, S.; Mertz, D. Fluorescent and Magnetic Stellate Mesoporous Silica for Bimodal Imaging and Magnetic Hyperthermia. *Appl. Mater. Today* **2019**, *16*, 301–314.
(17) Stolik, S.; Delgado, J. A.; Pérez, A.; Anasagasti, L. Measurement of the Penetration Depths of Red and near Infrared Light in Human "Ex Vivo" Tissues. *J. Photochem. Photobiol. B* **2000**, *57* (2), 90–93.
(18) Henderson, T. A.; Morries, L. D. Near-Infrared Photonic Energy Penetration: Can Infrared Phototherapy Effectively Reach the Human Brain? *Neuropsychiatr. Dis. Treat.* **2015**, *11*, 2191–2208.
(19) Scharlach, C.; Kratz, H.; Wiekhorst, F.; Warmuth, C.; Schnorr, J.; Genter, G.; Ebert, M.; Mueller, S.; Schellenberger, E. Synthesis of Acid-Stabilized Iron Oxide Nanoparticles and Comparison for Targeting Atherosclerotic Plaques: Evaluation by MRI, Quantitative MPS, and TEM Alternative to Ambiguous Prussian Blue Iron Staining. *Nanomedicine Nanotechnol. Biol. Med.* **2015**, *11* (5), 1085–1095.
(20) Millward, J. M.; Schnorr, J.; Taupitz, M.; Wagner, S.; Wuerfel, J. T.; Infante-Duarte, C. Iron Oxide Magnetic Nanoparticles Highlight Early Involvement of the Choroid Plexus in Central Nervous System Inflammation. *ASN Neuro* **2013**, *5* (2), AN20120081.

General Introduction

In 2020, cancer was responsible for the death of 10.0 million people worldwide (International Agency for Research on Cancer) and the global cancer burden is expected to be 28.4 million cases in 2040.[1] Lungs, liver and colorectal cancers represent approximately one third of the total cancers (**Figure 1**). Cancers occur when normal cells are transformed into neoplastic cells, which induces their uncontrolled growth and the formation of a tumor. When cancer cells break away for the original tumor, they can disseminate and reach other healthy organs through the bloodstream; this process is called metastasis. The mechanisms of cancer formation and spreading are still not completely unraveled. However, it has been shown that both external factors as chemicals and radiations exposure, infections, smoking and internal factors as genetic mutations and immune conditions may act together or independently to initiate and spread cancer.[2]

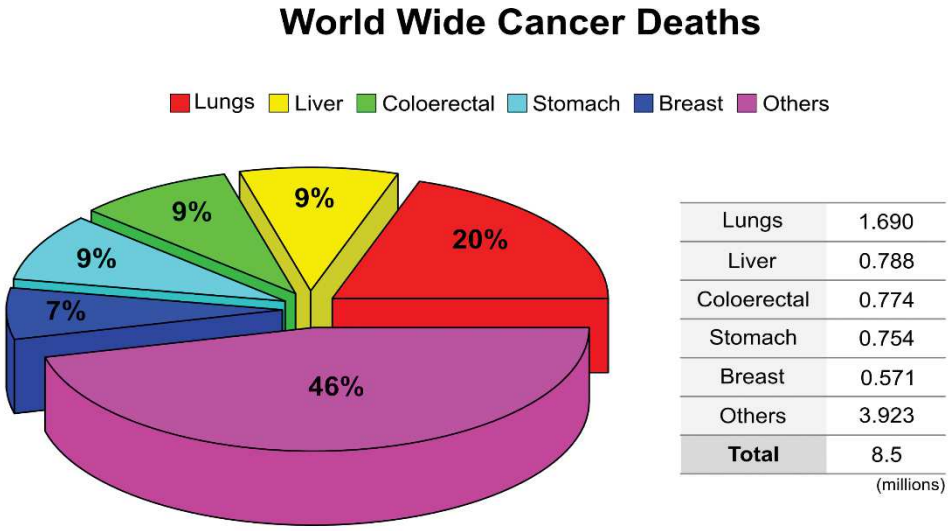

Figure 14. The worldwide percentage distribution of cancer types in 2012.[3]

These cells are very efficient to hide from immune system and usually cancer involves the use of aggressive treatments for the patient. In addition, even if many progresses have been done in cancer treatment in the last years, a lot of improvements and breakthroughs have to be found to cure this disease. Indeed, a main inconvenient of actual treatments is the lack of selectivity towards the diseased cells and many side effects can appear which makes some treatments hardly tolerable. Generally speaking, it is a common knowledge that the earlier the cancer is diagnosed, the better the prognosis. Because of the complexity of the disease, diagnosis is not so easy and the declaration of cancer can be made thanks to different examinations and screening tests. Several imaging techniques already exist today but improvements of the existing protocols are needed to have efficient and very early diagnosis.

Nanomedicine aims at using nanotechnologies at interfaces with various areas (biology, medicine, chemistry) to develop new treatments to fight against diseases such as cancers. One of the major challenges is to produce efficient nanoplatforms able to combine in a single object diagnosis and therapeutic functions (theranostic) customized to each patient and disease. In order to improve the comfort of patient, the future of medicine will be to be able to follow the evolution of the disease while treating it. Multimodal imaging combining two or more imaging modalities will ensure a very fine follow-up of the biological processes involved in the evolution of the disease. The nanoplatforms can be suitably designed to associate various imaging modes such as magnetic resonance imaging (MRI), optical imaging and therapy techniques such as chemotherapy, phototherapy or radiotherapy.

Moreover, because of the permeability of the tumor vasculature (leaky blood vessels),[4] nanoparticles (NPs) can passively target the tumor by escaping through blood vessel walls into disease tissues. The lymphatic drainage is also less effective, which contributes to the retention of the NPs inside tumor tissues. These phenomena are known as enhanced permeability and retention (EPR) effect and is the basis of many tumor targeting strategies. Additionally, active targeting ligands can also be attached to the nanoformulation to reach specifically tumor tissues, which overexpress some receptors. Peptides, oligonucleotides or antibodies are mainly used as targeting ligand.

With the growth of nanotechnologies and the current progresses in complex nanoplatforms synthesis methods, the production of multifunctional NPs has emerged and today offers new perspectives for modern oncology. Such strategies may bring great opportunities for patient survival and quality of life. A vast variety of nanomaterials has been developed to build these functional nanoplatforms including organic nanoparticles such as liposomes, lipids, polymers, conjugates or viral nanomaterials but also inorganic nanoparticles made of hafnium oxide, silica, gold, silver and carbon-based nanomaterials such as carbon nanotubes (CNT) or fullerenes (**Figure 2**). Today several inorganic NPs formulations are approved and used in the clinic (**Table 1**). Recent Covid-19 pandemic shed the light on innovative therapies and mRNA vaccines based on liposomal nanoformulations are a concrete example of the potential of nanotechnologies.

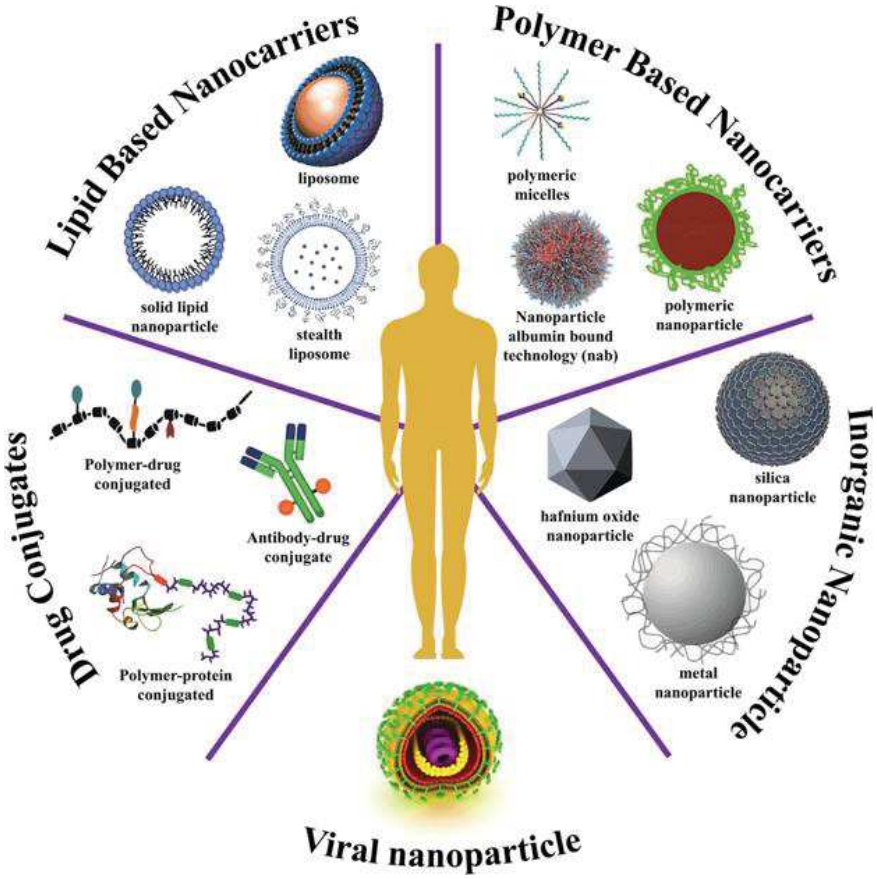

Figure 15. Summary of nanomedicines for cancer treatment.[5]

Among attractive nano-objects, ferrite-based nanomaterials are of particular interest as they are easy to handle, are good contrast agents for MRI and can be heated by remote triggers such as alternating magnetic field (AMF) or near-infrared (NIR) light. In this field, iron oxide (IO) based nanoparticles are promising materials due to their low cost, biodegradability and biocompatibility. In clinical use, iron oxides NPs are already available as T_2 contrast agents for MRI. As medical suspensions, IO NPs are functionalized with organic ligands to ensure their colloidal stability, a defined aggregation state, good biodistribution and an optimal diffusion of water molecules in order to obtain good MRI contrast. Among contrast agents Endorem® and Resovist® are well-known examples of commercial nanoformulations, both coated with dextran derivatives, since disapproved for medical uses because of a lack of sensibility and sensitivity.[6,7] Still on the subject of dextran-coated IO NPs, Sienna^{+}®, is a new nanoformulation used for magnetic susceptometry imaging and the detection of cancerous lymph nodes. In recent years, IO NPs have also shown interest for therapeutic applications via magnetic hyperthermia (MHT). This involves applying an alternating magnetic field of chosen intensity and frequency to a suspension. By their movement and/or magnetic moment relaxation, the NPs generate heat locally that propagates to the external environment. This has the effect of killing or weakening cancer cells, which are usually more sensitive to temperature elevation than healthy cells.[8–10] It also enhances the effectiveness of combined treatments such as chemotherapy or radiotherapy. Nanotherm® developed by a german company, MagForce Nanotech AG, is the first and only therapy based on this principle using

IO NPs to be approved in Europe (in 2011) for the treatment of brain tumors but other products are starting clinical or preclinical trials like Magnablate (**Table 2**).[7] By acting on cancer cells viability but also enhancing sensitivity to chemo- and radiotherapy, or inducing a local release of drugs, a wide range of perspectives is thus opening up for IO based nanoformulations. One of the limitations of MHT for clinical use of the currently available products is their relatively low heating power which thus requires intratumoral injection of large amount of NPs (about 20-30 mg iron oxide per cm^3 of tumor as median dose).[10,11] One of the challenges is to provide very efficient NPs to significantly reduce the injected doses and thus the potential side effects. This involves having optimal structural and magnetic properties (high saturation magnetization and high magnetocrystalline anisotropy).

In addition, it has been recently shown that IO NPs are suitable agents for photothermal therapy (PTT). By irradiating with an appropriate NIR light, it is possible to generate significant heating. First evidence of photothermal effect from IO was reported by Yu *et al*.[11] with iron oxide/alumina systems in 2011. The use of light in the NIR region is very appealing for biological applications because it allows a deeper penetration in tissues than the visible region, due to low absorbance and scattering of water, blood, fat and skin. However, they usually exhibit a lack of stability in biological media which reduces their hyperthermia properties and they cannot carry large amount of drugs due to their low surface area.

Besides IO NPs, carbon nanotubes (CNTs) are also particularly attractive for biomedical applications and especially in field of smart composite materials. Indeed, they have unique physical properties such as high electric and thermal conductivities and very high absorbance on a wide range of wavelength. They exhibit intrinsic fluorescence in the NIR II region and they can be very efficient at releasing local heat when irradiated with NIR light. Thus, they are also very promising for imaging and PTT of cancer. Moreover, CNTs have good mechanical properties: high tensile strength and Young's modulus. This makes them great materials to incorporate into polymer scaffolds such as hydrogels or electrospun fibers, and to load with high amount of drugs for drug delivery applications for instance. CNTs can be single-wall (SWCNTs) or multi-walls (MWCNTs) and are hydrophobic structures when unmodified after synthesis. The properties of CNTs strongly depend on their size, wall number but also on their coating and functionalization which is needed to render them water-dispersible and more biocompatible. Their surface area ranging from 1000 m^2/g for SWCNT to 50 m^2/g for thick MWCNT.[12]

In this context, this research area is today facing several challenges such as limiting the NP toxicity, improving the colloidal stability and the lack of surface functionality, or ensuring suitable drug loading and pulsed delivery etc... It appears thus as very promising to combine these attractive theranostic properties of IO and CNTs with other materials affording new features able to overcome these challenges.

In association with other materials, in particular IO or CNTs, the use of silica in magneto- and photoresponsive systems has been poorly investigated, as it will be detailed in the next chapter.

Addition of silica to IO and CNTs materials is a huge opportunity to design new smart mesoporous core-shell NPs. Indeed, the porosity of silica and the high surface area can be advantageously used for effective loading of a wide range of molecules. The pores can be engineered in order to load very different drugs, peptides or proteins. The density of mesoporous silica being relatively low, it would make the nanocomposite relatively light. A silica coating would also drastically improve the biocompatibility of the core, thus making possible the use of many materials for biomedical applications. Finally, its surface chemistry is very versatile and can be modified for effective targeting and on-demand drug delivery. To date, only one nanocomposite formulation is involved in clinical trials and is based on silica-coated gold nanoparticles for photothermal ablation applications, Aurolase® by Nanospectra Biosciences. **Hence, the synthesis of nanocomposites that have an engineered silica shell coating an inorganic core (core-shell NPs) would pave the way towards an innovative class of biomedical materials that would combine the properties of both materials, thus creating marketable multimodal nanoplatforms.**

Thus, the aim of my PhD thesis is the design of silica-based core-shell NPs with a core material that can be activated by generating heat when a remote trigger is applied (AMF or NIR light). These nanoplatforms have been designed with an engineered porous silica shell to stabilize, functionalize and load drugs within a unique external field-responsive nanoplatform. Obviously, silica coating is not without consequence and should inevitably have an influence on the properties of the core and in particular on the heating behavior under stimuli. This fundamental characterization is yet very little reported. Thus, there is a need to understand the impact of the silica shell around a core material when its physical properties such as thickness and porosity are modulated.

In a first work (**chapter 2**), we aimed at controlling the synthesis parameters of mesoporous silica (MS) shells around IO cores and the influence of the MS type on the nanocomposite magnetothermal properties was studied. By a fine control of the synthesis parameters, we showed that it is possible to produce different morphologies and thicknesses of silica. Especially, in this chapter, the impact that silica shell engineering has on the MRI contrast agent and magnetothermal properties of IO was studied (**Figure 3**).

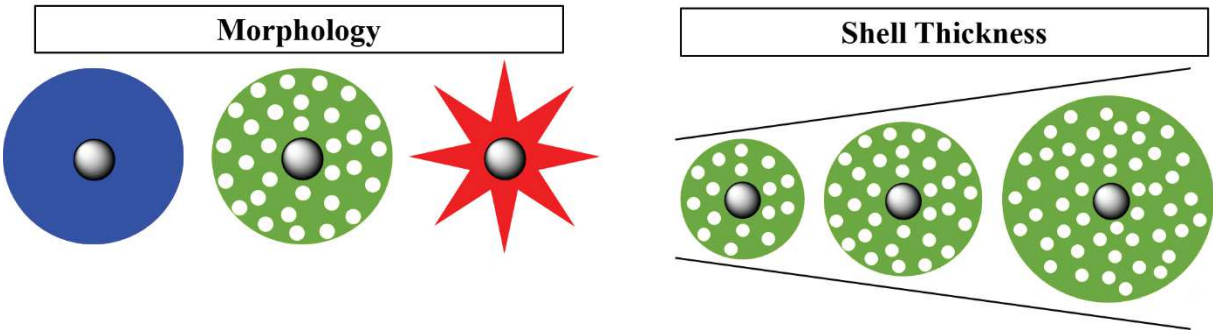

Figure 16. Scheme of the modulation of the silica pore morphology and the shell thickness around IO cores (see Chapter 2)**.**

In addition to provide stability and protect the core, the coating with silica itself has many advantages. Indeed, as said above, by dramatically increasing the surface area, mesoporous silica coated NPs are very adapted to carry drugs. **In a second work (chapter 3),** we focused on the objective to develop a drug delivery carrier associated with photothermic applications. However, an important challenge besides having a high drug loading is to be able to retain the drugs in the silica porosity and to be able to release this drug on-demand. This implies to create interactions/bonds between drug and silica surface strong enough to keep the drug in it while being weak enough for an efficient release upon heating. That is why the design of smart surface chemistry for the drug loading and release behavior is crucial. Thus in this work, we looked at the drug loading capacity of IO@MS as a function of the surface chemistry and the pH of the loading solution. In this study, by irradiation with a NIR laser, the photothermal properties of IO@MS systems were investigated and the associated drug release behavior was quantified. The use of IO and MS as photothermal agents is a very innovative field[13,14] and we proposed here a formulation able to associate this remote treatment with drug delivery applications as a dual treatment (**Figure 4**).

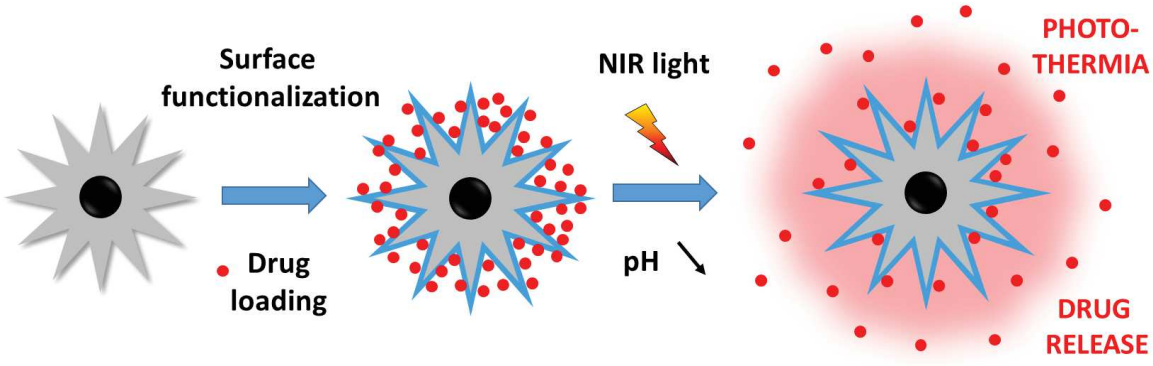

Figure 17. Scheme of the formulation developed for dual therapy modes (see Chapter 3).

NPs for biomedical applications can be designed for circulating formulations, i.e. that the treatment is injected in the patient and circulates via the blood circulation to its target. But another level of organization can be added to the formulation by incorporating the NPs in implantable matrixes such as hydrogels. This has the advantage to prevent any dissemination of the NPs in the body which can be a health concern and to provide sustained drug delivery without repeated injection. Hydrogels, though, have usually very limited mechanical strength properties. **In a third work (chapter 4)**, with the aim to design adapted implantable scaffolds, we have extended our concept of mesoporous silica-coated NPs to another material: CNTs. CNTs are known for their peculiar properties of high mechanical strength, high absorbance in the NIR region and potentially intrinsic fluorescence. However, CNTs have shown some toxicity due to their shape.[15,16] Hence, CNT@MS were formulated in order to extend their use to biocompatible implantable systems. For this, CNT@MS served as a nanoplatform for immobilization of an enzyme able to trigger the self-assembly of a peptide into a supramolecular hydrogel. This smart gel was studied as an original scaffold loaded with drugs whose release can be activated with NIR light (**Figure 5**).

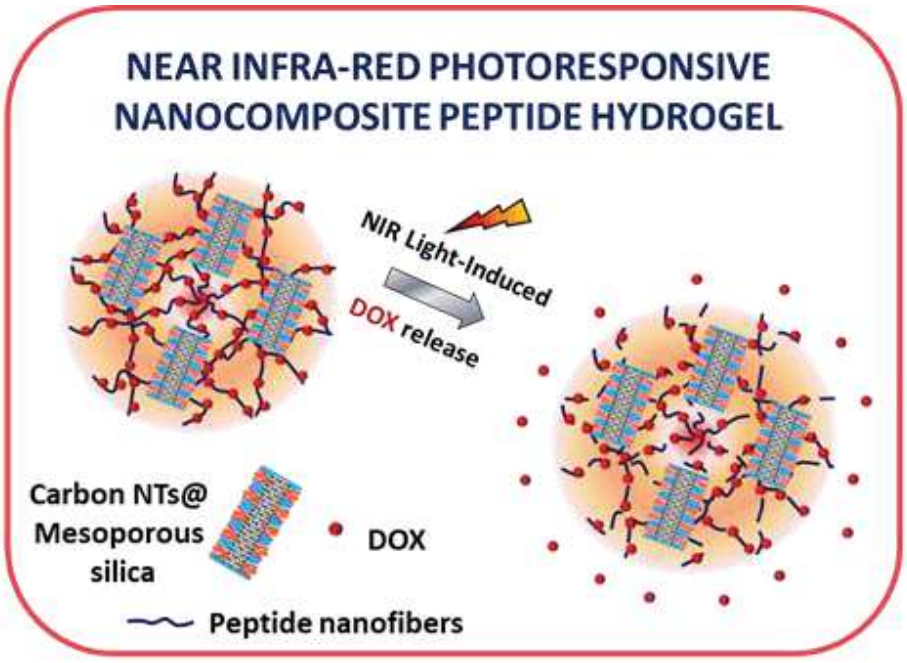

Figure 18. Scheme of the concept for the use of CNTs@MS as implantable hydrogel (see Chapter 4).

This PhD thesis is structured into five chapters:

- **Chapter 1** introduces the state of the art in the synthesis of MS NPs, IO NPs and CNTs as well as the composites IO@MS and CNTs@MS. The physicochemical properties of each system will be discussed as well as their biological applications, the most relevant nanoformulations and their potential limitations.
- **Chapter 2** will focus on the synthesis of MS shell around IO cores by sol-gel methods. These systems will be characterized and the influence of size and structure of MS shells on the heating properties upon AMF will be discussed in order to design efficient multimodal nano-objects.
- After having identified the most suited silica shell, **Chapter 3** will be devoted to the study of IO@MS as drug carriers and PTT agents. These are designed as injectable circulating nanoformulations for synergetic dual-therapy of cancer. Influence of the surface chemistry and pH will be discussed to load and release high amount of drugs.
- **Chapter 4** will be centered on the coating of CNTs with MS and their use in self-assembled supramolecular scaffold for smart implantable formulation able to remotely trigger drug delivery.
- **Chapter 5** will summarize the collaborations and different projects achieved with other research teams in the frame of this PhD thesis.

Table 1. Approved inorganic nanoparticles formulations for medical uses.[17]

Name (Company)	Particle Type	Payload	Applications/Indications	Approval (year)
Cancer				
NBTXR3 Hensify (Nanobiotix)	Hafnium oxide nanoparticles	External radiation to enhance tumor cell death	Squamous cell carcinoma	CE Mark (2019)
Iron-replacement				
CosmoFer Ferrisat (Pharmacosmos)	Iron dextran colloid	Iron	Iron deficient anemia	FDA (1992)
DexFerrum DexIron (American Regent)	Iron dextran colloid	Iron	Iron deficient anemia	FDA (1996)
Ferrlecit (Sanofi)	Iron gluconate colloid	Iron	Iron replacement for anemia treatment	FDA (1999)
Venofer (American Regent)	Iron sucrose colloid	Iron	Iron replacement for anemia treatment	FDA (2000)
Feraheme (AMAG) Rienso (Takeda) Ferumoxytol	Iron polyglucose sorbitol carboxymethylether colloid	Iron	Iron deficiency	FDA (2009)
Injectafer Ferinject (Vifor)	Iron carboxymaltose colloid	Iron	Iron deficient anemia	FDA (2013)
Monofer (Pharmacosmos)	10% iron isomaltoside 1000 colloid	Iron	Iron deficient anemia	Some of Europe (2009)
Diafer (Pharmacosmos)	5% iron isomaltoside 1000 colloid	Iron	Iron deficient anemia	Some of Europe (2013)
Imaging agents				
Feridex I.V. (AMAG) Endorem	Iron dextran colloid	Iron	Imaging of liver lesions	FDA (1996) Discontinued (2008)
Ferumoxtran-10 Combidex Sinerem (AMAG)	Iron dextran colloid	Iron	Imaging lymph node metastases	Only available in the Netherlands (2013)
Resovist (Bayer Schering Pharma) Cliavist	Iron carboxydextran colloid	Iron	Imaging of liver lesions	Some of Europe (2001) Discontinued (2009)

Table 2. Inorganic nanoparticles currently in clinical trials.[7,17]

Name (Company)	Particle Type	Application/Indication
Iron-based		
EO2002 (Emmecell)	Magnetic nanoparticles with cultured human corneal endothelial cells	Corneal edema
Magnablate (University College London)	Magnetic iron nanoparticles	Thermal ablation for prostate cancer
MagProbe (University of New Mexico)	Magnetic IO nanoparticles	Detection of Leukemia
Sienna+ (Endomagnetics)	IO NP coated with carboxydextran	Markage and location of cancerous lymph nodes prior to surgery
SPIONS (Second Affiliated Hospital, School of Medicine, Zhejiang University)	Superparamagnetic iron oxide nanoparticles (SPIONs) with spinning magnetic field	Osteosarcoma
Gold-based		
AuroLase (Nanospectra Biosciences)	PEG-coated silica-gold nanoshells	Thermal ablation of solid primary and/or metastatic lung tumors
CYT-6091 (Cytimmune Sciences)	PEGylated colloidal Gold-rhTNF	Adult Solid Tumor; Primary or Metastatic Cancer
NU-0129 (Northwestern)	Nucleic acids arranged on the surface of a spherical gold nanoparticle	Glioblastoma
NANOM (Ural Medical University)	Gold nanoparticles with iron oxide-silica shells	Plasmonic photothermal and stemm cell therapy of artherosclerosis
Silica-based		
Cornell Dots	Silica nanoparticles with a NIR fluorophore	Imaging of melanoma and malignant brain tumors
Gadolinium-based		
AGuIX (National Cancer Institute, France)	Polysiloxane gadolinium chelates based nanoparticles	Various cancers
Carbon-based		
Carbon nanoparticles	Activated carbon nanoparticles	Lymph node tracer in rectal, breast, gatric cancers
Buckypaper (University of Roma La Sapienza)	Carbon nanotubes	Hernia of abdominal wall; Incisional hernia
Silver-based		
SilvaSorb (Madigan Army Medical Center)	Silver nanoparticle gel	Antibacterial
Silver nanoparticles	Silver nanoparticles	Fungal and bacterial infection
Titanium-based		
Titanium Dioxide Nanoparticles (Cairo University)	Titanium dioxide danoparticles	Candida infection; denture stomatitis
Zinc-based		
Zinc oxide nanoparticles	Zinc oxide nanoparticles	Foot dermatoses; dental caries
Composite		
Silver/Calcium hydroxide (Cairo University)	Silver nanoparticles/Calcium hydroxide	Postoperative pain

Chapter I

Mesoporous silica–based core-shell nanoparticles for biomedical applications and cancer therapy

Chapter I. Mesoporous silica–based core-shell nanoparticles for biomedical applications and cancer therapy

I.1. Mesoporous silica in nanomedicine

I.1.1. Synthesis of mesoporous silica nanoparticles

In the early 1990s, two groups of scientists from Mobil Oil Corporation[18] and Kuroda's group,[19,20] reported independently the synthesis of mesoporous silica using surfactants as templating agents. The production of these structures, in particular the famous MCM-41 and all the M41S-family[21], was a major discovery and it immediately attracted attention from materials science community. Till today, it is a major field of research due to numerous applications and possibilities these materials are offering. The products obtained exhibited high surface specific area whose pore dimensions were easily tunable between 2 and 10 nm by adding co-solvents or changing the surfactant. The regularity of the pores' arrangement in the structures was demonstrated by well-defined X-ray diffraction patterns from this amorphous material that is silica. The formation mechanism of these materials was called liquid crystal templating (LCT) by analogy with liquid crystal phases involving mixtures of water and alkyltrimethylammonium salt surfactants. **Figure 1-1** shows the first supposed liquid crystal-initiated synthesis pathway.[21]

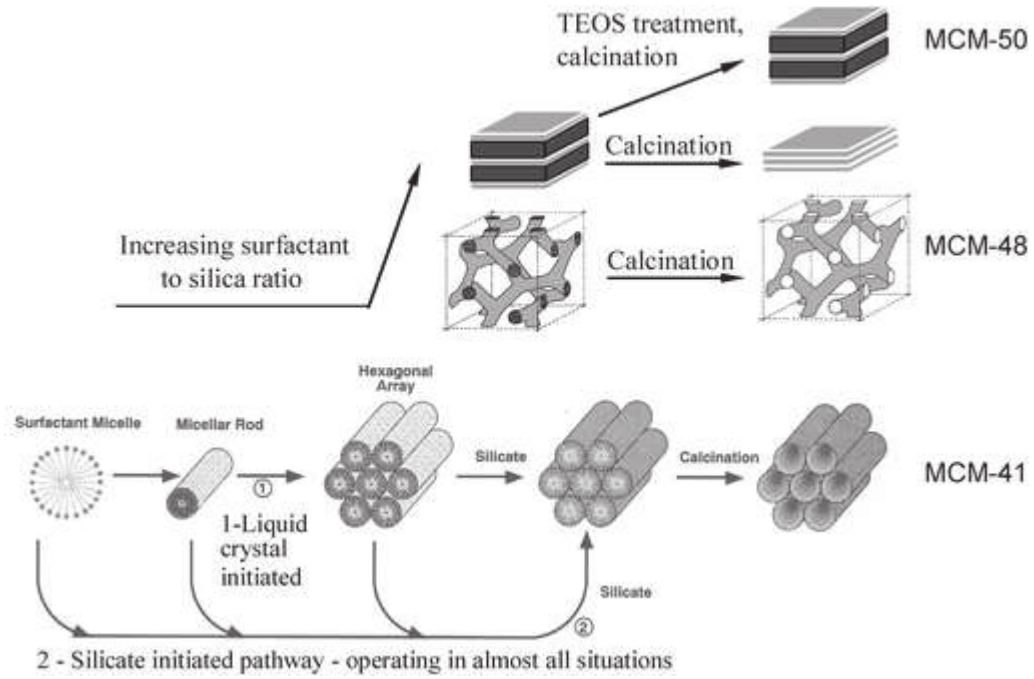

Figure 1-1. The initially proposed LCT mechanism of formation pathways (lower half) and its further additions (upper half).[22]

However, by keeping all the synthesis conditions constant but modifying the amount of silica precursor in the reactive mixture (change of surfactant/silica precursor molar ratio), they formed other structures know as MCM-48 (cubic) and MCM-50 (lamellar) for example. Thus, these experiments invalidated the hypothesis of preformed liquid crystalline phase prior to the formation of the silica network.[22] It is the interaction of the silicate species (anionic) formed during the reaction with the surfactant micelles (cationic) which lead to the formation of the different silica phases following a mechanism named cooperative self-assembly. Silica oligomer anions exchange with HO^- and Br^- (in case of cetyltrimethylammonium bromide (CTAB)) to form inorganic-organic aggregates whose structures are different from the initial surfactant micelles. By strongly screening the electrostatic repulsion these aggregates can self-assemble into an organized mesophase.[23] Since then, a broad variety of materials have been developed inspired by the synthesis strategy of the M41S family, including monolithic, micro-sized and nano-sized materials.

The development of nanometric MCM-41 particles were reported only a few years after the original paper of Mobil Oil Corp.'s group.[24–26] Still today, a wide majority of the mesoporous (MS) NPs are synthesized by using CTAB surfactant and tetraethyl orthosilicate (TEOS) as precursors .The silica condensation is catalyzed in basic conditions which usually yields to hexagonally packed mesopores around 3 nm. Similarly to the previous materials, the porosity can be tuned either by the addition of co-solvents in order to swell the surfactant template pores or the use of surfactants with longer hydrophobic chains.[27–29] Mesitylene is a well-known swelling agent used to increase the pore diameter.[30] With addition of ethanol and/or ethyl acetate in water and varying the volume ratio ethanol/ethyl acetate, it was possible to modify the pore structure from parallel to radial and to worm-like.[31] The use of nonionic amphiphilic block copolymers instead of cationic surfactants as directing agents also allows the synthesis of silica materials with different pore sizes. Diblock or triblock copolymers made of commercially available poly(ethylene oxide) (PEO), poly(propylene oxide) (PPO) or poly(ethyl ethylene) (PEE) are mostly used. These have the advantage that their ordering properties can be very finely tuned by adjusting the copolymer architecture, the ratio and composition of hydrophobic/hydrophilic parts, the molecular weight and the solvent used.[32,33] In the last two decades, an extensive research about MS materials led to their diversification into a variety of research fields.

I.1.2. Biomedical applications of mesoporous silica nanoparticles

MS NPs are particularly popular for biomedical applications due to their controllable particle size,[34] tunable pore size and distribution,[27] large surface area and high pore volume, versatile surface modifications[35] and good biocompatibility.[36] In 2001 Vallet-Regi *et al.*[37] reported the first use of MCM-41 as drug delivery systems. Since then, the use of MS NPs in nanomedicine has been the object of intense research as proved by the large number of scientific reviews about this.[38] The remarkable advantages of large specific surface and pore volume as well as large pore diameter are very well suited for the transport of large amount of small drug molecules and bulky biomolecules, DNA, RNA, peptides

and proteins.[39] As an inconvenient, MS NPs are relatively high cost to produce mainly due to the price of silica precursor as tetraethyl orthosilicate (TEOS) compared to other silica sources. A major challenge to overcome in the future to produce safe clinical products is about the degradability of the MS NPs. MS NPs have been shown to degrade in biological media into silicic acid $Si(OH)_4$ which is nontoxic and water-soluble.[40] However, because of its good stability, the rate of degradation is relatively slow (at least few weeks to months) and thus the retention in the body during this period can cause adverse effects. To have an efficient circulation half-time, the size of the NP is a fundamental parameter. A prolonged retention within the blood circulation and mitigated renal clearance can be obtained by optimizing the size.[41] Indeed particles in the micrometric range could be easily metabolized by active phagocytosis via the mononuclear phagocyte system. On the other hand, very small NPs (< 5 nm) which are capable to pass easily through cell membranes are quickly eliminated via renal clearance.[42]

Today the research aims to develop efficient smart nanocarriers. This refers at stimuli-responsive drug delivery systems which will carry the therapeutics in the body to the required site in the safest and most efficient manner. First generation of cargo nanocarriers as lipid NPs or liposomes usually show adverse effects coming from their fragility, a nonspecific biodistribution, limited targeting and uncontrollable drug release.[43] On-demand drug delivery systems based on MS NPs have shown very promising results by reducing premature unwanted leakage.[44,45] This new step toward smart nanocarriers was possible by the addition of responsive nanocap to block the pores, known as gatekeepers.[46] Today a variety of gatekeepers has been developed to trigger the release when applying a defined stimulus. Internal stimuli deal with the use of a pH change, redox potential or enzyme to stimulate the drug release. External or remote stimuli are based on the application of light, magnetic field or temperature change. Internal triggers are directly related to the chemical and biological environment of the target site in body. For instance (endo)lysosomal pH is decreased between 5.5 to 4.5, protease concentration increases and ionic force changes.[47] pH in cancer tumors are also known to be lower than physiological pH.[48] All these phenomena can be advantageously used to design smart nanocarriers.

In conclusion, MS materials are quite easy to synthesize in mild conditions and controlled environment and have remarkable properties. Their combination with other materials would thus lead to a new generation of nano-architectures. These nanocomposites would have new modalities combining properties of each material and thus new imaging and therapy properties; i.e. triggering drug delivery, responding to external stimuli, bearing imaging agents, while having key physicochemical features such as colloidal stability, non-toxicity and versatile functionalization. Surface properties are brought by the silica that is why we would like to coat iron oxide or CNTs with a mesoporous silica layer. Many strategies have been developed to deposit a silica shell around these core materials.

I.2. Iron oxide@Silica NPs for biomedical applications

I.2.1. Iron oxide generalities

I.2.1.1. Structure

Iron oxide compounds are very common materials widespread on Earth that can be found in eight different crystallized structures.[49] The particularly interesting structures having magnetic properties include Fe_3O_4 magnetite, α-Fe_2O_3 hematite, γ-Fe_2O_3 maghemite or FeO wüstite. Among these, iron oxide spinel phases, magnetite and maghemite are the most promising as they show ferrimagnetic behavior as bulk and superparamagnetism at the nanometric scale.

Magnetite Fe_3O_4 is an inverse spinel structure AB_2O_4 with divalent cations in B sites. The crystalline unit cell is based on 32 oxygen anions forming a face-centered cubic structure. It generates 64 tetrahedral and octahedral sites. ⅛ of the tetrahedral sites are occupied by Fe^{3+} cations (A sites) and ½ of the octahedral sites are occupied by Fe^{2+} and Fe^{3+} (B sites); leading to the formula $(Fe^{3+})_A[Fe^{2+}Fe^{3+}]_B(O^{2-})_4$. Maghemite is an oxidized form of magnetite keeping a cubic structure. To compensate the oxidation of Fe^{2+} into Fe^{3+}, vacancies appear in the octahedral sites in order to have an overall neutral structure and it can be written as $(Fe^{3+})[(Fe^{3+})_{5/3}\square_{1/3}]O_4$ (**Figure 1-2**).

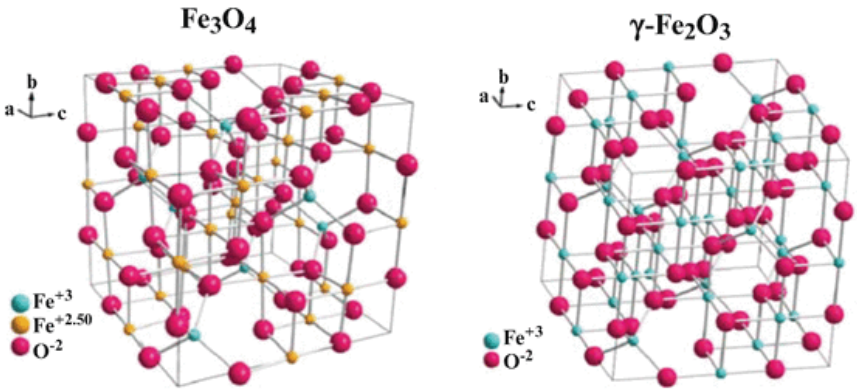

Figure 1-2. Crystal structure of magnetite (left) and maghemite (right).

I.2.1.2. Superparamagnetism

Historically, magnetite was considered as a ferromagnetic material until Louis Néel discovered ferrimagnetism and changed its classification. As a bulk material, magnetite is ferrimagnetic which means that inside the material the magnetic moments are antiparallel distributed but with different amplitudes; resulting in a remaining spontaneous magnetization. The bulk magnetite is composed of magnetic domains in which the magnetization has a uniform direction. By decreasing the size of the material, the number of domain decreases until a critical diameter D_c where individual objects are composed of a unique magnetic domain (**Figure 1-3**). Thus the total magnetization of the NP is a single giant magnetic moment coming from the sum of all magnetic atoms moments and is represented as one macrospin. D_c is around 30-40 nm for IO NPs.

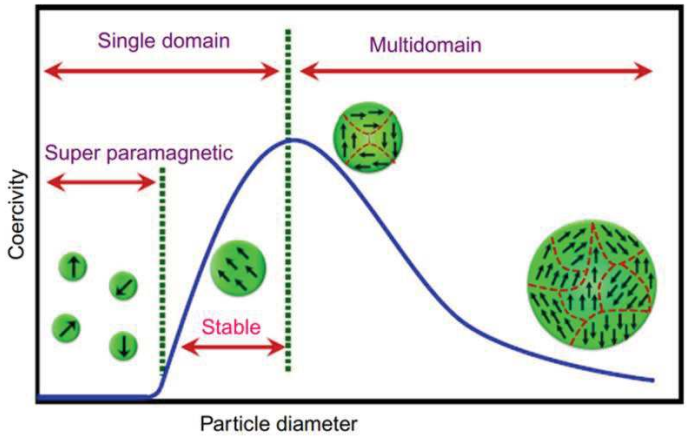

Figure 1-3. Size-reliant domain structures from superparamagnetism to ferromagnetism.[50]

The energy of such single-domain NP is generally dependent on the magnetization direction with respect to the easy axis. The macrospin has two equilibria antiparallel directions along the magnetization easy axis. To switch from one direction to the other (Néel relaxation), it is necessary to overcome an energy barrier KV_p (anisotropy energy) with K the magnetic anisotropy constant and V_p the volume of the particle (**Figure 1-4**).[50] Thus, in the single-domain range, at any given temperature, there is a critical size below which thermal agitation is sufficient to cross this barrier and rotate the NP magnetization. Therefore, when no magnetic field is applied, the orientations of the macrospins are distributed randomly and the sum of the macrospins of the NPs is zero. When an external magnetic field is applied, the NPs tend to align in the field direction, resulting to a net magnetization which disappears when the magnetic field is switched off. This phenomenon is referred as superparamagnetism. For IO NPs, the critical size for blocked single-domain and superparamagnetic behavior is about 20 nm depending on the composition, shape… Inversely for a given size where NPs are superparamagnetic ($k_BT >> KV$), by decreasing the temperature, there is a given temperature for which the energy is lower than the anisotropy energy; called the blocking temperature.

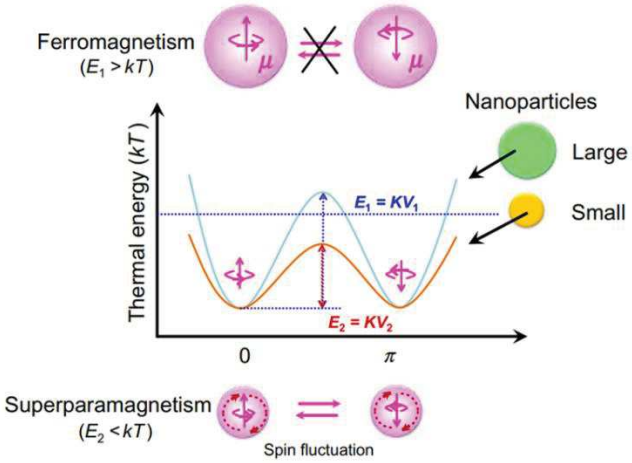

Figure 1-4. Energy diagram of single-domain NPs corresponding to different macrospin alignment ferromagnetism in bigger particles (up) and superparamagnetism in NP (down).[50]

I.2.2. Iron oxide synthesis

Syntheses routes for IO NPs are today much diversified and allow to obtain high-quality magnetite NPs. Three main routes can be distinguished: physical, chemical and biological. Physical methods include electron beam lithography, gas phase deposition, pulsed laser ablation, pyrolysis and mechanical techniques. They can be easy to perform but the morphology and size of the NPs are more difficult to control. It also requires expensive equipment. Wet chemical routes represent the oldest way of synthesizing IO and the more mature area. The methods are very diverse and by finely tuning the reaction conditions, it is possible to obtain narrow size distributions and precise composition. Biological routes deal with the use of bacteria and microorganism to synthesize the NPs. They are usually of excellent quality but very time consuming and complicate to handle after synthesis. We will briefly review the chemical methods as they are the most reported routes to produce IO NPs and they have low production costs and high yield. Among these methods, the most famous include coprecipitation method, polyol method, hydrothermal method, microemulsion and thermal decomposition.

Coprecipitation method

Coprecipitation from aqueous solutions is the most common method to synthesize commercial IO NPs due to the low cost of the reactant, the very short reaction time and its ease to upscale for an industrial production. It consists in the precipitation of Fe(II) and Fe(III) salts solution by the addition of an aqueous basic solution (dissolved sodium hydroxide or ammonia for example). As a result, a black dispersion of IO NPs is produced whose shape and size depend on different reaction parameters. pH and ionic strength are crucial parameters to control the size of the particles. In the 1980s, Massart was one of the first to report the alkaline synthesis of such IO NPs by using ferric and ferrous chloride salts.[51] The high surface-to-volume ratio usually pushed the NPs to aggregate to decrease the surface energy. That is why surfactants,[52] polysaccharides,[53] proteins, polyelectrolytes can be used as dispersing agents to stabilize the obtained NPs.[54,55] Many synthesis parameters have to be taken into account and have an impact on the properties of the resulting IO NPs. Indeed, the counterions, the concentration of cations, the choice of the base, the reaction temperature, the stirring rate influence the size, the phase (the composition) and the shape leading to the variability of the physico-chemical properties.[56–60] Even if tremendous efforts have been done to really improve the obtained NPs and the reproducibility of the syntheses, the resulting IO NPs present large polydipsersity and not well controlled shape. To overcome these limitations, other chemical processes have been developed.

Polyol Method

The shape and size control by the polyol method is really improved compared to the classical coprecipitation. Here the solvents used, polyols or polyethylene glycol, have a high dielectric constant

and a high boiling point which offer the possibility to operate on a broad range of temperatures. Polyols act as the solvent (they can dissolve inorganic compounds) but also have a function of both reducing and stabilizing agents. Thus, they have a major role in the control of the NPs growth and prevent their aggregation. Shape, size and yield of the reaction depend on the choice of polyols, ratio of iron salts, concentration and the used as other additives.[61,62]

Hydrothermal Method

Hydrothermal method is the second most used routes for the synthesis of IO NPs.[63] The reaction occurs in aqueous solution in a closed reactor or autoclave. By heating above the standard boiling point of the solvent, the pressure of the liquid increases and it is possible to reach high pressure (>100 bar) and high temperature (> 200 °C). Compared to the coprecipitation which uses equivalent reactants, the size and the shape control of the IO nanocrystals is really improved. Unfortunately, more energy is needed and the reaction time is relatively long. So to be more efficient, microwave-assisted hydrothermal method has been implemented.[64,65] A complete study of the different synthesis parameters has been reported by Hao *et al*. to verify the influence of precursors, time, temperature on the obtained IO NPs.[66]

Thermal decomposition

This process consists in heating at high temperature a metallic complex in order to induce its decomposition. Organic solvents with high boiling points are needed as well as surfactants to stabilize the formed NPs. When decomposing, the metal ions present in the complex crystallize which forms nuclei that will further grow to form the NPs. This leads to highly monodisperse IO NPs very well stabilized in organic solvents thanks to the coating of surfactant (**Figure 1-5**). For example, oleic acid allows a good stability in chloroform or THF. This method is appropriate to synthesize high quality IO NPs with a narrow size distribution as the nucleation step and the growth step can be easily separated.

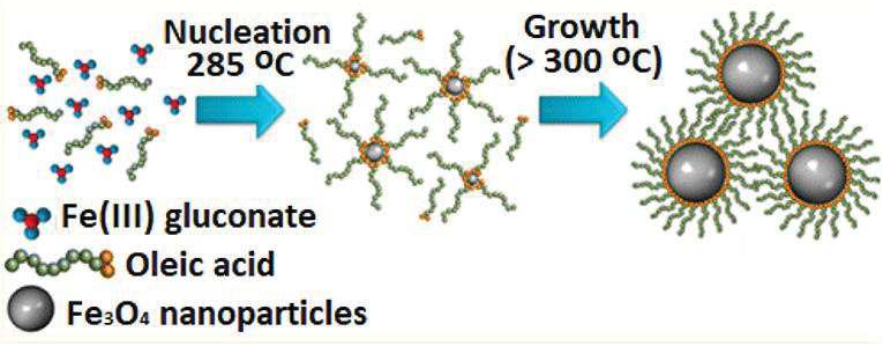

Figure 1-5. An example of thermal decomposition of iron(III) gluconate to synthesize superparamagnetic Fe_3O_4 nanoparticles.[67]

Few iron precursors are commonly used to produce IO NPs, especially magnetite NPs. Among them, Fe(acac)n,[68,69] iron oleate[70], carbonyls Fe(CO)x[71,72] or iron stearate[73,74] is the most represented. In

short, this method offers the best control of the synthesis parameters and allows to produce IO NPs with precise size and shape. At the end of the reaction, the stabilization by surfactant leads to good stability in organic solvents which will be advantageously used to synthesize the mesoporous silica shell (see chapter 2).

I.3. Iron oxide coated with mesoporous silica core-shell nanoparticles

I.3.1. Non-porous silica shell coating around iron oxide

Once IO NPs have been synthesized, the concept is to use them as cores for silica shell coating. This would lead to their complete coating with non-porous or porous silica shell. This shell has an important impact on the properties of the newly formed nanocomposite. In terms of stability, the silica protects the IO core from dissolution while bringing a very good colloidal stability in various solvents and especially in aqueous buffer thanks to the charged surface. It also prevents any aggregation between the magnetic cores originating from their dipolar interactions or/and hydrophobic surface chemistry. IO NPs that were synthesized by thermal decomposition are coated with ligands like oleic acid and thus are stable in organic solvents, such as chloroform or tetrahydrofuran. Thus they need to be transferred into aqueous medium so that the silicate species can polymerize around the IO cores.

I.3.1.1. Non-porous silica coating by Stöber sol-gel method

Probably the most direct and facile method is to coat IO NPs with non-porous silica using surfactant-free, low tech and low cost process.[75] This facile and famous route is known as Stöber, Fink and Bohn process and is among the first method used to coat inorganic NPs with silica.[76] The synthesis involves the dispersion of IO NPs in ethanolic solution, followed by the hydrolysis/condensation of the silica precursor (commonly TEOS) onto the surface of IO NPs.[75,77,78] The reaction is usually catalyzed by ammonia. The generation of silica from silica precursors follows a mechanism named as hydrolysis/condensation. First in the presence of ammonia, in ethanol solution, the alkoxide (Si-O-R) hydrolyzes so that alkoxy groups (O-R) are replaced by silanol (Si-OH) monomers (**Eq.1**). Then the silanol monomers condense to form siloxane bonds (Si-O-Si). This generates branched siloxane clusters which will further react together to form silica nuclei and trigger the growth of silica nanoparticles (**Eq.2**). Silanol monomers can also react with non-hydrolyzed silica precursor (TEOS) via direct condensation between silanol and alkoxy groups which will participate to silica network formation (**Eq.3**).[79]

$$Si(OEt)_4 + xH_2O \rightleftharpoons Si(OEt)_{4-x}(OH)_x + x\ EtOH \quad (\textbf{Eq.1})$$

$$2\ Si(OEt)_{4-x}(OH)_x \rightleftharpoons (EtO)_{8-2x}(Si\text{-}O\text{-}Si)(OH)_{2x-2} + H_2O \quad (\textbf{Eq.2})$$

$$Si(OEt)_4 + Si(OEt)_{4-x}(OH)_x \rightleftharpoons (EtO)_{7-x}(Si\text{-}O\text{-}Si)_1(OH)_{x-1} + EtOH \quad (\textbf{Eq.3})$$

Hydrolysis of TEOS occurs via a nucleophilic substitution of ethoxy groups for OH groups. The addition of ammonia in the mixture increases the concentration of HO^- ions which are a lot more efficient nucleophiles compared to H_2O. Moreover, when bulky groups (OEt) are removed for OH, the hydrolysis rate increases by lowering the steric hindrance around Si atoms. For its part, condensation between neighbor silanols also involves a nucleophilic attack. However, in these basic conditions, the condensation is much faster than the hydrolysis because the silanol groups, which are the actors of the nucleophilic substitution, are deprotonated more easily than water molecules. Si atom thus becomes more electrophilic (more electropositive) which is favorable for the attack. By doing so, we understand that silanols preferentially condense into large branched siloxane networks rather than onto small oligomers. This leads to a relatively good size control by favoring growth over nucleation. The kinetic balance between hydrolysis and condensation is fundamental to have a monodisperse NPs distribution. Silica shells with thickness between 2 to 100 nm can be obtained by controlling the reaction parameters such as coating time, reactant concentrations, presence of catalyst or other precursors than TEOS.[80] This synthesis method is usually more adapted to IO NPs that is not coated with surfactants. A major limitation is usually the lack of control and the polydispersity of the silica thickness. To circumvent this issue, reverse microemulsion routes were developed.

I.3.1.2. Non-porous silica coating by reverse microemulsion process

Microemulsion synthesis is a form of seed-mediated growth process. The IO cores are previously synthesized and act as seeds for the silica shell growth. This process requires to have IO NPs capped with organic ligand such as classical oleic acid and dispersed in non-water-soluble organic solvent. Hence, reverse emulsion (water in oil) can be set up to obtain homogenous non-porous silica shells. The dispersion is mixed to a surfactant solution and aqueous ammonia is added in order to form an emulsion.[26] By further addition of silica precursors and its subsequent partial hydrolysis, the IO NPs enter the ammonia droplets where the silica condenses around the cores.[82] Uniform coating of single can thus be obtained by controlling the ratio between the number of droplets and the number of IO NPs. Modification of the synthesis parameters leads to modulated silica thickness (**Figure 1-6**). Thus each IO NP is found within a droplet which constitutes a microreactor. Compared to Stöber process, this method results in much more controlled non-porous silica shell.

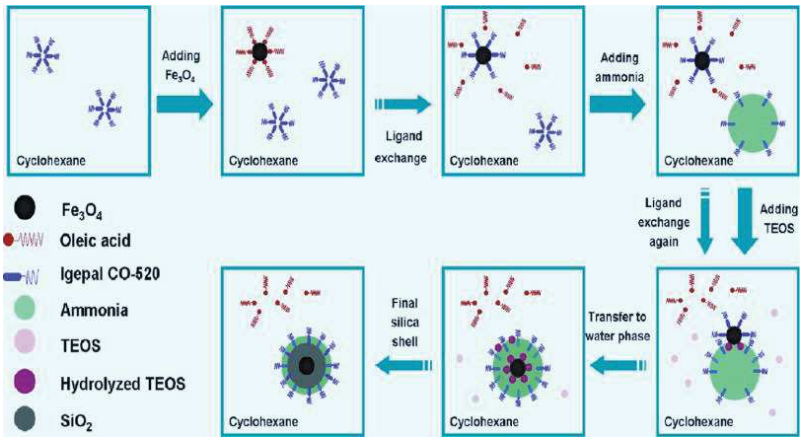

Figure 1-6. Mechanism of coating of IO NPs with silica via microemulsion.[82]

In order to develop mesoporous silica shells, other methods have been developed. They involve the use of surfactants whose organization in presence of silica precursor creates periodically distributed hybrid inorganic/surfactant domains. After the removal of the surfactant, this results into mesopores in the structure.

I.3.1.3. Mesoporous silica on IO NPs via direct templating

A first method is equivalent to the synthesis of MCM-41 using surfactant in aqueous solution but in presence of IO NPs. Duguet and coworkers[83] developed this method to coat IO NPs synthesized by coprecipitation. Surfactants are very useful molecules in many areas thanks to their specific structures. They are composed of a polar head and a non-polar tail, which allow them to assemble at the water/oil interface. The most famous and widespread surfactants are the ones based on quaternary ammonium, in particular cetyltrimethyl ammonium bromide (CTAB). In aqueous solution, the hydrophobic parts assemble themselves to form micelles with hydrophobic cores. However, the hydrolyzed silica precursor is water-soluble and thus silica oligomers will condense around the ammonium polar head. This complex interaction between the surfactant and silica oligomers leads to the formation of cylindrical hybrid micelles whose walls solidify as the silica forms. This is why CTAB plays the role of templating agent. However, it can be difficult for silica-CTAB complex to anchor directly to uncoated IO. Deng *et al.*[84] prepared IO nanoclusters by solvothermal method which are thus not prone for coating with surfactant. They proposed to first synthesize a sublayer of non-porous silica via Stöber method, which then allowed a good coverage with CTAB, and subsequent mesoporous silica.

I.3.1.4. Mesoporous silica coating on IO NPs through direct emulsion

IO NPs that are synthesized with the best shape and size control method, e.g. by thermal decomposition, are stabilized with organic ligands which make them dispersible in apolar organic solvents. To coat these NPs, new methods have been established and imply passing through an emulsion step. Direct emulsions use surfactants in order to stabilize in water the non-water dispersible IO NPs.

IO NPs capped with organic ligand and dispersed in non-water-soluble organic solvent are needed. Shortly, the organic-solvent IO NPs suspension is added to an aqueous solution of surfactant (such as CTAB) and a base. Under strong agitation, the organic solvent mix into the aqueous phase to form an oil-in-water microemulsion which is stabilized by the surfactant.[85] Then the organic solvent is removed by controlled evaporation. By slowly heating and removing the organic solvent, the surfactant molecules will interact with the coating molecules of IO NPs by hydrophobic interactions between the alkyl chains. This forms a thermodynamically defined interdigitated bilayer structure of surfactant around the NPs in order to stabilize them in an aqueous phase as shown in **Figure 3-17**. Hyeon *et al.*[86] reported in 2006 the first encapsulation of IO NPs via this method using CTAB as the stabilizing and templating agent. The hydrophobic properties of the IO NPs ensure an optimal distribution of the magnetic cores into the micellar phase.[87] As the IO NPs that we used are coated with oleic acid, this is the preferred method for the deposition of the silica shell. This results in very monodisperse and homogeneous IO@MS NPs.

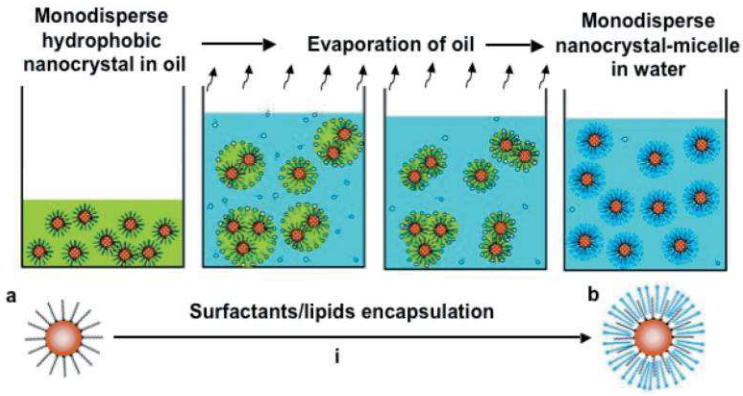

Figure 1-7. Representation of the formation of water-dispersible IO NPs through surfactant encapsulation.[88]

The control of the shell thickness growth is one of the most important features. In the case of this synthesis method, the ratio of CTAB surfactant and TEOS is primordial. Ye *et al.*[85] showed that a large excess of CTAB during the reaction results in the formation of mesoporous silica without IO core. As detailed above for the synthesis of mesoporous silica NPs, the use of a swelling agent such as mesitylene or the increase of the length of the alkyl chain of the surfactant allow to increase the width of the mesopores. In an original method, Yang *et al.*[89] coated IO nanoclusters via biphasic oil-in-water coating strategy in which the oil phase enables a swelling of the pores resulting in large dendritic open pores.

I.3.1.5. Coating of silica in gas phase

It is also interesting to highlight a physical method operating in gas phase and producing silica coated IO NPs. The gas phase deposition method uses flame spray pyrolysis (FSP) which decompose mixture of iron oxide and silica precursors.[90,91] Other reactors such as plasma or arc discharge can also be used.[92] A premixed oxidizing fuel gas drives the droplets of the colloidal precursor solution until a

burner. The particles are produced in the flame before being collected onto a filter. IO@MS is produced in a single step. This process could allow a continuous flow production but the as-synthesized NPs are still very polydisperse and inhomogeneous.[90]

The combination of IO with MS gives rise to core-shell nanocomposites IO@MS which have unique features. Their main properties are described in the following paragraphs.

I.3.2. Physical properties of IO@MS as theranostic agents

As detailed above, the main interest to design IO@MS for biomedical application is to combine the therapy and diagnosis abilities of each compound. Thus IO@MS can be used as MRI contrast agents thanks to the IO core but also as therapy vehicles with MHT treatment and as drug delivery carriers (chemotherapy) thanks to the porous MS shell.

I.3.2.1. IO@MS as contrast agents

I.3.2.1.1. MRI and contrast agent principles

Magnetic resonance imaging (MRI) is today a very common non-invasive medical imaging technique used for the diagnosis and follow-up of many diseases in particular cancers whose solid tumors can be detected. MRI is based on the physical phenomenon of nuclear magnetic resonance of hydrogen atoms. These atoms are particularly abundant in the human body; especially in water and fat which represent about 63% of the body mass. When the protons are exposed to a strong static magnetic field B_0 (along the z-axis), their spin align (parallel or antiparallel) to the direction of this field and they precess under the Larmor frequency ω_0. Parallel orientation is the lower state thus it is slightly preferred. This results in a net magnetization vector M_z parallel to B_0. Then a resonant radiofrequency pulse (RF) with a resonance frequency equal to the Larmor frequency is applied perpendicularly to B_0. This irradiation is absorbed by the protons (nuclei of hydrogen atoms) whose spins jump from parallel state to the higher level of antiparallel state and secondly, the spins are "whipped" to precess in phase. The effect of all this is that the net magnetization M_z flips 90° from the z-axis to transverse plane.[93] The magnetic moment of the protons is a vector having two contributions: M_z, the longitudinal magnetization parallel to B_0 and M_{xy} the transverse magnetization. As RF stops, the nuclear spins relax and return back to their initial equilibrium state. **Figure 1-8 (a and b)** summarizes this mechanism. In **Figure 1-8 (c and d)** are depicted, the two relaxation processes that proceed independently: i) longitudinal relaxation which consists in the realignment with B_0. The characteristic time of this process is T_1 and corresponds to 63% of the equilibrium value. ii) transverse relaxation for which the magnetization component on the transverse plane (M_{xy}) returns to zero. T_2 is the characteristic time and corresponds to a drop of 37% of the initial magnitude on xy plane. From these relaxation times, it is possible to reconstruct a 3D image of the patient's tissues.

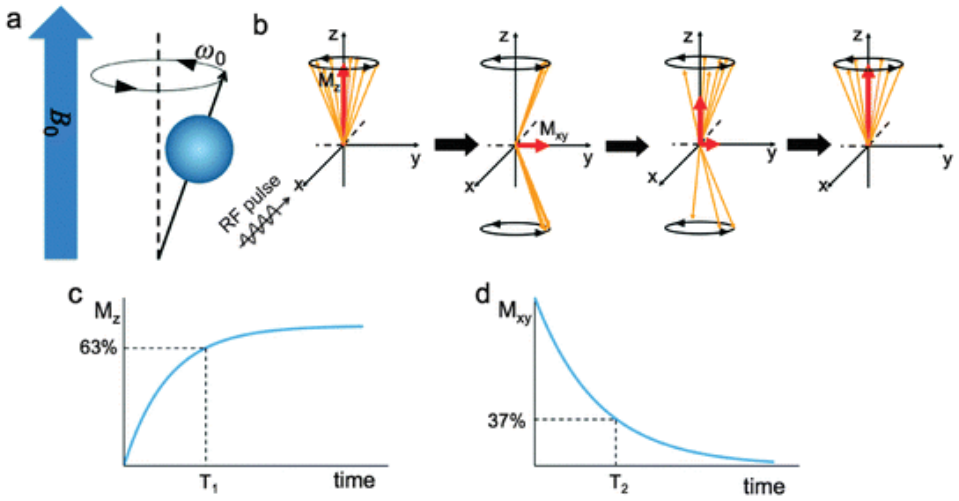

Figure 1-8. Principles of magnetic resonance imaging (MRI). (a) In magnetic field, the hydrogen nuclear spins align with (parallel) or against (antiparallel) the external magnetic field. (b) Irradiation of resonant RF results in decrease in longitudinal magnetization (M_z) and generation of transverse magnetization (M_{xy}). Subsequently, the nuclear spins return to their initial state, referred to as relaxation. (c and d) T_1 is the time required for longitudinal magnetization to recover to 63% of its equilibrium (c), and T_2 is the time required for transverse magnetization to drop to 37% of its initial magnitude (d).[94]

In the body, the intrinsic contrast is often not sufficient to provide clear images of abnormal tissues and contrast agents (CAs) can be injected in the patient to modify the relaxation times of protons around them and thus enhance the overall contrast. Among the most common CAs, paramagnetic ions or complexes such as gadolinium (Gd^{3+}) and manganese (Mn^{2+}) are used as T_1 CAs by reducing the longitudinal relaxation time. The locations around these CAs are highlighted and brighter than without CAs. Ferri- or ferromagnetic compounds such as iron oxide will induce local magnetic field gradients which shorten the transversal relaxation T_2 resulting in hypocontrast, i.e. a dark contrast in T_2-weighted images. The relaxation rate R and the relaxivity r are proportional to the inverse of the relaxation times. For both relaxation process, R_1 and R_2 (in s^{-1}) and r_1 and r_2 (in $mM^{-1}.s^{-1}$) can be calculated from T_1 and T_2 respectively. In the presence of a CA, we have:

$$R_{i,obs} = R_{i,0} + r_{i,CA}.C = \frac{1}{T_i} + r_{i,CA}.C$$

where $R_{i,obs}$ is the observed relaxation rate, $R_{i,0}$ the relaxation rate of protons in absence of CA, $r_{i,CA}$ the contrast agent relaxivity ($mM^{-1}.s^{-1}$), C the concentration of CA (in mM^{-1}) and T_i the relaxation time.

MRI CAs act in two ways on a molecular point of view, on the diffusion of water molecules (hence protons) and inner and outer-relaxation sphere processes need to be considered **(Figure 1-9)**. Inner sphere relaxation is based on the direct energy transfer between protons and electrons of the first hydration sphere around the CA. It requires close accessibility of water molecules to the CA molecules or NPs and is strongly dependent on the exchange rate of water molecules. Water protons need to be in close proximity of paramagnetic ions to experience fast relaxation. T_1-contrasting effect is based on this inner-sphere relaxation. For T_2-contrasting agents, the dominant contribution comes from the outer-

sphere relaxation. This interaction at greater distance comes from the interaction of protons with the local magnetic field generated by superparamagnetic NPs. The nature of the coating of IO NPs is fundamental as it modifies the interaction with water molecules and thus the contrast produced in MRI.

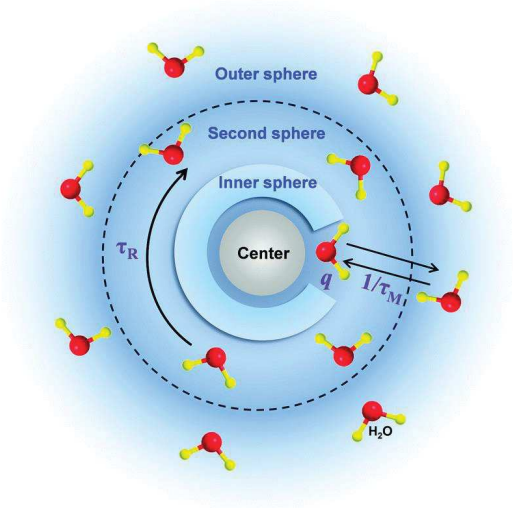

Figure 1-9. Inner sphere and outer sphere can influence relaxation rates of MRI CAs.[95]

I.3.2.1.2. IO@MS contrast agents

The coating of non-magnetic silica shell around the IO NPs influence the relaxivities of the nanocomposites. Ye *et al.*[96] studied the influence of the thickness of a mesoporous silica shell around IO NPs on the r_1 and r_2 relativities. They showed that IO NPs with a CTAB coating (IO-CTAB) have a r_1 relaxivity about 10 times higher compared to the same NPs coated with a mesoporous silica shell with small pores between 1 and 3 nm. This is attributed to the difference of mobility of water molecules around and inside this coating layers. For IO@MS, the increase of thickness of the coating, also leads to a decrease of r_1 which is explained by the ability of the MS shell to separate water from the surface of magnetite NPs. Concerning r_2, they showed that transverse relaxivity decreases by increasing MS shell thickness which can be attributed to a weakening of the locally generated magnetic field by IO cores. Pinho *et al.*[97,98] coated maghemite NPs with non-porous, amorphous silica shells. They also obtained a decrease of r_1 and r_2 relaxivities due to the decrease of the inner and outer-sphere contributions respectively. Zhang *et al.*[99] also demonstrated that for the same thickness, the use of more hydrophobic silica-based shell decreases r_2 while r_1 keeps constant. By using cleverly the pores of MS to load paramagnetic gadolinium ions in iron oxide-mesoporous silica core-shell nanocomposites, Gao *et al.*[100] managed to produce a dual T_1 and T_2 contrast agent.

I.3.2.2. Design of IO@MS for magnetic hyperthermia

I.3.2.2.1. Magnetic Hyperthermia principles

Magnetic hyperthermia (MHT) refers to a therapeutic treatment which consists in heating a region of the body above the normal physiological temperature, i.e. 37 °C for human body. Due to their more chaotic organization and the defecting architecture of the vascular supply, cancer cells are particularly sensitive to temperature elevation and thus less tolerant to high temperature than healthy tissues. Temperatures over 41- 42 °C can deeply affect their viability. Cellular functions are affected leading to cell degradation and finally cell death or apoptosis. This method can thus be an alternative or a complement in the cancer treatment. If the temperature is higher, the cell membrane ruptures and the reaction is more inflammatory leading to tissue necrosis which is known as thermal ablation. Hyperthermia and thermal ablation are two techniques to destroy cancerous tissues. It has been shown that moderate hyperthermia (42-45 °C) can kill cancer cells in 15-60 min and it is shortened at 4-6 min with thermal ablation (> 50 °C).[101] In this frame, magnetic nanoparticles can be used to induce the heating by the application of an alternating magnetic field (AMF). Gilchrist *et al.* was a pioneer in the experimentation of this treatment by using magnetic particles to heat locally lymph nodes in 1957.[102] Since then and until today, magnetic hyperthermia (MHT) therapy by the use of magnetic nanoparticles as mediators and in particular IO NPs have gained interest in the community.[103,104] In our nanocomposites IO@MS, the magnetic IO core is the active part in an AMF; the silica does not interact with the magnetic field and thus no heat from it is generated. That is why the properties of only IO to generate heat and act as mediator for MH are discussed. However, the silica layer can influence the heat transfer. The modulation and engineering of the silica thickness and morphology will be studied in the Chapter 2 of this thesis.

The ability of a material to generate heat is calculated by its specific absorption rate (SAR). It is expressed as the capacity of one gram of material to increase the temperature of the sample in a certain amount of time. $\mathrm{SAR} = \frac{\Delta T}{\Delta t} * c * \frac{m_{sample}}{m_{NP}}$ (in W/g) where $\frac{\Delta T}{\Delta t}$ is the variation of temperature in a defined time, c is the specific heat capacity of the sample, m_{sample} is the mass of the sample and m_{NP} is the mass of nanoparticles in the sample.[104] This value depends on the amplitude and the frequency of the applied magnetic field as it will influence the heat generated.[105] The intrinsic loss power (ILP) is an alternative physical value, proposed to normalize the SAR value, which is defined by $\mathrm{ILP} = \frac{SAR}{H^2 f}$. This quantity allows to compare the results obtained by the different groups and for different materials as it is independent of the applied field amplitude and frequency. However, ILPs are not always calculated and scarcely reported in the publications. One of the main reasons is that, to be comparable, the magnetic behavior and the heat generated have to be proportional to the applied AMF which is not always the case. Hergt *et al.*[106] showed that magnetic susceptibility χ"(t) is strongly dependent on the frequency of the magnetic field.

During this thesis, we used superparamagnetic IO NPs. Hence no hysteresis is observed on the magnetization curve and no heat loss can be generated by this phenomenon. However, as it was said before (part I.2.1.2 about superparamagnetism), IO NPs are blocked in one spin orientation. The AMF supplies the energy needed to overcome the energy barrier. Thus the orientation of the macrospin of superparamagnetic IO NPs continuously change at a defined frequency. Two mechanisms result in the dissipation of thermal energy upon this stimulus: Néel relaxation coming from the internal friction of the crystal lattice with the reorienting magnetic moment and Brown relaxation which originates from the viscous energy dissipation from the NP turning in the surrounding medium.[107] As a function of the composition, size, shape, crystalline anisotropy, aggregation state of the NPs as well as the viscosity of the surrounding medium, the relative contribution of each mechanism will be different. With large particles and low viscosities, Brownian relaxation dominates whereas with small particles, highly viscous fluid or trapped NPs (in solid matrix for example) Néel relaxation gets a majority. Both mechanisms can occur simultaneously and the overall effective relaxation time of the ferrofluid will be the result of both phenomena (**Figure 1-10**).

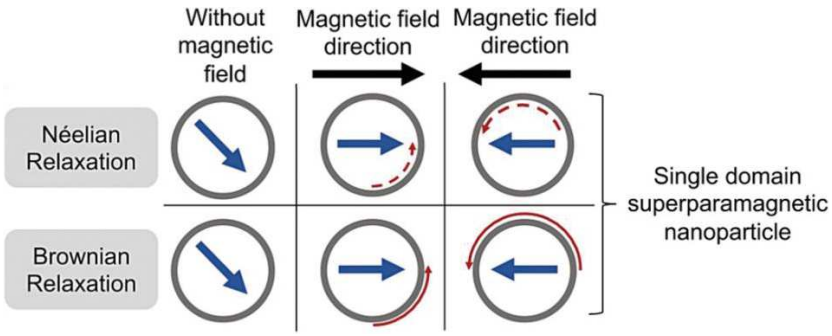

Figure 1-10. Mechanisms of heat generation in magnetic nanoparticles (MNPs) upon exposure to an alternating magnetic field (AMF). Gray circles represent MNPs, blue arrows indicate direction of magnetic moment. In the case of single domain MNPs, magnetic relaxation occurs in the form of internal changes in the magnetic moment direction (Néel, dashed red arrows) or physical movement (Brown, solid red arrows) as the particles attempt to align with the applied magnetic field.

As a result, it is important to take into account the parameters influencing the relaxations mechanisms in order to design IO@MS NPs adapted for MHT and for the temperature elevation expected in the system. Several parameters play a crucial role to have effective nano-objects. These can be divided between extrinsic and intrinsic parameters.

I.3.2.2.2. Main parameters influencing MHT potential

Extrinsic parameters

Viscosity of the environment. As we stated before, the contribution of each relaxation mechanisms depends in part on the environment in which the NPs are settled. Viscosity of the fluid is of crucial importance because the friction of rotating NPs in this fluid participates to the heating.[104] By slowing

down or blocking the NPs in more viscous media, it is possible to evaluate the contribution of Brown relaxation for heat loss. By studying systematically the influence of different parameters on the SAR values, De la Presa *et al.*[108] showed that by increasing the viscosity of the liquid, the heating power of large NPs decreases whereas it remains stable for smaller NPs. This experimentally confirms that for small NPs heat loss mainly occurs through Néel relaxation while Brown relaxation mechanism is predominant for large NPs.

AMF amplitude and frequency. Dissipated heat depends on the amplitude and the frequency of the magnetic field. This means that the SAR values increase by increasing the amplitude and/or the frequency of the AMF applied. The typical range of frequencies (f) is 100-700 kHz and between 10 to 30 $kA.m^{-1}$ for the amplitude (H). It is commonly admitted that for clinical uses the product H*f should be lower than 5.10^9 $A.m^{-1}.s^{-1}$ [109,110] in order to avoid non-localized temperature increase due to the generation of Eddy currents.[111] This value was established in the 1980s but to date it remains a reference and a basis for work even if the evaluation of this limit has not been the subject of recent investigations.

Intrinsic parameters

The heating power of the NPs depends on their magnetic properties. MHT is influenced by the particle anisotropy, the blocking temperature and the Brown and Néel relaxation times but the size is also among the main parameters.

Size. As seen above, the size of the IO NP and especially if it is monodomain or not is of key importance. Above 100 nm, the hysteresis loss is predominant for large blocked NPs. For superparamagnetic NPs, Néel and Brown relaxation are predominant. Depending on the size, the proportion of each relaxation mechanisms is different. The influence of core size has been the subject of many studies.[106,112] However the reported optimal size differs from one publication to the other and this mainly comes from the physical properties of the NPs and the synthesis method which can induce polydispersity and crystalline phase defects.[113,114] However optimal values for IO cores are reported for diameter between 12 and 25 nm.[115,116]

Particle anisotropy. Magnetocrystalline anisotropy and shape anisotropy are key factors to optimize the heat generation under AMF. When a magnetic field is applied, the superparamagnetic NPs tend to align in the field direction and the energy needed to do this is called crystal anisotropy. It is primarily due to spin-orbit coupling. Among the iron oxides, magnetite as the highest anisotropy 11-14 $kJ.m^{-3}$ compared to maghemite for which it is about 4.6 $kJ.m^{-3}$. On the other hand, the modification of the shape is also a way to improve the MHT effect. At the surface of the NP, changes in the neighboring atoms and in the crystal orientation may lead to changes in the local magnetization with respect to the surface.

For instance, cubic or faceted NPs show higher SAR values than spheres – nanocubes of 19 nm were found to have an impressive SAR value of 2453 $W.g^{-1}$ at 29 $kA.m^{-1}$ and 520 kHz.[117]

Core-shell NPs IO@MS are more and more studied in the literature for magnetic hyperthermia treatment but the influence of the silica shell is scarcely discussed. An appropriate design is needed in order to keep the magnetothermal properties of the IO core while adding the loading, stability and chemical versatility of silica.

I.3.2.3. Design of IO@MS for photothermal therapy

Photothermal therapy (PTT) is another kind of thermal treatment which is induced by the application of light and especially laser. This method has demonstrated to be very efficient to destroy cancerous tumors. However, the heat sink effect (heat dissipation to the environment) dissipates heat and decreases the potency of thermal effect. Using laser directly to ablate cancerous tumor would require high energy setups causing damages to normal tissues. Thus traditional laser-induced photothermal therapy has been considered to be non-reliable and limited to superficial tumors as the human tissues absorb light in the visible range of the electromagnetic spectrum. Nanotechnologies are thus particularly suited to overcome these issues. To improve the efficiency of PTT, light-absorbing nanomaterials called photothermal agents have been developed. These nanoparticles convert the light into heat. The heating is thus local and surrounding healthy tissues stay at normal body temperature. The most light-absorbing tissues from human body are the skin (melanin), the fat, water and hemoglobin. It is thus necessary to find a range of wavelengths were these tissues are partially transparent in order to have minimal scattering and absorbance, to preserve healthy cells and to penetrate the deeper possible up to the photothermal agents. This range is called a biological window. One window is found around 800 nm and is known as the first biological near-infrared (NIR) window. A second biological window extends between 1000 nm and 1350 nm (**Figure 1-11**).

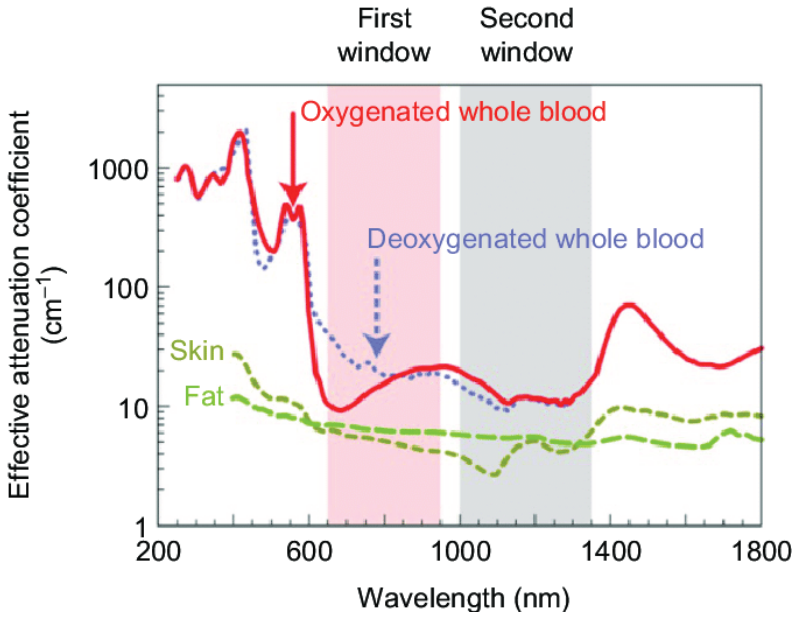

Figure 1-11. Extinction coefficient of light in different biological components of human tissue.[118]

Melamed *et al.* defined the criteria needed for a good photothermal agent: (i) minimal toxicity/maximal biocompatibility, (ii) diameter between 30 and 200 nm to promote long circulation and enhanced tumor accumulation (iii) the ability to absorb NIR light, and (iv) a high absorption cross section to maximize light-to-heat conversion.[119] A vast set of nanomaterials are today available as photothermal agents of different composition, shape, size, structure and surface coating. Among the inorganic NPs reported, gold-based nanomaterials are the most tested and represented. Indeed, metallic nanostructures and especially gold has a unique photophysical property: the local surface plasmon resonance (LSPR). When an electromagnetic wave interacts with a plasmonic material, the oscillating electric field of the radiation results in synchronized oscillations of the conduction-band electrons at the surface of the nanoparticles. Within NPs, the oscillating electrons further collide with the nuclei and as a result, energy is transferred into vibrational modes of lattice (phonon) and converted into heat.[120] At the so-called LSPR wavelength, the oscillation is maximal. This excitation state is transitory and the electrons are de-excited through a non-radiative decay which thus generates heat. Aurolase® is a product currently performing clinical trials which is based on gold NPs and this phenomenon for PTT. Silver NPs produce about 10 times more heat at its plasmon resonance but due to its chemical instability, gold is still favored for biomedical applications.

Beside gold and metallic NPs, other materials have shown to absorb NIR light. Recently, non-metallic inorganic nanoparticles and in particular magnetite Fe_3O_4 has shown to produce a photothermal effect when irradiated by NIR light.[120,121] The physical mechanism which generates heat is slightly different from plasmon resonance. For these electronic transition materials, the photothermal transduction is led by transitions of the electrons from the valence band to the conduction band. When the electron relax back, heat or light are generated. **Figure 1-12** details the approximate band structures of Fe_3O_4 NPs between the valence band of the O(2p) to the empty Fe(4s). Radiative and non-radiative

decays are both involved. The exact mechanism is still unclear and it certainly results from several processes such as fast decay of electrons and release of phonons instead of photons.[121]

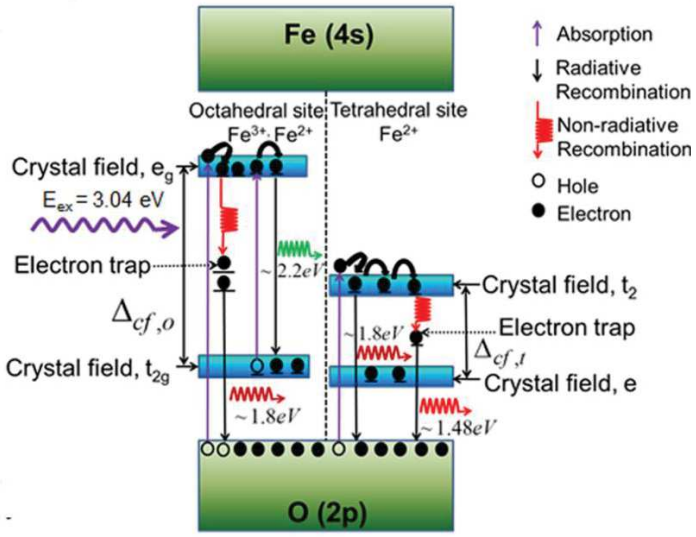

Figure 1-12. Schematic of the energy bands of the magnetite NPs system.

I.3.2.3.1. Parameters influencing photothermal effect

We defined above the criteria for an ideal photothermal agent. It is important that NPs interact optimally with NIR light to convert it into heat and to exploit the biological tissues windows. They also have to be non-toxic and stable enough to reach the target area (tumors). Gold NPs are very efficient to convert NIR light into heat and Zhang *et al.*[122] showed how the shape of the particles is a fundamental parameter to optimize the photothermal effect. Anisotropic NPs generate a more defined charge separation when their SPR is excited, and by optimizing the intensity of SPR, the heat released can consequently be more efficient.

Furthermore, the size is always a fundamental parameter when dealing with NPs as surface properties predominate over volume effects. By a careful control of the synthesis, it is possible to fit the absorption wavelengths with the incident wavelength emitted by the laser or diode, thus the heat production is also maximized. This is true for plasmonic NPs. However as detailed above, the mechanism of photothermal conversion of IO NPs is very different as it primarily originates from the transitions of electrons of neighboring Fe ions within the lattice. As a consequence, as long as the emitted wavelength is in the NIR range, the mid-bandgap states trap the excited "hot" electrons and produce phonons that carry heat.[123]

When optimized, PTT is a very local therapy and the location of the NPs has an impact on the treatment efficiency. *In vitro* experiments have compared the efficiency of PTT on extracellular and intracellular treatments. They showed that PTT was more efficient when gold nanorods were directly internalized by the cells than when gold nanorods were outside of the cells.[124] PTT results in different physiological and biological modifications in the tumor tissue which can improve therapeutic effects

and enhance the efficacy of secondary treatments such as chemotherapy. The localized heat enhances the permeability of cell membranes and tumor vasculature, thus allowing a better drug uptake.[125,126]

Photothermal therapies use continuous or pulsed wave lasers. These two types are very different and induce different mechanisms of damaging cells as they have different time profiles and intensities. Optimum laser intensity depends on the cell type, the used photothermal agent and the cell environment. Efficient treatments are carried with a power laser range from 0.5 to approximately 100 $W.cm^{-2}$.[120]

I.3.2.4. Design of IO@MS as carrier for drug delivery

As detailed above, silica coating has several advantages which are i) providing not only stability to the IO cores in aqueous solution but also avoid interparticle interactions leading to aggregation ii) variation of silica shell properties (thickness, porosity) can be easily controlled and iii) IO@MS possess a good biocompatibility. Silica coating is also a great chemical platform to bind covalently or not therapeutics molecules and to load them into and onto the pores and plethora of strategies have been developed. A lot of parameters influence the drug loading. The most important are the NPs functionalization and surface charge, nature of soaking media, pH of the soaking media when aqueous solution, presence of gatekeeper molecules or coupling agent for covalent bonding.

To describe the ability to load a drug, 3 main parameters are generally used in the literature: feed weight ratio (fwr), Drug Loading Content (DLC), Drug Loading Efficiency (DLE).

$$\text{fwr} = \frac{\text{mass of drug given in soaking media}}{\text{mass of carrier}} * 100$$

$$\text{DLC} = \frac{\text{mass of drug loaded}}{\text{mass of carrier}} * 100$$

$$\text{DLE} = \frac{\text{mass of drug loaded}}{\text{mass of drug given in soaking media}} * 100$$

Yang *et al.*[127,128] described two methods to load DOX inside the same NPs with the same fwr. First loading was performed in ethanol with unmodified silica surface and the second was carried out in PBS buffer with amine-functionalized surface. He obtained a maximum DLC of 2.16% in the first case and 4.7% in the second. This is a clear demonstration of the importance of the choice of soaking media and the nature of the surface of the NPs. Vallet-Regi's group[129,130] showed a similar effect for the loading of model drugs like ibuprofen and bisphosphonate with amine-functionalized silica compared to unmodified silica surface.

Coupling agent such as urea bonds to covalently conjugate the DOX on the NPs, considerably improve DLCs as compared to only hydrophobic, van der Waals or electrostatic interactions. For example, Li *et al.*[131] showed that DLC increased from 13% to 39% by making a urea bond with the reaction of isocyanate-silane with the amine group of DOX.

Different strategies of drug gatekeeping and triggered release at the surface of IO@MS NPs were described in the literature. Shao *et al.*[132] managed to load about 20 wt% of DOX in the bare NPs' pores and observed that at acidic pH (pH = 5.5) a lot more DOX is released compared to pH = 7.4. Peralta *et al.*[133] grafted PNIPAM-co-MPS polymer on IO@MS NPs. During the polymerization, the comonomer MPS, 3-(Trimethoxysilyl)propyl methacrylate) acts as an anchor group on the silica surface. The empty pores of the silica shell were filled with ibuprofen drug model. At 40 °C, the lower critical solution temperature (LCST) of the polymer, about 5 times more drugs were released as compared to 20 °C, thus showing the gatekeeper role of the polymer for thermoresponsive release. Saint-Cricq *et al.*[134] modified IO@MS with APTES, then azo-PEG was coupled to the surface. Under AMF, the azo bonds break and the drug (here rhodamine 6G as proof-of-concept dye) was released. Zhu *et al.*[135] reported the use of double-strand DNA as gatekeeper to cap IO@MS NPs. Upon heating, the denaturation of the dsDNA unleashed the DOX stored in the pores. Disulfide bonds are also interesting gatekeepers as they are stable in blood circulation ad their degradation is only triggered by reduced glutathione or thiols and in particular by glutathione reductase (GSH) whose concentration in usually twice higher in tumors compared to normal tissues.[127]

I.3.2.5. Nanothermometry

When speaking about MHT or PTT, this is the temperature of the whole macroscopic sample, in a tube, *in vitro* cell culture or *in vivo* tissue that is generally considered. However, the heat dissipates locally from the NPs to their environment. To know the temperature into or at least at the surface of these nano-objects can be of crucial importance when the NPs carry thermally sensitive molecules such as some biomolecules, proteins, peptides, DNA, RNA... When the NPs are in direct contact with cells, the local temperature can also have a huge impact on the surrounding cellular structures such as the cell walls or the nearby organelles even if the macroscopic temperature does not generate overheating. This local heating or "hot-spot effect" can thus be advantageously used for biomedical applications.[136] Indeed, the temperature profile of NPs can be used to induce a thermal trigger for drug delivery without damaging the area of interest; for example, in the case of activation of biological functions[137] or delivery of sensitive siRNA to specific cells that do not have to be thermally killed. Potential side effects are limited. However evidence of the local heating involved in the nanoscale hot-spots is not an easy task as it cannot be measured with usual macroscopic tools such as thermometers or infrared cameras.

Several molecular or nano-tools have been developed to get proof of the local temperature state. Thermosensitive chemical reactions are the most developed way to sense the local temperature. Zink and coworkers reported many systems and ways to probe it such as the retro Diels-Alder reaction which was used and monitored by MHT on superparamagnetic doped iron oxide@mesoporous silica core-shell NPs.[138] Pores filled with fluorescein were closed by bulky cyclodextrins which were bound to adamantane groups by supramolecular groups. The temperature was set at 0 °C. To get an equivalent release of fluorescein without local trigger, the reaction should be performed at 65 °C thus demonstrating

the thermal local effect of AMF stimulation. Thermoresponsive block copolymers were also used as nanothermometers on magnetic NPs. PNIPAM was copolymerized with a fluorescent monomer and when the lower critical solution temperature (LCST) was reached, the polymer get to shrinking and a change of fluorescence was observed.[139] Griffete *et al.*[140] showed an induced polymerization under AMF from magnetic NPs. This polymerization should occur at temperatures above 60 °C but with AMF they obtained it under a macroscopic temperature of 31 °C demonstrating the local effect. In another example, IO@MS NPs loaded with fluorescein and coated with a thermoresponsive polymer shell was stimulated by AMF. Even if the polymer was at a distance of 20 nm away from the nanocarrier, LCST transition was observed under AMF.[141] These results demonstrated how local thermal effect can become of great interest for the design of the next generation of magnetic NPs for nanomedicine applications.

Thus the "hot-spot" effect was first explored by macroscopic observations resulting from nanoscale-derived effect. Less attempt has been made to directly sense the temperature profile into and outside the nanoparticle. Jaque *et al.*[142,143] reviewed the use of optical techniques and in particular the use of luminescent nanothermometers such as quantum dots whose luminescence is dependent of the temperature (**Figure 1-13**). Dong and Zink[144] used up-conversion nanocrystals $NaYF_4:Yb^{3+},Er^{3+}$ whose fluorescence emission spectrum is modified when temperature is changed. These latter nanocrystals were incorporated inside a mesoporous silica nanoparticle together with superparamagnetic IO NPs. Inside the silica matrix a more rapid increase of the temperature of 45 °C was detected as compared to a bulk temperature increase of 20 °C. This concept is of prime importance to elucidate temperature profile distribution near the hot spot. Pellegrino *et al.*[145] demonstrated that it is possible the measure a temperature gradient as a function of the distance of the NP hot-spot surface. For this, they used a fluorescent dye linked by an azo bond and spaced by various length chain PEG linkers to the IO NP. They showed that the temperature increase depends on the amplitude of the magnetic field (magnetic power). More importantly, their results indicated that the local temperature is 50 °C higher than the macroscopic temperature at the surface of the NPs while the difference between these two temperatures fall down in few nanometers (2-3 nm) to zero.

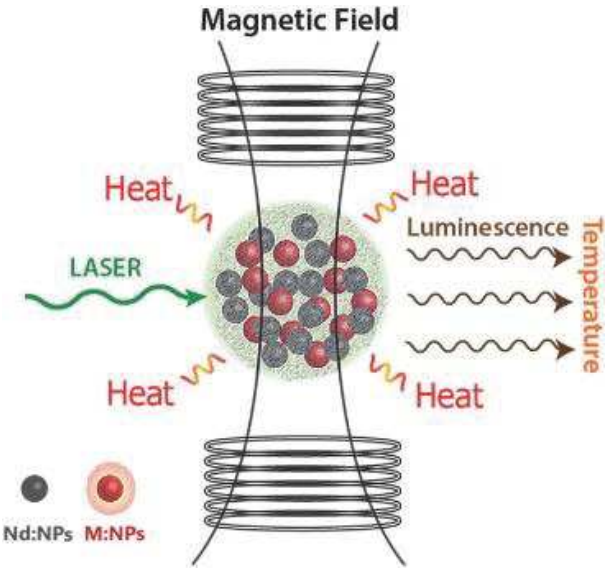

Figure 1-13. Scheme to illustrate an experiment of nanothermometry under magnetic field using luminescent nanothermometer.[142]

Optically activated NPs (for PPT application) could use exactly the same kind of nanothermometers and temperature-sensing methods. The measurement of temperature profiles on the nanometer scale is today still very challenging as specific setups are scarcely available and fluorescence shift can be very sensitive to numerous environmental changes. However, the impact for biological applications could be very promising in particular for the control and monitoring of magnetic and/or light-induced hyperthermia.

I.4. Carbon Nanotubes coated with Mesoporous Silica (CNTs@MS)

Carbon is one of the most important elements and the base of life on Earth. Due to its peculiar electronic configuration, it can form various covalent bonds and be implied in numerous chemical reactions. Its allotropes have unique structures and very interesting physical properties. Nobel Prize in Chemistry was awarded in 1996 for the discovery of fullerenes and especially C_{60}, the most famous family member. This created enthusiasm in the scientific community and many carbon-based materials have emerged since then. Among them carbon black, graphite, graphene, carbon dots and carbon nanotubes find today applications in the research and in the industry in various fields such as catalysis, optics, electricity, electronics, sensors and biomedicine.[146,147]

I.4.1. Carbon nanotubes generalities

Carbon nanotubes (CNTs) is one of the allotropic form of carbon belonging to family of fullerenes. They are composed of one or several sheets of graphene wrapped on themselves to form a tube. This tube can be closed or open at the extremities. Single-walled carbon nanotubes (SWCNT) and multi-walled carbon nanotubes (MWCNT) distinguished themselves from their structures and properties. SWCNT has a diameter of few nanometers whereas MWCNT can be thicker than 100 nm and they are chemically more resistant (**Figure 1-14**).

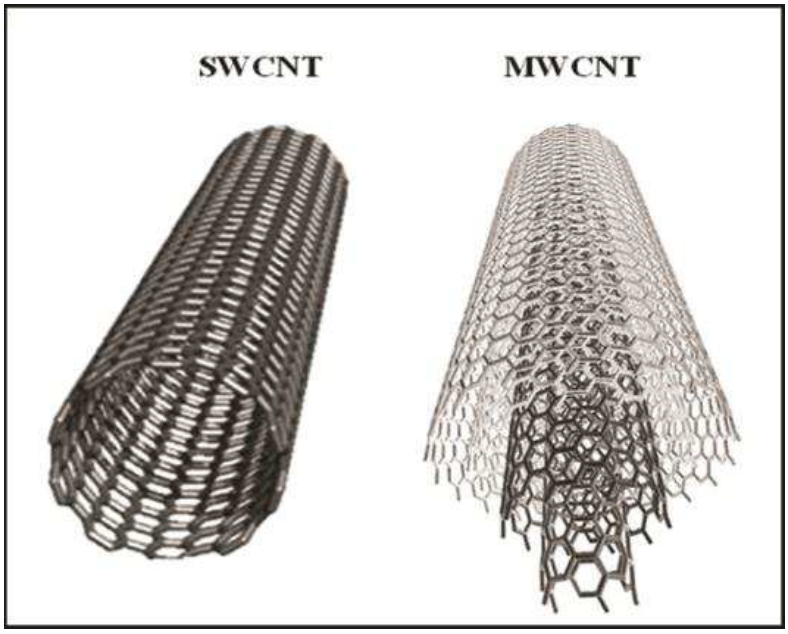

Figure 1-14. Schematic drawing of SWCNT (left) and MWCNT (right).[148]

I.4.2. CNT synthesis

Reported syntheses of CNTs include various pathways and, in particular, chemical vapor deposition (CVD), laser ablation and arc-discharge as the main routes.

Arc-discharge method

Arc-discharge method is the first one thanks to which CNT was discovered. It is based on the evaporation at very high temperature in vacuum chambers of graphite electrodes. An arc discharge is produced using high DC current which leads to the sublimation of the graphite in the anode. The anode is usually doped with metallic ions and thus many impurities can be found in the resulting material.[149]

Laser ablation

Laser ablation uses a pulsed laser which evaporates a heated graphite target into a vacuum chamber. On the other side of the chamber, which is cooler, the vapor condenses and CNTs can be collected. The yield of production is good around 70% but slow and SWCNT are primarily obtained with diameter determined by the reaction temperature.

Chemical vapor deposition

Chemical vapor deposition is today the most preferred technique as it has a low cost and is easily scalable to mass production. Shortly, the method is based on the decomposition at high temperature of a hydrocarbon vapor passing through a tubular reactor in presence of a catalyst material. CNTs grows at the site of the catalyst. The mechanism involved is still studied. Catalyst support may include MgO or Al_2O_3. The synthesis parameters such as the temperature, the catalyst, the carbon sources, etc. will greatly influence the size, morphology and characteristic of the as-synthesized CNT.

I.4.3. Properties

CNTs are very appealing due to their unique mechanical, thermal and optical features. Mechanically, CNTs are considered to be potentially one of the strongest materials. As CNTs have sp^2 bonds between individual carbon atoms, their tensile strength is higher than steel. Calculations estimated that a perfect SWCNT could have a Young's modulus of about 1 TPa which is comparable to diamond.[150] CNTs are also very flexible and when exposed to high axial compression forces, they twist and bend so well that no deep damages can be detected in the structure. Of course, greater forces can induce defects and deformation in the structure.[151] Depending on the electronic structure, CNTs can act as semiconductors or as metals. In a random SWCNT population about 2/3 are semiconducting ones and are 1/3 metallic ones. By increasing the number of walls, the inter-wall interactions lead to an increase of the metallic population.[152]

From a thermal point of view, CNTs exhibit excellent thermal conductivity along their long axis mainly due to phonon ballistic heat transport.[153] By simulation calculations, Berber *et al.*[154] evaluated the thermal conductivity of an isolated SWCNT to be 6600 $W.m^{-1}.K^{-1}$ at room temperature which is absolutely huge compared to the thermal conductivity of magnetite which is about 6 $W.m^{-1}.K^{-1}$ at 300

K.[155] Of course, the purity, the tube length, the defects and the atomic arrangement influence deeply the thermal conductivity.[156]

CNTs have a strong absorbance on a wide range of wavelengths. In particular, SWCNT can absorb in the NIR region, i.e. in the optical biological window. Moreover, SWCNT exhibits a strong luminescence in NIR region and does not photobleach or blink which is a problem of many other systems.[157,158] Thanks to their particular light absorbance, they can also be used for PTT applications as this absorbed light can be converted in local heat. Robinson *et al.*[159] compared the performances of gold nanorods with SWCNT to eliminate tumor by PTT. By using a 808 nm laser, they showed that they were able to eliminate effectively tumors using lower laser power (0.6 vs 2 $W.cm^{-2}$) and 10 times lower injected doses (in mass of NPs) with SWCNTs compared to gold nanorods. This early paper proves the great opportunities there are to use CNTs for biomedical applications and cancer therapy.

I.5. Silica shell coating around carbon nanotubes

I.5.1. Coating methods

However, one of the major drawbacks of CNTs is their lack of chemical versatility and their high hydrophobicity which makes them difficult to disperse in aqueous and biological media and thus not much biocompatible. To overcome this issue, many coatings have shown to improve the dispersibility. Among them, silica is a very suited coating as it was explained above (see Chapter I.1.). The addition of silica properties to CNT could lead to a new generation of highly performant biomedical devices. These nanocomposites have the features of both CNTs and MS which make them promising for triggered drug delivery, tissue engineering, PTT and imaging.

To make the silica precursor condense around CNTs, modification of the surface is needed. First strategies developed to bring new chemical functionalities on the surface of CNT suited for silica coating was the use of organosilanes.[160] This allows to build a thin sublayer which will then be used to deposit the coating of non-porous silica following a modified Stöber process.[161] As mentioned above as-produced CNTs are usually contaminated with traces of various metals. Mixture of H_2SO_4/HNO_3 is usually used to purify them. By pre-treating them in strong acids solution it also “activates” the walls, i.e. CNTs become more hydrophilic and bear hydroxyl or carboxylic acid groups at the surface, the silica sol-gel process can also take place on the surface of CNTs.[162] A silica surface is much more versatile and is usually used to bind a variety of other molecules as peptides for biological interests.

However, in many cases, mesoporous silica is much more appealing because of the much larger surface area as well as defined and tunable pore size. This plays a key role in the choice of the cargo molecules that the carrier can transport.[163] To synthesize a mesoporous silica shell around CNTs a

similar procedure was used than mentioned above (see I.3.1.2). It is based on the dispersion of hydrophobic nanomaterials into an aqueous solution of surfactant, usually CTAB. Thus a stable dispersion is obtained and CTAB serves as templating agent for the polymerization of the silica precursor (in particular TEOS).[86] The method is really similar to the route used to coat oleic acid-capped IO NPs. However, CNTs usually have a bare surface and it is more difficult for CTAB to anchor on it. Deng *et al.*[164] developed a layer-by-layer in order to have a polymer layer suited for CTAB anchoring. By adjusting the ratio CTAB/CNTs, Zhang et al were able to use such nanoplatform for selective protein size separation. The amount of TEOS precursor, sol-gel reaction time and amount a base, our group reported the synthesis of such CNTs@MS with pore size between 2-4 nm.[165,166] Interestingly few papers also showed the possibility to decorate CNTs with magnetic NPs in particular IO NPs in order to bring complementary magnetic properties. Either coprecipitation method[167] or thermal decomposition[168] have been reported to grow IO NPs on CNTs which where them coated with MS.

Mesopores bigger than 5 nm are nonetheless the most promising as they allow to load very important amounts of a variety of molecules such as small drugs and big proteins. Indeed, small pores can limit the penetration of drugs inside the pore channels. The most common way to produce large pores is to change the common CTAB for other surfactants leading to large pore channels[169] like biocompatible phospholipid surfactant as it was reported by Zhang *et al* (**Figure 1-15)**[170] It is to note that in this case the porosity also depends on the ratio of the different chemicals and an excess of phospholipid leads to the production of numerous uncoating spherical silica NPs beside CNTs.

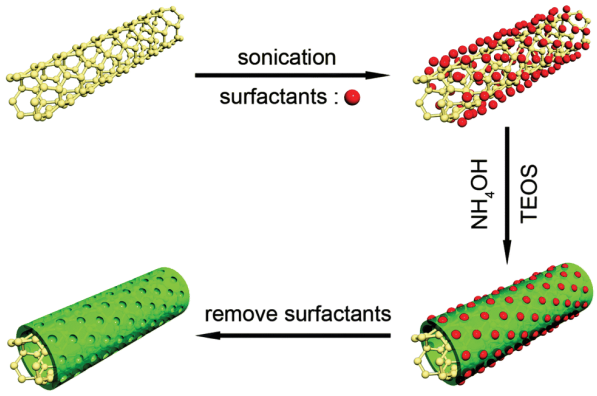

Figure 1-15. The synthesis procedure of the CNTs@ mesoporous SiO_2.[170]

I.5.2. Physical properties of CNTs@MS for biomedical applications

I.5.2.1. Biosensing

The specific hexagonal arrangement of sp^2 hybridized carbon atoms composing CNTs, makes them really good electric conductors and sensitive to the electrical changes and thus promising as biosensors. They can serve as scaffolds for biomolecules immobilization and their unique properties makes them very suited for signal transduction associated with the recognition of analytes.[171] A lot of different classes of CNT biosensors have been developed to probe numerous biomarkers thanks to the

recognition of specific proteins, peptides, antibodies, enzymes or DNA conjugation. In particular, CNTs led to the development of highly sensitive biosensors which could detect very small number of molecules useful for the early-stage detection of diseases such as cancer.[172,173] Canevari *et al.*[174] produced a mesoporous silica-based hybrid material containing CNTs to serve as an electrode for detection at low concentrations of dopamine, uric acid and acetaminophen. Guo *et al*.[175] reported the synthesis of silica-coated carbon nanotubes by sol-gel method to serve as support for loading metal NPs such as Au NPs, Pt NPs or Au/Ag core-shell NPs. This allows them to produce very effective electrodes for detection of several molecules and could be used as surface-enhanced Raman scattering (SERS).

I.5.2.2. Imaging

Most biological imaging probes are today working in the visible light range. However, as we detailed above, most tissues as well as hemoglobin exhibit strong absorbance as well as autofluorescence in this range. If, for *in vitro* cell cultures this not necessarily a major issue, it is more problematic when dealing with thick tissues. Single-walled carbon nanotubes (SWCNTs) show strong absorption on a wide wavelength range and fluorescence in the second biological window (1000-1700 nm).[176] Takeuchi *et al.* developed an imaging probe showing strong fluorescence at 1300 nm through excitation at 980 nm.[177] This allows a non-invasive imaging in deep tissues and tracking of biomolecular events.[178,179] Robinson *et al.*[180] reported the synthesis of surface-functionalized water-dispersible SWCNTs. By EPR effect and photoluminescence, they were able to achieve high accumulation and have a very good contrast of the tumor even 72 h after injection. Fei *et al.*[181] showed the synthesis of silica-coated CNTs with CdTe quantum dots to improve the imaging properties. Singh *et al.*[167] also added superparamagnetic IO NPs to CNTs@MS nanocomposites in order to bring a new MRI T_2-imaging contrast feature.

I.5.2.3. Photothermal Therapy

Carbon-based nanomaterials and especially CNTs are considered among the darkest objects, i.e. they have an exceptional absorbance on a wide range of wavelengths including NIR region (biological windows). Light is thus certainly the most suited trigger to use in order to induce a suitable response. We detailed above how IO NPs are able to generate heat when exposed to NIR light. Similar mechanism is at work in the case CNTs. Jablonski diagram (**Figure 1-16**) sums up the mechanisms involved. From the ground state (PS_0), the molecule absorbs light and thus leaves it for an excited state with a high energy content (Sn). Within the electronically excited state, there are several sublevels composing the vibrational and rotation states and by vibrational relaxation and internal conversion phenomena, the molecule joins the lowest excited state (PS_1). From there, several pathways can be taken to dissipate the energy and go back to PS_0. These are intersystem crossing, radiative dissipation (light emission i.e. luminescence) and vibrational relaxation. This process involves intramolecular movements and collisions with surrounding molecules resulting in heat generation. Non-radiative decay processes such as vibrational relaxation, internal conversion, intersystem crossing produce mechanical energy which is

converted into heat.[182] By being a very effective, light absorber, CNTs are particular efficient at heat generation through light irradiation.

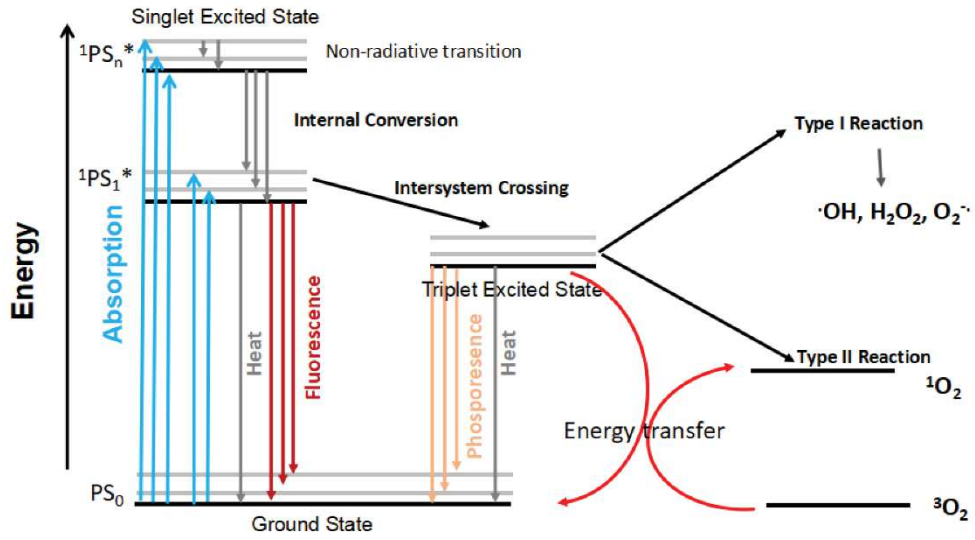

Figure 1-16. Jablonski diagram, showing the ways of the molecule from light adsorption. ^{1}PSn*: excited state; $^1PS_1$*: lowest excited state; PS_0: ground state.[182]

To date, intensive research has been done in order to optimize the photothermal effect using SWCNTs or MWCNTs. Our group reported the fabrication of CNTs@MS in order to perform photothermal therapy and light-triggered chemotherapy.[165,166] Burke et al.[183] reported very efficient tumor ablation and long-term remission by using MWCNTs and a single 30 s laser irradiation. PEGylated-MWCNTs demonstrated to be powerful nanoobjects for melanoma cancer[184] and solid tumor therapy in general.

Furthermore, CNTs-based nanoplatforms have also been mainly studied for combined phototherapy and chemotherapy thanks to their responsive behavior and loading capacity. Liu and coworkers[185] as well as Li *et al.*[186] reported the use of such nanomaterials to induce a very effective cancerous cell death by this dual treatment. Aside killing the cells through heating, phototherapy can also cause indirect cytotoxic effect, especially the reduction of blood flow in the tumor and therefore hypoxia of cancerous cells. It also potentiates the action of chemotherapy treatment by rendering the cells more sensitive to the drugs.[186]

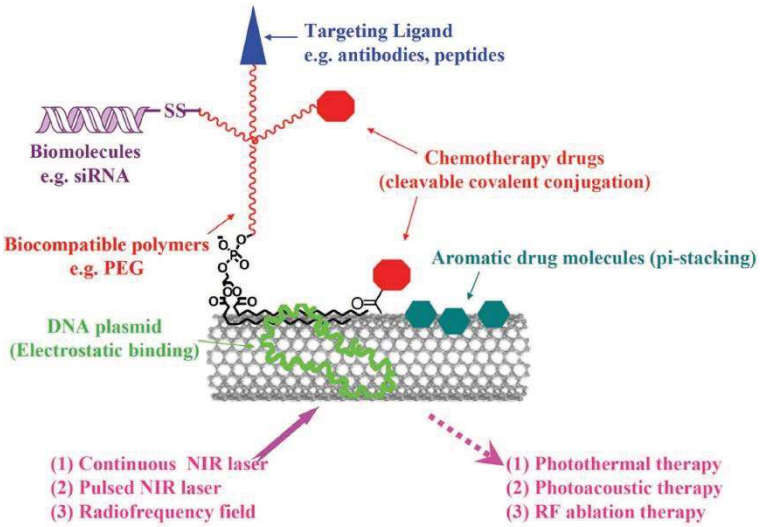

Figure 1-17. Schematic drawing showing various approaches for CNT-based cancer therapies.[187]

Functionalized CNTs are generally needed in order to load drug molecules. MS in particularly suited due to its hydrophilicity, high surface area and large pore size. **Figure 1-17** shows the different approaches applied for cancer therapy and drug delivery. Therapeutic drugs can be attached to CNTs via covalent bond or non-covalent adsorption. Esterification, amidation and 1,3-dipolar cycloaddition are usually involved in order to link drugs to activated CNTs bearing carboxylic acids groups (thanks to oxidizing acidic treatment).[188,189] CNT@MS with copolymers were synthesized by Liu and coworkers to be used as anticancer multifunctional platforms.[190] This system shows an improved drug loading capacity and an enhanced the multi-stimuli triggered release dynamics and thus an effective cancer cell destruction by synergetic combination of PTT and chemotherapy.

I.6. Biological applications of IO@MS and CNTs@MS core-shell NPs

I.6.1. IO@MS NPs – *in vitro* / *in vivo* cancer therapy applications

Nanotechnology is quite a recent research field and it definitely changed the way therapeutics are designed and formulated. Conventional injectable therapeutics exhibit some major disadvantages such as lack of selectivity, low aqueous solubility, low bioavailability and a rapid fall in the plasma concentration due to rapid clearance of the drug. Injectable treatments which can deliver sustained controlled release would allow to reduce repeated administrations and hospitalizations by maintaining therapeutic drug levels in the plasma. The size of nanoparticles and their high area to surface ratio, targeting ability by surface functionalization, receptor attachment or EPR effect make these objects very suited for disease such cancers, autoimmune diseases or diabetes. Enhanced radiotherapy, hyperthermia, targeted drugs and DNA/siRNA delivery, development of contrast agents for MRI, CT imaging are among the new possibilities offered by injectable nanoformulations. The advantages of such injectable nanoformulations over conventional therapeutics are numerous but can also have some limitations such

as difficult in-depth penetration in tumor tissues, possible early opsonization and phagocytosis and difficult cell internalization. These will depend on the particle size, shape, surface charge and stabilizing-ligands.[191]

In particular, core-shell NPs IO@MS and CNT@MS thanks to their high loading capacity, versatile surface chemistry and intrinsic properties can find a variety of biomedical applications and numerous publications report them *in vitro* and *in vivo* promising application for cancer therapy.[191–194]

Recently, Sanchez-Salcedo *et al.*[195] investigated the simultaneous delivery of two different molecules, daunorubicin and anti-TWIST siRNA from IO@MS core-shell NPs coated with polyethyleneimine (PEI) as anchoring layers for deposition of zwiterrionic groups. This showed excellent low-fouling protein adsorption and, under AMF stimulation, the co-release of the drugs resulted in improved synergistic cytotoxicity of Ovcar8 (ovarian cancer cells). Avedian *et al.*[196] synthesized IO@MS NPs coated with folic-acid-modified PEI and used for delivery of Erlotinib. They observed that PEI acts as pH-sensitive coating and the presence of folic acid increased the cytotoxicity for HeLa cells.

Pon-on *et al.*[197] developed magnetic-silica nanoparticles encapsulated in a dual pH and temperature-responsive chitosan biopolymer NP (chitosan-g-NIPAM). Thanks to the superparamagnetic IO core, AMF stimulation can trigger the release of DOX. A burst release is obtained at pH=4 at 45 °C whereas at physiological pH and temperature the release was low. The cytotoxicity of the DOX is decreased when it is encapsulated inside the nanocomposite compared to the free DOX. Gao *et al.*[100] described the synthesis of IO@MS modified with a tumor-penetrating peptide and loaded with DOX. *In vitro* results showed the significant role of the conjugated peptide by enhancing cellular uptake and cytotoxicity of the NPs. *In vivo* experiments also showed the better accumulation in tumor tissue thus the antitumor effect of DOX-loaded NPs and an improved MRI signal.

Glioma is the most lethal type of cancer which accounts for majority of deaths and with very poor survival rate. Glioma treatments are mainly limited by the fact that it involves the crossing of the blood-barrier barrier (BBB) which is poorly permeable to the drugs.[198] Hegganvar *et al.*[199] developed an *in vitro* BBB model of human primary glioblastoma cells (U87 MG). They synthesized BBB-permeable nanoparticles consisting of IO@MS loaded with DOX and conjugated with modified Pluronic F-127 bearing at its endtip transferrin (Tf) to have a sustain and targeted release of anticancer DOX. The cytotoxicity assay of this nanocomposite clearly showed a lower IC_{50} than non-loaded NPs against U87 MG cells and thus efficient anticancer activity. Under magnetic trigger, the nanocomposite enhanced its permeability across human brain microvascular endothelial cells which facilitates DOX uptake.

The gene therapy by DNA/siRNA delivery has a huge potential in cancer therapy as they have unique functions as the knockdown of targeted genes or specific triggering of other genes. Xiong and coworkers[200] developed in this context an IO@MS core-shell NPs with large pores (12 nm) in order to load siRNA and release it under AMF. The silica shell was modified by aminosilane and the global

nanocomposite was coated with acid-liable tannic acid to serve as pH-responsive coating. The study showed a high loading capacity for siRNA (up to 2 wt%) and an enhanced release when magnetic field is applied. Tannic acid provided stability and siRNA was successfully delivered into the cytoplasm of KHOS (human osteosarcoma) cancer cells *in vitro* in a pH-responsive manner.

Recently, immunotherapy has been expanding rapidly in the biomedical community. It is based on the strengthening or the suppression of the patient's immune system to fight disease and, in particular, to treat cancers. Zheng *et al.*[201] developed a nanoplatform for immunotherapy by using IO@MS coated with PEG and filled with cytosine-guanine containing oligodeoxynucleotides (CpG ODN) which can be recognized as danger signals by the immune system. However, to date it is difficult to use free CpG ODN due to unfavorable *in vivo* biodistribution, lack of specificity and poor cellular uptake. The APTES functionalization and PEGylation allow high CpG loading capacity. They managed to activate macrophages and inhibit tumor cells when combined with chemotherapeutics while exhibiting negligible cytotoxicity *in vitro*. *In vivo*, these nanocomposites showed excellent immuno-stimulating activity.

I.6.2. CNT@MS – *in vitro* / *in vivo* cancer therapy applications

Efficient drug administration is a central theme and a real concern in the medical field. Low selectivity and/or low half-time multiply drug administrations and thus their side effects. In the last years, numerous reports and reviews have been published about the use of CNTs in biomedical applications due to their versatile properties like expected biocompatibility and suitable size in order to be used as smart nanocarriers for drug delivery and cancer treatment.[202–204] Indeed, their characteristic shape like "nano-needle" makes them very interesting to cross cell membrane and provide high cell transfection capabilities for drug delivery like DOX,[205,206] 10-hydrocamptothecin[207] but also for siRNA,[208,209] DNA[210] or proteins[211] delivery. In addition, CNTs can be used as diagnosis for early detection of cancer and the strong optical absorption in the NIR region is interesting for photothermal therapy applications. A lot of *in vitro* and *in vivo* studies have been achieved for the use of CNTs as efficient nanomaterials for cancer therapy.[212]

However, few studies concentrated on the potential of core-shell CNT@MS. Ma et al. synthesized mesoporous silica nanotubes by using CNT as a template for the silica deposition which is then removed by calcination. The obtained nanomaterials showed very large surface area (1000 $m^2.g^{-1}$), improved metformin loading compared to MCM-41 and pH-controlled release kinetics.[213] El-Shahawy *et al.*[214] designed CNTs@MS coated with chitosan in order to load high amount of DOX and have an oral treatment for breast cancers. On the other hand, in our team, we used CNTs@MS for drug delivery combined with photothermal therapy. Wells *et al.*[166] demonstrated that DOX loaded CNTs@MS is an efficient nanoplatforms for drug delivery activated either by acidic pH and/or remote NIR-light irradiation. Li *et al.*[165] confirmed the potential of this kind of nanomaterial. A human serum layer (HSA) layer was added around it for improved biocompatibility and biodistribution and the release kinetics

when NIR light is applied onto *in vitro* cell cultures was studied. The temperature increase due to photothermal effect and the resulting drug release played a synergetic role in tumor cell death.

However, when dealing with nanoparticles for biomedical applications, one of the first concerns should be about the potential impact on human health and environment. In the case of mesoporous silica NPs, they were shown to be non- toxic with few long-term issues and in most of the cases, excreted by urinary way and/or degraded in the body into safe silicic acid in few days/months. In contrast, more concerning issues are dealing with the biosafety of CNTs for medical usages. Indeed, it has been shown that CNTs may interfere with organs or cells and could be the source of varying severity and sometimes fatal issues due to disease development as described by Madani *et al.*[215] CNTs toxicity and biodistribution are linked to several parameters such as functionalization, dispersion, size and length. Non-covalently functionalized CNTs tend to accumulate more in liver and spleen than functionalized ones. PEGylation and other hydrophilic linkages allow good colloidal stability of CNTs. Functionalization of CNTs usually involves acidic treatments to activate and purify them and thus CNTs can be cut in small parts during the process. Non-functionalized hydrophobic CNTs tends to agglomerate and they usually accumulate quickly and possibly damage neighboring cells. They are easily detected by the immune system but not always properly phagocytosed because of their length compared to the size of macrophages.[216] The toxicity of suitable doses for administration is also a delicate question.

In summary, when considered as free circulating particles, there are persisting legitimate questions for the biomedical uses of CNTs but also nanoparticles in general. That is why a new trend in the research nowadays is to bring a new level of organization by building substrates or polymer scaffolds in which these particles are immobilized. This would lead to new devices in which the probability of NPs leaking of in the body would be considerably reduced. They could either biodegrade in the body and be naturally expulsed or being removable when therapeutics actions are accomplished. Several formulations have already been studied in particular for biosensing, imaging and diagnostic based on biopolymer or biodegradable multi-responsive scaffolds.

I.6.3. Smart scaffolds using AMF and/or NIR light as trigger

One of the main advantages to use remote external stimuli (magnetic fields, electric fields or light) is the possibility to activate on demand the nanocomposite, in particular to trigger the release of drugs or heating in a precise zone of the body. It also allows to have sustained drug delivery and thus maintaining therapeutic activity over a long time compared to the burst level of drugs by intravenous or oral administration. To overcome the problem of circulating NPs as explained above, some examples of smart polymer scaffolds (hydrogels, electrospun fibers…) responding to AMF and/or NIR light are detailed here in particular for drug delivery and cancer treatment.

As detailed above, Fe_3O_4 magnetite NPs placed in an appropriate AMF generate heat in their surrounding environment. Satarkar *et al.*[217] demonstrated the possibility to use this magnetothermal effect for remote drug delivery applications. They loaded superparamagnetic IO NPs in a

thermosensitive PNIPAAm-based crosslinked hydrogel with vitamin B12 and methylene blue. They were able to trigger the release of the drugs. By applying AMF for few minutes, the temperature raised above the LCST resulting in the gel shrinkage. Campbell *et al.*[218] prepared a subcutaneous injectable hydrogel whose crosslinking takes place by the condensation of aldehyde-functionalized dextran with IO NPs functionalized with hydrazide-modified PNIPAAm. Gelation is rapid when both components were mixed together. The gel was biocompatible *in vitro* and *in vivo* and remote and controlled drug release was shown when AMF was applied. On the other hand, Kim *et al.*[219] synthesized PNIPAAm electrospun nanofibers loaded with DOX and IO NPs. By AMF application, the fibers deswelled and released DOX. It successfully induced the death of human melanoma cancer cells (COLO 679) by synergetic effect of hyperthermia and chemotherapy. More advanced biological studies were conducted by Xie *et al.*[220] who injected into mice a cross-linked chitosan-PEG hydrogel loading with DOX, docetaxel and IO NPs. This gel showed self-healing and thermoresponsive behavior while being biocompatible. Upon AMF, the heating combined to the release of both drugs resulted in very efficient synergetic antitumor action *in vitro* and *in vivo*.

Concerning the use of NIR-light as a trigger to induce photothermal responsive behavior, gold NPs, up-converting NPs and carbon-based materials embedded into polymer scaffolds are the most represented. However, carbon-based materials@MS as photothermal source in a polymer scaffold was found to our knowledge the most advanced for NIR light-induced drug release. Graphene oxide (GO) was used by Wu and coworkers[221] to be incorporated inside a peptide hydrogel and loaded with DOX. They demonstrated that NIR light stimulation resulted in temperature increase thus releasing DOX due to the unfolding of the β-sheet structures of the peptide.

CNTs were also used for electrically-triggered drug delivery as detailed by Spizzirri's team.[222] For example they incorporated MWCNTs into cross-linked gelatin microsphere with a drug. By the application of a 9V tension on the beads, they showed that it induced shrinkage and consequently a drug release. Servant *et al.*[223] showed that pristine MWCNTs incorporated in the methacrylic acid-polymerized matrix with a drug allowed pulsatile drug delivery by electric pulses. Interestingly, the delivery rate came quickly back to normal when the electric pulse was stopped. The biomedical applications of CNTs@MS combining the features of both materials incorporated into macroscopic scaffolds are gaining much interest but still very few papers report their use. Although CNTs@MS nanoplatforms have been synthesized, there is still a lot of investigations to do about their applications for cancer therapy but also tissue engineering, bone regeneration, nerve repairing, wound healing, antimicrobial surface... that are not detailed here.

I.7. Conclusion

Core-shell nanocomposites, which exhibit very appealing properties offer promising applications as smart nanoplatforms for cancer therapy. Moreover, by combining the features of at least two materials, they extend the possibilities to perform dual-therapy of cancer which is a determining key to go further in the treatment of this disease. In this state-of-the-art, we showed that IO@MS and CNTs@MS are very well suited biocompatible nanoplatforms to perform hyperthermia treatment induced either by AMF or NIR and combined with drug delivery.

Nevertheless, there is always progress to do in the design of these nanoplatforms to optimize their antitumoral action and to make them safer. Before further translation into clinical trials, their physicochemical behaviors under external field can still be improved and better characterized. In particular, the control of the heat dissipation from the core of the NP to the external environment is fundamental for efficient hyperthermia or thermal ablation applications and to understand the therapeutic mode of action of the nano-objects when they are in tissues and in cells. Furthermore, the amount of drug delivered to the target sites remains quite low and that is probably because the interactions of the drug with the pore walls of the silica carrier are not completely controlled. Finally, injection and dissemination of NPs in human body stills remains a sensitive issue which strongly hamper their application in clinical uses and this should be taken into account for further development of nanotechnologies in the medical field.

In this context, the objectives will be to face some of these challenges by:

1) Synthesizing different silica shells around IO core to understand its influence on the heat transfer when the nanocomposite is placed in an AMF. This would help to better design the silica shell for further hyperthermia applications.
2) Studying the influence of the surface functionalization and the pH on the drug loading and the drug release behaviors.
3) Designing an original supramolecular hydrogel in which the NPs would be embedded in order to create a smart implant able to deliver drug under external trigger.

I.8. References

(1) Sung, H.; Ferlay, J.; Siegel, R. L.; Laversanne, M.; Soerjomataram, I.; Jemal, A.; Bray, F. Global Cancer Statistics 2020: GLOBOCAN Estimates of Incidence and Mortality Worldwide for 36 Cancers in 185 Countries. *CA: A Cancer Journal for Clinicians* **2021**, *71* (3), 209–249.

(2) Feng, S.-S.; Chien, S. Chemotherapeutic Engineering: Application and Further Development of Chemical Engineering Principles for Chemotherapy of Cancer and Other Diseases. *Chemical Engineering Science* **2003**, *58* (18), 4087–4114.

(3) Gurunathan, S.; Kang, M.-H.; Qasim, M.; Kim, J.-H. Nanoparticle-Mediated Combination Therapy: Two-in-One Approach for Cancer. *International Journal of Molecular Sciences* **2018**, *19* (10), 3264.

(4) Matsumura, Y.; Maeda, H. A New Concept for Macromolecular Therapeutics in Cancer Chemotherapy: Mechanism of Tumoritropic Accumulation of Proteins and the Antitumor Agent Smancs. *Cancer Res* **1986**, *46* (12 Part 1), 6387–6392.

(5) Aghebati-Maleki, A.; Dolati, S.; Ahmadi, M.; Baghbanzhadeh, A.; Asadi, M.; Fotouhi, A.; Yousefi, M.; Aghebati-Maleki, L. Nanoparticles and Cancer Therapy: Perspectives for Application of Nanoparticles in the Treatment of Cancers. *Journal of Cellular Physiology* **2020**, *235* (3), 1962–1972.

(6) Wang, Y.-X. J. Current Status of Superparamagnetic Iron Oxide Contrast Agents for Liver Magnetic Resonance Imaging. *World Journal of Gastroenterology* **2015**, *21* (47), 13400–13402.

(7) Huang, H.; Feng, W.; Chen, Y.; Shi, J. Inorganic Nanoparticles in Clinical Trials and Translations. *Nano Today* **2020**, *35*, 100972.

(8) Cavaliere, R.; Ciocatto, E. C.; Giovanella, B. C.; Heidelberger, C.; Johnson, R. O.; Margottini, M.; Mondovi, B.; Moricca, G.; Rossi-Fanelli, A. Selective Heat Sensitivity of Cancer Cells. Biochemical and Clinical Studies. *Cancer* **1967**, *20* (9), 1351–1381.

(9) Overgaard, J. Effect of Hyperthermia on Malignant Cells in Vivo: A Review and a Hypothesis. *Cancer* **1977**, *39* (6), 2637–2646.

(10) van der Zee, J. Heating the Patient: A Promising Approach? *Annals of Oncology* **2002**, *13* (8), 1173–1184.

(11) Yu, T.-J.; Li, P.-H.; Tseng, T.-W.; Chen, Y.-C. Multifunctional Fe3O4/Alumina Core/Shell MNPs as Photothermal Agents for Targeted Hyperthermia of Nosocomial and Antibiotic-Resistant Bacteria. *Nanomedicine* **2011**, *6* (8), 1353–1363.

(12) Peigney, A.; Laurent, Ch.; Flahaut, E.; Bacsa, R. R.; Rousset, A. Specific Surface Area of Carbon Nanotubes and Bundles of Carbon Nanotubes. *Carbon* **2001**, *39* (4), 507–514.

(13) Kolosnjaj-Tabi, J.; Kralj, S.; Griseti, E.; Nemec, S.; Wilhelm, C.; Plan Sangnier, A.; Bellard, E.; Fourquaux, I.; Golzio, M.; Rols, M.-P. Magnetic Silica-Coated Iron Oxide Nanochains as Photothermal Agents, Disrupting the Extracellular Matrix, and Eradicating Cancer Cells. *Cancers* **2019**, *11* (12), 2040.

(14) Nemec, S.; Kralj, S.; Wilhelm, C.; Abou-Hassan, A.; Rols, M.-P.; Kolosnjaj-Tabi, J. Comparison of Iron Oxide Nanoparticles in Photothermia and Magnetic Hyperthermia: Effects of Clustering and Silica Encapsulation on Nanoparticles' Heating Yield. *Applied Sciences* **2020**, *10* (20), 7322.

(15) Firme, C. P.; Bandaru, P. R. Toxicity Issues in the Application of Carbon Nanotubes to Biological Systems. *Nanomedicine: Nanotechnology, Biology and Medicine* **2010**, *6* (2), 245–256.

(16) Kobayashi, N.; Izumi, H.; Morimoto, Y. Review of Toxicity Studies of Carbon Nanotubes. *Journal of Occupational Health* **2017**, *advpub*.

(17) Anselmo, A. C.; Mitragotri, S. Nanoparticles in the Clinic: An Update Post COVID-19 Vaccines. *Bioengineering & Translational Medicine* **2021**, *6* (3), e10246.

(18) Beck, J. S.; Vartuli, J. C.; Roth, W. J.; Leonowicz, M. E.; Kresge, C. T.; Schmitt, K. D.; Chu, C. T. W.; Olson, D. H.; Sheppard, E. W.; McCullen, S. B.; Higgins, J. B.; Schlenker, J. L. A New Family of Mesoporous Molecular Sieves Prepared with Liquid Crystal Templates. *J. Am. Chem. Soc.* **1992**, *114* (27), 10834–10843.

(19) Inagaki, S.; Fukushima, Y.; Kuroda, K. Synthesis of Highly Ordered Mesoporous Materials from a Layered Polysilicate. *J. Chem. Soc., Chem. Commun.* **1993**, No. 8, 680–682.

(20) Yanagisawa, T.; Shimizu, T.; Kuroda, K.; Kato, C. The Preparation of Alkyltrimethylammonium–Kanemite Complexes and Their Conversion to Microporous Materials. *BCSJ* **1990**, *63* (4), 988–992.

(21) Kresge, C. T.; Leonowicz, M. E.; Roth, W. J.; Vartuli, J. C.; Beck, J. S. Ordered Mesoporous Molecular Sieves Synthesized by a Liquid-Crystal Template Mechanism. *Nature* **1992**, *359* (6397), 710–712.

(22) Kresge, C. T.; Roth, W. J. The Discovery of Mesoporous Molecular Sieves from the Twenty Year Perspective. *Chem. Soc. Rev.* **2013**, *42* (9), 3663–3670.

(23) Firouzi, A.; Kumar, D.; Bull, L. M.; Besier, T.; Sieger, P.; Huo, Q.; Walker, S. A.; Zasadzinski, J. A.; Glinka, C.; Nicol, J.; Margolese, D.; Stucky, G. D.; Chmelka, B. F. Cooperative Organization of Inorganic-Surfactant and Biomimetic Assemblies. *Science* **1995**, *267* (5201), 1138–1143.

(24) Fowler, C. E.; Khushalani, D.; Lebeau, B.; Mann, S. Nanoscale Materials with Mesostructured Interiors. *Advanced Materials* **2001**, *13* (9), 649–652.
(25) Nooney, R. I.; Thirunavukkarasu, D.; Chen, Y.; Josephs, R.; Ostafin, A. E. Synthesis of Nanoscale Mesoporous Silica Spheres with Controlled Particle Size. *Chem. Mater.* **2002**, *14* (11), 4721–4728.
(26) Cai, Q.; Luo, Z.-S.; Pang, W.-Q.; Fan, Y.-W.; Chen, X.-H.; Cui, F.-Z. Dilute Solution Routes to Various Controllable Morphologies of MCM-41 Silica with a Basic Medium. *Chem. Mater.* **2001**, *13* (2), 258–263.
(27) Knežević, N. Ž.; Durand, J.-O. Large Pore Mesoporous Silica Nanomaterials for Application in Delivery of Biomolecules. *Nanoscale* **2015**, *7* (6), 2199–2209.
(28) Du, X.; He, J. Fine-Tuning of Silica Nanosphere Structure by Simple Regulation of the Volume Ratio of Cosolvents. *Langmuir* **2010**, *26* (12), 10057–10062.
(29) Wang, S.-G.; Wu, C.-W.; Chen, K.; Lin, V. S.-Y. Fine-Tuning Mesochannel Orientation of Organically Functionalized Mesoporous Silica Nanoparticles. *Chemistry – An Asian Journal* **2009**, *4* (5), 658–661.
(30) Cho, Y.; Shi, R.; Ivanisevic, A.; Borgens, R. B. A Mesoporous Silica Nanosphere-Based Drug Delivery System Using an Electrically Conducting Polymer. *Nanotechnology* **2009**, *20* (27), 275102.
(31) Wu, L.; Jiao, Z.; Wu, M.; Song, T.; Zhang, H. Formation of Mesoporous Silica Nanoparticles with Tunable Pore Structure as Promising Nanoreactor and Drug Delivery Vehicle. *RSC Adv.* **2016**, *6* (16), 13303–13311.
(32) Zhao, D.; Huo, Q.; Feng, J.; Chmelka, B. F.; Stucky, G. D. Nonionic Triblock and Star Diblock Copolymer and Oligomeric Surfactant Syntheses of Highly Ordered, Hydrothermally Stable, Mesoporous Silica Structures. *J. Am. Chem. Soc.* **1998**, *120* (24), 6024–6036.
(33) Zhao, D.; Feng, J.; Huo, Q.; Melosh, N.; Fredrickson, G. H.; Chmelka, B. F.; Stucky, G. D. Triblock Copolymer Syntheses of Mesoporous Silica with Periodic 50 to 300 Angstrom Pores. *Science* **1998**, *279* (5350), 548–552.
(34) Croissant, J. G.; Fatieiev, Y.; Khashab, N. M. Degradability and Clearance of Silicon, Organosilica, Silsesquioxane, Silica Mixed Oxide, and Mesoporous Silica Nanoparticles. *Advanced Materials* **2017**, *29* (9), 1604634.
(35) Liberman, A.; Mendez, N.; Trogler, W. C.; Kummel, A. C. Synthesis and Surface Functionalization of Silica Nanoparticles for Nanomedicine. *Surface Science Reports* **2014**, *69* (2), 132–158.
(36) Feng, Y.; Panwar, N.; Tng, D. J. H.; Tjin, S. C.; Wang, K.; Yong, K.-T. The Application of Mesoporous Silica Nanoparticle Family in Cancer Theranostics. *Coordination Chemistry Reviews* **2016**, *319*, 86–109.
(37) Vallet-Regi, M.; Rámila, A.; del Real, R. P.; Pérez-Pariente, J. A New Property of MCM-41: Drug Delivery System. *Chem. Mater.* **2001**, *13* (2), 308–311.
(38) Croissant, J. G.; Fatieiev, Y.; Almalik, A.; Khashab, N. M. Mesoporous Silica and Organosilica Nanoparticles: Physical Chemistry, Biosafety, Delivery Strategies, and Biomedical Applications. *Advanced Healthcare Materials* **2018**, *7* (4), 1700831.
(39) Zhou, S.; Zhong, Q.; Wang, Y.; Hu, P.; Zhong, W.; Huang, C.-B.; Yu, Z.-Q.; Ding, C.-D.; Liu, H.; Fu, J. Chemically Engineered Mesoporous Silica Nanoparticles-Based Intelligent Delivery Systems for Theranostic Applications in Multiple Cancerous/Non-Cancerous Diseases. *Coordination Chemistry Reviews* **2022**, *452*, 214309.
(40) Hosseinpour, S.; J. Walsh, L.; Xu, C. Biomedical Application of Mesoporous Silica Nanoparticles as Delivery Systems: A Biological Safety Perspective. *Journal of Materials Chemistry B* **2020**, *8* (43), 9863–9876.
(41) Shubayev, V. I.; Pisanic, T. R.; Jin, S. Magnetic Nanoparticles for Theragnostics. *Advanced Drug Delivery Reviews* **2009**, *61* (6), 467–477.
(42) Soo Choi, H.; Liu, W.; Misra, P.; Tanaka, E.; Zimmer, J. P.; Itty Ipe, B.; Bawendi, M. G.; Frangioni, J. V. Renal Clearance of Quantum Dots. *Nat Biotechnol* **2007**, *25* (10), 1165–1170.
(43) Liu, D.; Yang, F.; Xiong, F.; Gu, N. The Smart Drug Delivery System and Its Clinical Potential. *Theranostics* **2016**, *6* (9), 1306–1323.
(44) Lai, C.-Y.; Trewyn, B. G.; Jeftinija, D. M.; Jeftinija, K.; Xu, S.; Jeftinija, S.; Lin, V. S.-Y. A Mesoporous Silica Nanosphere-Based Carrier System with Chemically Removable CdS Nanoparticle Caps for Stimuli-Responsive Controlled Release of Neurotransmitters and Drug Molecules. *J. Am. Chem. Soc.* **2003**, *125* (15), 4451–4459.
(45) Schlossbauer, A.; Kecht, J.; Bein, T. Biotin–Avidin as a Protease-Responsive Cap System for Controlled Guest Release from Colloidal Mesoporous Silica. *Angewandte Chemie International Edition* **2009**, *48* (17), 3092–3095.
(46) Hernandez, R.; Tseng, H.-R.; Wong, J. W.; Stoddart, J. F.; Zink, J. I. An Operational Supramolecular Nanovalve. *J. Am. Chem. Soc.* **2004**, *126* (11), 3370–3371.
(47) Canton, I.; Battaglia, G. Endocytosis at the Nanoscale. *Chem. Soc. Rev.* **2012**, *41* (7), 2718–2739.

(48) Tannock, I. F.; Rotin, D. Acid PH in Tumors and Its Potential for Therapeutic Exploitation. *Cancer Res* **1989**, *49* (16), 4373–4384.
(49) Cornell, R. M.; Schwertmann, U. *The Iron Oxides: Structure, Properties, Reactions, Occurrences and Uses*; John Wiley & Sons, 2003.
(50) Lekha, G. M.; George, S. Colloidal Magnetic Metal Oxide Nanocrystals and Their Applications. In *Colloidal Metal Oxide Nanoparticles*; Elsevier, 2020; pp 289–335.
(51) Massart, R. Preparation of Aqueous Magnetic Liquids in Alkaline and Acidic Media. *IEEE Transactions on Magnetics* **1981**, *17* (2), 1247–1248.
(52) Kim, D. K.; Mikhaylova, M.; Zhang, Y.; Muhammed, M. Protective Coating of Superparamagnetic Iron Oxide Nanoparticles. *Chem. Mater.* **2003**, *15* (8), 1617–1627.
(53) Aziz, T.; Masum, S. M.; Qadir, M. R.; Gafur, A.; Huq, D. Physicochemical Characterization of Iron Oxide Nanoparticle Coated with Chitosan for Biomedical Application. *International Research Journal of Pure and Applied Chemistry* **2016**, 1–9.
(54) Hasany, S. F.; Ahmed, I.; Jose, R.; A.Rehman. Systematic Review of the Preparation Techniques of Iron Oxide Magnetic Nanoparticles. *Nanoscience and Nanotechnology* **2011**, *1(1): 1-11*.
(55) Fazel-Rezai, R. *Biomedical Engineering: Frontiers and Challenges*; BoD – Books on Demand, 2011.
(56) Jolivet, J.-P.; Henry, M.; Livage, J. *Metal Oxide Chemistry and Synthesis: From Solution to Solid State*; John Wiley: Chichester ; New York, 2000.
(57) Karaagac, O.; Kockar, H.; Beyaz, S.; Tanrisever, T. A Simple Way to Synthesize Superparamagnetic Iron Oxide Nanoparticles in Air Atmosphere: Iron Ion Concentration Effect. *IEEE Transactions on Magnetics* **2010**, *46* (12), 3978–3983.
(58) Karaagac, O.; Kockar, H. Effect of Synthesis Parameters on the Properties of Superparamagnetic Iron Oxide Nanoparticles. *J Supercond Nov Magn* **2012**, *25* (8), 2777–2781.
(59) Jolivet, J.-P.; Froidefond, C.; Pottier, A.; Chanéac, C.; Cassaignon, S.; Tronc, E.; Euzen, P. Size Tailoring of Oxide Nanoparticles by Precipitation in Aqueous Medium. A Semi-Quantitative Modelling. *J. Mater. Chem.* **2004**, *14* (21), 3281–3288.
(60) Jolivet, J.-P.; Chanéac, C.; Tronc, E. Iron Oxide Chemistry. From Molecular Clusters to Extended Solid Networks. *Chem. Commun.* **2004**, No. 5, 481–483.
(61) Fievet, F.; Lagier, J. P.; Blin, B.; Beaudoin, B.; Figlarz, M. Homogeneous and Heterogeneous Nucleations in the Polyol Process for the Preparation of Micron and Submicron Size Metal Particles. *Solid State Ionics* **1989**, *32–33*, 198–205.
(62) Joseyphus, R. J.; Shinoda, K.; Kodama, D.; Jeyadevan, B. Size Controlled Fe Nanoparticles through Polyol Process and Their Magnetic Properties. *Materials Chemistry and Physics* **2010**, *123* (2), 487–493.
(63) Ali, A.; Zafar, H.; Zia, M.; Haq, I. ul; Phull, A. R.; Ali, J. S.; Hussain, A. Synthesis, Characterization, Applications, and Challenges of Iron Oxide Nanoparticles. *NSA* **2016**, *9*, 49–67.
(64) Verma, S.; Joy, P. A.; Khollam, Y. B.; Potdar, H. S.; Deshpande, S. B. Synthesis of Nanosized MgFe2O4 Powders by Microwave Hydrothermal Method. *Materials Letters* **2004**, *58* (6), 1092–1095.
(65) Khollam, Y. B.; Dhage, S. R.; Potdar, H. S.; Deshpande, S. B.; Bakare, P. P.; Kulkarni, S. D.; Date, S. K. Microwave Hydrothermal Preparation of Submicron-Sized Spherical Magnetite (Fe3O4) Powders. *Materials Letters* **2002**, *56* (4), 571–577.
(66) Hao, Y.; Teja, A. S. Continuous Hydrothermal Crystallization of α–Fe2O3 and Co3O4 Nanoparticles. *Journal of Materials Research* **2003**, *18* (2), 415–422.
(67) Gul, S.; Khan, S. B.; Rehman, I. U.; Khan, M. A.; Khan, M. I. A Comprehensive Review of Magnetic Nanomaterials Modern Day Theranostics. *Frontiers in Materials* **2019**, *6*, 179.
(68) Sun, S.; Zeng, H.; Robinson, D. B.; Raoux, S.; Rice, P. M.; Wang, S. X.; Li, G. Monodisperse MFe2O4 (M = Fe, Co, Mn) Nanoparticles. *J. Am. Chem. Soc.* **2004**, *126* (1), 273–279.
(69) Sun, S.; Zeng, H. Size-Controlled Synthesis of Magnetite Nanoparticles. *J. Am. Chem. Soc.* **2002**, *124* (28), 8204–8205.
(70) Park, J.; An, K.; Hwang, Y.; Park, J.-G.; Noh, H.-J.; Kim, J.-Y.; Park, J.-H.; Hwang, N.-M.; Hyeon, T. Ultra-Large-Scale Syntheses of Monodisperse Nanocrystals. *Nature Mater* **2004**, *3* (12), 891–895.
(71) Shipway, A. N.; Katz, E.; Willner, I. Nanoparticle Arrays on Surfaces for Electronic, Optical, and Sensor Applications*. **2000**, 35.
(72) Herman, D. A. J.; Cheong-Tilley, S.; McGrath, A. J.; McVey, B. F. P.; Lein, M.; Tilley, R. D. How to Choose a Precursor for Decomposition Solution-Phase Synthesis: The Case of Iron Nanoparticles. *Nanoscale* **2015**, *7* (14), 5951–5954.
(73) Cotin, G.; Perton, F.; Petit, C.; Sall, S.; Kiefer, C.; Begin, V.; Pichon, B.; Lefevre, C.; Mertz, D.; Greneche, J.-M.; Begin-Colin, S. Harnessing Composition of Iron Oxide Nanoparticle: Impact of Solvent-Mediated Ligand–Ligand Interaction and Competition between Oxidation and Growth Kinetics. *Chem. Mater.* **2020**, *32* (21), 9245–9259.

(74) Blanco-Andujar, C.; Walter, A.; Cotin, G.; Bordeianu, C.; Mertz, D.; Felder-Flesch, D.; Begin-Colin, S. Design of Iron Oxide-Based Nanoparticles for MRI and Magnetic Hyperthermia. *Nanomedicine* **2016**, *11* (14), 1889–1910.

(75) Barnakov, Y. A.; Yu, M. H.; Rosenzweig, Z. Manipulation of the Magnetic Properties of Magnetite−Silica Nanocomposite Materials by Controlled Stober Synthesis. *Langmuir* **2005**, *21* (16), 7524–7527.

(76) Stöber, W.; Fink, A.; Bohn, E. Controlled Growth of Monodisperse Silica Spheres in the Micron Size Range. *Journal of Colloid and Interface Science* **1968**, *26* (1), 62–69.

(77) Andrade, A. L.; Souza, D. M.; Pereira, M. C.; Fabris, J. D.; Domingues, R. Z. Synthesis and Characterization of Magnetic Nanoparticles Coated with Silica through a Sol-Gel Approach. *Cerâmica* **2009**, *55*, 420–424.

(78) Im, S. H.; Herricks, T.; Lee, Y. T.; Xia, Y. Synthesis and Characterization of Monodisperse Silica Colloids Loaded with Superparamagnetic Iron Oxide Nanoparticles. *Chemical Physics Letters* **2005**, *401* (1), 19–23.

(79) Han, Y.; Lu, Z.; Teng, Z.; Liang, J.; Guo, Z.; Wang, D.; Han, M.-Y.; Yang, W. Unraveling the Growth Mechanism of Silica Particles in the Stöber Method: In Situ Seeded Growth Model. *Langmuir* **2017**, *33* (23), 5879–5890.

(80) Deng, Y.-H.; Wang, C.-C.; Hu, J.-H.; Yang, W.-L.; Fu, S.-K. Investigation of Formation of Silica-Coated Magnetite Nanoparticles via Sol–Gel Approach. *Colloids and Surfaces A: Physicochemical and Engineering Aspects* **2005**, *262* (1), 87–93.

(81) Vogt, C.; Toprak, M. S.; Muhammed, M.; Laurent, S.; Bridot, J.-L.; Müller, R. N. High Quality and Tuneable Silica Shell–Magnetic Core Nanoparticles. *J Nanopart Res* **2010**, *12* (4), 1137–1147.

(82) Ding, H. L.; Zhang, Y. X.; Wang, S.; Xu, J. M.; Xu, S. C.; Li, G. H. Fe3O4@SiO2 Core/Shell Nanoparticles: The Silica Coating Regulations with a Single Core for Different Core Sizes and Shell Thicknesses. *Chem. Mater.* **2012**, *24* (23), 4572–4580.

(83) Liu, J.; Detrembleur, C.; Pauw-Gillet, M.-C. D.; Mornet, S.; Vander Elst, L.; Laurent, S.; Jérôme, C.; Duguet, E. Heat-Triggered Drug Release Systems Based on Mesoporous Silica Nanoparticles Filled with a Maghemite Core and Phase-Change Molecules as Gatekeepers. *Journal of Materials Chemistry B* **2014**, *2* (1), 59–70.

(84) Deng, Y.; Qi, D.; Deng, C.; Zhang, X.; Zhao, D. Superparamagnetic High-Magnetization Microspheres with an Fe3O4@SiO2 Core and Perpendicularly Aligned Mesoporous SiO2 Shell for Removal of Microcystins. *J. Am. Chem. Soc.* **2008**, *130* (1), 28–29.

(85) Ye, F.; Laurent, S.; Fornara, A.; Astolfi, L.; Qin, J.; Roch, A.; Martini, A.; Toprak, M. S.; Muller, R. N.; Muhammed, M. Uniform Mesoporous Silica Coated Iron Oxide Nanoparticles as a Highly Efficient, Nontoxic MRI T2 Contrast Agent with Tunable Proton Relaxivities. *Contrast Media & Molecular Imaging* **2012**, *7* (5), 460–468.

(86) Kim, J.; Lee, J. E.; Lee, J.; Yu, J. H.; Kim, B. C.; An, K.; Hwang, Y.; Shin, C.-H.; Park, J.-G.; Kim, J.; Hyeon, T. Magnetic Fluorescent Delivery Vehicle Using Uniform Mesoporous Silica Spheres Embedded with Monodisperse Magnetic and Semiconductor Nanocrystals. *J. Am. Chem. Soc.* **2006**, *128* (3), 688–689.

(87) Nyalosaso, J. L.; Rascol, E.; Pisani, C.; Dorandeu, C.; Dumail, X.; Maynadier, M.; Gary-Bobo, M.; Him, J. L. K.; Bron, P.; Garcia, M.; Devoisselle, J. M.; Prat, O.; Guari, Y.; Charnay, C.; Chopineau, J. Synthesis, Decoration, and Cellular Effects of Magnetic Mesoporous Silica Nanoparticles. *RSC Adv.* **2016**, *6* (62), 57275–57283.

(88) Fan, H.; Leve, E.; Gabaldon, J.; Wright, A.; Haddad, R. E.; Brinker, C. J. Ordered Two- and Three-Dimensional Arrays Self-Assembled from Water-Soluble Nanocrystal–Micelles. *Advanced Materials* **2005**, *17* (21), 2587–2590.

(89) Yang, J.; Shen, D.; Wei, Y.; Li, W.; Zhang, F.; Kong, B.; Zhang, S.; Teng, W.; Fan, J.; Zhang, W.; Dou, S.; Zhao, D. Monodisperse Core-Shell Structured Magnetic Mesoporous Aluminosilicate Nanospheres with Large Dendritic Mesochannels. *Nano Res.* **2015**, *8* (8), 2503–2514.

(90) Guo, B.; Yim, H.; Khasanov, A.; Stevens, J. Formation of Magnetic FexOy/Silica Core-Shell Particles in a One-Step Flame Aerosol Process. *Aerosol Science and Technology* **2010**, *44* (4), 281–291.

(91) Li, D.; Teoh, W. Y.; Selomulya, C.; Woodward, R. C.; Amal, R.; Rosche, B. Flame-Sprayed Superparamagnetic Bare and Silica-Coated Maghemite Nanoparticles: Synthesis, Characterization, and Protein Adsorption−Desorption. *Chem. Mater.* **2006**, *18* (26), 6403–6413.

(92) Fernández-Pacheco, R.; Arruebo, M.; Marquina, C.; Ibarra, R.; Arbiol, J.; Santamaría, J. Highly Magnetic Silica-Coated Iron Nanoparticles Prepared by the Arc-Discharge Method. *Nanotechnology* **2006**, *17* (5), 1188–1192.

(93) van Geuns, R.-J. M.; Wielopolski, P. A.; de Bruin, H. G.; Rensing, B. J.; van Ooijen, P. M. A.; Hulshoff, M.; Oudkerk, M.; de Feyter, P. J. Basic Principles of Magnetic Resonance Imaging. *Progress in Cardiovascular Diseases* **1999**, *42* (2), 149–156.

(94) Lee, N.; Hyeon, T. Designed Synthesis of Uniformly Sized Iron Oxide Nanoparticles for Efficient Magnetic Resonance Imaging Contrast Agents. *Chem. Soc. Rev.* **2012**, *41* (7), 2575–2589.

(95) Ni, D.; Bu, W.; Ehlerding, E. B.; Cai, W.; Shi, J. Engineering of Inorganic Nanoparticles as Magnetic Resonance Imaging Contrast Agents. *Chem. Soc. Rev.* **2017**, *46* (23), 7438–7468.

(96) Ye, F.; Laurent, S.; Fornara, A.; Astolfi, L.; Qin, J.; Roch, A.; Martini, A.; Toprak, M. S.; Muller, R. N.; Muhammed, M. Uniform Mesoporous Silica Coated Iron Oxide Nanoparticles as a Highly Efficient, Nontoxic MRI T2 Contrast Agent with Tunable Proton Relaxivities. *Contrast Media & Molecular Imaging* **2012**, *7* (5), 460–468.

(97) Pinho, S. L. C.; Pereira, G. A.; Voisin, P.; Kassem, J.; Bouchaud, V.; Etienne, L.; Peters, J. A.; Carlos, L.; Mornet, S.; Geraldes, C. F. G. C.; Rocha, J.; Delville, M.-H. Fine Tuning of the Relaxometry of γ-Fe2O3@SiO2 Nanoparticles by Tweaking the Silica Coating Thickness. *ACS Nano* **2010**, *4* (9), 5339–5349.

(98) Pinho, S. L. C.; Laurent, S.; Rocha, J.; Roch, A.; Delville, M.-H.; Mornet, S.; Carlos, L. D.; Vander Elst, L.; Muller, R. N.; Geraldes, C. F. G. C. Relaxometric Studies of γ-Fe2O3@SiO2 Core Shell Nanoparticles: When the Coating Matters. *J. Phys. Chem. C* **2012**, *116* (3), 2285–2291.

(99) Zhang, C.; Wängler, B.; Morgenstern, B.; Zentgraf, H.; Eisenhut, M.; Untenecker, H.; Krüger, R.; Huss, R.; Seliger, C.; Semmler, W.; Kiessling, F. Silica- and Alkoxysilane-Coated Ultrasmall Superparamagnetic Iron Oxide Particles: A Promising Tool To Label Cells for Magnetic Resonance Imaging. *Langmuir* **2007**, *23* (3), 1427–1434.

(100) Gao, L.; Yu, J.; Liu, Y.; Zhou, J.; Sun, L.; Wang, J.; Zhu, J.; Peng, H.; Lu, W.; Yu, L.; Yan, Z.; Wang, Y. Tumor-Penetrating Peptide Conjugated and Doxorubicin Loaded T_1 -T_2 Dual Mode MRI Contrast Agents Nanoparticles for Tumor Theranostics. *Theranostics* **2018**, *8* (1), 92–108.

(101) Habash, R. W. Y.; Bansal, R.; Krewski, D.; Alhafid, H. T. Thermal Therapy, Part 1: An Introduction to Thermal Therapy. *CRB* **2006**, *34* (6).

(102) Gilchrist, R. K.; Medal, R.; Shorey, W. D.; Hanselman, R. C.; Parrott, J. C.; Taylor, C. B. Selective Inductive Heating of Lymph Nodes. *Ann Surg* **1957**, *146* (4), 596–606.

(103) Laurent, S.; Dutz, S.; Häfeli, U. O.; Mahmoudi, M. Magnetic Fluid Hyperthermia: Focus on Superparamagnetic Iron Oxide Nanoparticles. *Advances in Colloid and Interface Science* **2011**, *166* (1), 8–23.

(104) Périgo, E. A.; Hemery, G.; Sandre, O.; Ortega, D.; Garaio, E.; Plazaola, F.; Teran, F. J. Fundamentals and Advances in Magnetic Hyperthermia. *Applied Physics Reviews* **2015**, *2* (4), 041302.

(105) Rosensweig, R. E. Heating Magnetic Fluid with Alternating Magnetic Field. *Journal of Magnetism and Magnetic Materials* **2002**, *252*, 370–374.

(106) Glöckl, G.; Hergt, R.; Zeisberger, M.; Dutz, S.; Nagel, S.; Weitschies, W. The Effect of Field Parameters, Nanoparticle Properties and Immobilization on the Specific Heating Power in Magnetic Particle Hyperthermia. *J. Phys.: Condens. Matter* **2006**, *18* (38), S2935–S2949.

(107) Hergt, R.; Dutz, S.; Müller, R.; Zeisberger, M. Magnetic Particle Hyperthermia: Nanoparticle Magnetism and Materials Development for Cancer Therapy. *J. Phys.: Condens. Matter* **2006**, *18* (38), S2919–S2934.

(108) de la Presa, P.; Luengo, Y.; Multigner, M.; Costo, R.; Morales, M. P.; Rivero, G.; Hernando, A. Study of Heating Efficiency as a Function of Concentration, Size, and Applied Field in γ-Fe2O3 Nanoparticles. *J. Phys. Chem. C* **2012**, *116* (48), 25602–25610.

(109) Hergt, R.; Dutz, S. Magnetic Particle Hyperthermia—Biophysical Limitations of a Visionary Tumour Therapy. *Journal of Magnetism and Magnetic Materials* **2007**, *311* (1), 187–192.

(110) Hugounenq, P.; Levy, M.; Alloyeau, D.; Lartigue, L.; Dubois, E.; Cabuil, V.; Ricolleau, C.; Roux, S.; Wilhelm, C.; Gazeau, F.; Bazzi, R. Iron Oxide Monocrystalline Nanoflowers for Highly Efficient Magnetic Hyperthermia. *J. Phys. Chem. C* **2012**, *116* (29), 15702–15712.

(111) Atkinson, W. J.; Brezovich, I. A.; Chakraborty, D. P. Usable Frequencies in Hyperthermia with Thermal Seeds. *IEEE Transactions on Biomedical Engineering* **1984**, *BME-31* (1), 70–75.

(112) Jordan, A.; Rheinländer, T.; Waldöfner, N.; Scholz, R. Increase of the Specific Absorption Rate (SAR) by Magnetic Fractionation of Magnetic Fluids. *Journal of Nanoparticle Research* **2003**, *5* (5), 597–600.

(113) Basly, B.; Popa, G.; Fleutot, S.; Pichon, B. P.; Garofalo, A.; Ghobril, C.; Billotey, C.; Berniard, A.; Bonazza, P.; Martinez, H.; Felder-Flesch, D.; Begin-Colin, S. Effect of the Nanoparticle Synthesis Method on Dendronized Iron Oxides as MRI Contrast Agents. *Dalton Trans.* **2013**, *42* (6), 2146–2157.

(114) Kossatz, S.; Ludwig, R.; Dähring, H.; Ettelt, V.; Rimkus, G.; Marciello, M.; Salas, G.; Patel, V.; Teran, F. J.; Hilger, I. High Therapeutic Efficiency of Magnetic Hyperthermia in Xenograft Models Achieved with Moderate Temperature Dosages in the Tumor Area. *Pharm Res* **2014**, *31* (12), 3274–3288.

(115) Lee, J.-H.; Huh, Y.-M.; Jun, Y.; Seo, J.; Jang, J.; Song, H.-T.; Kim, S.; Cho, E.-J.; Yoon, H.-G.; Suh, J.-S.; Cheon, J. Artificially Engineered Magnetic Nanoparticles for Ultra-Sensitive Molecular Imaging. *Nat Med* **2007**, *13* (1), 95–99.
(116) Patsula, V.; Moskvin, M.; Dutz, S.; Horák, D. Size-Dependent Magnetic Properties of Iron Oxide Nanoparticles. *Journal of Physics and Chemistry of Solids* **2016**, *88*, 24–30.
(117) Guardia, P.; Di Corato, R.; Lartigue, L.; Wilhelm, C.; Espinosa, A.; Garcia-Hernandez, M.; Gazeau, F.; Manna, L.; Pellegrino, T. Water-Soluble Iron Oxide Nanocubes with High Values of Specific Absorption Rate for Cancer Cell Hyperthermia Treatment. *ACS Nano* **2012**, *6* (4), 3080–3091.
(118) Smith, A. M.; Mancini, M. C.; Nie, S. Second Window for in Vivo Imaging. *Nature Nanotech* **2009**, *4* (11), 710–711.
(119) Melamed, J. R.; Edelstein, R. S.; Day, E. S. Elucidating the Fundamental Mechanisms of Cell Death Triggered by Photothermal Therapy. *ACS Nano* **2015**, *9* (1), 6–11.
(120) Sharma, S. K.; Shrivastava, N.; Rossi, F.; Tung, L. D.; Thanh, N. T. K. Nanoparticles-Based Magnetic and Photo Induced Hyperthermia for Cancer Treatment. *Nano Today* **2019**, *29*, 100795.
(121) Sadat, M. E.; Kaveh Baghbador, M.; Dunn, A. W.; Wagner, H. P.; Ewing, R. C.; Zhang, J.; Xu, H.; Pauletti, G. M.; Mast, D. B.; Shi, D. Photoluminescence and Photothermal Effect of Fe3O4 Nanoparticles for Medical Imaging and Therapy. *Appl. Phys. Lett.* **2014**, *105* (9), 091903.
(122) Zhang, Z.; Wang, J.; Chen, C. Near-Infrared Light-Mediated Nanoplatforms for Cancer Thermo-Chemotherapy and Optical Imaging. *Advanced Materials* **2013**, *25* (28), 3869–3880.
(123) Pązik, R.; Zachanowicz, E.; Pożniak, B.; Małecka, M.; Zięcina, A.; Marciniak, Ł. Non-Contact Mn1−xNixFe2O4 Ferrite Nano-Heaters for Biological Applications – Heat Energy Generated by NIR Irradiation. *RSC Adv.* **2017**, *7* (29), 18162–18171.
(124) Zhou, W.; Liu, X.; Ji, J. More Efficient NIR Photothermal Therapeutic Effect from Intracellular Heating Modality than Extracellular Heating Modality: An in Vitro Study. *J Nanopart Res* **2012**, *14* (9), 1128.
(125) Gormley, A. J.; Larson, N.; Banisadr, A.; Robinson, R.; Frazier, N.; Ray, A.; Ghandehari, H. Plasmonic Photothermal Therapy Increases the Tumor Mass Penetration of HPMA Copolymers. *Journal of Controlled Release* **2013**, *166* (2), 130–138.
(126) Fay, B. L.; Melamed, J. R.; Day, E. S. Nanoshell-Mediated Photothermal Therapy Can Enhance Chemotherapy in Inflammatory Breast Cancer Cells. *Int J Nanomedicine* **2015**, *10*, 6931–6941.
(127) Yang, C.; Guo, W.; Cui, L.; An, N.; Zhang, T.; Guo, G.; Lin, H.; Qu, F. Fe3O4@mSiO2 Core–Shell Nanocomposite Capped with Disulfide Gatekeepers for Enzyme-Sensitive Controlled Release of Anti-Cancer Drugs. *J. Mater. Chem. B* **2015**, *3* (6), 1010–1019.
(128) Yang, C.; Guo, W.; An, N.; Cui, L.; Zhang, T.; Tong, R.; Chen, Y.; Lin, H.; Qu, F. Enzyme-Sensitive Magnetic Core–Shell Nanocomposites for Triggered Drug Release. *RSC Adv.* **2015**, *5* (98), 80728–80738.
(129) Balas, F.; Manzano, M.; Horcajada, P.; Vallet-Regí, M. Confinement and Controlled Release of Bisphosphonates on Ordered Mesoporous Silica-Based Materials. *J. Am. Chem. Soc.* **2006**, *128* (25), 8116–8117.
(130) Manzano, M.; Aina, V.; Areán, C. O.; Balas, F.; Cauda, V.; Colilla, M.; Delgado, M. R.; Vallet-Regí, M. Studies on MCM-41 Mesoporous Silica for Drug Delivery: Effect of Particle Morphology and Amine Functionalization. *Chemical Engineering Journal* **2008**, *137* (1), 30–37.
(131) Li, S.; Ma, Y.; Yue, X.; Cao, Z.; Dai, Z. One-Pot Construction of Doxorubicin Conjugated Magnetic Silica Nanoparticles. *New J. Chem.* **2009**, *33* (12), 2414–2418.
(132) Shao, D.; Wang, Z.; Dong, W.; Zhang, X.; Zheng, X.; Xiao, X.; Wang, Y.; Zhao, X.; Zhang, M.; Li, J.; Huo, Q.; Chen, L. Facile Synthesis of Core–Shell Magnetic Mesoporous Silica Nanoparticles for PH-Sensitive Anticancer Drug Delivery. *Chemical Biology & Drug Design* **2015**, *86* (6), 1548–1553.
(133) Peralta, M. E.; Jadhav, S. A.; Magnacca, G.; Scalarone, D.; Mártire, D. O.; Parolo, M. E.; Carlos, L. Synthesis and in Vitro Testing of Thermoresponsive Polymer-Grafted Core-Shell Magnetic Mesoporous Silica Nanoparticles for Efficient Controlled and Targeted Drug Delivery. *Journal of Colloid and Interface Science* **2019**, *544*, 198–205.
(134) Saint-Cricq, P.; Deshayes, S.; Zink, J. I.; Kasko, A. M. Magnetic Field Activated Drug Delivery Using Thermodegradable Azo-Functionalised PEG-Coated Core–Shell Mesoporous Silica Nanoparticles. *Nanoscale* **2015**, *7* (31), 13168–13172.
(135) Zhu, Y.; Tao, C. DNA-Capped Fe3O4/SiO2 Magnetic Mesoporous Silica Nanoparticles for Potential Controlled Drug Release and Hyperthermia. *RSC Adv.* **2015**, *5* (29), 22365–22372.
(136) Cazares-Cortes, E.; Cabana, S.; Boitard, C.; Nehlig, E.; Griffete, N.; Fresnais, J.; Wilhelm, C.; Abou-Hassan, A.; Ménager, C. Recent Insights in Magnetic Hyperthermia: From the "Hot-Spot" Effect for Local Delivery to Combined Magneto-Photo-Thermia Using Magneto-Plasmonic Hybrids. *Advanced Drug Delivery Reviews* **2019**, *138*, 233–246.

(137) Huang, H.; Delikanli, S.; Zeng, H.; Ferkey, D. M.; Pralle, A. Remote Control of Ion Channels and Neurons through Magnetic-Field Heating of Nanoparticles. *Nature Nanotech* **2010**, *5* (8), 602–606.
(138) Rühle, B.; Datz, S.; Argyo, C.; Bein, T.; Zink, J. I. A Molecular Nanocap Activated by Superparamagnetic Heating for Externally Stimulated Cargo Release. *Chem. Commun.* **2016**, *52* (9), 1843–1846.
(139) Polo-Corrales, L.; Rinaldi, C. Monitoring Iron Oxide Nanoparticle Surface Temperature in an Alternating Magnetic Field Using Thermoresponsive Fluorescent Polymers. *Journal of Applied Physics* **2012**, *111* (7), 07B334.
(140) Griffete, N.; Fresnais, J.; Espinosa, A.; Taverna, D.; Wilhelm, C.; Ménager, C. Thermal Polymerization on the Surface of Iron Oxide Nanoparticles Mediated by Magnetic Hyperthermia: Implications for Multishell Grafting and Environmental Applications. *ACS Appl. Nano Mater.* **2018**, *1* (2), 547–555.
(141) Guisasola, E.; Baeza, A.; Talelli, M.; Arcos, D.; Moros, M.; de la Fuente, J. M.; Vallet-Regí, M. Magnetic-Responsive Release Controlled by Hot Spot Effect. *Langmuir* **2015**, *31* (46), 12777–12782.
(142) Ortgies, D. H.; Teran, F. J.; Rocha, U.; de la Cueva, L.; Salas, G.; Cabrera, D.; Vanetsev, A. S.; Rähn, M.; Sammelselg, V.; Orlovskii, Y. V.; Jaque, D. Optomagnetic Nanoplatforms for In Situ Controlled Hyperthermia. *Advanced Functional Materials* **2018**, *28* (11), 1704434.
(143) Jaque, D.; Vetrone, F. Luminescence Nanothermometry. *Nanoscale* **2012**, *4* (15), 4301–4326.
(144) Dong, J.; Zink, J. I. Taking the Temperature of the Interiors of Magnetically Heated Nanoparticles. *ACS Nano* **2014**, *8* (5), 5199–5207.
(145) Riedinger, A.; Guardia, P.; Curcio, A.; Garcia, M. A.; Cingolani, R.; Manna, L.; Pellegrino, T. Subnanometer Local Temperature Probing and Remotely Controlled Drug Release Based on Azo-Functionalized Iron Oxide Nanoparticles. *Nano Letters* **2013**, *13* (6), 2399–2406.
(146) Nasir, S.; Hussein, M. Z.; Zainal, Z.; Yusof, N. A. Carbon-Based Nanomaterials/Allotropes: A Glimpse of Their Synthesis, Properties and Some Applications. *Materials* **2018**, *11* (2), 295.
(147) Bezzon, V. D. N.; Montanheiro, T. L. A.; de Menezes, B. R. C.; Ribas, R. G.; Righetti, V. A. N.; Rodrigues, K. F.; Thim, G. P. Carbon Nanostructure-Based Sensors: A Brief Review on Recent Advances. *Advances in Materials Science and Engineering* **2019**, *2019*, e4293073.
(148) Choudhary, V.; Gupta, A. *Polymer/Carbon Nanotube Nanocomposites*; IntechOpen, 2011.
(149) Rahman, G.; Najaf, Z.; Mehmood, A.; Bilal, S.; Shah, A. ul H. A.; Mian, S. A.; Ali, G. An Overview of the Recent Progress in the Synthesis and Applications of Carbon Nanotubes. *C* **2019**, *5* (1), 3.
(150) Lee, C.; Wei, X.; Kysar, J. W.; Hone, J. Measurement of the Elastic Properties and Intrinsic Strength of Monolayer Graphene. *Science* **2008**.
(151) Eatemadi, A.; Daraee, H.; Karimkhanloo, H.; Kouhi, M.; Zarghami, N.; Akbarzadeh, A.; Abasi, M.; Hanifehpour, Y.; Joo, S. W. Carbon Nanotubes: Properties, Synthesis, Purification, and Medical Applications. *Nanoscale Research Letters* **2014**, *9* (1), 393.
(152) Monthioux, M.; Serp, P.; Caussat, B.; Flahaut, E.; Razafinimanana, M.; Valensi, F.; Laurent, C.; Peigney, A.; Mesguich, D.; Weibel, A.; Bacsa, W.; Broto, J.-M. Carbon Nanotubes. In *Springer Handbook of Nanotechnology*; Bhushan, B., Ed.; Springer Handbooks; Springer: Berlin, Heidelberg, 2017; pp 193–247.
(153) Coleman, J. N.; Khan, U.; Blau, W. J.; Gun'ko, Y. K. Small but Strong: A Review of the Mechanical Properties of Carbon Nanotube–Polymer Composites. *Carbon* **2006**, *44* (9), 1624–1652.
(154) Berber, S.; Kwon, Y.-K.; Tománek, D. Unusually High Thermal Conductivity of Carbon Nanotubes. *Phys. Rev. Lett.* **2000**, *84* (20), 4613–4616.
(155) Slack, G. A. Thermal Conductivity of MgO, Al_2O_3, $MgAl_2O_4$ and Fe_3O_4 Crystals from 3° to 300°K. *Phys. Rev.* **1962**, *126* (2), 427–441.
(156) Han, Z.; Fina, A. Thermal Conductivity of Carbon Nanotubes and Their Polymer Nanocomposites: A Review. *Progress in Polymer Science* **2011**, *36* (7), 914–944.
(157) Li, C.; Shi, G. Carbon Nanotube-Based Fluorescence Sensors. *Journal of Photochemistry and Photobiology C: Photochemistry Reviews* **2014**, *19*, 20–34.
(158) Hendler-Neumark, A.; Bisker, G. Fluorescent Single-Walled Carbon Nanotubes for Protein Detection. *Sensors (Basel)* **2019**, *19* (24), 5403.
(159) Robinson, J. T.; Welsher, K.; Tabakman, S. M.; Sherlock, S. P.; Wang, H.; Luong, R.; Dai, H. High Performance in Vivo Near-IR (>1 Mm) Imaging and Photothermal Cancer Therapy with Carbon Nanotubes. *Nano Res.* **2010**, *3* (11), 779–793.
(160) Hemraj-Benny, T.; Wong, S. S. Silylation of Single-Walled Carbon Nanotubes. *Chem. Mater.* **2006**, *18* (20), 4827–4839.
(161) Fu, Q.; Lu, C.; Liu, J. Selective Coating of Single Wall Carbon Nanotubes with Thin SiO2 Layer. *Nano Lett.* **2002**, *2* (4), 329–332.
(162) Li, A.; Li, W.; Ling, Y.; Gan, W.; Brady, M. A.; Wang, C. Effects of Silica-Coated Carbon Nanotubes on the Curing Behavior and Properties of Epoxy Composites. *RSC Adv.* **2016**, *6* (28), 23318–23326.

(163) Zhang, T.; Huang, B.; Elzatahry, A. A.; Alghamdi, A.; Yue, Q.; Deng, Y. Synthesis of Podlike Magnetic Mesoporous Silica Nanochains for Use as Enzyme Support and Nanostirrer in Biocatalysis. *ACS Appl. Mater. Interfaces* **2020**, *12* (15), 17901–17908.
(164) Deng, X.; Qin, P.; Luo, M.; Shao, E.; Zhao, H.; Yang, X.; Wang, Y.; Shen, H.; Jiao, Z.; Wu, M. Mesoporous Silica Coating on Carbon Nanotubes: Layer-by-Layer Method. *Langmuir* **2013**, *29* (23), 6815–6822.
(165) Li, B.; Harlepp, S.; Gensbittel, V.; Wells, C. J. R.; Bringel, O.; Goetz, J. G.; Begin-Colin, S.; Tasso, M.; Begin, D.; Mertz, D. Near Infra-Red Light Responsive Carbon Nanotubes@mesoporous Silica for Photothermia and Drug Delivery to Cancer Cells. *Materials Today Chemistry* **2020**, *17*, 100308.
(166) Wells, C.; Vollin-Bringel, O.; Fiegel, V.; Harlepp, S.; Van der Schueren, B.; Bégin-Colin, S.; Bégin, D.; Mertz, D. Engineering of Mesoporous Silica Coated Carbon-Based Materials Optimized for an Ultrahigh Doxorubicin Payload and a Drug Release Activated by PH, T, and NIR-Light. *Advanced Functional Materials* **2018**, *28* (17), 1706996.
(167) Singh, R. K.; Patel, K. D.; Kim, J.-J.; Kim, T.-H.; Kim, J.-H.; Shin, U. S.; Lee, E.-J.; Knowles, J. C.; Kim, H.-W. Multifunctional Hybrid Nanocarrier: Magnetic CNTs Ensheathed with Mesoporous Silica for Drug Delivery and Imaging System. *ACS Appl. Mater. Interfaces* **2014**, *6* (4), 2201–2208.
(168) Tong, Y.; Zhang, M.; Xia, P.; Wang, L.; Zheng, J.; Li, W.; Xu, J. Progammed Synthesis of Magnetic Mesoporous Silica Coated Carbon Nanotubes for Organic Pollutant Adsorption. *Journal of Magnetism and Magnetic Materials* **2016**, *406*, 35–41.
(169) Dillon, F. C.; Moghal, J.; Koós, A.; Lozano, J. G.; Miranda, L.; Porwal, H.; Reece, M. J.; Grobert, N. Ceramic Composites from Mesoporous Silica Coated Multi-Wall Carbon Nanotubes. *Microporous and Mesoporous Materials* **2015**, *217*, 159–166.
(170) Zhang, M.; Zheng, J.; Xia, P.; Zheng, Y.; Xu, J.; Chen, L.; He, X.; Fang, Q. Zwitterionic Surfactant Assisted Fabrication of Mesoporous Silica Coated Carbon Nanotubes for Organic Pollutants. *New J. Chem.* **2014**, *38* (7), 3212–3219.
(171) Tîlmaciu, C.-M.; Morris, M. C. Carbon Nanotube Biosensors. *Frontiers in Chemistry* **2015**, *3*, 59.
(172) Wang, Z.; Dai, Z. Carbon Nanomaterial-Based Electrochemical Biosensors: An Overview. *Nanoscale* **2015**, *7* (15), 6420–6431.
(173) Choi, Y.-E.; Kwak, J.-W.; Park, J. W. Nanotechnology for Early Cancer Detection. *Sensors* **2010**, *10* (1), 428–455.
(174) Canevari, T. C.; Raymundo-Pereira, P. A.; Landers, R.; Benvenutti, E. V.; Machado, S. A. S. Sol–Gel Thin-Film Based Mesoporous Silica and Carbon Nanotubes for the Determination of Dopamine, Uric Acid and Paracetamol in Urine. *Talanta* **2013**, *116*, 726–735.
(175) Guo, S.; Li, J.; Ren, W.; Wen, D.; Dong, S.; Wang, E. Carbon Nanotube/Silica Coaxial Nanocable as a Three-Dimensional Support for Loading Diverse Ultra-High-Density Metal Nanostructures: Facile Preparation and Use as Enhanced Materials for Electrochemical Devices and SERS. *Chem. Mater.* **2009**, *21* (11), 2247–2257.
(176) Boghossian, A. A.; Zhang, J.; Barone, P. W.; Reuel, N. F.; Kim, J.-H.; Heller, D. A.; Ahn, J.-H.; Hilmer, A. J.; Rwei, A.; Arkalgud, J. R.; Zhang, C. T.; Strano, M. S. Near-Infrared Fluorescent Sensors Based on Single-Walled Carbon Nanotubes for Life Sciences Applications. *ChemSusChem* **2011**, *4* (7), 848–863.
(177) Takeuchi, T.; Iizumi, Y.; Yudasaka, M.; Kizaka-Kondoh, S.; Okazaki, T. Characterization and Biodistribution Analysis of Oxygen-Doped Single-Walled Carbon Nanotubes Used as in Vivo Fluorescence Imaging Probes. *Bioconjugate Chem.* **2019**, *30* (5), 1323–1330.
(178) Mann, F. A.; Lv, Z.; Großhans, J.; Opazo, F.; Kruss, S. Nanobody-Conjugated Nanotubes for Targeted Near-Infrared In Vivo Imaging and Sensing. *Angewandte Chemie International Edition* **2019**, *58* (33), 11469–11473.
(179) Fakhri, N.; Wessel, A. D.; Willms, C.; Pasquali, M.; Klopfenstein, D. R.; MacKintosh, F. C.; Schmidt, C. F. High-Resolution Mapping of Intracellular Fluctuations Using Carbon Nanotubes. *Science* **2014**, *344* (6187), 1031–1035.
(180) Robinson, J. T.; Hong, G.; Liang, Y.; Zhang, B.; Yaghi, O. K.; Dai, H. In Vivo Fluorescence Imaging in the Second Near-Infrared Window with Long Circulating Carbon Nanotubes Capable of Ultrahigh Tumor Uptake. *J. Am. Chem. Soc.* **2012**, *134* (25), 10664–10669.
(181) Fei, Q.; Xiao, D.; Zhang, Z.; Huan, Y.; Feng, G. A Novel Silica-Coated Multiwall Carbon Nanotube with CdTe Quantum Dots Nanocomposite. *Spectrochimica Acta Part A: Molecular and Biomolecular Spectroscopy* **2009**, *74* (2), 597–601.
(182) Dias, L. D.; Buzzá, H. H.; Stringasci, M. D.; Bagnato, V. S. Recent Advances in Combined Photothermal and Photodynamic Therapies against Cancer Using Carbon Nanomaterial Platforms for In Vivo Studies. *Photochem* **2021**, *1* (3), 434–447.
(183) Burke, A.; Ding, X.; Singh, R.; Kraft, R. A.; Levi-Polyachenko, N.; Rylander, M. N.; Szot, C.; Buchanan, C.; Whitney, J.; Fisher, J.; Hatcher, H. C.; D'Agostino, R.; Kock, N. D.; Ajayan, P. M.; Carroll, D. L.;

Akman, S.; Torti, F. M.; Torti, S. V. Long-Term Survival Following a Single Treatment of Kidney Tumors with Multiwalled Carbon Nanotubes and near-Infrared Radiation. *PNAS* **2009**, *106* (31), 12897–12902.

(184) Sobhani, Z.; Behnam, M. A.; Emami, F.; Dehghanian, A.; Jamhiri, I. Photothermal Therapy of Melanoma Tumor Using Multiwalled Carbon Nanotubes. *IJN* **2017**, *12*, 4509–4517.

(185) Liu, X.; Tao, H.; Yang, K.; Zhang, S.; Lee, S.-T.; Liu, Z. Optimization of Surface Chemistry on Single-Walled Carbon Nanotubes for in Vivo Photothermal Ablation of Tumors. *Biomaterials* **2011**, *32* (1), 144–151.

(186) Li, Y.; Li, X.; Doughty, A.; West, C.; Wang, L.; Zhou, F.; Nordquist, R. E.; Chen, W. R. Phototherapy Using Immunologically Modified Carbon Nanotubes to Potentiate Checkpoint Blockade for Metastatic Breast Cancer. *Nanomedicine: Nanotechnology, Biology and Medicine* **2019**, *18*, 44–53.

(187) Liu, Z.; Robinson, J. T.; Tabakman, S. M.; Yang, K.; Dai, H. Carbon Materials for Drug Delivery & Cancer Therapy. *Materials Today* **2011**, *14* (7), 316–323.

(188) Quintana, M.; Spyrou, K.; Grzelczak, M.; Browne, W. R.; Rudolf, P.; Prato, M. Functionalization of Graphene via 1,3-Dipolar Cycloaddition. *ACS Nano* **2010**, *4* (6), 3527–

(189) Peretz, S.; Regev, O. Carbon Nanotubes as Nanocarriers in Medicine. *Current Opinion in Colloid & Interface Science* **2012**, *17* (6), 360–368.

(190) Liu, J.; Wang, C.; Wang, X.; Wang, X.; Cheng, L.; Li, Y.; Liu, Z. Mesoporous Silica Coated Single-Walled Carbon Nanotubes as a Multifunctional Light-Responsive Platform for Cancer Combination Therapy. *Advanced Functional Materials* **2015**, *25* (3), 384–392.

(191) Kalyane, D.; Kumar, N.; Anup, N.; Rajpoot, K.; Maheshwari, R.; Sengupta, P.; Kalia, K.; Tekade, R. K. Recent Advancements and Future Submissions of Silica Core-Shell Nanoparticles. *International Journal of Pharmaceutics* **2021**, *609*, 121173.

(192) Kesse, X.; Adam, A.; Begin-Colin, S.; Mertz, D.; Larquet, E.; Gacoin, T.; Maurin, I.; Vichery, C.; Nedelec, J.-M. Elaboration of Superparamagnetic and Bioactive Multicore–Shell Nanoparticles (γ-Fe2O3@SiO2-CaO): A Promising Material for Bone Cancer Treatment. *ACS Appl. Mater. Interfaces* **2020**, *12* (42), 47820–47830.

(193) Lu, C.-W.; Hung, Y.; Hsiao, J.-K.; Yao, M.; Chung, T.-H.; Lin, Y.-S.; Wu, S.-H.; Hsu, S.-C.; Liu, H.-M.; Mou, C.-Y.; Yang, C.-S.; Huang, D.-M.; Chen, Y.-C. Bifunctional Magnetic Silica Nanoparticles for Highly Efficient Human Stem Cell Labeling. *Nano Lett.* **2007**, *7* (1), 149–154.

(194) Hartono, S. B.; Yu, M.; Gu, W.; Yang, J.; Strounina, E.; Wang, X.; Qiao, S.; Yu, C. Synthesis of Multi-Functional Large Pore Mesoporous Silica Nanoparticles as Gene Carriers. *Nanotechnology* **2014**, *25* (5), 055701.

(195) Sanchez-Salcedo, S.; Vallet-Regí, M.; Shahin, S. A.; Glackin, C. A.; Zink, J. I. Mesoporous Core-Shell Silica Nanoparticles with Anti-Fouling Properties for Ovarian Cancer Therapy. *Chemical Engineering Journal* **2018**, *340*, 114–124.

(196) Avedian, N.; Zaaeri, F.; Daryasari, M. P.; Akbari Javar, H.; Khoobi, M. PH-Sensitive Biocompatible Mesoporous Magnetic Nanoparticles Labeled with Folic Acid as an Efficient Carrier for Controlled Anticancer Drug Delivery. *Journal of Drug Delivery Science and Technology* **2018**, *44*, 323–332.

(197) Pon-On, W.; Tithito, T.; Maneeprakorn, W.; Phenrat, T.; Tang, I.-M. Investigation of Magnetic Silica with Thermoresponsive Chitosan Coating for Drug Controlled Release and Magnetic Hyperthermia Application. *Materials Science and Engineering: C* **2019**, *97*, 23–30.

(198) Naz, S.; Shamoon, M.; Wang, R.; Zhang, L.; Zhou, J.; Chen, J. Advances in Therapeutic Implications of Inorganic Drug Delivery Nano-Platforms for Cancer. *International Journal of Molecular Sciences* **2019**, *20* (4), 965.

(199) Heggannavar, G. B.; Hiremath, C. G.; Achari, D. D.; Pangarkar, V. G.; Kariduraganavar, M. Y. Development of Doxorubicin-Loaded Magnetic Silica–Pluronic F-127 Nanocarriers Conjugated with Transferrin for Treating Glioblastoma across the Blood–Brain Barrier Using an in Vitro Model. *ACS Omega* **2018**, *3* (7), 8017–8026.

(200) Xiong, L.; Bi, J.; Tang, Y.; Qiao, S.-Z. Magnetic Core–Shell Silica Nanoparticles with Large Radial Mesopores for SiRNA Delivery. *Small* **2016**, *12* (34), 4735–4742.

(201) Zheng, H.; Wen, S.; Zhang, Y.; Sun, Z. Organosilane and Polyethylene Glycol Functionalized Magnetic Mesoporous Silica Nanoparticles as Carriers for CpG Immunotherapy In Vitro and In Vivo. *PLOS ONE* **2015**, *10* (10), e0140265.

(202) Adeli, M.; Soleyman, R.; Beiranvand, Z.; Madani, F. Carbon Nanotubes in Cancer Therapy: A More Precise Look at the Role of Carbon Nanotube–Polymer Interactions. *Chem. Soc. Rev.* **2013**, *42* (12), 5231–5256.

(203) Hwang, Y.; Park, S.-H.; Lee, J. W. Applications of Functionalized Carbon Nanotubes for the Therapy and Diagnosis of Cancer. *Polymers* **2017**, *9* (1), 13.

(204) Amenta, V.; Aschberger, K. Carbon Nanotubes: Potential Medical Applications and Safety Concerns. *WIREs Nanomedicine and Nanobiotechnology* **2015**, *7* (3), 371–386.
(205) Liu, Z.; Sun, X.; Nakayama-Ratchford, N.; Dai, H. Supramolecular Chemistry on Water-Soluble Carbon Nanotubes for Drug Loading and Delivery. *ACS Nano* **2007**, *1* (1), 50–56.
(206) Liu, Z.; Fan, A. C.; Rakhra, K.; Sherlock, S.; Goodwin, A.; Chen, X.; Yang, Q.; Felsher, D. W.; Dai, H. Supramolecular Stacking of Doxorubicin on Carbon Nanotubes for In Vivo Cancer Therapy. *Angewandte Chemie* **2009**, *121* (41), 7804–7808.
(207) Wu, W.; Li, R.; Bian, X.; Zhu, Z.; Ding, D.; Li, X.; Jia, Z.; Jiang, X.; Hu, Y. Covalently Combining Carbon Nanotubes with Anticancer Agent: Preparation and Antitumor Activity. *ACS Nano* **2009**, *3* (9), 2740–2750.
(208) Bartholomeusz, G.; Cherukuri, P.; Kingston, J.; Cognet, L.; Lemos, R.; Leeuw, T. K.; Gumbiner-Russo, L.; Weisman, R. B.; Powis, G. In Vivo Therapeutic Silencing of Hypoxia-Inducible Factor 1 Alpha (HIF-1α) Using Single-Walled Carbon Nanotubes Noncovalently Coated with SiRNA. *Nano Res.* **2009**, *2* (4), 279–291.
(209) Ladeira, M. S.; Andrade, V. A.; Gomes, E. R. M.; Aguiar, C. J.; Moraes, E. R.; Soares, J. S.; Silva, E. E.; Lacerda, R. G.; Ladeira, L. O.; Jorio, A.; Lima, P.; Leite, M. F.; Resende, R. R.; Guatimosim, S. Highly Efficient SiRNA Delivery System into Human and Murine Cells Using Single-Wall Carbon Nanotubes. *Nanotechnology* **2010**, *21* (38), 385101.
(210) Sanz, V.; Tilmacîu, C.; Soula, B.; Flahaut, E.; Coley, H. M.; Silva, S. R. P.; McFadden, J. Chloroquine-Enhanced Gene Delivery Mediated by Carbon Nanotubes. *Carbon* **2011**, *49* (15), 5348–5358.
(211) Shi Kam, N. W.; Jessop, T. C.; Wender, P. A.; Dai, H. Nanotube Molecular Transporters: Internalization of Carbon Nanotube−Protein Conjugates into Mammalian Cells. *J. Am. Chem. Soc.* **2004**, *126* (22), 6850–6851.
(212) Maiti, D.; Tong, X.; Mou, X.; Yang, K. Carbon-Based Nanomaterials for Biomedical Applications: A Recent Study. *Frontiers in Pharmacology* **2019**, *9*, 1401.
(213) Ma, J.; Lin, H.; Xing, R.; Li, X.; Bian, C.; Xiang, D.; Guo, W.; Qu, F. Synthesis of PH-Responsive Mesoporous Silica Nanotubes for Controlled Release. *J Sol-Gel Sci Technol* **2014**, *69* (2), 364–369.
(214) El-Shahawy, A. A. G.; Elnagar, N.; Zohery, M.; Abd Elhafeez, M. S.; El-Dek, S. I. Smart Nanocarrier-Based Chitosan @silica Coated Carbon Nanotubes Composite for Breast Cancer Treatment Approach. *International Journal of Polymeric Materials and Polymeric Biomaterials* **2021**, *0* (0), 1–13.
(215) Madani, S. Y.; Mandel, A.; Seifalian, A. M. A Concise Review of Carbon Nanotube's Toxicology. *Nano Reviews* **2013**, *4* (1), 21521.
(216) Ali-Boucetta, H.; Kostarelos, K. Pharmacology of Carbon Nanotubes: Toxicokinetics, Excretion and Tissue Accumulation. *Advanced Drug Delivery Reviews* **2013**, *65* (15), 2111–2119.
(217) Satarkar, N. S.; Hilt, J. Z. Magnetic Hydrogel Nanocomposites for Remote Controlled Pulsatile Drug Release. *Journal of Controlled Release* **2008**, *130* (3), 246–251.
(218) Campbell, S. B.; Patenaude, M.; Hoare, T. Injectable Superparamagnets: Highly Elastic and Degradable Poly(N-Isopropylacrylamide)–Superparamagnetic Iron Oxide Nanoparticle (SPION) Composite Hydrogels. *Biomacromolecules* **2013**, *14* (3), 644–653.
(219) Kim, Y.-J.; Ebara, M.; Aoyagi, T. A Smart Hyperthermia Nanofiber with Switchable Drug Release for Inducing Cancer Apoptosis. *Advanced Functional Materials* **2013**, *23* (46), 5753–5761.
(220) Xie, W.; Gao, Q.; Guo, Z.; Wang, D.; Gao, F.; Wang, X.; Wei, Y.; Zhao, L. Injectable and Self-Healing Thermosensitive Magnetic Hydrogel for Asynchronous Control Release of Doxorubicin and Docetaxel to Treat Triple-Negative Breast Cancer. *ACS Appl. Mater. Interfaces* **2017**, *9* (39), 33660–33673.
(221) Wu, J.; Chen, A.; Qin, M.; Huang, R.; Zhang, G.; Xue, B.; Wei, J.; Li, Y.; Cao, Y.; Wang, W. Hierarchical Construction of a Mechanically Stable Peptide–Graphene Oxide Hybrid Hydrogel for Drug Delivery and Pulsatile Triggered Release in Vivo. *Nanoscale* **2015**, *7* (5), 1655–1660.
(222) Spizzirri, U. G.; Hampel, S.; Cirillo, G.; Nicoletta, F. P.; Hassan, A.; Vittorio, O.; Picci, N.; Iemma, F. Spherical Gelatin/CNTs Hybrid Microgels as Electro-Responsive Drug Delivery Systems. *International Journal of Pharmaceutics* **2013**, *448* (1), 115–122.
(223) Servant, A.; Bussy, C.; Al-Jamal, K.; Kostarelos, K. Design, Engineering and Structural Integrity of Electro-Responsive Carbon Nanotube- Based Hydrogels for Pulsatile Drug Release. *J. Mater. Chem. B* **2013**, *1* (36), 4593–4600.

Chapter II

Engineering of the silica shell around IO NPs to modulate magnetothermal properties

Chapter II. Engineering of the silica shell around IO NPs to modulate magnetothermal properties

II.1. Introduction

IO NPs have promising properties for biomedical and theranostic applications as it was detailed in Chapter 1. They can be used as contrast agents for MRI and magnetothermal agents for MHT. Their efficiency for each modality depends on their properties and in particular their size. For MRI properties, R_2 relaxation rate overall increases with the increasing size of the NPs.[1] Indeed, for spherical IO NPs, maximal transverse relaxivities were obtained for maghemite and magnetite NPs with a mean diameter of 25 and 27 nm respectively.[2,] However, it remains difficult with the current synthesis method to produce homogeneous IO NPs with size bigger than 20 nm while it also corresponds to the size limit for blocked single domain i.e. superparamagnetic NPs.[3] On the other hand, we also saw in Chapter 1 that the optimal size for MHT i.e. heat generation from magnetite NPs is the range 12 – 25 nm. In summary for both MRI and MHT applications, IO NPs should have a diameter around 20 nm.

Starting from this information about the appropriate size for IO core, it is now important to think about the best design for the silica shell in order to produce efficient IO@SiO_2 core-shell NPs. The evaluation of their MRI and MHT properties should then help us to choose the most appropriate system for efficient therapies. So, in this chapter, we will implement the synthesis of the silica shell and the reaction parameters that allow to modulate the pore morphology and the shell thickness. Then, the influence of this silica shell on the heating ability under AMF will be studied. While IO@MS systems have already been reported in particular for MRI properties, the influence of the silica shell design and how its porous structure can modify the heat transfer from the central core to the environment has been scarcely studied.

Upon AMF, magnetic interactions with IO cores and subsequent Néel and Brown relaxations processes (described in Chapter 1) lead to the release of heat from the center of the NP to the surrounding environment. For local hyperthermia treatment, but also regarding the potential thermal degradation of some fragile drugs in the pores, a reasonable question quickly arises about the temperature inside and on the surface of the NP. Indeed, standard temperature-probe can only detect a temperature change on a macroscopic scale with a resolution of maximum few mm^3. However, Guisasola *et al.*[4] demonstrated that treatment without global heating can be achieved because IO NPs act as very local "hot-spots" when submitted to AMF. Knowledge of the local temperature of the NP is

capital to design appropriate trigger for drug delivery or to cause controlled damages in cell organelles or cell wall structures.

This chapter is divided into three main parts:

i) In a first section (II.2), we focus on particular systems producing mesoporous silica shells whether with stellate or with worm-like morphologies. We report that the sol-gel reaction temperature is a fundamental parameter to control the surfactant micelles self-assembly and then the silica pore condensation. Deep transformations in the pores morphology (pores width and orientation) are observed and this affects the MRI features and the heat transfer to the environment upon AMF application.

ii) Then, in a second section (II.3), the range of porous silica shell materials is extended to other pore shapes, widths and silica thicknesses, in order to study in more details the influence of the silica properties on the magnetothermal characteristic parameters, in particular on the SAR values.

iii) Finally, a promising concept to detect the local temperature at the surface of the NPs is proposed (II.4). We tried to advantageously use the luminescence of quantum dots grafted at the core-shell IO@MS NPs to elucidate the local nanoscale temperature. This method is called nanothermometry and should allow us to monitor the local temperature upon the application of an AMF.

II.2. Influence of the reaction temperature on the pores morphology

This work has been adapted from "Orienting the Pore Morphology of Core-Shell Magnetic Mesoporous Silica with the Sol-Gel Temperature. Influence on MRI and Magnetic Hyperthermia Properties. *Molecules* **26**, 971 (2021)".[5]

Alexandre Adam[1], Ksenia Parkhomenko[2], Paula Duenas-Ramirez[1], Clémence Nadal[1], Geoffrey Cotin[1], Paul Emmanuel Zorn[3,4], Philippe Choquet[3,4,5,6], Sylvie Bégin-Colin[1] and Damien Mertz[1]

[1] Institut de Physique et Chimie des Matériaux de Strasbourg (IPCMS), UMR-7504 CNRS-Université de Strasbourg, 23 rue du Lœss, 67034 Strasbourg, France

[2] Institut de Chimie et Procédés pour l'Energie, l'Environnement et la Santé (ICPEES), UMR-7515 CNRS-Université de Strasbourg, 25 rue Becquerel, 67087 Strasbourg, France

[3] Imagerie Préclinique—UF6237, Pôle d'imagerie, Hôpitaux Universitaires de Strasbourg, 67000 Strasbourg, France

[4] Service de Radiologie 2, Hautepierre, Pôle d'imagerie, Hôpitaux Universitaires de Strasbourg, 67000 Strasbourg, France

[5] Icube, équipe MMB, CNRS, Université de Strasbourg, 67000 Strasbourg, France

[6] Fédération de Médecine Translationnelle de Strasbourg, Faculté de Médecine, Université de Strasbourg, 67000 Strasbourg, France

Abstract: The controlled design of robust, well reproducible and functional nanomaterials made according to simple processes is of key importance to envision future applications. In the field of porous materials, tuning nanoparticle features such as specific area, pore size and morphology by adjusting simple parameters such as pH, temperature or solvent is highly needed. In this work, we address the tunable control of the pore morphology of mesoporous silica (MS) nanoparticles (NPs) with the sol-gel reaction temperature (T_{sg}). We show that the pore morphology of MS NPs alone or of MS shell covering iron oxide nanoparticles (IO NPs) can be easily tailored with T_{sg} orienting either towards stellar (ST) morphology (large radial pore of around 10 nm) below 80 °C or towards a worm-like (WL) morphology (small randomly oriented pores channel network, of 3-4 nm pore size) above 80 °C. The relaxometric and magnetothermal features of IO@STMS or IO@WLMS core shell NPs having respectively stellar or worm-like morphologies, are compared and discussed to understand the role of the pore structure for MRI and magnetic hyperthermia applications.

II.2.1. Introduction

Among range of inorganic nanomaterials, mesoporous silica (MS) are particularly appealing given their specific controlled pore morphology, high pore volume and large surface area.[6–8] In addition, their synthesis process is usually robust and scalable and silanol groups at the MS surface allows to envision the grafting of a versatile range of chemical functions.[9–11] Given these features, MS are promising for range of applications including catalysis[12,13], depollution[14,15] or drug delivery.[16–18]

In general, MS are formed through surfactant-mediated assembly which means that the first step of the process consists in the self-organization of surfactant phase which acts as a soft template for the silica network formation.[19–21] This template which dictates the resulting pore size and morphology of the MS network is usually removed after silica condensation. The most reported methods to synthesize MS NPs which are adapted historically from well-established MCM41 MS nanoparticle synthesis[22,23], make use of hexadecyltrimethylammonium bromide (CTAB), a quaternary ammonium surfactant, which in presence of silicate precursors, typically tetraethoxysilane (TEOS), and in basic conditions, self-organizes into a hexagonal micellar phase.[24–26] This process results in MS NPs having an ordered hexagonal pore structure of *ca.* 2.5-3.0 nm pore size, corresponding to the initial diameter of the micellar rods.

To afford tunability over the pore network structures, various methods were developed to change the pore morphology and size, by playing on various synthesis parameters. Hence, increasing surfactant concentration[27] or surfactant to silica ratio allows to tune the surfactant phase nature and then the ordered pore structures.[28] The pore diameter can be modulated by varying the surfactant chain length or by using pore expandable agent such as trimethylbenzene interacting with the micellar phase.[29–31] The pore morphology (stellar, radial, worm-like) was also modified with the use of appropriate co-solvents during the synthesis.[32–34] At last, bimodal pore structures in submicron MS were also achieved by using an anionic polyelectrolyte that self-assemble with the CTAB surfactant to form macromolecular template which upon silica condensation provide two distribution of pores : one small usual pores of 2.5 and 20-50 nm pore due to polymer silica segregation during the sol gel reaction.[35,36]

Recently, Zhang, Bonneviot *et al.* introduced an elegant method to finely control, in a robust and reproducible manner, the pore morphology of MS NPs having size in the range of 100 nm.[37] In this work, the authors have used small organic amines (SOA) to control the silica growth allowing hence to reach a high level of NPs monodispersity. Moreover, they showed that when MS NPs synthesis is performed in mild basic conditions (pH near 7 due to low amount of SOAs), the nature of the surfactant counterion used, determines completely the pore structure of the resulting MS NP. Indeed, in mild basic conditions, the use of tosylate anion (Tos^-) as a counterion of hexadecyltrimethylammonium (CTA^+) leads to weak templating promoting silica condensation around packed CTA^+ micelles whereas the use of bromide anion (Br^-) leads to a stronger templating resulting in an individual coverage of the micellar rods by silica around. Hence, in these conditions, CTA^+ templating with Tos^- orientates the pore

morphology towards stellar large pore structure (10-15 nm pore size) while Br^- orientates towards small pores structures resulting in so-called raspberry structures. Furthermore, when the concentration of the SOA is increased the authors reported that the counterion is not anymore the factor determining the pore structure and a new phase called worm-like (WL) is formed. This latter supposes high level of surfactant interpenetration during silica condensation. Despite the wide range of parameters investigated, the authors achieved the synthesis only at a reaction temperature set at 80 °C and the influence of this fundamental parameter was to the best of our knowledge not reported for such MS structure. However, modulating this parameter experimentally would be very easy to achieve, and changing the pore morphology by this way would afford a new controlled and simplified process leading to new structural features on MS NPs but also on MS shell deposited at the surface of inorganic cores such as carbon nanotubes CNTs, iron oxide or gold NPs, which are well known to be activable by external fields.

In our previous works, we have recently developed various functionalization strategies using synthesized stellate MS NPs to develop innovative nanomaterials for luminescence bioimaging in vivo[38] or efficient chelating metal capture in a biological media.[39] MS stellate shells were also deposited around iron oxide NPs for combined imaging and hyperthermia applications[40] or to ensure formulation of a new generation of magnetic glasses.[41] In all these examples, the stellate morphologies were performed at the same temperature synthesis set at of 75-80 °C which determine similar stellar morphology and pore size.

Herein, the influence of the temperature as a simple synthesis parameter was investigated with the aim to modulate the pore structure morphology of MS NPs and MS shell coated around IO core. We report here that above a certain threshold of the sol gel reaction temperature (T_{sg}) measured at around 80 °C the pore structure is found to change from a stellar (ST) to a worm-like (WL) morphology (**Scheme 2- 1**).

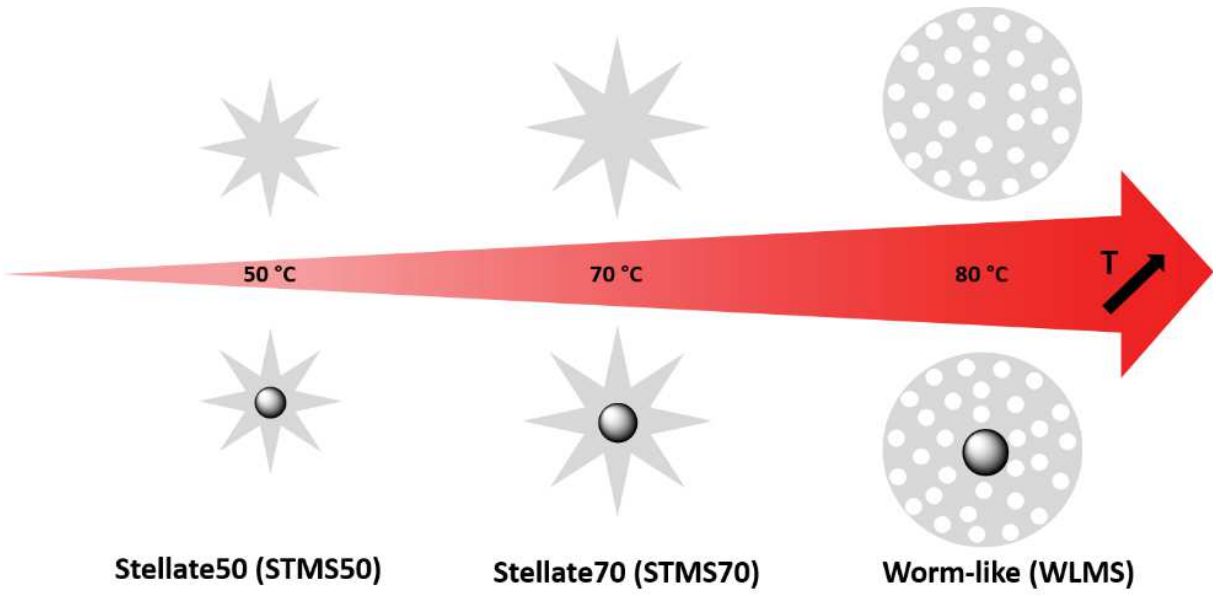

Scheme 2- 1. Scheme illustrating the thermally controlled process to orient the pore morphology of MS and IO@MS NPs from stellate (STMS) to worm like (WLMS).

Hence, in a first part of this work, the reaction temperature during the MS NPs synthesis in precise conditions (CTATos used as a surfactant, in mild basic conditions pH 7, with TEOS as the silica source) was hence varied in the range of 50 to 85 °C. The resulting MS NPs size distribution, morphology and pore structure were carefully characterized by transmission electron microscopy (MET) and N_2 adsorption-desorption isotherm to understand the structural changes and decipher micro and mesoporosity. In a second part, we carried out this reaction at two different temperatures in the presence IO NPs, of 18 nm diameter, made by thermal decomposition, to investigate the possibilities to obtained magnetic core shell having a MS shell with a tuned pore structure, namely IO@STMS or IO@WLMS morphology.

With the aim to highlight the potential of such magnetic core shell as T_2-weighted MRI contrast agents, the relaxometric properties of the IO@STMS or IO@WLMS are investigated by measuring the longitudinal and transversal relaxivities. In order to emphasize their potential as magnetic nanoheaters for magnetic field induced hyperthermia, temperature profiles under an alternating magnetic field (AMF) are traced and measurements of the specific absorption rates (SAR) are achieved and compared to discuss on the influence of the pore morphology on magnetically induced heat dissipation useful for magnetic hyperthermia treatment.

II.2.2. Experimental section

II.2.2.1. Chemicals

Tetraethyl orthosilicate (TEOS, ≥99.0%)), 2-amino-2-(hydroxymethyl)-1,3-propanediol (AHMPD, ≥99.9%), cetyltrimethylammonium tosylate (CTATos, ≥98.0%), ammonium nitrate (NH_4NO_3), ferric chlorid (99%) and squalane (96%) were obtained from Sigma–Aldrich (France). Nitric acid 65% (HNO_3) was purchased from Carlo-Erba. Sodium stearate (98.8%) was obtained from TCI. Oleic acid (99%) was purchased from Alfa Aesar while dibenzylether (DBE, 99%) was purchased from Acros Organic.

II.2.2.2. Synthesis of ST and WL mesoporous silica nanoparticles (MS NPs)

The protocol was adapted and modified from Zhang *et al*.[37] In a typical procedure, CTATos (3.8 g, 8.3 mmol), AHMPD (436 mg, 4.15 mmol) and distilled water (200 ml) were added into a 500 ml Erlenmeyer flask. For full dissolution, the mixture was heated up to a defined temperature depending on the desired morphology. For stellate morphology (STMS) the temperature is set between 50 °C and 70 °C. Once the set temperature is reached, TEOS (3.25 ml) is immediately added. In order to get worm-like morphology (WL), the mixture is heated above 80 °C and stirred at least 1.5 h. The silica precursor TEOS (3.24 ml, 2.15 mmol) is then added. After TEOS addition, the mixture was stirred for 2 h. The NPs were then collected by centrifugation (12,000 × g, 12 min) and calcinated at 550 °C for 6 h to remove the surfactant and any organic material. Finally, the MS NPs were crushed and dispersed in ethanol for further use and conservation.

II.2.2.3. Synthesis of IO core–MS shell nanoparticles (IO@STMS and IO@WLMS)

Oleic acid-stabilized iron oxide nanospheres with a mean diameter around 18 nm have been synthesized by thermal decomposition following a recently reported procedure.[42] Briefly, iron stearate (III) was prepared by precipitation of sodium stearate and ferric chloride salts in an aqueous solution as described.[43] The synthesized iron(III) stearate (1.85 g, 2 mmol) was mixed with oleic acid (1.89 g, 6.7 mmol) in squalane (15.8 g, 19.5 mL) and DBE (0.53 g, 0.5 mL) in a two-neck round-bottom flask. The mixture was heated under stirring to 120 °C and kept at this temperature for 60 min. The condenser was then connected to the flask, and the solution was heated to 330 °C and kept under reflux for 60 min under air. After cooling to room temperature, the viscous suspension was solubilized in chloroform (10 mL). The NPs were precipitated by addition of an excess of acetone and washed three times with chloroform and acetone (ratio 1:4) and centrifuged at 14,000 rpm for 5 min. The NPs were redispersed in chloroform and stored until further use.

To incorporate the iron oxide core, the previous protocol was slightly adapted in order to achieve the phase transfer of IO NPs from chloroform to the aqueous phase. CTATos (192 mg), AHMPD (22

mg) and distilled water (20 ml) were added into a 50 ml Erlenmeyer flask. In order to get STMS morphology, the mixture was brought to 65 °C and then 5 mg of IO NPs dispersed in chloroform were added under vigorous stirring. The mixture was let to stir for at least 20 min. The color of the dispersion changed from hazy grey after addition to limpid dark black after full chloroform evaporation. Then the silica precursor TEOS (1.6 ml) was added and the sol-gel reaction starts. Ten minutes after TEOS addition the temperature was set to 70 °C and the mixture was stirred for 2 h.

For the WLMS morphology, the same mixture of CTATos, AHMPD and distilled water was heated up to 80 °C. Then 8 mg of IO NPs in chloroform was added and the reaction medium was stirred for 20 min. The sol-gel reaction starts after TEOS (400 µl) addition. The mixture is stirred for 2 h. NPs were then collected by centrifugation (12,000 × g, 12 min) and dispersed in water:EtOH (1:1). CTATos extraction from the silica pores was done by mixing the NPs with NH_4NO_3 (20 mL, 20 mg.mL^{-1} in EtOH) followed by stirring and heating at 60 °C during at least 1 h. The CTATos extraction was done several times and followed by zeta potential analysis. After the synthesis, the NPs have a zeta potential above +30 mV at pH = 7. With surfactant extractions, it decreases until it reaches a plateau around -20 mV. Finally, the NPs were dispersed in EtOH, were denoted IO@STMS or IO@WLMS NPs and were stored at room temperature until further use.

II.2.2.4. Characterization techniques

Transmission electron microscopy (TEM).

The MS NPs and IO@MS NPs were deposited on carbon-coated copper grids. TEM images were acquired with a JEOL 2100 TEM instrument operating at 200 kV. The software Image J was used to determine the size distribution of the NPs.

N_2 adsorption desorption isotherms.

The textural properties of the prepared samples were studied by N_2 adsorption-desorption measurements at -196 °C. The nanoparticles were degassed under vacuum at ambient temperature (around 20 °C) for 3 h to desorb the moisture before analysis. Specific surface area was calculated by Brunauer-Emmet-Teller (BET) method. Pore volume and pore distribution were determined using desorption branch by the Barrett-Joyner-Halenda (BJH) method. Horvath-Kawazoe model was used for determining pore-size distribution in a micropore analysis from a single adsorption isotherm (dosing of nitrogen 2 cm^3, stability time 3 h).

Iron dosage by NMR ^{1}H-relaxometry.

The amount of iron in the NPs was quantified by T_1 relaxation time measurements. Previously, a calibration curve was established by measuring the longitudinal relaxivity r_1 of a standard solution of iron III nitrate at 2 wt% HNO_3. This allows to plot the variation of the relaxation rates ($1/T_1$) as a function

of [Fe^{3+}] from 0 to 3.6 mmol.L^{-1}. The IO@MS nanocomposite suspension was digested with concentrated nitric acid (65 wt%) until full dissolution of iron oxide. Moderated heating at 60 °C could be used to accelerate the digestion. The sample is then diluted to reach 2 wt% HNO_3 and the T_1 relaxation time was measured and compared with the calibration curve to determine the iron content.

Relaxivity measurements.

The measurements of longitudinal T_1 and transversal T_2 relaxation times of IO@STMS and IO@WLMS NPs were acquired with a Bruker Minispec 60 (Karlsruhe, Germany) working at a Larmor frequency of 60 MHz (1.41 T) at 37 °C. The longitudinal relaxivity r_1 and transverse relaxivity r_2 values were calculated according to the general equation of relaxivity: $R = R_0 + r$*[IO@SiO_2] where R is the relaxation rate ($1/T$) in the presence of the core-shell IO@SiO_2 nanoparticles, R_0 the relaxation rate of the aqueous medium (in the absence of the NPs) and r the relaxivity value of the core-shell IO@SiO_2.

In vitro phantom images.

In vitro MRI-phantoms images were obtained on a clinical MRI (GE signa HDxt 3T, GE Healthcare, Milwaukee, USA) running with a magnetic fiel of 3 T. T_1 images were acquired with a spin echo sequence (TR = 400 m, TE = 10 ms) and the T_2 images were acquired with a fast spin echo sequence (TR = 2 s, TE = 52 ms).

Magnetothermal experiments and specific absorption rate (SAR) determination.

To evaluate, their use as magnetothermal agents, the specific absorption rates (SAR) of each sample in water was measured by calorimetry method. This method involves the following of the temperature of the sample when the AMF is applied. The device used is a DM 100 instrument and DM applicator (Nanoscale Biomagnetics™, nB) under MaNIaC software. Vials adapted for magnetothermal measurements and filled with 1.0 mL of the samples (IO@MS) were submitted to alternating magnetic fields (796 kHz; 200 Gauss). The increase of temperature was recorded for 2 min. A second order polynomial function was used to fit the plot and to determine $[dT/dt]_{t=0}$ as described by Perigo et al.[44] to finally calculate the SAR value by using the following equation:

$$\mathrm{SAR} = m_s \cdot \frac{C_s}{m_{Fe}} \cdot \left[\frac{dT}{dt}\right]_{t=0}$$

where m_s and C_s are respectively the mass (kg) and the heat capacity (J kg^{-1} K^{-1}) of the sample, m_{Fe} (g) is the mass of iron element present in the sample and $(dT/dt)_{t=0}$ the derivative function of the temperature at $t = 0$ (K.s^{-1}). To determine this term, the temperature curves were fitted with a second order polynomial equation whose equation is: $\mathrm{T(t)} = \mathrm{T_0} + \left[\frac{dT}{dt}\right]_{t=0} . \mathrm{t} - \mathrm{a}.\mathrm{t}^2$ (**Figure 2-1**).

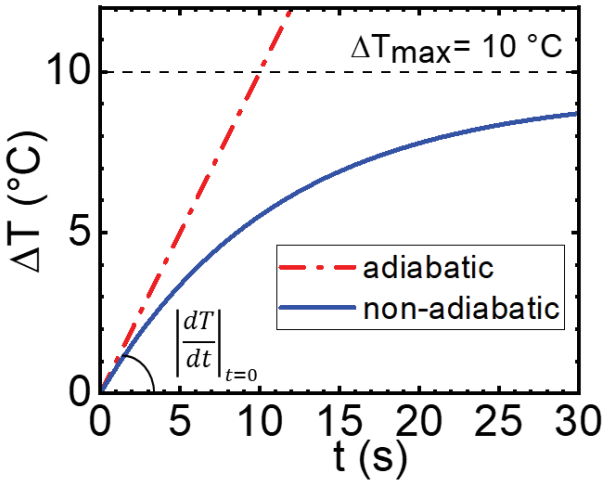

Figure 2-1. Theoretical shape of temperature curves upon AMF.

II.2.3. Results and Discussion

In a first study, the reaction temperature of the CTATos-mediated sol-gel MS NPs synthesis was modulated from 50 °C to 85 °C. For STMS NPs synthesis, the CTATos surfactant solution was heated up to the desired temperature (< 80 °C) and TEOS was added without delay to the reaction flask. Concerning WLMS NPs, the temperature was set above 80 °C and the solution was stirred more than one hour before TEOS addition. 80 °C was found as a frontier temperature: below it, STMS were formed and above it, WLMS NPs were obtained. That is why a dwell time of one hour before the introduction of the TEOS silica precursor at T ≥ 80 °C was added in order to let the time for the WL phase to stabilize and thus get very reliable syntheses. Without this delay, it happened that some intermediate phases between ST and WL were produced. It is to note that adding a dwell time below 80 °C has no influence and it usually leads to stellate morphology. Finally, surfactant was removed by calcination and TEM imaging was performed on the MS NPs obtained at six different temperatures: 50, 65, 70, 75, 80 and 85 °C (see **Figure 2-2**).

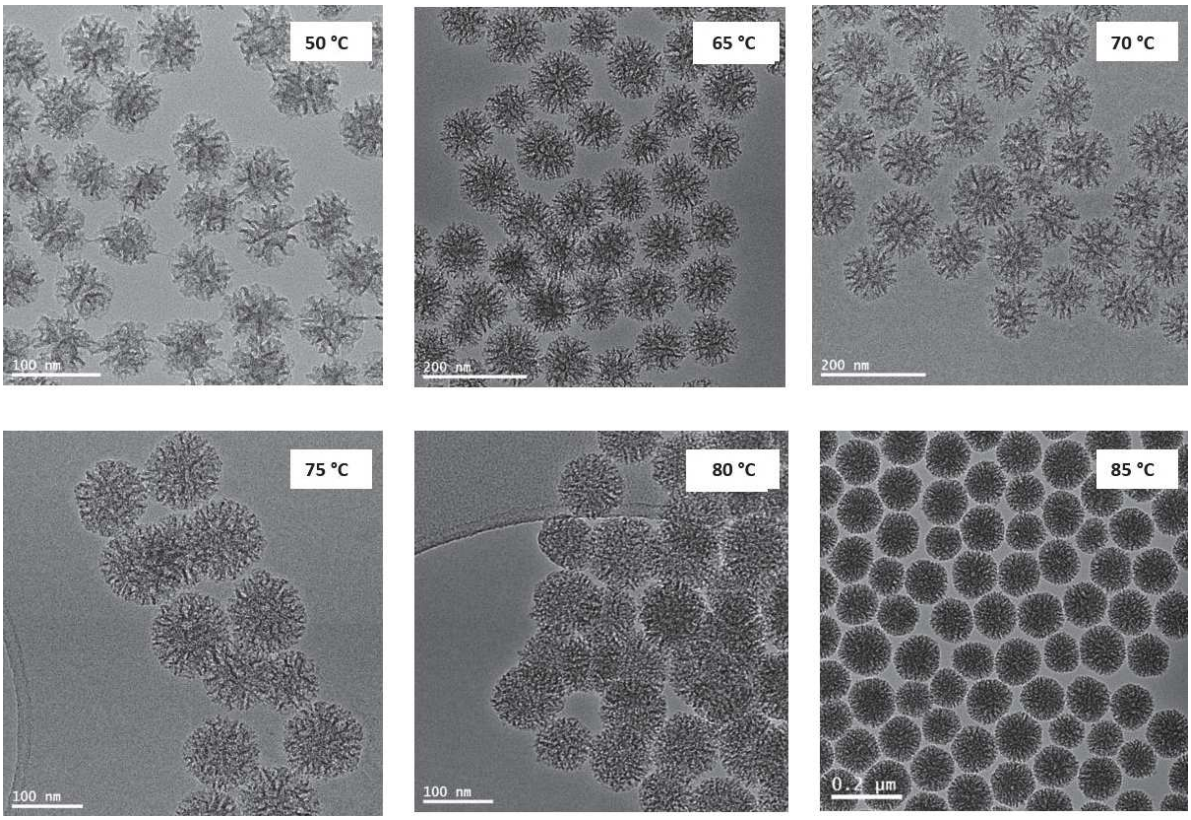

Figure 2-2. TEM images of MS NPs for different sol-gel reaction temperature: 50, 65, 70, 75, 80 and 85 °C. Below 75 °C, the MS present ST pore morphology whereas above 80 °C, WL type appears.

TEM images show that a change of the pore morphology appears from 75 °C to 85 °C. Below 75 °C, NPs have a stellate morphology whereas above 80 °C smaller pores are clearly observed. The average diameter of the MS NPs was measured as a function of the temperature (see). For STMS, the size increases from 70 ± 7 nm at 50 °C to 105 ± 10 nm in the range of 65 to 75 °C. WLMS are even bigger, around 120 ± 12 nm when they are synthesized at 85 °C. Overall, the NPs diameter increases with the reaction temperature, indicating that the condensation of the silica precursor, TEOS, is favored at higher temperatures. Observation of the TEM images indicates that the as synthesized MS NPs display a narrow size distribution (**Figure 2-3**).

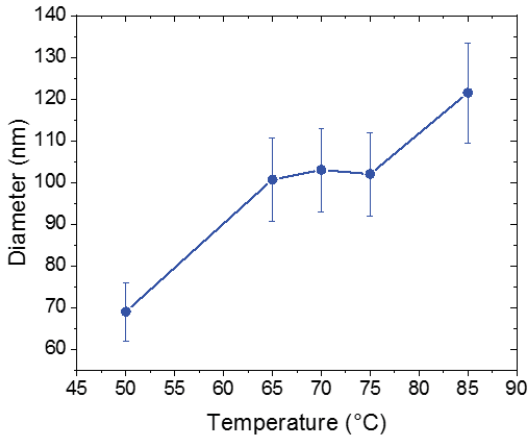

Figure 2-3. Evolution of the MS NPs diameter with the sol-gel reaction temperature.

N_2 adsorption-desorption isotherms were performed with the aim to analyze the pore structure of the MS NPs, especially their mesoporosity and microporosity in correlation with the TEM images. Stellate NPs obtained at 50 °C (STMS50) were investigated and compared with WLMS NPs synthesized at 80 °C (WLMS80) (**Figure 2-4**).

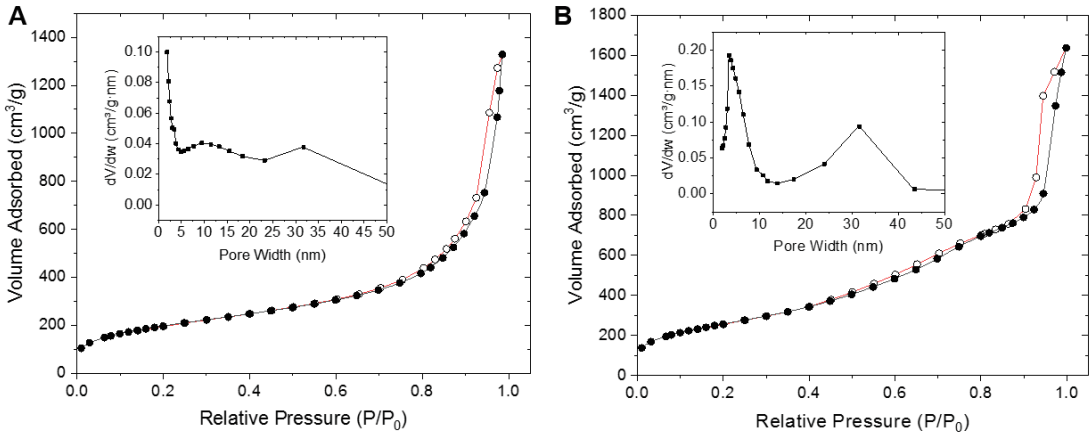

Figure 2-4. Adsorption-desorption isotherms at high relative pressures for the samples STMS50 (A) and WLMS80 (B) including BJH desorption pore volume plots for STMS50 (inset A) and WLMS80 (inset B).

The BET method of the studied samples indicates specific surface areas of 713 m^2 g^{-1} for STMS50 and 950 m^2 g^{-1} for WLMS80. The form of the isotherms at high relative pressure (**Figure 2-4.A and B**) shows the micro-mesoporous character of the samples (type IV). The sharp uptake on these isotherms at the relative pressure of around 0.8-1.0 is due to the small particles nanoscale and corresponds to the interparticle adsorption or void volume between particles. It is difficult to predict the shape of the mesopores because the hysteresis loops are not representative, but it is possible to confirm that the materials have micro-mesoporous morphology – long flat adsorption with small hysteresis loop.[45] Indeed, the mesopores presence in STMS50 was evidenced by the presence of two small peaks on the BJH desorption pore size distribution plot (**inset Figure 2-4.A**) corresponding to 10 nm (mesopores of the STMS50) and 30 nm (interparticle voids). Then, by increasing the sol-gel reaction

temperature from STMS50 to WLMS80 a change in the textural properties is clearly observed by the BJH desorption pore size distribution plots. **Figure 2-4.B** shows that the mesopore size distribution stays bimodal with 4 nm (mesopores of the WLMS80) and 30 nm (interparticle voids). Hence, the majority of the 10 nm mesopores in STMS50 disappeared and is replaced by 4 nm mesopores in WLMS80. Pore volume of mesopores (V_{meso},**Table 2-1**) was calculated by integration of the adsorbed volume of nitrogen from BJH pore volume distribution plot including only the pores from 2 to 15 nm.

The isotherms at low relative pressure (**Figure 2-5.A and B**) correspond to microporous character of the materials (Type I). V_{micro} includes only micropores and was calculated by integration of the adsorbed volume of nitrogen from Horvarth-Kawazoe differential pore volume plot and it corresponds absolutely to the pore volume calculated at the single point of the relative pressure equal to 0.0004 (**Table 1**). On the pore size distribution of the STMS50 material, it is clear that STMS50 has a big quantity of very small micropores with the maximum pore size around 0.5 nm (**inset Figure 2-5.A**). Regarding WLMS80, the most present micropores size switched from 0.5 to 0.8 nm and the quantity of mesopores largely increased (**Figure 2-5.B and Figure 2-4.B)**.

The calculated ratio between pore volumes corresponding to mesopores and to micropores (see **Table 2-1**) shows an increase of mesoporosity due to the treatment at 80 °C. Indeed, the V_{meso} / V_{micro} ratio increased from 6.6 to 8.8. The increased temperature probably collapsed small micropores of ≤ 0.5 nm size in favor of the micropores with bigger size that tend to mesoporosity. It is visible in comparison of **Figure 2-5.A and B** (pore size distribution plots) that the volume of micropores did not decrease but the distribution of pores size tends to switch to bigger values. Probably increasing the synthesis temperature also densified the walls of the bigger pores thus creating more mesoporosity that is in correspondence with the increased specific surface area and slight increase of the micro- and mesopores volumes. For the both cases, the volume of mesopores represents the largest part of the total pore volume (**Table 2-1**). This confirms their crucial importance as the mesopores are mainly on the surface of the NPs, interacting with their environment.

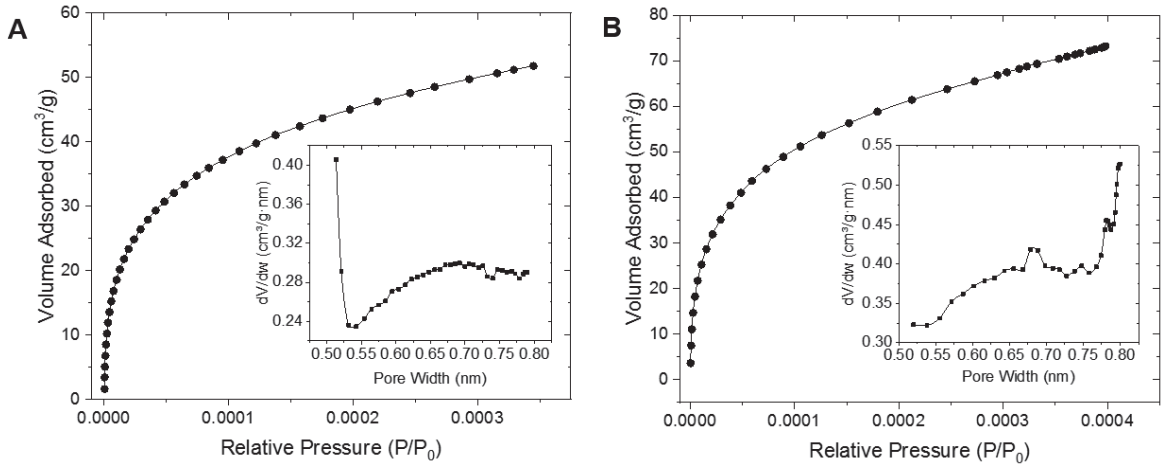

Figure 2-5. Adsorption isotherms at small relative pressures for STMS50 (a) and WLMS80 (b) including Horvarth-Kawazoe differential pore volume plots for STMS50 (inset a) and WLMS80 (inset b).

Table 2-1. Textural properties of the samples.

Sample	S_{BET}, $m^2\ g^{-1}$	$V^{¤}_{micro}$, $cm^3\ g^{-1}$	$V^{§}_{meso}$, $cm^3\ g^{-1}$	V_{meso} / V_{micro}	$D_{p\text{-}micro}$, nm	$D_{p\text{-}meso}$, nm
STMS50	713	0.08	0.53	6.6	≤ 0.5	10
WLMS80	951	0.11	0.97	8.8	≥ 0.8	4

[¤] Integrated volume of adsorbed nitrogen from 0.5 to 0.8 nm from Horvarth-Kawazoe differential pore volume plot

[§] Integrated volume of adsorbed nitrogen from 2 to 15 nm from BJH desorption pore volume plot

For a reaction temperature under 75 °C stellate phase MS NPs are produced. Their formation certainly follows the mechanism proposed earlier by Zhang *et al.*[37] The tosylate counterion (Tos^-) plays here a major role in the structural organization of the CTA^+ micelles. Tos^- competes against the adsorption of the silicate oligomers forming through the hydrolysis/condensation of TEOS in the presence of an organic base (AHMPD). The CTA^+ micelles, which are partially silicated, are then pushed together to self-assemble into bigger bundles. These latter led to the described big mesoporosity around 10 nm after surfactant removal. From our experiments, this process is valid in a range between 50 °C to 75 °C. Above 80 °C this kind of self-assembly does not occur anymore. The micellar rods seem to interpenetrate each other certainly due to thermal agitation. By raising up the reaction temperature, the hydrolysis/condensation rate of TEOS is increased. Consequently, the density of silanolates in the reaction solution is increased, which results in a displacement of the equilibrium towards a better coverage of the surfactant micelles by silicate. Self-assembly into big bundles is thus prevented. On the hand, Tos^-/CTA^+ micelle electrostatic interaction plays a major role because it competes with the deposition of silicate on individual micelles. The increase of the temperature could destabilize this interaction by a better solubilization of Tos^- which thus less competes on the surface of the micelles. Both phenomena would promote stronger templating conditions that lead to a worm-like organization of the pore channels. Thus, big pores of 10 nm diameter in STMS disappear and are replaced by smaller 4 nm pores in WLMS.

Furthermore, the coating of inorganic NPs with silica is very attractive as it improves the stability of the cores, it brings a chemically versatile surface and leads to a very good colloidal stability in aqueous environments. Hence, in a second study, the previously described approach was transposed to the coating of magnetic iron oxide cores (IONPs) as pictured in **Scheme 2-2**. The influence of the silica morphology was then studied.

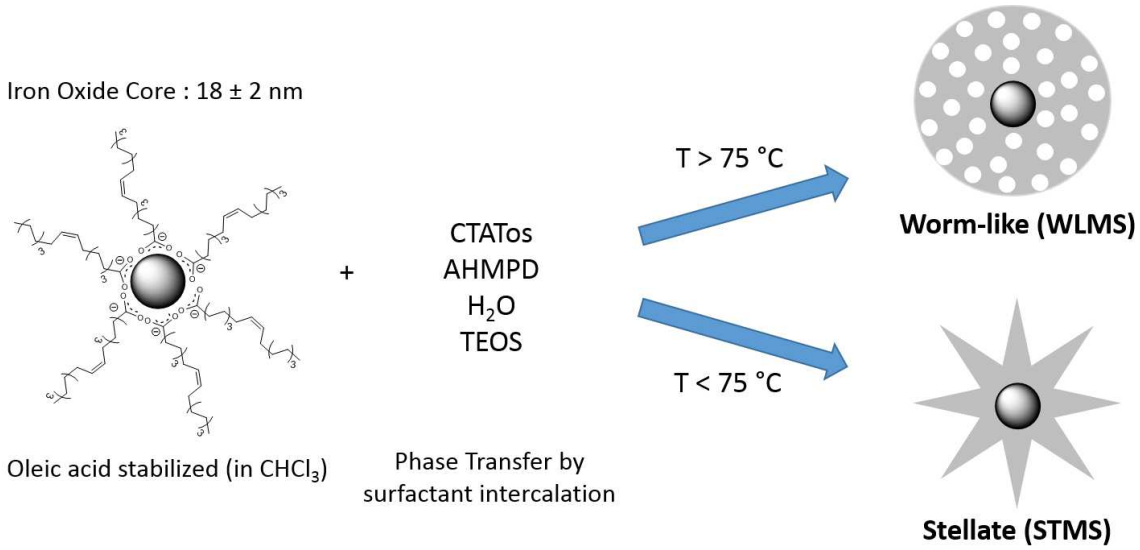

Scheme 2-2. Coating of IONPs with stellate (STMS) or worm-like (WLMS) mesoporous silica morphologies.

Spherical oleic acid-stabilized iron oxide NPs synthesized by thermal decomposition of *ca.* 18 nm diameter is known to have superparamagnetic behavior at room temperature. Such 18 nm IO NPs were shown to be suitable for magnetic hyperthermia and MRI applications.[40,46–48] MS shells of various morphology were thus formed around the magnetic core redispersed in chloroform by phase transfer in CTATos surfactant aqueous solution. Similar procedures as described above without magnetic core were carried out at 70°C and 80°C. After washing and surfactant extraction steps, TEM images were performed (**Figure 2-6**). TEM images show that the previous protocol is applicable and transposable to the coating of oleic acid-capped inorganic NPs. Stellate morphology (IO@STMS) was obtained at sol gel temperature of 70 °C and worm-like morphology at 80 °C. The synthesized NPs presented a very good homogeneity with very few NPs without IO core and a narrow size polydispersity: 100 ± 10 nm for IO@STMS and 75 ± 6 nm for IO@WLMS. Even if it is assumed that the mechanisms of the silica condensation and pore morphology formation in presence of IO cores and without core are very similar, it is noted that IO@WLMS display a smaller diameter than without IO cores as seen above. This is more likely due to the slight variation of the synthesis ratio IO cores/TEOS/surfactant than by the effect of the temperature itself. Iron oxide playing the role of seeds here, this difference of parameters governing silica formation may induce different resulting diameters in the presence or in absence of IO cores.

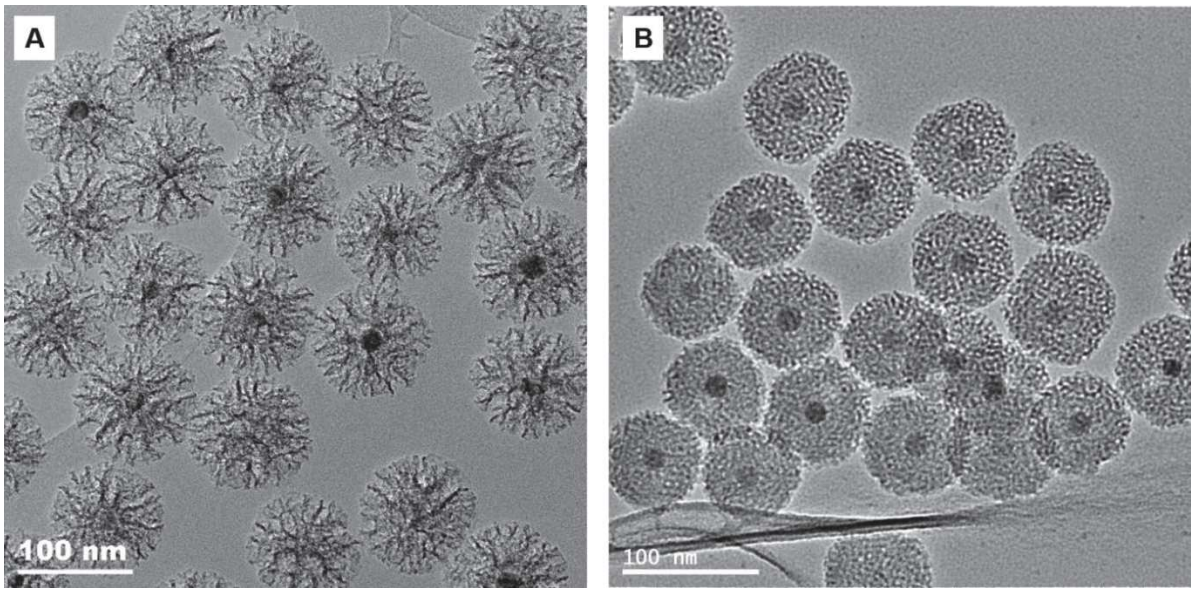

Figure 2-6. IO@STMS synthesized at 70 °C (A) and IO@WLMS synthesized at 80 °C (B).

We expected here that the pore morphology had an important impact on the environment around the magnetic core. The organization and the structure of the silica pores (meso and micro) should thus influence the relaxometric and magnetothermal properties of the nanocomposites IO@MS NPs[49,50] as observed in previous works. Hence to address these questions, the relaxometric and magnetothermal properties of these materials were evaluated for the two morphologies: IO@STMS and IO@WLMS.

IO NPs are well known as hypocontrast T_2-weighted MRI contrast agents. Transversal and longitudinal relaxation times of water protons (T_2 and T_1 respectively) were recorded as a function of the iron concentration, i.e., as a function of the core-shell NPs concentration, for the two silica pore morphologies (STMS and WLMS). **Figure 2-7**shows the variation of the relaxation rates $R_2 = 1/T_2$ and $R_1 = 1/T_1$ as a function of [Fe]. The graphs indicate linear profiles and the slope corresponds to the transversal relaxivity (r_2) and longitudinal relaxivity (r_1). Results indicate that IO@STMS has a transversal relaxivity twice higher than IO@WLMS (307 $mM^{-1}.s^{-1}$ vs 156 $mM^{-1}.s^{-1}$) (**Table 2-2**). This suggests that the diffusion of water molecules in and around the silica shell is better with a stellate morphology as compared to the worm-like one. Regarding longitudinal relaxivity r_1, the measured value for IO@STMS is more than ten times higher than r_1 of IO@WLMS. For the same IO core, such a higher value implies that water molecules have an enhanced accessibility to the central core when the pore morphology is stellate. Moreover, the MRI contrast of the solutions were tested on a 3T clinical instrument. On **Figure 2-7.C**, phantom images show a strong T_2-weighted hypocontrast effect for both pore morphologies. This hypocontrast of the nanocomposites is very strong and complete darkening is observed already at low iron concentrations – almost no more signal at 0.5 mM. IO@STMS show a slightly highest hyposignal than IO@WLMS which is in agreement with the previous relaxivity measurements.

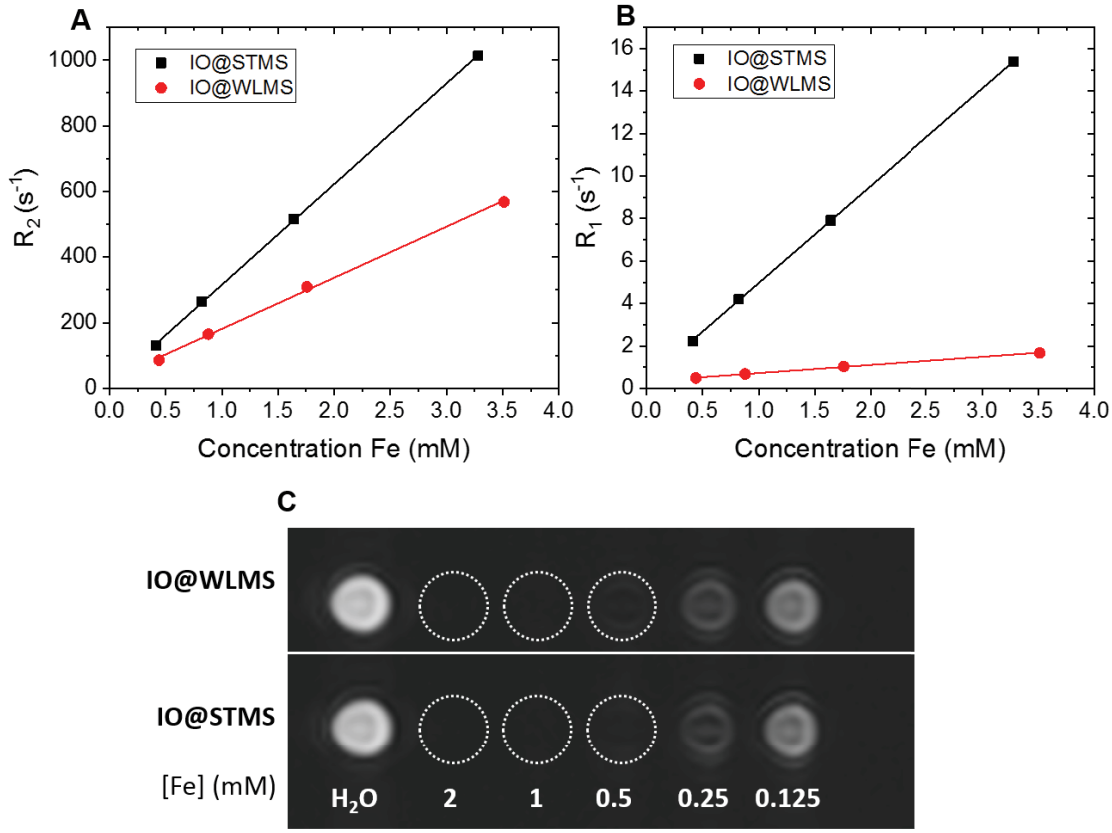

Figure 2-7. Transversal $R_2 = 1/T_2$ (s^{-1}) relaxation rates (A) and longitudinal $R_1 = 1/T_1$ (s^{-1}) relaxation rate (B) as a function of [Fe] (mM) for IO@STMS and IO@WLMS in water at 37 °C and 1.41 T; T_2-weighted (C) MRI of IO@WLMS and IO@STMS, white dotted-line circles indicates sample positions.

Overall, these results show that the silica pore morphology have an impact on the MRI imaging properties. Stellate-like pore organization in IO@STMS allows a better water accessibility and diffusion in the nanocomposites compared to IO@WLMS. It can be rationalized that the very large open pores of the STMS shell is the key factor explaining this behavior. These effects on the relaxivities are in agreement with behaviors previously encountered with iron oxide@silica shell having micro porosities or small mesopores.

Table 2-2. Longitudinal and transversal relaxivities r_1 and r_2 for IO@WLMS and IO@STMS.

	r_1 ($mM^{-1}.s^{-1}$)	r_2 ($mM^{-1}.s^{-1}$)	r_2/r_1
IO@STMS	4.57	307	67
IO@WLMS	0.38	156	410

Furthermore, when superparamagnetic IONPs are placed in an alternating magnetic field (AMF), heat is generated and released in the surrounding medium. This heat (magnetothermal transfer) comes from the Brownian and Néel's spin relaxations.[44,46,51] A coating of a porous shell around IO core is a way to bring new features to the magnetic core : colloidal stability, high level of chemical

functionalization or drug loading.[40,52,53] As seen above in the relaxometric study, this MS shell have an influence on the properties of the core, and the magnetothermal properties as a function of the pore morphology are also investigated as follows.

Calorimetric measurements allow to evaluate the heat power dissipated by the NPs (per mass unit of material), which is also called the specific absorption rate (SAR). The temperature profiles as a function of time and SAR values acquired at the field parameters of H = 300 G (23.8 kA.m^{-1}) and f = 536.5 kHz for different concentrations of nanocomposites were studied and are shown in **Figure 2-8**. SAR were calculated following the procedure described in Materials & Methods section.

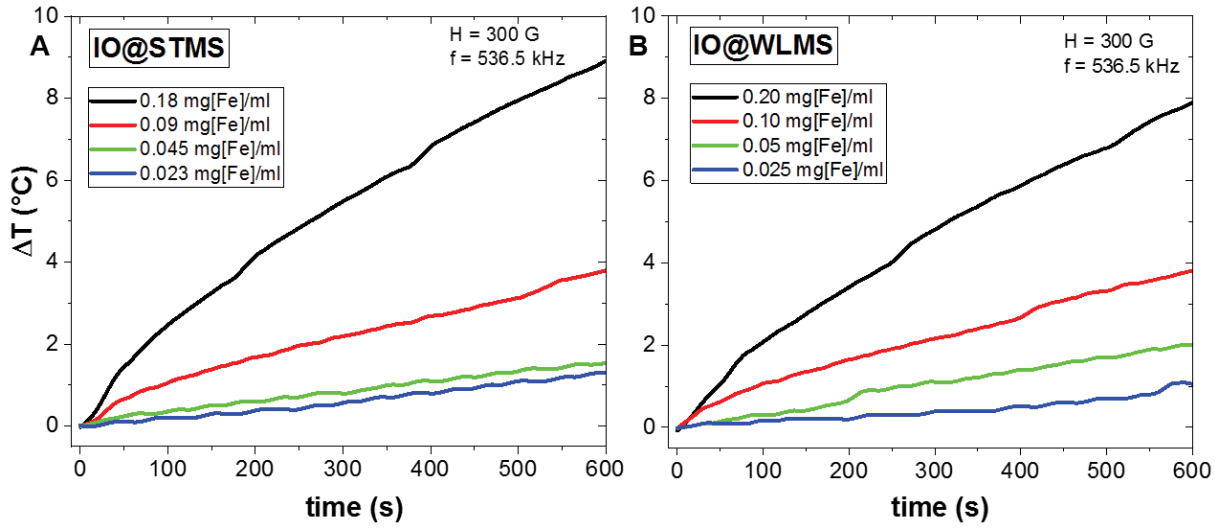

C

[NP] (mg/ml)	[Fe] (mg/ml)	SAR (W/g[Fe])
29	0.18	731
14.5	0.09	640
7.25	0.05	548
3.625	0.02	548

D

[NP] (mg/ml)	[Fe] (mg/ml)	SAR (W/g[Fe])
8.8	0.20	533
4.4	0.10	768
2.2	0.05	427
1.1	0.02	341

Figure 2-8. Temperature profiles as a function of time under AMF for different concentrations of IO@STMS (A) and IO@WLMS (B) including the corresponding SAR values for IO@STMS (C) and IO@WLMS (D).

First, for both types of magnetic core shell, temperature profiles curves (**Figure 2-8.A and B)** show a progressive temperature elevation of the samples dispersed in water. The measuring system is not perfectly adiabatic and some heat is lost to the environment – that is why the profiles do not describe perfect straight lines but have a damped profile. This is taken into account for the fitting of the curves and the SAR calculations.[44,54,55] For both samples, the concentration of iron oxide has a clear impact on the heating under AMF. The SAR values increase with the concentration of IO@MS (**Figure 2-8, tables C and D**). A temperature elevation of more than 8 K can be achieved in 10 min at low iron concentration (0.18-0.20 mg[Fe]/ml). As expected by the calculation formula, SAR values should be independent from the magnetic material concentration. Here slight fluctuations of SAR are observed. Even if the MS coating weakens the dipolar interactions, they could be attributed to partial aggregation of NPs or at least by different dispersion states between the samples when AMF is applied.

Nevertheless, with SAR values in the range of [548-731] W/g[Fe], and [341-768] W/g[Fe] for IO@STMS and IO@WLMS core shell respectively, it is clear that these nanocomposites are very good and performant objects to deliver heat locally with SAR suitable and adapted to perform hyperthermia treatments or heat-triggered drug delivery.[47,49,50,56] Other works reported SAR performances even for lower magnetic fields and frequencies suitable for biological applications.[38,46,47,57–59] From the tables in **Figure 2-8**, it is to note that the heat dissipation ability of IO@WLMS is though slightly lower than the IO@STMS. This can be attributed to the pore morphology. The worm-like pores are less open towards the exterior of the particle and the silica is denser. Heat diffusion is thus slowed down. In addition, the synthesized IO@WLMS NPs have a smaller diameter than IO@STMS (75 nm vs 100 nm) which means a thinner silica shell. We can assume that if the silica shell thickness of both morphologies would be equal, the damping effect of the IO@WLMS in comparison with IO@STMS would be even more pronounced.

II.2.4. Conclusion

In this work, we aimed at exploring a new way to tune pore morphology and the resulting structural/textural features of MS NPs or MS shell around iron oxide magnetic cores. We showed here that the resulting pore morphology of MS NPs, synthesized with CTA^+,Tos^- as pore structuring agent, AHMPD as a small organic amine basis acting as growth inhibitor and TEOS as sol gel silica source, can be tuned on a controlled manner simply by adjusting the sol gel reaction temperature T_{sg}. Hence, we showed that below 75-80 °C, stellate MS NPs are formed as described in our previous works whereas above 80 °C the morphology of the pore structure completely changes to a WL structure as observed by TEM and analyzed by nitrogen adsorption desorption isotherms. This process allowing to orient MS pore structure by simply adjusting the sol gel temperature is also successfully achieved around IO NPs yielding IO@STMS having a porous silica shell with stellate morphology when sol gel temperature is below 80 °C. IO@WLMS having a porous silica shell with WL morphology are obtained morphology with a temperature above 80 °C. The relaxometric and magnetothermal properties of the resulting core-shell magnetic silica IO@STMS and IO@WLMS displayed for both core shell NPs suitable features for T_2-MRI and hyperthermia treatments. IO@STMS as compared to IO@WLMS, is shown to have higher transversal relaxivity r_2 (respectively 307 vs 156 $mM^{-1}.s^{-1}$) and slightly higher SAR measurements (*ca.* 500 W/g depending on the concentration) which can be explained by a better accessibility of water within the stellar pore structures. The large pore STMS shell around IO core ensure probably a better transversal relaxation of water and a slightly better heat dissipation to the solution. These results indicate that controlling the pore morphology, while controlling interaction with solvent, surface functionalities and other properties, are essential for the design of suitable nanomaterials envisioned for combined imaging and therapy applications.

This previous published section dealt with the use of the temperature as a parameter to induce a change in the organization, shape and size of the silica shell's pores and the consequences on the heat transmission to the environment under AMF. In the next section, we go further in this study and a unique batch of IO core was used to be coated with silica shells obtained by different types of synthesis methods. Therefore, small pore silica (SPMS), large pore silica (STMS) and non-porous silica will be compared and the impact on the heat transfer will be discussed.

II.3. Modulation of the silica shell morphology to tune the magnetothermal properties

In this section, three synthesis protocols of silica have been applied to IO NPs of 16-17 nm size, (synthesized by thermal decomposition method) to tune silica shell thickness and pore morphology. In these three syntheses, the silica morphology is deeply influenced by the reaction conditions and especially the surfactants used. **Figure 2-9** represents the different synthesis pathways used to obtain the different silica morphologies. In the next paragraphs, experimental methods are described (II.3.1) and then a discussion is brought to describe the role of the reactants and in particular the role of the surfactants to build different silica morphologies will be discussed (II.3.2).

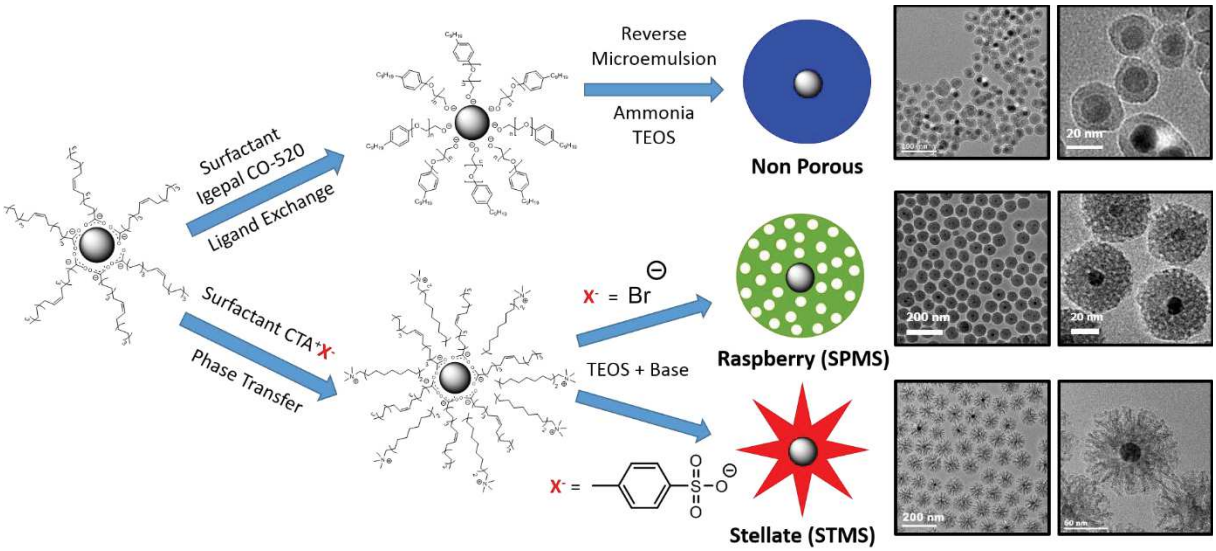

Figure 2-9. Summary of the different synthesis routes resulting in different pore morphologies.

II.3.1 Experimental methods for IO@silica core-shell synthesis with various pore sizes

II.3.1.1. Iron oxide nanoparticles

As magnetic core systems, IO NPs coated with oleic acid with diameter of 16.6 ± 1.9 nm (**Figure 2-10**) were synthesized by thermal decomposition method as described previously [60] and dispersed and stored in chloroform. In a typical procedure, iron (III) stearate (1.9 g, 2.10 mmol) were mixed together with oleic acid (1.24 g, 4.39 mmol), dibenzyl ether (0.54 g, 2.72 mmol) and squalane (15.8 g, 37.4 mmol). The mixture was heated up to 120 °C for 1 h. Then the temperature was further increased to 265 °C with a heating rate of 5 °C/min and kept 30 min at this temperature. The temperature was then brought to 350 °C at 5 °C/min and kept for 1 h. The as-synthesized IO NPs were washed several times with a mixture of chloroform: hot acetone (1:5) to remove unreacted iron stearate and free oleic acid.

Thereafter, around IO NPs, three kinds of MS shell were synthesized: non-porous, small pores and large pores.

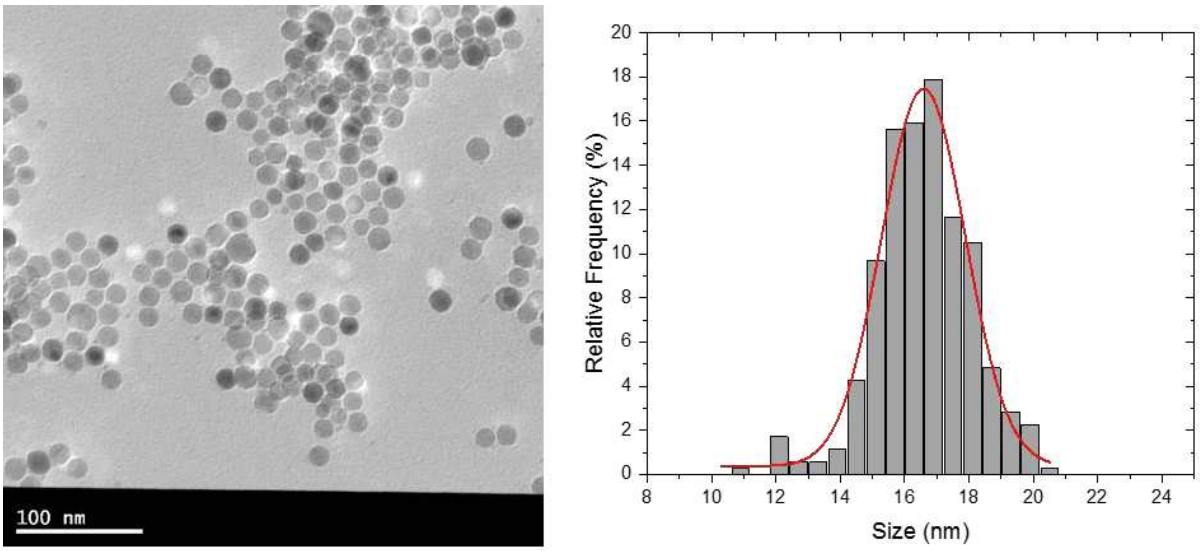

Figure 2-10. IO NPs synthesized by thermal decomposition and diameter size distribution.

II.3.1.2. Non-porous silica shell

Non-porous silica shell around IO NPs was synthesized by reverse microemulsion method via a procedure adapted from Ding *et al.*[61] IGEPAL CO-520 (1.36 g) is dissolved in 11 mL of cyclohexane and stirred with a magnetic bar for 10 min. Then, pre-synthesized 16.6 nm diameter IO NPs (3 mg Fe) dispersed in chloroform ([Fe] = 3.5 mg/mL) were added and let to stir 15 min. Thereafter, aqueous ammonia $NH_{3(aq)}$ 25% (100 µL) followed by TEOS (75 µL, 0.336 mmol) were added. The reaction was let to stir for 24 h. The resulting IO@nSiO_2 were collected by centrifugation (10000 g, 10 min) and washed three times with ethanol. Before further analysis, the core-shell NPs were stored in ethanol.

II.3.1.3. Small pore mesoporous silica shell (SPMS)

Small pore mesoporous silica (SPMS) shell was coated around IO NPs using a well-established method reported by Hyeon *et al.*[62] It consists in the phase transfer of hydrophobic IO NPs into aqueous dispersion by the use of a surfactant. The phase transfer results in highly stable and well-dispersed IO NPs. This technique is suitable for IO NPs that are coated with hydrophobic ligands and obtained from methods such as thermal decomposition, which allows a high control of the NP size.

First, a 28 mM CTAB solution in distilled water was prepared by adding 1.5 g CTAB in 150 mL water. The compound was not readily soluble so the mixture was heated to 60 °C for 30 min and a clear solution was obtained. Then 15 mL of this solution was added to a 100 mL one-neck round-bottom flask pre-heated at 30 °C. Then IO NPs dispersed in chloroform were added and strongly stirred for 30 min with a magnetic bar. The thickness of the silica was controlled by adjusting the amount of IO added. The mixture should turn from two separated non-miscible liquids to a hazy grey emulsion. Then the flask was opened and the emulsion was slowly heated up to 65 °C in order to evaporate the chloroform

and form a stable dispersion of IO NPs in aqueous phase. Thus the mixture should turn clear black. When the ebullition calmed down, the mixture was let to stir 15 more minutes. Meanwhile, basic water at pH = 10.8 was prepared by adding 14 µL NaOH 2 M into 30 mL of distilled water and then slowly poured into the round-bottom flask such that no brutal cooling happened. The mixture was heated to 70 °C and consecutively TEOS (300 µL, 1.35 mmol) and ethyl acetate (500 µL, 5.1 mmol) were added. The flask was closed and the mixture let to stir for 2 h. Finally, the resulting IO@SPMS were collected by centrifugation (13000 g, 20 min) and washed once with ethanol. Then CTAB surfactant was extracted by adding in the centrifuge tube an ethanolic solution of NH_4NO_3 (20 mL, 20 mg.mL^{-1} in ethanol) to IO@SPMS heated at 70 °C and stirred for 24 h. The particles were then washed twice with distilled water and twice with ethanol. They were kept suspended in ethanol for storage.

II.3.1.4. Stellate mesoporous silica shell (STMS)

Stellate mesoporous silica was also obtained by first a phase transfer from chloroform to aqueous phase.[40] CTATos (192 mg), AHMPD (22 mg) and distilled water (20 ml) were added into a 50 ml round-bottom flask. In order to get STMS morphology, the mixture was brought to 65 °C and then 5 mg of IO NPs dispersed in chloroform were added under vigorous stirring. The mixture was let to stir for at least 20 min. The color of the dispersion changed from hazy grey after addition to limpid dark black after full chloroform evaporation. Then the silica precursor TEOS (1.6 ml) was added and the sol-gel reaction starts. Ten minutes after TEOS addition the temperature was set to 70 °C and the mixture was stirred for 2 h. Finally, the resulting IO@STMS were collected by centrifugation (10000 g, 10 min) and washed once with ethanol. Then CTAB surfactant was extracted by adding in the centrifuge tube an ethanolic solution of NH_4NO_3 (20 mL, 20 mg.mL^{-1} in ethanol) to IO@SPMS heated at 70 °C and stirred for 24 h. The particles were then washed twice with distilled water and twice with ethanol. They were kept suspended in ethanol for storage.

II.3.2. Discussion

II.3.2.1. Non-porous silica shell IO@nSiO$_2$

Our IO NPs synthesized by thermal decomposition were coated with oleic acid and were thus stable in organic solvents such as chloroform or tetrahydrofuran (THF). Thus, it was not possible to put them directly in water to perform a Stöber-like silica condensation around the cores. The solution to produce this non-porous silica shell was to use a reverse microemulsion method developed by Ding and colleagues.[61] This method allowed to produce well-defined homogeneous silica shells. (See Scanning (SEM) and transmission (TEM) electron microscopy images of the three obtained silica morphologies summarized in **Figure 2-12**; non porous silica are on the **left column**). This method consists in producing a microemulsion of aqueous ammonia droplets dispersed in cyclohexane. The ammonia

droplets are stabilized by a non-ionic surfactant, IGEPAL CO-520, thus forming a stable water-in-oil emulsion (reverse emulsion). The surfactant was also used to make a first-ligand exchange with oleic acid at the surface of the IO NPs in cyclohexane. The driving force for this exchange is assumed to come from the hydroxyl-terminated PEG chains bounding to the iron oxide surface that replaces oleic acid. Then TEOS which is soluble in cyclohexane, was hydrolyzed at the interface droplets/cyclohexane and performed the ligand exchange with IGEPAL adsorbed on IO NPs, thus transferring NPs inside water droplets. In the droplet, the basic pH allowed for further hydrolysis and condensation of the silica around IO cores. The main challenge was to produce the same number of dispersed droplets than the number of added IO NPs, so each NP enters one droplet, thus leading to homogeneous monocore core-shell IO@nSiO_2. This number is defined by the molar ratio of surfactant and aqueous ammonia in cyclohexane. We found that for IO NPs with diameter of 16.6 ± 1.9 nm and 1.36 g of IGEPAL CO-520 for 100 µL ammonium hydroxide (25%) resulted in the formation of a non-porous silica shell with a thickness around 6.7 ± 1 nm (**Figure 2-12**)).

As detailed in Chapter 1, interactions between surfactants and silica oligomers and their organizations lead to controlled porosities (**Figure 2-11**): on one side hydrophilic heads of surfactants around which silica precursor condense and on the other side hydrophobic tails which organize to form silica-free domains. Thus, the presence of surfactants in the aqueous phase, where the silica is forming, is at the very origin of pores. IO NPs were coated with oleic acid and thus not dispersible in water. To produce mesoporous silica shell around IO core, we took advantage of their coating and we used a surfactant able to bring and stabilize the NPs in the aqueous phase by interacting with the hydrophobic coating. Then the excess of surfactant in solution would contribute to the organization of the silica during its condensation. The role of the surfactant in the silica thickness and the pore morphology is discussed in the next paragraph.

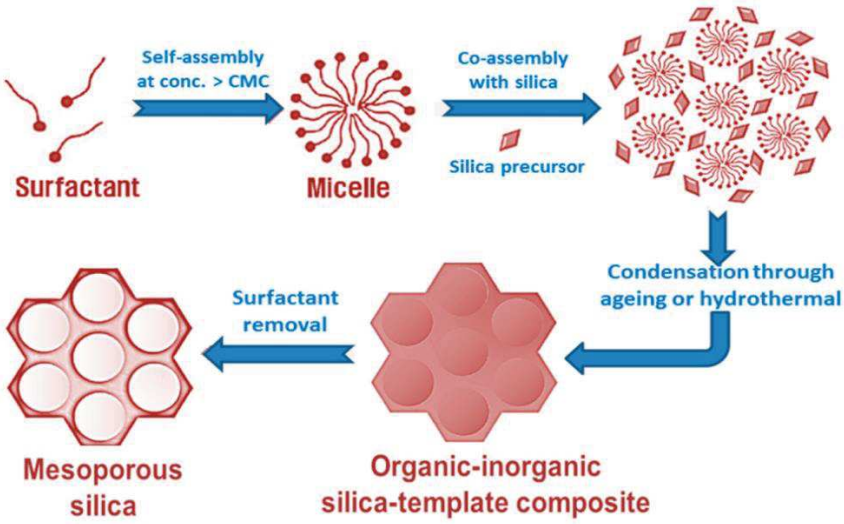

Figure 2-11. Synthesis for mesoporous silica using a surfactant-templated route.[63]

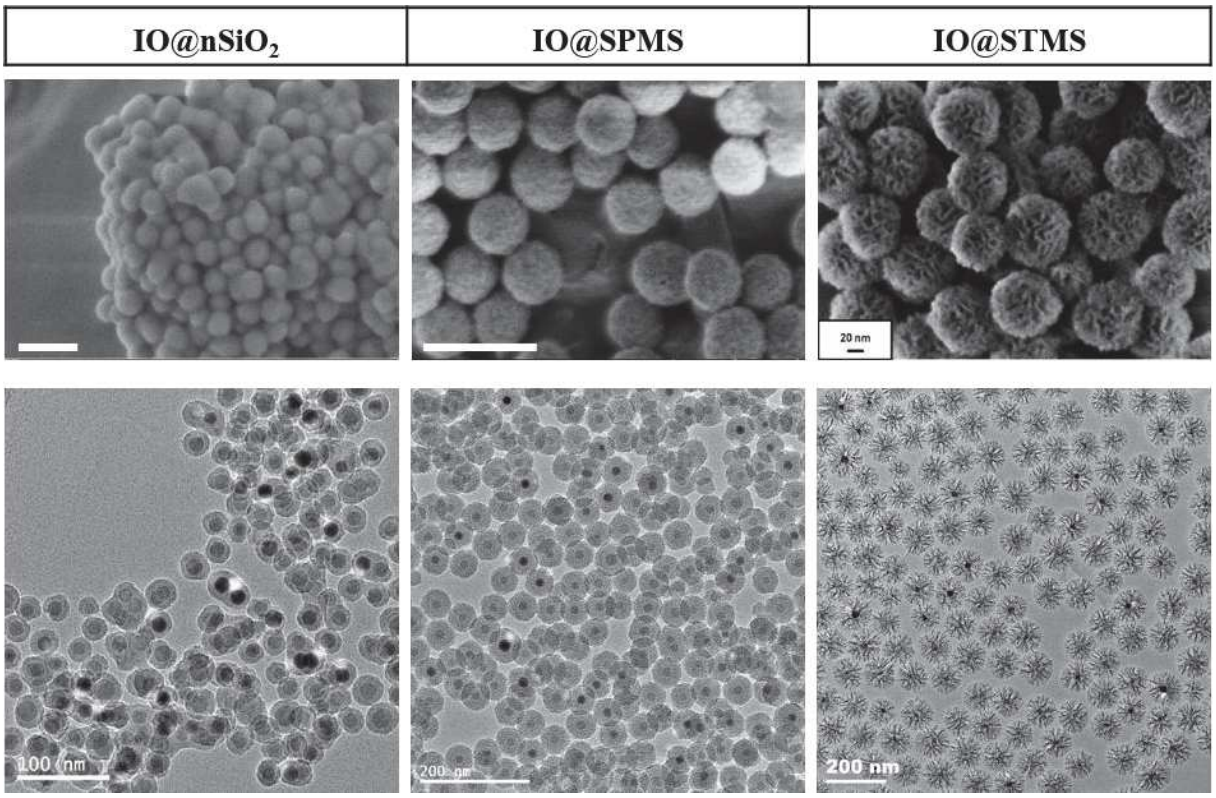

Figure 2-12. SEM (top) and TEM (bottom) images of the three morphologies synthesized. White scale bar represents 100 nm.

II.3.2.2. Small pore mesoporous silica shell and thickness modulation

The small pore morphology that we implemented is classical and was obtained by using CTAB, i.e. cetyltrimethylammonium cationic surfactant with bromide anion as counterion. By using few amount of sodium hydroxide as the base, the silica shell obtained in these basic conditions (pH=10.8 at the beginning of the reaction) had a raspberry morphology with pores diameter of 2-3 nm. These small pores gave the name of this shell structure: small pore mesoporous silica (SPMS) and the NPs were noted IO@SPMS NPs. (**Figure 2-12**, **middle column image**)

Then, we synthesized different silica shell thicknesses in order to study its impact on the magnetothermal properties. According to Ye *et al.*[64] the molar ratio between the iron oxide and the surfactant during the phase transfer step is crucial to control the silica shell thickness. Indeed, for a fixed amount of IO cores, an excess of CTAB results in SPMS NPs without IO core and a lack of CTAB limits the shell thickness even when more silica precursor TEOS is added. Thus, the concentration and volume of CTAB solution was fixed at 28 mM as well as the amount of TEOS and base added. The amount of IO NPs was the tuned parameter to modulate the silica shell thickness. So to 15 mL of CTAB solution, 3, 6 or 9 mg of [Fe] were added to the reactive mixture which corresponds to 0.85, 1.70 or 2.55 mL of IO NPs dispersion at a concentration of 3.53 mg[Fe]/mL. **Figure 2-13** shows the TEM images as well

as the size distributions. As expected, the increase of the [CTAB]/[Fe] ratio resulted in an increase of the shell thickness: size distributions give 30.6 ± 5.7 nm, 42.5 ± 4.3 nm, 52.2 ± 5.9 nm for [CTAB]/[Fe] respectively 2.6, 3.9,7.8.

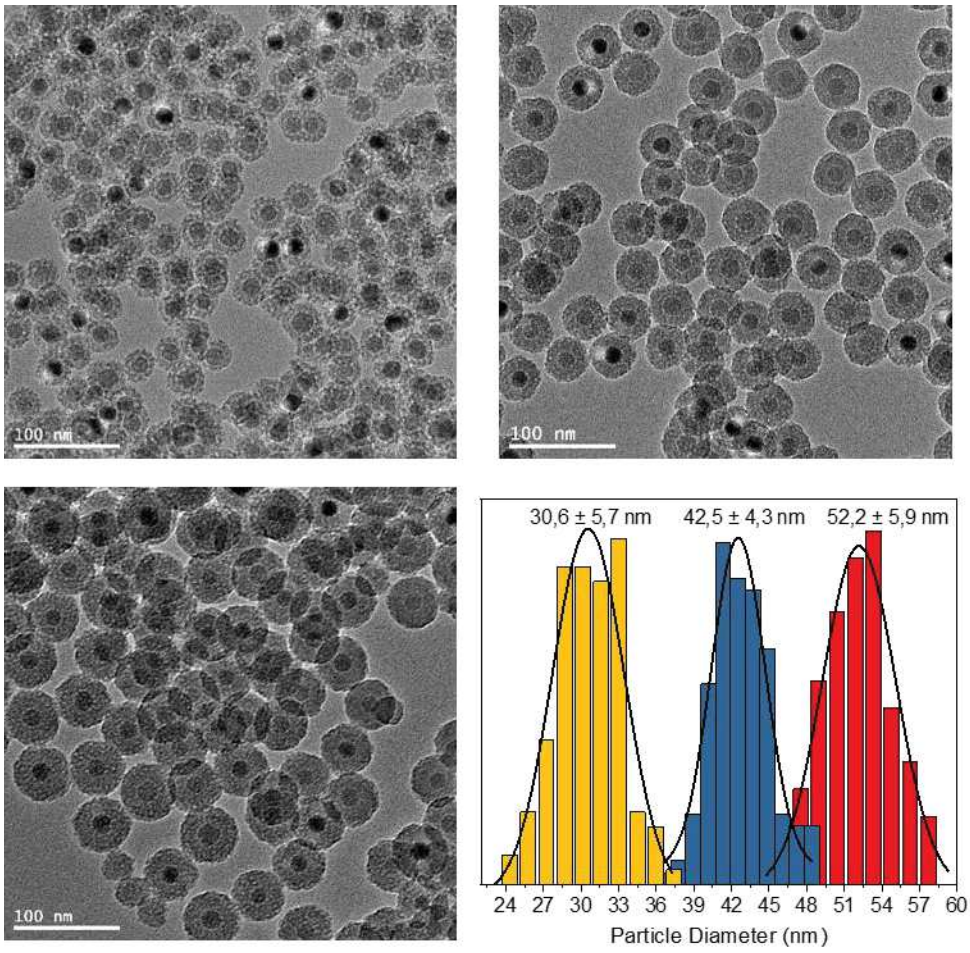

Figure 2-13. Different SPMS thicknesses obtained and corresponding TEM size distribution.

II.3.2.3. Large pore stellate silica: Influence of the counterion on the mesoporosity

To produce larger pores, the same cationic surfactant CTA^+ was used but with tosylate anion as counterion. Stellate mesoporous silica was obtained by first a phase transfer from chloroform to aqueous phase which is based on the same principle as described above. In the first section of this chapter, we described how the temperature modifies the interactions between the anionic counterions and the cationic micelles. The affinity of the counterion to interact with the ammonium head of the surfactant is a decisive parameter because it orients the way the silanolate species can interact with the micelles. Indeed, Br^- has a much lower affinity than tosylate Tos^- for the CTA^+ micelles. This can be explained from different points of view. First, the critical micellar concentration (CMC) of CTAB is much higher

than the CMC of CTATos. This means that CTAB dissolves better in water and this comes from a higher hydrophilicity of Br^- than Tos^-. Increasing counterion hydrophobicity indicates stronger interactions between the counterion and the micelles surface resulting in stronger electrostatic with the surfactant head group. From another point of view, the hydration of Br^- is more important than Tos^-, leading to an increase of their distance from the micellar surface, i.e. lower binding strength.[37,65,66] This explains that Tos^- competes more the adsorption of the forming silica (silanolates) on the micelles. The density of silanolates is too small to fully displace Tos^- resulting in the coverage of bundles of micelles, thus leading to the formation of big pores without the use of swelling agents. The other difference was the base used because this time no sodium hydroxide was used as for SPMS synthesis but a low amount of organic base 2-amino-2-(hydroxymethyl)propane-1,3-diol also knows as "Tris base" in order to catalyze the silica formation. This base is used in low concentration (pH ≈ 10) which also favors this competition. All these phenomenon lead to the formation of a mesoporous silica layer with big open pores with a stellate morphology IO@STMS (**Figure 2-12**, **right column**).

From TEM and SEM images, it appeared clearly that IO@STMS have the largest pores. The mesoporosity was also visible for IO@SPMS but obviously, no mesopores could be seen from the silica coating obtained by reverse microemulsion (IO@nSiO_2). BET analysis in the previous section (II.2) gave a surface area of 713 m^2/g for IO@STMS which is slightly higher than the core-free STMS synthesized by Zhang *et al.*[37] and open pores width around 10 nm. Concerning IO@SPMS synthesized by using CTAB templating, many publications reports the pore size between 2.5 and 3 nm without the use of swelling agents.[62,67] In our group we previously reported the synthesis of IO@SPMS whose specific surface area was shown to be depending on the thickness of the silica shell.[68] Indeed for small silica thicknesses, the spherical core participates significantly in the volume of the core-shell NP. Thus the volume fraction of silica is relatively limited (low total pore volume) and the surface area from the pores is low. For 50 nm IO@SPMS with a core of 10 nm diameter, the specific area found was about 120 m^2/g and a total pore volume of 0.35 cm^3/g [52] whereas for 88 nm IO@NP the specific area was found at 750 m^2/g and a pore volume of 0.84 cm^3/g. Thus we expect that for our NPs, the smaller core-shell exhibit the smaller surface area. This should increase by increasing the proportion of silica around the IO core. However, by further increase it should tend to decrease (surface to volume ratio). N_2 adsorption isotherms are currently being performed to elucidate the porosity of our IO@SPMS core-shell NPs. Regarding non-porous IO@nSiO_2, same analysis are in progress to determine if any microporosity can be detected.

II.3.3. Magnetic hyperthermia agent properties

As detailed above in Chapter 1, IO NPs with diameters about 20 nm are suited agents for cancer therapy by magnetic hyperthermia treatment (MHT). While effects of shape, size, composition of IO NP are well described in the literature, the influence of this silica shell (around these IO cores) on the heating properties is poorly reported. Moreover, this silica shell allows to combine multiple therapy and imaging modalities. As seen above, all these core-shell NPs have been made with the same iron oxide core (16.6 nm average diameter) and the same IO core coated with CTAB was used as a reference. An AMF at 200 G (15.9 kA/m) and 796 kHz was applied on these different NPs dispersions at a concentration of 1 mg[Fe]/mL. The temperature elevation was followed thanks to an adapted device (**Figure 2-14**).

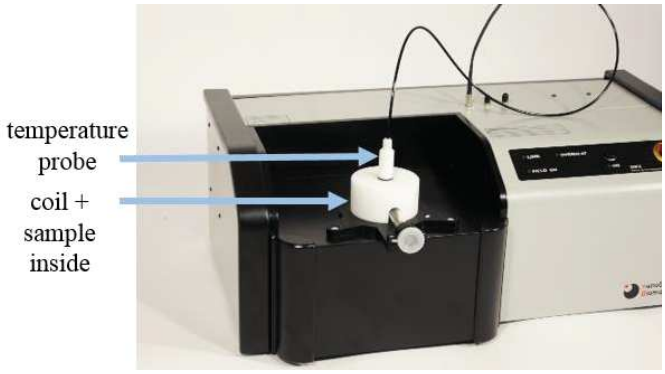

Figure 2-14. Picture of the device used for magnetothermal measurements.

The thermal profiles curves obtained are presented in **Figure 2-15** and associated SAR are provided in **Figure 2-16**. As a comparison with the previous paragraph (II.2), IO@STMS and IO@WLMS, synthesized above with a bigger IO core (18 nm average diameter) were added to the graph 2.15 (*Stellate 100* and *Worm-like 75*).

Regarding the SAR values, as compared to the IO@CTAB NPs, and for the same iron concentration, it clearly appeared that the silica coating decreased the temperature elevation and thus the associated SAR in all cases. This was expected as a silica shell is known to decrease the Brown relaxation time of the IO cores by blocking the NPs and to reduce their potential rotation in the fluid. However mesoporous silica shell SPMS and STMS resulted in much less damping of the heating than non-porous silica. After 80 seconds, the temperature rose by 6 °C for CTAB-coated IO, 5 to 4 °C with mesoporous silica and less than 3 °C with non-porous silica. This is also clearly seen with the calculated SAR (**Figure 2-16**). With no silica, the SAR was 550 W/gFe and it decreased to about 400 W/gFe for IO@SPMS, 305 W/gFe for IO@STMS and 243 W/gFe for dense, non-porous silica.

Zhu and Tao[50,69] reported the synthesis of stellate silica shell around polydisperse IO cores ranging between 15 and 20 nm, and SAR values of 9 and 12 W/g were obtained upon AMF at 409 kHz and 180 G. They also noticed a decreased of the heating behavior when a silica shell was coated around their IO cores. However, it is difficult to compare our well monodispersed IO NPs obtained by thermal

decomposition compared to the ones they produced by co-precipitation. Other papers[70] described SAR increase when adding a silica shell but this was mostly due to an increase of the colloidal stability and it prevented aggregation by dipolar interaction wich are known to decrease SAR values.

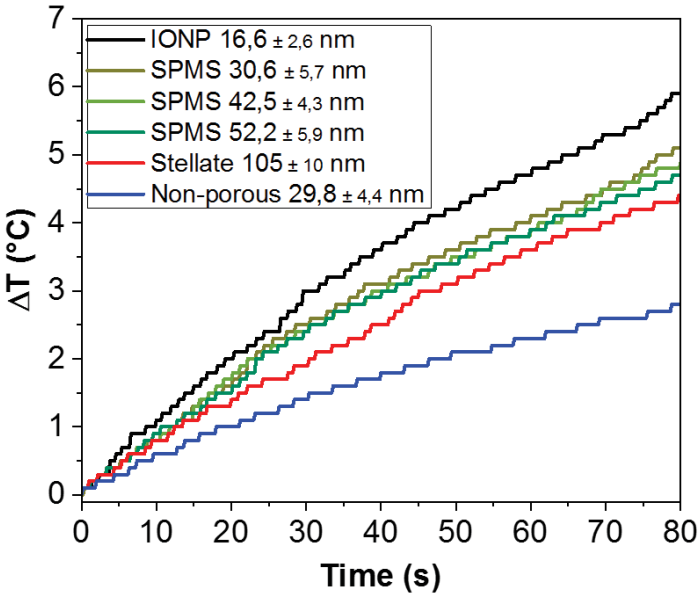

Figure 2-15. Temperature curves obtained for the different types of silica shell and IO NPs coated with CTAB.

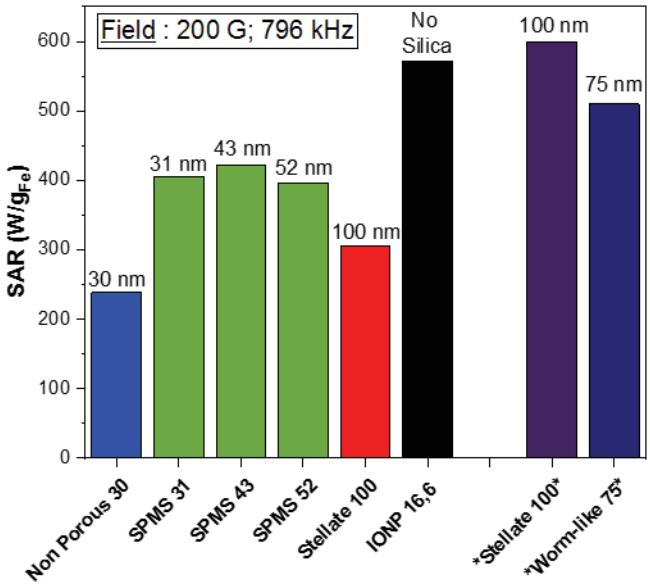

Figure 2-16. Calculated SAR for corresponding NPs.

Considering only the Brown relaxation is probably not enough to explain these results because if this was the only effect, the porosity of the silica should have only very little influence. However, the porosity seems to be a fundamental parameter. By comparing non-porous silica shell IO@nSiO$_2$ with small pore silica IO@SPMS, both with a size about 30 nm, i.e. a shell thickness of 6-7 nm, it appeared clearly that the denser non-porous silica was more insulating. Indeed, it decreased more the heating front

from the cores to the surrounding water resulting in less heating of the environment. Water molecules probably play an important role in the heat transport; a dense solid layer may inhibit convection heat transfer, which is known to be a lot more efficient than pure conduction. Erdogdu *et al.*[71] showed it by comparing heat behaviors of free and hydrogel-trapped water molecules. Hence, SPMS shell with mesopores of around 2-3 nm allowed to increase the heat transfer. Nevertheless, for the different SPMS shells synthesized (thicknesses of 6, 13 and 18 nm), no major influence of the thickness on the calculated SAR could be observed. In this range, the pore introduction to the silica shell had a greater impact than the thickness.

Stellate shaped silica (STMS) has the biggest pore opening, around 10-15 nm and thus is the structure with the less dense silica. Water molecules can easily circulate inside the STMS shell. However, the SAR calculated was found lower than the ones for SPMS. We explained this behavior by the fact that above a certain diameter, some thickness effects may play a role in the heat transfer. Between the larger IO@SPMS (52 m diameter) and IO@STMS (100 nm diameter), the silica thickness is doubled and thus the volume of the NPs is multiplied by 8. This is a huge difference and even if the structure is very porous the heat transfer might probably be damped over a long distance. It is to notice that even if the silica thickness is important for IO@STMS, its SAR was still higher than the non-porous thin silica layer for IO@nSiO_2. On the right of the graph, the SAR values of the IO@STMS and IO@WLMS structures obtained in the previous paragraph were added. IO cores used were a little larger (18 nm diameter) and thus more efficient for MHT which explains the overall greater SAR values. When this is taken into account, the comparison between stellate and worm-like silica morphologies, which had more a similar thickness, highlighted and confirmed that the larger the pore openings are, the more efficient the heat transfer is.

II.3.4. Conclusion

To conclude, in the last two sections, we were able to synthesize four different silica morphologies around iron oxide cores: non-porous, small pores, worm-like and stellate. The control of the porosity was obtained through two ways. First, by modifying only the reaction temperature, we were able to change the relative interactions between surfactant molecules and condensing silicate species and thus have the control to obtain stellate or worm-like silica shell (II.2.). The second way implied to change the reactants used and the reaction methods. Reverse microemulsion method allowed to produce non-porous silica whereas phase transfer resulted in mesoporous shells. In the last case, the choice of surfactant is fundamental because we showed that the cationic counterion plays a great role by its interactions with silicates and growing silicate-surfactant complexes. Thus it was possible to orient the production towards small pores or large dendritic pores (stellate).

II.4. Nanothermometry

Nanothermometry is a technique developed to measure temperature at the nanoscale by using material and physical phenomena able to probe temperature locally, at the contact of NPs for example. Luminescent nanothermometers are certainly the most promising but very few are easily available. These molecular or nanoparticulate probes exploit the relationship between temperature and luminescence properties and especially the variation of the emitted light when the temperature changes. Semiconductors quantum dots (QDs) belong to this family and they are already known to have various applications in biology and medicine for imaging. Chemical methods allow to synthesize nanocrystal semiconductors of various size between 1 to 10 nm with tunable emission from UV for infrared. Cadmium-based semiconductors such as CdSe, CdS, CdTe are the most common and usually a ZnS shell is added to protect the toxic core but it also enhances the photoluminescence yield.[72] In our team, Perton *et al*.[40] showed that it was possible to anchor CdSeS/ZnS QDs at the surface of STMS NPs and that these luminescent nanoobjects were very efficient at labeling cells. So we investigated the use of these QDs as nanothermometers for core-shell IO@MS NPs.

The first study aimed at establishing calibration curves by spectrofluorimetry to correlate emission spectra of QD to the surrounding temperature. Then in a second study, the emitted fluorescence when AMF is applied has been investigated in order to elucidate the local temperature at the surface of the QDs.

II.4.1. Establishing nanothermometry calibration curves by spectrofluorimetry

II.4.1.1 Free QDs in aqueous dispersion

The first step was to evidence the behavior of CdSeS/ZnS nanocrystals alone as nanothermometers. The QDs used are commercially available product purchased from Sigma-Aldrich and have a diameter of 6 nm. QDs dispersion was placed in a thermal bath whose temperature can be controlled. Then excitation was set at 350 nm and emission spectra of the dispersion were recorded as a function of the temperature (**Figure 2-17**).

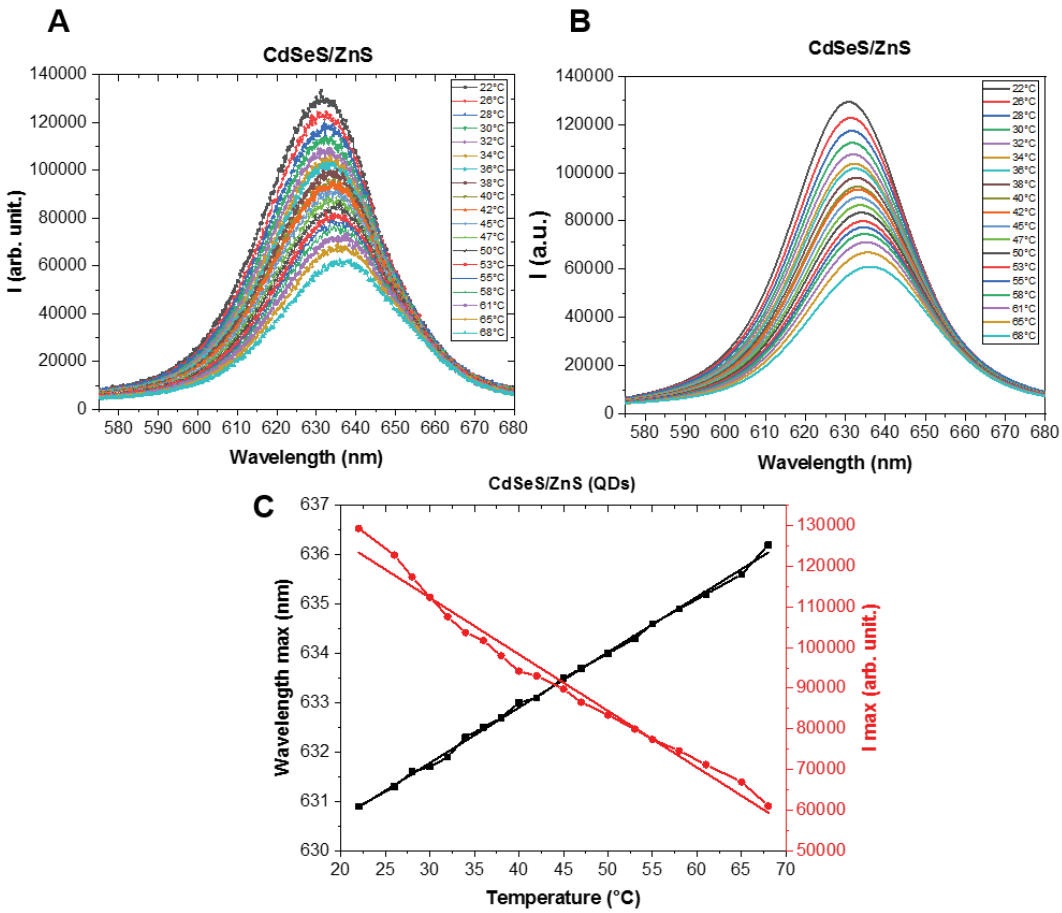

Figure 2-17. Fluorescence of CdSeS/ZnS QDs as a function of the temperature; **(A)** raw data, **(B)** fitted data with a Voigt model and **(C)** λ_{max} and I_{max} as a function of the temperature.

On the 22-68 °C temperature range, we clearly evidenced an effect of the temperature on the fluorescence profile. While increasing temperature, the maximum intensity I_{max} decreased, the peak enlarged and the wavelength for which the emission is maximum (λ_{max}) was shifted towards higher wavelengths. λ_{max} and I_{max} can be reported manually from the raw data curves but we wanted to develop a more systematized method in order to analyze data quicker. To do so, we decided to fit the data with a Voigt model. Indeed, this was the fit model that allowed the best description of the maximum position whose coordinates are (λ_{max}, I_{max}) compared to experimental data. Then, by plotting the variation of I_{max} and λ_{max} as a function of the temperature, a clear linear variation was observed on this temperature range and the linear fits gave: λ_{max} = 0.112*T + 628.4 and I_{max} = -1391.5*T + 153994 (**Figure 2-17.C**). Thus these commercial QDs are very promising luminescent nanothermometers in a temperature range adapted for biological applications.

The next step was to graft those QDs on IO@MS NPs. For this, we synthesized IO@SPMS core-shell NPs because the pores are smaller than QDs diameters. QDs could not penetrate inside the pores and thus would homogeneously decorate the surface of the NPs at a defined distance from the core.

II.4.1.2. QDs as nanothermometers grafted on the surface of core-shell

To graft QDs at the surface of IO@SPMS or IO@STMS, a first modification of the core-shell NPs with aminosilane has been realized. 10 mg of IO@MS NPs was dispersed into 2.75 mL of absolute ethanol. Aqueous ammonia (150 µL, 28 wt%) followed by (3-aminopropyl)triethoxysilane (APTES) (625 µL, 2.7 mmol). The mixture was agitated on a rotating wheel for 2 h. Then the NPs bearing amine groups IO@MS@APTES were collected by centrifugation (11,000 g, 11 min) and washed once with ethanol and twice with distilled water. QDs were grafted on IO@MS with a density of 2 wt%. In a typical procedure, carboxylated QDs (400 µL, 1 mg/mL) were added to a tube containing an aqueous dispersion of IO@MS@APTES NPs (20 mg in 3 mL). The mixture of both were stirred for one night. Then 20 µL of a solution of EDC (1-Ethyl-3-(3-dimethylaminopropyl)carbodiimide) (57 mg/mL) and 20 µL of a solution of NHS (*N*-Hydroxysuccinimide) (97 mg/mL) were successively added to the NPs. After 4 h of stirring, the resulting IO@SPMS@QDs were collected by centrifugation (10,000 g, 10 min), washed three times with water and stored in distilled water.

We also wanted to graft QD directly at the surface of IO NPs but an anchor sublayer was necessary. To do this IO NPs were coated with aminosilane APTES following a method described in our group by Wang *et al.*[73] To perform this, 1.4 mL of IO NPs (18 nm diameter) dispersed in chloroform (5.73 mg[Fe]/mL) were added into a tube and 0.6 mL chloroform were added to have a total 2 mL chloroform. To this, 5.6 mL absolute ethanol was added as well as 218.5 µL APTES and 267 µL acetic acid (25 wt%). The tube was shaken on a rotating wheel for 24 h. Then, resulting IO@APTES NPs were collected by centrifugation (14,000 g; 20 min), washed three times with ethanol and stored in the same solvent. To graft IO@APTES with 1 wt% QDs, 1.19 mL of IO@APTES ethanolic dispersion (1.68 mg[Fe]/mL) was added to a tube with 5.15 mL distilled water. Then carboxylated QDs (20 µL; 1 mg/mL) were added to the tube and let to stir 4 h. 2 µL EDC (57 mg/mL) and 3.2 µL NHS (97 mg/mL) were added to the NPs. The mixture was stirred for 4 h and the resulting IO@APTES@QDs were collected by centrifugation (14,000 g, 20 min) and washed three times with ethanol.

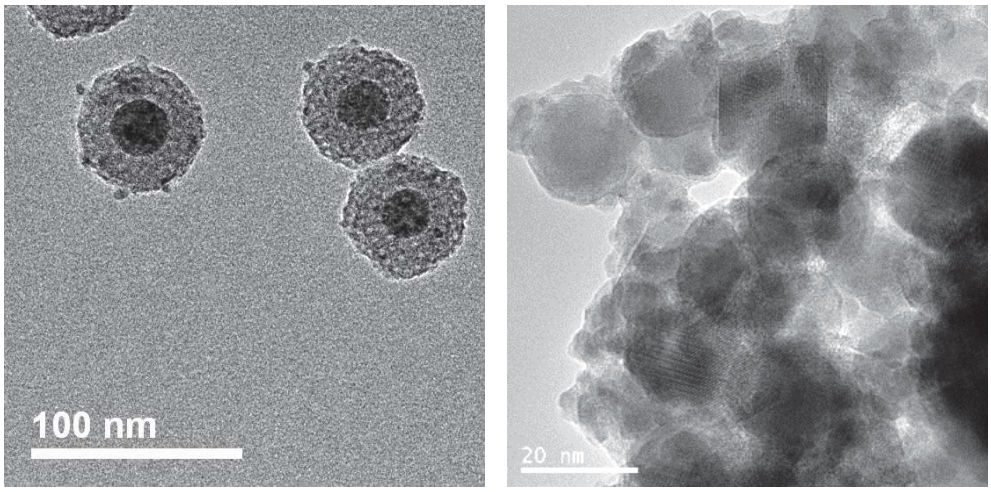

Figure 2-18. QDs grafted on IO@SPMS (left) and aminosilane-modified IO (right).

.

As for the free QDs, the fluorescence of IO@SPMS@QDs was followed as a function of the temperature. The results are represented in **Figure 2-19**.

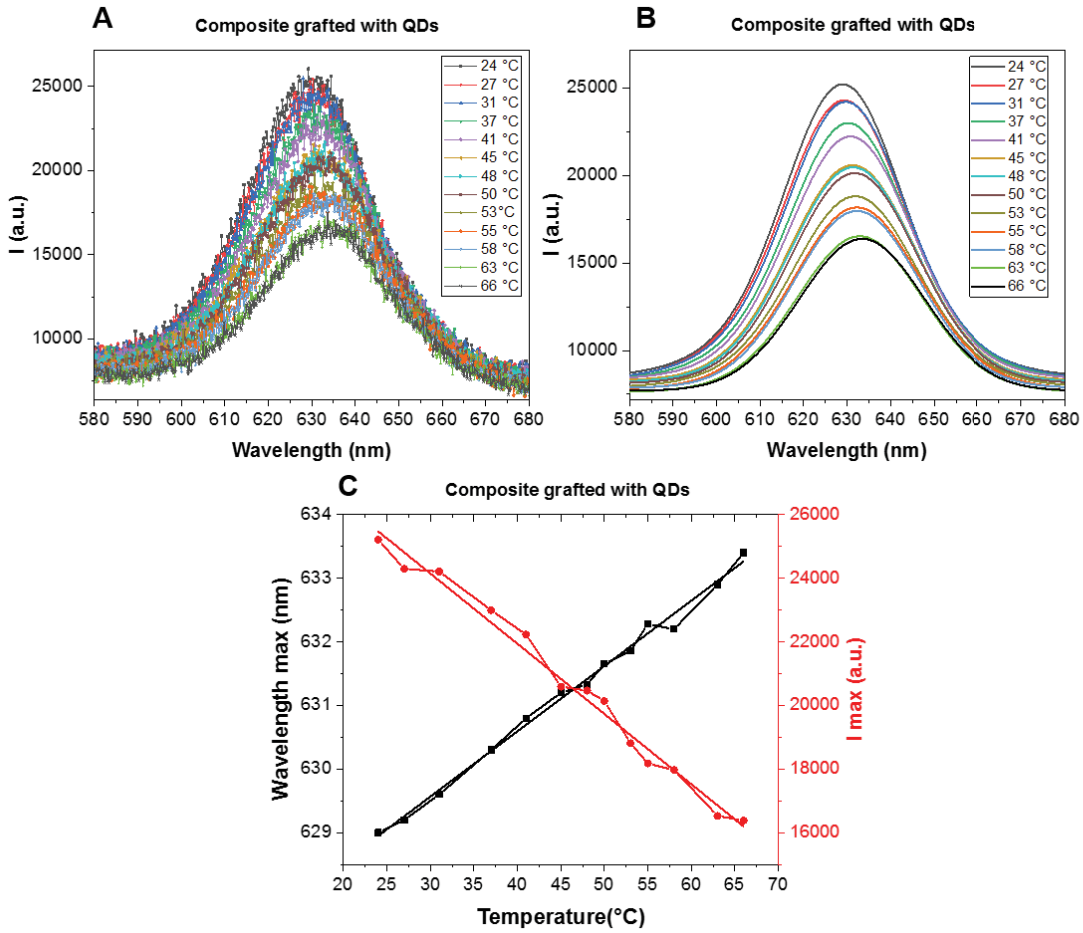

Figure 2-19. Fluorescence of QDs grafted on IO@SPMS as a function of the temperature.

It clearly appears that the QDs emission remained sensitive to the temperature and the grafting did not degrade its fluorescence. When comparing the linear variations of λ_{max} and I_{max} with the

temperature (summarized in **Table 2-3**), it is worth to note that the slope of the variation of λ_{max} keeps constant for both systems (about 0.1 nm/°C) whereas the intercept is slightly shifted. The variation of I_{max} is more affected by the grafting but this parameter depends on local the concentration of grafted QDs which is a parameter more difficult to control. The QDs are obviously less uniformly distributed in the volume as they are concentrated on the core-shell NPs. Some QDs can also be very close one from each other which can hinder the light absorption and emission. The IO core can also potentially absorb a part of the incident and emitted light. Thus the monitoring of the position of λ_{max} and its variation when the temperature changes, appears to be a good way to probe the temperature at the surface of our nanocomposites.

Table 2-3. Parameters (slope and intercept) of the variation of I_{max} and λ_{max} with the temperature for grafted and ungrafted QDs.

	Free QDs		Grafted QDs	
y=a*T (°C)+b	λ_{max}	I_{max}	λ_{max}	I_{max}
a	0.112	-1392	0.103	-220.1
b	628.4	153994	626.5	30771

II.4.2. Nanothermometry under alternating magnetic field

II.4.2.1 Calibration in oven

In collaboration with the *Laboratoire de Physique et Chimie des Nano-Objets de Toulouse* (LPCNO), we tried to measure the surface temperature of IO@MS when an AMF is applied. The approach was to collect, thanks to an optical fiber, the spectra of the emitted light from QDs when the AMF is on and off, and to compare both signals. A shift of the fluorescence would indicate that the QDs sense a NP surface localized temperature different from the global temperature, and using a calibration curve this local temperature would be determined. The sample was placed in a holder inside the magnetic coil and the optical fiber was placed at the top suspension (**Figure 2-20**). First we calibrated our IO@MS@QDs systems by using an oven to measure the fluorescence variation with the temperature in this setup. A very good correlation was found compared to the curves previously obtained in our own lab (λ_{max} slope of 0.12 nm/°C).

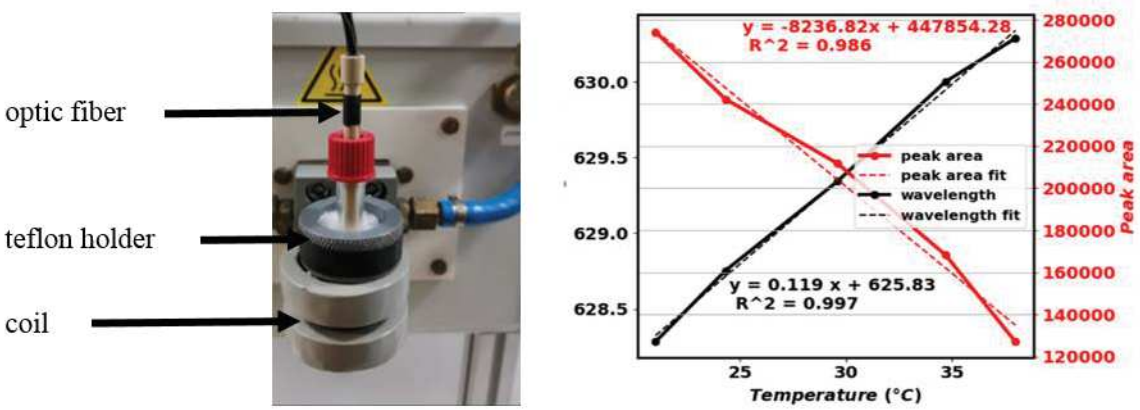

Figure 2-20. Setup used for simultaneous measurement of fluorescence and AMF application (left) and calibration curve of IO@MS@QDs obtained (right).

II.4.2.2 Measurements upon AMF application

Then we tried to measure the fluorescence shift under AMF. Measurements were performed at a frequency of 300 kHz and with a field intensity between 0 and 68 mT (680 G). 68 mT was the maximal field intensity that the coil could produce (H max). The intensity of the magnetic field was progressively increased to determine its effect on the emission shift. First, the sample was let to equilibrate with the room temperature and a first fluorescence measurement was recorded before any AMF application (H "off"). Then the field was turned on and the fluorescence was recorded 60 s after AMF application (H "on"). After measurement, the field was turned off and the sample was let to equilibrate to room temperature for 10 min. The process was repeated by starting to record again the fluorescence without AMF (H "off"), followed by an increase of the field intensity at each step (**Figure 2-21**). The variations of I_{max} and λ_{max} with the field strength H are shown in **Figure 2-22**. What was expected is that the signal at H "off" should remain constant (no local hot spot) during the whole experiment duration whereas the fluorescence at H "on" should progressively change with the field intensity (local hot spot).

Unfortunately, after different trials no clear effect of the AMF could be seen. In particular, by increasing the field intensity, λ_{max} should shift towards higher wavelengths and I_{max} should decrease (higher local temperature than the global temperature). However, either with the field on or the field off, a decrease of the fluorescence intensity I_{max} as a function of the field intensity was observed. This was mostly attributed to sedimentation of the NPs at the bottom of the cuvette during the measurement. Concerning variations of λ_{max}, no clear tendency could be evidenced. Some fluctuations could be observed and the wavelength seemed to increase with the increasing field intensity but the difference between fields off and on was not significant. Therefore, it is difficult to conclude if a local temperature (hot spot) was detected or not because of physical phenomena such as NPs sedimentation and interaction of the magnetic field with the temperature probe which masked the signal.

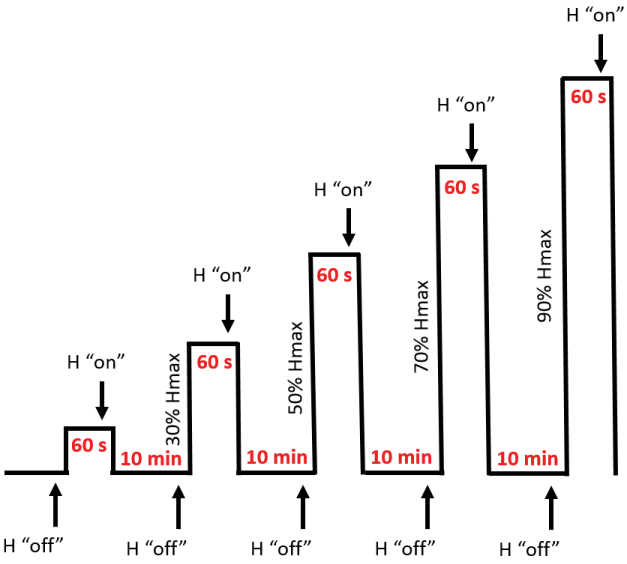

Figure 2-21. Scheme explaining the measurement protocol.

In summary, this is a promising experiment which could help us to better understand the heat dissipation from the iron oxide core to the environment. However, the setup, the grafting of QDs and the exploitation of the results have to be continued and improved. New experiments sessions have been programmed and should contribute to perfecting the system. Several options are on study to improve the system. In particular, the immobilization of the QD-grafted NPs in a gel or the deposition on a substrate, in order to overcome the sedimentation issue.

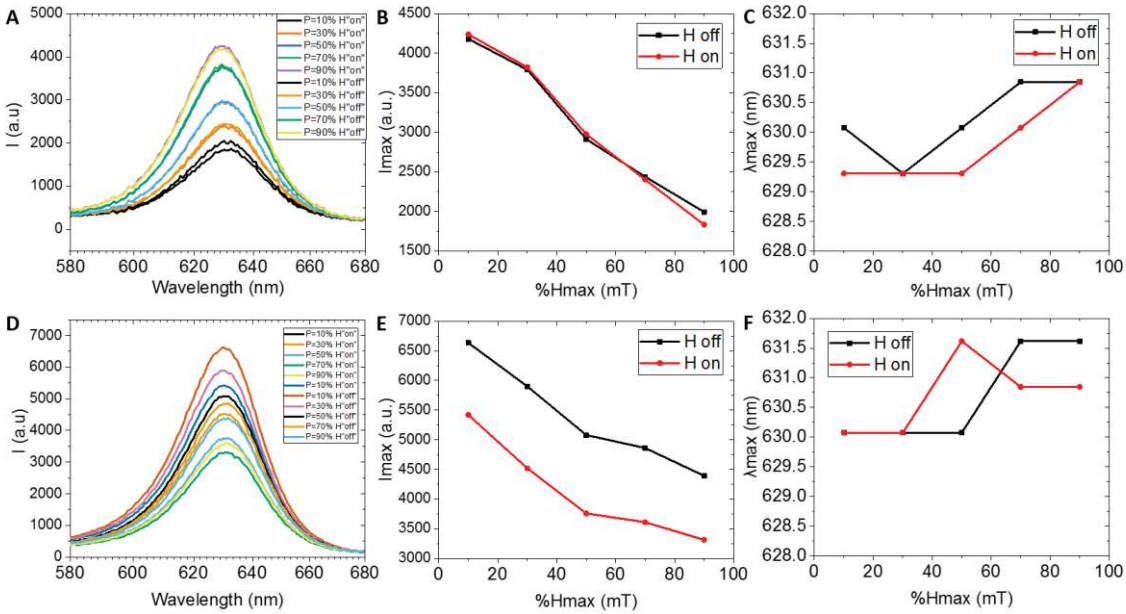

Figure 2-22. At the top, fluorescence curves of QDs grafted on IO@SPMS with field "on" and "off" (A), corresponding variations of Imax (B) and max (C); at the bottom, same graphs obtained with QDs grafted on aminosilane-modified IO (D,E,F) respectively.

II.5. Conclusion of Chapter II

In this chapter, we implemented the coating of silica shells having tunable thicknesses and pore morphologies around IO NPs synthesized by thermal decomposition. These cores stabilized by hydrophobic ligands were successfully coated with a silica shell either with or without mesoporosities. By engineering the operating reaction conditions, it was possible to synthesize three different mesoporous silica structures: SPMS, WLMS and STMS ranging from the smallest to the largest pore width (from 3 to 15 nm). In a first section, especially for the synthesis using CTATos surfactant, we demonstrated that the sol-gel temperature was a key parameter to direct the surfactant templating role allowing to modify the interactions with the condensing silica (WLMS vs STMS). Then, in a second section, we showed that the self-assembly of the cationic surfactant is important but the counterion is absolutely crucial to orient this organization, pushing from individually coated micelles and thus thin pores (SPMS) to the aggregation of micelles into big bundles resulting into large open pores (STMS).

The resulting silica shells have an important impact on the properties of the IO cores, in particular, the contrast imaging and magnetothermal properties. The thicker and the denser the silica shell is, the less the water molecules can enter the core-shell and interact with the magnetic core. This effect influences the MRI contrasting property and we showed that STMS with more open pores result in higher r_2 transverse relaxivity than WLMS. Regarding the magnetothermal transfer as a function of the silica pore structures, we showed that by thickening and closing the silica pores, the SAR and magnetothermal properties were decreased. The best heating properties would be obtained for thin and large pore silica.

In the last sub-section, an innovative method for nanothermometry measurements has been implemented. The use of QDs grafted to the NP surface is a promising tool to probe the local temperature of the core-shell. It relies on the monitoring of the fluorescence of the QDs when the sample is placed in an AMF. However, more experimental improvements are needed to confirm the local heating effect given some issues with magnetically field sensitive temperature probes or potential NPs sedimentation under field. The grafting of QDs directly on IO NPs or with the intermediate of very thin functionalized silica should allow us to elucidate the surface temperature. Computational simulation is another tool that will be explored in the future to corroborate the experimental data.

II.6. References

(1) Yoon, T.-J.; Lee, H.; Shao, H.; Weissleder, R. Highly Magnetic Core–Shell Nanoparticles with a Unique Magnetization Mechanism. *Angew. Chem.* **2011**, *123* (20), 4759–4762.

(2) Pöselt, E.; Kloust, H.; Tromsdorf, U.; Janschel, M.; Hahn, C.; Maßlo, C.; Weller, H. Relaxivity Optimization of a PEGylated Iron-Oxide-Based Negative Magnetic Resonance Contrast Agent for T2-Weighted Spin–Echo Imaging. *ACS Nano* **2012**, *6* (2), 1619–1624.

(3) Daou, T. J.; Pourroy, G.; Bégin-Colin, S.; Grenèche, J. M.; Ulhaq-Bouillet, C.; Legaré, P.; Bernhardt, P.; Leuvrey, C.; Rogez, G. Hydrothermal Synthesis of Monodisperse Magnetite Nanoparticles. *Chem. Mater.* **2006**, *18* (18), 4399–4404.

(4) Guisasola, E.; Baeza, A.; Talelli, M.; Arcos, D.; Moros, M.; de la Fuente, J. M.; Vallet-Regí, M. Magnetic-Responsive Release Controlled by Hot Spot Effect. *Langmuir* **2015**, *31* (46), 12777–12782.

(5) Adam, A.; Parkhomenko, K.; Duenas-Ramirez, P.; Nadal, C.; Cotin, G.; Zorn, P.-E.; Choquet, P.; Bégin-Colin, S.; Mertz, D. Orienting the Pore Morphology of Core-Shell Magnetic Mesoporous Silica with the Sol-Gel Temperature. Influence on MRI and Magnetic Hyperthermia Properties. *Molecules* **2021**, *26* (4), 971.

(6) Narayan, R.; Nayak, U. Y.; Raichur, A. M.; Garg, S. Mesoporous Silica Nanoparticles: A Comprehensive Review on Synthesis and Recent Advances. *Pharmaceutics* **2018**, *10* (3), 118.

(7) Knežević, N. Ž.; Durand, J.-O. Large Pore Mesoporous Silica Nanomaterials for Application in Delivery of Biomolecules. *Nanoscale* **2015**, *7* (6), 2199–2209.

(8) Wu, S.-H.; Mou, C.-Y.; Lin, H.-P. Synthesis of Mesoporous Silica Nanoparticles. *Chem. Soc. Rev.* **2013**, *42* (9), 3862–3875.

(9) Wang, Y.; Sun, Y.; Wang, J.; Yang, Y.; Li, Y.; Yuan, Y.; Liu, C. Charge-Reversal APTES-Modified Mesoporous Silica Nanoparticles with High Drug Loading and Release Controllability. *ACS Appl. Mater. Interfaces* **2016**, *8* (27), 17166–17175.

(10) Giret, S.; Wong Chi Man, M.; Carcel, C. Mesoporous-Silica-Functionalized Nanoparticles for Drug Delivery. *Chem. – Eur. J.* **2015**, *21* (40), 13850–13865.

(11) Alberti, S.; Soler-Illia, G. J. A. A.; Azzaroni, O. Gated Supramolecular Chemistry in Hybrid Mesoporous Silica Nanoarchitectures: Controlled Delivery and Molecular Transport in Response to Chemical, Physical and Biological Stimuli. *Chem. Commun.* **2015**, *51* (28), 6050–6075.

(12) Davidson, M.; Ji, Y.; Leong, G. J.; Kovach, N. C.; Trewyn, B. G.; Richards, R. M. Hybrid Mesoporous Silica/Noble-Metal Nanoparticle Materials—Synthesis and Catalytic Applications. *ACS Appl. Nano Mater.* **2018**, *1* (9), 4386–4400.

(13) Liang, J.; Liang, Z.; Zou, R.; Zhao, Y. Heterogeneous Catalysis in Zeolites, Mesoporous Silica, and Metal–Organic Frameworks. *Adv. Mater.* **2017**, *29* (30), 1701139.

(14) Bellat, J.-P.; Bezverkhyy, I.; Weber, G.; Royer, S.; Averlant, R.; Giraudon, J.-M.; Lamonier, J.-F. Capture of Formaldehyde by Adsorption on Nanoporous Materials. *J. Hazard. Mater.* **2015**, *300*, 711–717.

(15) Awual, Md. R. Novel Nanocomposite Materials for Efficient and Selective Mercury Ions Capturing from Wastewater. *Chem. Eng. J.* **2017**, *307*, 456–465.

(16) Watermann, A.; Brieger, J. Mesoporous Silica Nanoparticles as Drug Delivery Vehicles in Cancer. *Nanomaterials* **2017**, *7* (7), 189.

(17) Maggini, L.; Cabrera, I.; Ruiz-Carretero, A.; Prasetyanto, E. A.; Robinet, E.; Cola, L. D. Breakable Mesoporous Silica Nanoparticles for Targeted Drug Delivery. *Nanoscale* **2016**, *8* (13), 7240–7247.

(18) Vallet-Regí, M.; Colilla, M.; Izquierdo-Barba, I.; Manzano, M. Mesoporous Silica Nanoparticles for Drug Delivery: Current Insights. *Molecules* **2018**, *23* (1), 47.

(19) Beck, J. S.; Vartuli, J. C.; Roth, W. J.; Leonowicz, M. E.; Kresge, C. T.; Schmitt, K. D.; Chu, C. T. W.; Olson, D. H.; Sheppard, E. W.; McCullen, S. B.; Higgins, J. B.; Schlenker, J. L. A new family of mesoporous molecular sieves prepared with liquid crystal templates

(20) Kresge, C. T.; Roth, W. J. The Discovery of Mesoporous Molecular Sieves from the Twenty Year Perspective. *Chem. Soc. Rev.* **2013**, *42* (9), 3663–3670.

(21) Kresge, C. T.; Leonowicz, M. E.; Roth, W. J.; Vartuli, J. C.; Beck, J. S. Ordered Mesoporous Molecular Sieves Synthesized by a Liquid-Crystal Template Mechanism. *Nature* **1992**, *359* (6397), 710–712.

(22) Grün, M.; Lauer, I.; Unger, K. K. The Synthesis of Micrometer- and Submicrometer-Size Spheres of Ordered Mesoporous Oxide MCM-41. *Adv. Mater.* **1997**, *9* (3), 254–257.

(23) Cai, Q.; Lin, W.-Y.; Xiao, F.-S.; Pang, W.-Q.; Chen, X.-H.; Zou, B.-S. The Preparation of Highly Ordered MCM-41 with Extremely Low Surfactant Concentration. *Microporous Mesoporous Mater.* **1999**, *32* (1), 1–15.

(24) Cai, Q.; Luo, Z.-S.; Pang, W.-Q.; Fan, Y.-W.; Chen, X.-H.; Cui, F.-Z. Dilute Solution Routes to Various Controllable Morphologies of MCM-41 Silica with a Basic Medium. *Chem. Mater.* **2001**, *13* (2), 258–263.

(25) Manzano, M.; Aina, V.; Areán, C. O.; Balas, F.; Cauda, V.; Colilla, M.; Delgado, M. R.; Vallet-Regí, M. Studies on MCM-41 Mesoporous Silica for Drug Delivery: Effect of Particle Morphology and Amine Functionalization. *Chem. Eng. J.* **2008**, *137* (1), 30–37.

(26) Kumar, D.; Schumacher, K.; du Fresne von Hohenesche, C.; Grün, M.; Unger, K. K. MCM-41, MCM-48 and Related Mesoporous Adsorbents: Their Synthesis and Characterisation. *Colloids Surf. Physicochem. Eng. Asp.* **2001**, *187–188*, 109–116.

(27) Lombardo, D.; Kiselev, M. A.; Magazù, S.; Calandra, P. Amphiphiles Self-Assembly: Basic Concepts and Future Perspectives of Supramolecular Approaches https://www.hindawi.com/journals/acmp/2015/151683/ (accessed 2020 -12 -26).

(28) Vartuli, J. C.; Schmitt, K. D.; Kresge, C. T.; Roth, W. J.; Leonowicz, M. E.; McCullen, S. B.; Hellring, S. D.; Beck, J. S.; Schlenker, J. L. Effect of Surfactant/Silica Molar Ratios on the Formation of Mesoporous Molecular Sieves: Inorganic Mimicry of Surfactant Liquid-Crystal Phases and Mechanistic Implications. *Chem. Mater.* **1994**, *6* (12), 2317–2326.

(29) Yasmin, T.; Müller, K. Synthesis and Surface Modification of Mesoporous Mcm-41 Silica Materials. *J. Chromatogr. A* **2010**, *1217* (20), 3362–3374.

(30) Martins, L.; Cardoso, D. Influence of Surfactant Chain Length on Basic Catalytic Properties of Si-MCM-41. *Microporous Mesoporous Mater.* **2007**, *106* (1), 8–16.

(31) Jana, S. K.; Nishida, R.; Shindo, K.; Kugita, T.; Namba, S. Pore Size Control of Mesoporous Molecular Sieves Using Different Organic Auxiliary Chemicals. *Microporous Mesoporous Mater.* **2004**, *68* (1), 133–142.

(32) Wang, X.; Zhang, Y.; Luo, W.; Elzatahry, A. A.; Cheng, X.; Alghamdi, A.; Abdullah, A. M.; Deng, Y.; Zhao, D. Synthesis of Ordered Mesoporous Silica with Tunable Morphologies and Pore Sizes via a Nonpolar Solvent-Assisted Stöber Method. *Chem. Mater.* **2016**, *28* (7), 2356–2362.

(33) Du, X.; He, J. Fine-Tuning of Silica Nanosphere Structure by Simple Regulation of the Volume Ratio of Cosolvents. *Langmuir* **2010**, *26* (12), 10057–10062.

(34) Wu, L.; Jiao, Z.; Wu, M.; Song, T.; Zhang, H. Formation of Mesoporous Silica Nanoparticles with Tunable Pore Structure as Promising Nanoreactor and Drug Delivery Vehicle. *RSC Adv.* **2016**, *6* (16), 13303–13311.

(35) Wang, J.-G.; Zhou, H.-J.; Sun, P.-C.; Ding, D.-T.; Chen, T.-H. Hollow Carved Single-Crystal Mesoporous Silica Templated by Mesomorphous Polyelectrolyte−Surfactant Complexes. *Chem. Mater.* **2010**, *22* (13), 3829–3831.

(36) Liu, J.-Y.; Wang, J.-G.; Li, N.; Zhao, H.; Zhou, H.-J.; Sun, P.-C.; Chen, T.-H. Polyelectrolyte–Surfactant Complex as a Template for the Synthesis of Zeolites with Intracrystalline Mesopores. *Langmuir* **2012**, *28* (23), 8600–8607.

(37) Zhang, K.; Xu, L.-L.; Jiang, J.-G.; Calin, N.; Lam, K.-F.; Zhang, S.-J.; Wu, H.-H.; Wu, G.-D.; Albela, B.; Bonneviot, L. Facile Large-Scale Synthesis of Monodisperse Mesoporous Silica Nanospheres with Tunable Pore Structure. *J. Am. Chem. Soc.* **2013**, *135* (7), 2427–2430.

(38) Perton, F.; Harlepp, S.; Follain, G.; Parkhomenko, K.; Goetz, J. G.; Bégin-Colin, S.; Mertz, D. Wrapped Stellate Silica Nanocomposites as Biocompatible Luminescent Nanoplatforms Assessed in Vivo. *J. Colloid Interface Sci.* **2019**, *542*, 469–482.

(39) Duenas-Ramirez, P.; Bertagnolli, C.; Müller, R.; Sartori, K.; Boos, A.; Elhabiri, M.; Bégin-Colin, S.; Mertz, D. Highly Chelating Stellate Mesoporous Silica Nanoparticles for Specific Iron Removal from Biological Media. *J. Colloid Interface Sci.* **2020**, *579*, 140–151.

(40) Perton, F.; Tasso, M.; Muñoz Medina, G. A.; Ménard, M.; Blanco-Andujar, C.; Portiansky, E.; van Raap, M. B. F.; Bégin, D.; Meyer, F.; Begin-Colin, S.; Mertz, D. Fluorescent and Magnetic Stellate Mesoporous Silica for Bimodal Imaging and Magnetic Hyperthermia. *Appl. Mater. Today* **2019**, *16*, 301–314.

(41) Orives, J. R.; Pichon, B. P.; Mertz, D.; Sartori, K.; Begin-Colin, S.; Viali, W. R.; Lima Ribeiro, S. J.; Nalin, M. Phosphate Glasses Containing Monodisperse Fe3−δO4@SiO2 Stellate Nanoparticles Obtained by Melt-Quenching Process. *Ceram. Int.* **2020**, *46* (8, Part B), 12120–12127.

(42) Cotin, G.; Perton, F.; Petit, C.; Sall, S.; Kiefer, C.; Begin, V.; Pichon, B.; Lefevre, C.; Mertz, D.; Greneche, J.-M.; Begin-Colin, S. Harnessing Composition of Iron Oxide Nanoparticle: Impact of Solvent-Mediated Ligand–Ligand Interaction and Competition between Oxidation and Growth Kinetics. *Chem. Mater.* **2020**, *32* (21), 9245–9259.

(43) Cotin, G.; Kiefer, C.; Perton, F.; Ihiawakrim, D.; Blanco-Andujar, C.; Moldovan, S.; Lefevre, C.; Ersen, O.; Pichon, B.; Mertz, D.; Bégin-Colin, S. Unravelling the Thermal Decomposition Parameters for The Synthesis of Anisotropic Iron Oxide Nanoparticles. *Nanomaterials* **2018**, *8* (11), 881.

(44) Perigo, E. A.; Hemery, G.; Sandre, O.; Ortega, D.; Garaio, E.; Plazaola, F.; Teran, F. J. Fundamentals and Advances in Magnetic Hyperthermia. *Appl. Phys. Rev.* **2015**, *2* (4), 041302.
(45) De Lange, M. F.; Vlugt, T. J. H.; Gascon, J.; Kapteijn, F. Adsorptive Characterization of Porous Solids: Error Analysis Guides the Way. *Microporous Mesoporous Mater.* **2014**, *200*, 199–215.
(46) Blanco-Andujar, C.; Walter, A.; Cotin, G.; Bordeianu, C.; Mertz, D.; Felder-Flesch, D.; Begin-Colin, S. Design of Iron Oxide-Based Nanoparticles for MRI and Magnetic Hyperthermia. *Nanomed.* **2016**, *11* (14), 1889–1910.
(47) Mertz, D.; Sandre, O.; Bégin-Colin, S. Drug Releasing Nanoplatforms Activated by Alternating Magnetic Fields. *Biochim. Biophys. Acta BBA - Gen. Subj.* **2017**, *1861* (6), 1617–1641.
(48) Walter, A.; Billotey, C.; Garofalo, A.; Ulhaq-Bouillet, C.; Lefèvre, C.; Taleb, J.; Laurent, S.; Vander Elst, L.; Muller, R. N.; Lartigue, L. Mastering the Shape and Composition of Dendronized Iron Oxide Nanoparticles to Tailor Magnetic Resonance Imaging and Hyperthermia. *Chem. Mater.* **2014**, *26* (18), 5252–5264.
(49) Tao, C.; Zhu, Y.; Li, X.; Hanagata, N. Magnetic Mesoporous Silica Nanoparticles for CpG Delivery to Enhance Cytokine Induction via Toll-like Receptor 9. *RSC Adv.* **2014**, *4* (86), 45823–45830.
(50) Tao, C.; Zhu, Y. Magnetic Mesoporous Silica Nanoparticles for Potential Delivery of Chemotherapeutic Drugs and Hyperthermia. *Dalton Trans.* **2014**, *43* (41), 15482–15490.
(51) Laurent, S.; Dutz, S.; Häfeli, U. O.; Mahmoudi, M. Magnetic Fluid Hyperthermia: Focus on Superparamagnetic Iron Oxide Nanoparticles. *Adv. Colloid Interface Sci.* **2011**, *166* (1–2), 8–23.
(52) Ménard, M.; Meyer, F.; Affolter-Zbaraszczuk, C.; Rabineau, M.; Adam, A.; Ramirez, P. D.; Bégin-Colin, S.; Mertz, D. Design of Hybrid Protein-Coated Magnetic Core-Mesoporous Silica Shell Nanocomposites for MRI and Drug Release Assessed in a 3D Tumor Cell Model. *Nanotechnology* **2019**, *30* (17), 174001.
(53) Wang, Y.; Gu, H. Core–Shell-Type Magnetic Mesoporous Silica Nanocomposites for Bioimaging and Therapeutic Agent Delivery. *Adv. Mater.* **2015**, *27* (3), 576–585.
(54) Ferjaoui, Z.; Jamal Al Dine, E.; Kulmukhamedova, A.; Bezdetnaya, L.; Soon Chang, C.; Schneider, R.; Mutelet, F.; Mertz, D.; Begin-Colin, S.; Quilès, F.; Gaffet, E.; Alem, H. Doxorubicin-Loaded Thermoresponsive Superparamagnetic Nanocarriers for Controlled Drug Delivery and Magnetic Hyperthermia Applications. *ACS Appl. Mater. Interfaces* **2019**, *11* (34), 30610–30620.
(55) Kesse, X.; Adam, A.; Begin-Colin, S.; Mertz, D.; Larquet, E.; Gacoin, T.; Maurin, I.; Vichery, C.; Nedelec, J.-M. Elaboration of Superparamagnetic and Bioactive Multicore–Shell Nanoparticles (γ-Fe2O3@SiO2-CaO): A Promising Material for Bone Cancer Treatment. *ACS Appl. Mater. Interfaces* **2020**, *12* (42), 47820–47830.
(56) Cazares-Cortes, E.; Cabana-Montenegro, S.; Boitard, C.; Nehling, E.; Griffete, N.; Fresnais, J.; Wilhelm, C.; Abou-Hassan, A.; Ménager, C. Recent Insights in Magnetic Hyperthermia: From the "Hot-Spot" Effect for Local Delivery to Combined Magneto-Photo-Thermia Using Magneto-Plasmonic Hybrids. *Adv. Drug Deliv. Rev.* **2019**, *138*, 233–246.
(57) Meneses-Brassea, B. P.; Cyr, C. M.; Martinez, I.; Botez, C. E.; El-Gendy, A. A. Facile Synthesis of Superparamagnetic Fe3O4 Nanoparticles at Therapeutic Temperature Range for Magnetic Hyperthermia Therapy. *J. Nanoparticle Res.* **2020**, *22* (11), 348.
(58) Pourmiri, S.; Tzitzios, V.; Hadjipanayis, G. C.; Meneses Brassea, B. P.; El-Gendy, A. A. Magnetic Properties and Hyperthermia Behavior of Iron Oxide Nanoparticle Clusters. *AIP Adv.* **2019**, *9* (12), 125033.
(59) Salem, N. F. A.; Abouelkheir, S. S.; Yousif, A. M.; Meneses-Brassea, B. P.; Sabry, S. A.; Ghozlan, H. A.; El-Gendy, A. A. Large Scale Production of Superparamagnetic Iron Oxide Nanoparticles by the Haloarchaeon Halobiforma Sp. N1 and Their Potential in Localized Hyperthermia Cancer Therapy. *Nanotechnology* **2020**, *32* (9), 09LT01.
(60) Cotin, G.; Perton, F.; Petit, C.; Sall, S.; Kiefer, C.; Begin, V.; Pichon, B.; Lefevre, C.; Mertz, D.; Greneche, J.-M.; Begin-Colin, S. Harnessing Composition of Iron Oxide Nanoparticle: Impact of Solvent-Mediated Ligand–Ligand Interaction and Competition between Oxidation and Growth Kinetics. *Chem. Mater.* **2020**, *32* (21), 9245–9259.
(61) Ding, H. L.; Zhang, Y. X.; Wang, S.; Xu, J. M.; Xu, S. C.; Li, G. H. Fe3O4@SiO2 Core/Shell Nanoparticles: The Silica Coating Regulations with a Single Core for Different Core Sizes and Shell Thicknesses. *Chem. Mater.* **2012**, *24* (23), 4572–4580.
(62) Kim, J.; Kim, H. S.; Lee, N.; Kim, T.; Kim, H.; Yu, T.; Song, I. C.; Moon, W. K.; Hyeon, T. Multifunctional Uniform Nanoparticles Composed of a Magnetite Nanocrystal Core and a Mesoporous Silica Shell for Magnetic Resonance and Fluorescence Imaging and for Drug Delivery. *Angew. Chem.* **2008**, *120* (44), 8566–8569.
(63) Pal, N.; Lee, J.-H.; Cho, E.-B. Recent Trends in Morphology-Controlled Synthesis and Application of Mesoporous Silica Nanoparticles. *Nanomaterials* **2020**, *10* (11), 2122.

(64) Ye, F.; Laurent, S.; Fornara, A.; Astolfi, L.; Qin, J.; Roch, A.; Martini, A.; Toprak, M. S.; Muller, R. N.; Muhammed, M. Uniform Mesoporous Silica Coated Iron Oxide Nanoparticles as a Highly Efficient, Nontoxic MRI T2 Contrast Agent with Tunable Proton Relaxivities. *Contrast Media Mol. Imaging* **2012**, *7* (5), 460–468.

(65) Gamboa, C.; Rios, H.; Sepulveda, L. Effect of the Nature of Counterions on the Sphere-to-Rod Transition in Cetyltrimethylammonium Micelles. *J. Phys. Chem.* **1989**, *93* (14), 5540–5543.

(66) Bartet, D.; Gamboa, C.; Sepulveda, L. Association of Anions to Cationic Micelles. *J. Phys. Chem.* **1980**, *84* (3), 272–275.

(67) Han, L.; Wei, H.; Tu, B.; Zhao, D. A Facile One-Pot Synthesis of Uniform Core–Shell Silver Nanoparticle@mesoporous Silica Nanospheres. *Chem. Commun.* **2011**, *47* (30), 8536–8538.

(68) Ménard, M. Synthèse de Nanoparticules Hybrides de Type Coeur-Coquille à Visées Théranostiques. These de doctorat, Strasbourg, 2017.

(69) Zhu, Y.; Tao, C. DNA-Capped Fe3O4/SiO2 Magnetic Mesoporous Silica Nanoparticles for Potential Controlled Drug Release and Hyperthermia. *RSC Adv.* **2015**, *5* (29), 22365–22372.

(70) Majeed, J.; Pradhan, L.; Ningthoujam, R. S.; Vatsa, R. K.; Bahadur, D.; Tyagi, A. K. Enhanced Specific Absorption Rate in Silanol Functionalized Fe3O4 Core–Shell Nanoparticles: Study of Fe Leaching in Fe3O4 and Hyperthermia in L929 and HeLa Cells. *Colloids Surf. B Biointerfaces* **2014**, *122*, 396–403.

(71) Erdoğdu, F.; Uyar, R.; Palazoğlu, T. K. Experimental Comparison of Natural Convection and Conduction Heat Transfer. *J. Food Process Eng.* **2010**, *33* (s1), 85–100.

(72) Brites, C. D. S.; Lima, P. P.; Silva, N. J. O.; Millán, A.; Amaral, V. S.; Palacio, F.; Carlos, L. D. Thermometry at the Nanoscale. *Nanoscale* **2012**, *4* (16), 4799.

(73) Wang, X.-Y.; Mertz, D.; Blanco-Andujar, C.; Bora, A.; Ménard, M.; Meyer, F.; Giraudeau, C.; Bégin-Colin, S. Optimizing the Silanization of Thermally-Decomposed Iron Oxide Nanoparticles for Efficient Aqueous Phase Transfer and MRI Applications. *RSC Adv.* **2016**, *6* (96), 93784–93793.

Chapter III

Core-shell IO@STMS for combined photothermal therapy and drug delivery

Chapter III. Core-shell IO@STMS for combined photothermal therapy and drug delivery

Context

In the previous chapter, we showed that our iron oxide@mesoporous silica core-shell NPs have a great potential to combine MRI imaging and magnetothermal treatment. We showed that such properties could be modulated, only by modifying the silica shell structure (thickness, pore morphology). Iron oxide-based nanomaterials have already been reported for their use in magnetic hyperthermia treatment of cancer. The better example of this application is the clinical approval of Nanotherm® formulation from MagForce® company to be used in cancer therapy (see Chapter 1). However, aside the development of IO NPs for magnetic hyperthermia, other appealing applications of remotely activated IO NPs emerged very recently. Indeed, IO NPs have also a very good potential for photothermal therapy (PTT) because releasing heat when exposed to near-infrared (NIR) laser.

In this chapter, this photothermal effect, scarcely exploited in the literature, was investigated for our core-shell NPs with the goal to have a system able to trigger the death of cancerous cells. Moreover we coupled this feature of the IO core with the high surface area of the stellate mesoporous silica (STMS) shell to load a model antitumor drug (doxorubicin) resulting in a nanoplatform combining dual therapy modes: NIR-induced photothermia and drug delivery. In this work, the photothermal properties of these core shell NPs are for the first time evaluated in detail. Moreover, key parameters for the drug loading and delivery, such as the buffer pH and/or the surface chemistry were found as crucial parameters and were studied in-depth. This study, which is discussed in the first section of this chapter (III.1), is the object of a publication in the journal *Colloids and Surfaces A: Physicochemical and Engineering Aspects* entitled "**Core-shell iron oxide@stellate mesoporous silica for combined near- infrared photothermia and drug delivery: influence of pH and surface chemistry**".

Thereafter, in a second section, preliminary results of biological studies made on *in vitro* and zebra fish *in vivo* models with such drug loaded IO@STMS NPs are presented (III.2). This work is conducted in collaboration with Dr. Sébastien Harlepp and Dr. Jacky Goetz from the INSERM U1109 and University of Strasbourg.

III.1. Core-shell iron oxide@stellate mesoporous silica for combined near- infrared photothermia and drug delivery: influence of pH and surface chemistry

Alexandre Adam[1], Sébastien Harlepp[2,3,4,5], Fiorela Ghilini[6], Geoffrey Cotin[1], Barbara Freis[1], Jacky Goetz[2,3,4,5], Sylvie Bégin[1], Mariana Tasso [6], Damien Mertz[1,*]

[1]Institut de Physique et Chimie des Matériaux de Strasbourg (IPCMS), UMR-7504 CNRS-Université de Strasbourg, 23 rue du Lœss, BP 34 67034, Strasbourg Cedex 2, France.

[2]INSERM UMR_S1109, Tumor Biomechanics, Strasbourg, F-67000, France.

[3]Université de Strasbourg, Strasbourg, F-67000, France.

[4]Fédération de Médecine Translationnelle de Strasbourg (FMTS), Strasbourg, F-67000, France.

[5]Equipe Labellisée Ligue Contre le Cancer.

[6]Instituto de Investigaciones Fisicoquímicas Teóricas y Aplicadas (INIFTA), Departamento de Química, Facultad de Ciencias Exactas, Universidad Nacional de La Plata - CONICET, Diagonal 113 y 64, 1900 La Plata, Argentina.

ABSTRACT. The chemical design of smart nanocarriers, providing in one nanoformulation combined anticancer therapies, still remains a challenge in the field of nanomedicine. Among nanomaterials, iron oxide-based core-shell nanostructures have been already studied for their intrinsic magnetic hyperthermia features that may be coupled with drug delivery. However, despite the great interest today for photo-induced hyperthermia, very few studies investigated the potential of such nanocarriers to combine photothermia and drug delivery. In this work, our aim was to design functional iron oxide@stellate mesoporous silica nanoparticles (denoted IO@STMS NPs) loaded with a drug and able to combine in a same formulation near-infrared (NIR) light induced photothermia with antitumor drug release. Herein, the NIR photothermal properties (SAR, specific absorption rates) of such nanomaterials were quantified for the first time as a function of the laser power and the NP amount. Aside the response to NIR light, the conditions to obtain very high drug loading (drug payloads up to 91 wt%) of the model antitumor drug doxorubicin (DOX) were optimized by varying different parameters, such as the NP surface chemistry (BARE (Si-OH), aminopropylsilane (APTES) and isobutyramide (IBAM)) and the pH of the drug impregnation aqueous solution. The drug release study of these core-shell systems in the presence or absence of NIR light demonstrated that the DOX release efficiency is mainly influenced by two parameters: surface chemistry (BARE ≥ IBAM ≥ APTES) and pH (pH 5.5 ≥ pH 6.5 ≥ pH 7.5). Furthermore, the temperature profiles under NIR light are found similar and independent from the pH range, the surface chemistry and the cycle number. Hence, the combination

of local photothermia with lysosomal-like pH induced drug delivery (up to 40% release of the loaded drug) with these nanostructures could open the way towards new drug delivery nanoplatforms for nanomedicine applications.

Graphical Abstract.

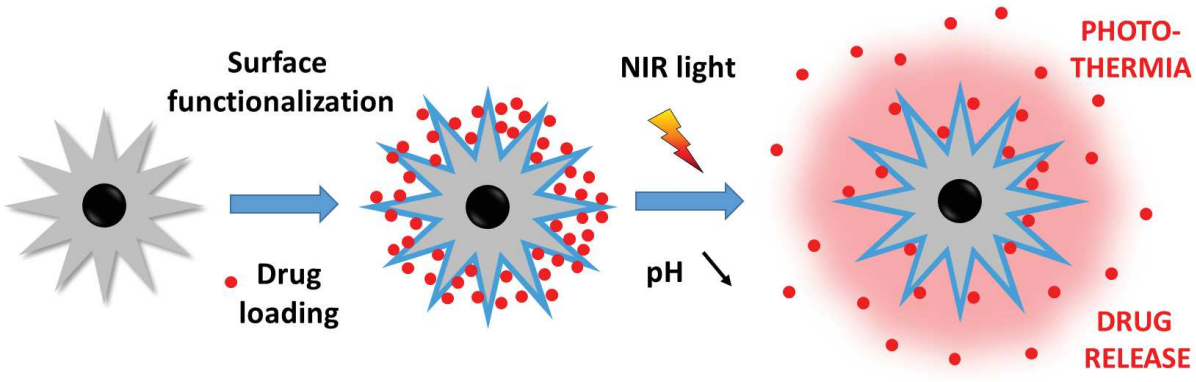

III.1.1. Introduction

Today, the use of smart or functional nanoparticles for the treatment of many diseases such as cancer has become a true medical challenge in the field of nanomedecine.[1,2] Such multifunctional nanoparticles, endowed with multiple imaging, targeting or therapy functionalities, are crucial for developing a personalized medicine, avoiding potential side effects and allowing enhanced therapeutic activity.[3–5] Among various existing reported nanosystems, iron oxide nanoparticles (IO NPs) are particularly appealing systems given their magnetic properties, low toxicity and biodegradability.[6,7] IO NPs have been mainly used in imaging and disease treatment given their magnetic properties. Indeed, they have been used as T_2 contrast agents for MRI,[8–10] they are known to have a limited toxicity and to be degraded within cells, being then less toxic to the organism as compared to other magnetic nanomaterials.[6,11,12] For instance, these external fields-responsive IO NPs show great promise as new theranostics for localized and remotely activated magnetic hyperthermia therapy[13–16] which may be followed with MRI. Upon alternative magnetic field application, they produce a local heat which is used for tumor treatment by magnetic field induced hyperthermia. This effect is already used in many preclinical studies and in the clinics,[17–19] with the example of MagForce in Berlin (Germany) where this effect is shown to promote cancer cell apoptosis.

Besides the magnetic field, another external field of interest is near-infrared (NIR) light laser applications. Indeed, due to its simplicity and low cost, NIR light can be easily applied through a range of lasers with tunable power and wavelength. As compared to visible light, NIR light has a better tissue penetration in the 800 – 1300 nm range, reaching up to 3 cm.[20,21] NIR laser-induced hyperthermia is actually developed as a minimally invasive treatment where photothermal organic or inorganic sensitizers turn this absorbed light into localized heating at the nanoparticle scale.[22–26] For instance, the company Nanospectra Biosciences (USA) has clinically developed photothermal ablation based on gold@silica core shell nanoparticles for the treatment of prostate cancer and the non-toxicity of their gold and silica NPs was demonstrated.[27] As an alternative to gold nanoparticles, IO NPs have been recently shown to be attractive NIR light mediators and to have a great potential for photothermal treatment.[28–31] Recent studies demonstrated that NIR laser powers between 0.5 and 1 $W.cm^{-2}$ combined with IO NPs are beneficial for in vitro phototherapy.

In addition to these hyperthermia treatments, the localized release of drugs remotely stimulated by external fields is currently a great challenge. The design, in recent years, of organic, polymeric[32–35] or porous silica shells[36–38] around such iron oxide cores to control the magnetothermal response and to form a reservoir of drugs that can be delivered through these external fields to the target site paved the way towards very high achievements in the field of activated therapy and drug delivery.[39–43] Especially, with regards to the use of these NPs in a physiological medium, the NPs must be functionalized with appropriate surface ligands or shells to ensure colloidal stability, biocompatibility and drug loading and release. To address these latter problems, mesoporous silica (MS) as a shell coating is particularly

attractive. Indeed, MS are stable, easily chemically modifiable and have a high drug release capacity thanks to their large pore volume.[36,44–47] Moreover, given the possibility to render them stimuli responsive, especially for drug release, they are particularly suited for the treatment of various diseases.[48–50] In our team, we have developed in-depth expertise in the synthesis of a range of MS nanostructures with well-controlled pore sizes (from 2.5 to 15 nm).[51–54] Recently we showed that the pore morphology of MS alone or as layers covering IO NPs can be easily oriented with the sol-gel reaction temperature either towards stellar (ST) (large radial pores of about 10 nm) for $T \leq 80$ °C or "worm-like" (WL) morphologies (channels with random pores of 3–4 nm pore size) for $T \geq 80$ °C.[54] The relaxometric (for MRI) and magnetothermal (SAR) characteristics of both core-shell NPs having respectively stellar or WL-type morphologies, were shown to be perfectly suited for MRI and magnetic hyperthermia applications. However, at this stage, their photoresponsive behavior, especially when they are loaded with drugs, has never been investigated.

Herein, we address for the first time the use of iron oxide core@stellate large pore mesoporous silica (denoted IO@STMS) for combined photothermal and drug release properties **(Figure 1**). ST morphology has been chosen as their large pores promote the drug loading and improve heat dissipation from the central core to the surrounding medium. First, the photothermal properties of these core-shell NPs upon NIR light excitation were investigated by tracing temperature profiles and evaluating their specific absorption rates (SAR) in non-adiabatic conditions as a function of the laser power and the NPs' concentration. Secondly, the effect of key parameters, such as the pH of the drug impregnation aqueous solution, the surface chemistry or the presence of an iron oxide core (STMS vs. IO@STMS) on the drug loading capacity were unraveled. With the aim to cover the drug loaded core-shell NPs with a biocompatible layer, the adsorption of human serum albumin (HSA) onto this system was further studied in terms of NP-bound protein amount, and drug leaking after washings with buffers and after storage at 4 °C. The drug release of IO@STMS@DOX@HSA core-shell systems with a high drug loading (DLC $\geq 20\%$) was then evaluated as a function of the pH (pH = 5.5, 6.5, 7.5) and of the surface chemistry. A very classical way to improve drug loading/release on silica nanoparticles as compared to the BARE surface is the modification by aminosilane and particularly APTES[53,55,56] which is tested here with IO@STMS. In a more original way, the amine groups are then modified into isobutyramide (IBAM) functions which are known to favor immobilization of biomacromolecules like proteins.[57,58] The suitability of these three functions to load and release DOX is studied. Cumulative drug release values were obtained after several daily cycles in the presence or absence of NIR light. Furthermore, the temperature profiles resulting from the application of the NIR light were plotted as a function of the pH, the surface chemistry or the cycle number to demonstrate the possibility of activating phototherapy at each cycle whatever the conditions.

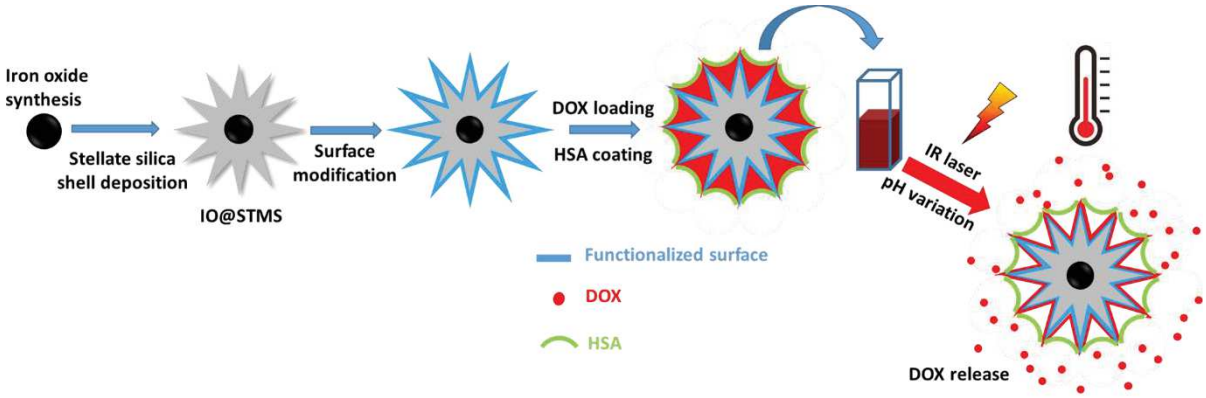

Figure 3-1. Schematic representation depicting the step-by-step preparation of drug loaded core-shell nanocomposites and the combined properties of NIR light-induced photothermia and pH-triggered drug release.

III.1.2. Experimental section

III.1.2.1 Chemicals

Tetraethyl orthosilicate (TEOS, ≥99.0%)), cetyltrimethylammonium tosylate (CTATos, ≥98.0%), 2-amino-2-(hydroxymethyl)-1,3-propanediol (AHMPD, ≥99.9%), ammonium nitrate (NH_4NO_3), (3-aminopropyl)triethoxysilane (APTES, 99%), isobutyryl chloride (IBC, 98%) and triethylamine (Et_3N, ≥99%) were obtained from Sigma–Aldrich (France). Nitric acid 70% (HNO_3, 70%) and N,N-Dimethylformamide (DMF, ≥99.9%) were purchased from Carlo-Erba. Ammonium hydroxide (25% in water) was obtained from Fluka. Iron(III) stearate ($FeSt_3$) was obtained from TCI. Oleic acid (99%) was purchased from Alfa Aesar while squalane (99%) was purchased from Acros Organic. Doxorubicin hydrochloride was obtained from OChem Inc. The Pierce BCA protein assay kit was from Thermo Scientific.

III.1.2.2. Synthesis protocols

Iron oxide core synthesis.

1.9 g (2 mmol) of commercial $FeSt_3$, 1.9 g (6.7 mmol) oleic acid and 20 mL squalane were mixed in a two-neck round-bottom flask and heated to 110 °C for one hour to remove water traces and dissolve the components. Then the temperature was increased to 310 °C for two hours to start the thermal decomposition of the iron precursor. The iron oxide nanoparticles finally obtained were washed several times with a mixture of hot acetone under stirring and collected thanks to a magnet. The washed iron oxide nanoparticles were then dispersed in chloroform for further use.

Synthesis of iron oxide core@stellate mesoporous silica (IO@STMS).

To synthesize the mesoporous silica shell, the iron oxide cores need to be phase-transferred into aqueous phase. Typically, 240 mg (0.53 mmol) CTATos, 27.6 mg (0.26 mmol) AHMPD and 25 mL distilled water were mixed in a 50 mL round-bottom flask. The mixture was heated up to 50 °C for 30 min to dissolve every chemical. Then, 10 mg of iron oxide nanoparticles dispersed in chloroform was

added under strong agitation and the temperature was increased to 65 °C in order to evaporate the chloroform. The mixture was let to stir at 65 °C for 30 min. Afterwards, 2 mL of TEOS was added, the temperature was increased to 70 °C and the reaction was let to stir for two hours. The reaction was stopped by cooling down the mixture and followed by centrifugation at 12,000 g for 12 min to recover the nanoparticles. The particles were washed twice with 15 mL of a mixture of distilled water and ethanol (1:1). The templating surfactant was removed by dispersing the nanoparticles in NH_4NO_3 ethanolic solution (20 mL, 20 mg.mL^{-1} in EtOH) under stirring and heating at 70 °C for one night (16 hours). Then the nanoparticles were washed once with 20 mL distilled water and twice with 20 mL absolute ethanol. The extraction efficiency was checked by zeta potential (ZP) analysis. Before extraction, the ZP is positively charged as the CTA^+ surfactant, adsorbed on the IO@STMS, governs the NP charge. During the CTA^+ surfactant extraction, the NP reverse its surface charge and the extraction is considered as completed when the ZP has reached a plateau of negative ZP values (usually between -20 and -30 mV in water at pH = 7.5, bare silica). The extraction with ammonium nitrate solution was needed to be repeated several times. Finally, the synthesized core-shell IO@MS were dispersed in ethanol and kept in the fridge at 4 °C for storage.

Synthesis of stellate mesoporous silica (STMS).

To obtain stellate mesoporous silica NPs, 3.8 g (8.3 mmol) CTATos and 0.436 g (4.15 mmol) AHMPD were dissolved in a 500 mL Erlenmeyer flask with 200 mL distilled water. The mixture was heated up to 65 °C to ensure full dissolution. Afterwards 30.2 g (32.1 mL, 145 mmol) TEOS were added under agitation. 15 min later the temperature was set to 70 °C. Two hours after TEOS addition, the reaction was stopped by cooling down the mixture to room temperature. The NPs were collected by centrifugation (13,000 g; 15 min) and calcinated in an oven at 550 °C for 6 h. Finally, the STMS NPs were crushed with a mortar and dispersed in ethanol for further use. The concentration of STMS was determined by drying a precise volume of the dispersion and weighting the powder.

APTES functionalization (IO@STMS@APTES).

10 mg of core-shell IO@STMS were dispersed in a centrifuge tube in 2.75 mL of absolute ethanol. Then 150 µL of aqueous ammonia $NH_{3(aq)}$ 25% and 625 µL of APTES were added successively. The reaction was performed at room temperature for two hours and continuously stirred on a stirring wheel at 40 rpm. The nanoparticles were then centrifuged (12,000 g, 10 min) and washed twice with 5 mL ethanol.

IBAM functionalization (IO@STMS@IBAM).

The previously synthesized IO@STMS@APTES were washed twice with DMF and centrifuged (12,000 g, 10 min). The supernatant was removed and 1.5 mL of DMF and 200 µL of Et_3N were added. The mixture was vortexed and sonicated to disperse the nanoparticles properly. Afterwards a mixture of 275 µL of IBC dissolved in 1.5 mL DMF was added to the particles' dispersion. The reaction was let to

stir on a mechanical wheel for two hours. Then, 1 mL of distilled water was added to dissolve the ammonium chloride precipitate formed during the reaction. Finally, the nanoparticles were recovered by centrifugation (12,000 g, 10 min) and washed twice with DMF.

Loading of doxorubicin (DOX).

Typically, 2.5 mg of core-shell nanoparticles, functionalized or not, i.e. IO@STMS, IO@STMS@APTES or IO@STMS@IBAM, were washed twice with an aqueous 100 mM HEPES buffer at a defined pH (5.5, 6.5 or 7.5). Then 1 mL of DOX solution at a given concentration in the same buffer was added and agitated for 24 h on a mechanical wheel at room temperature and in the dark. After loading, the supernatant was removed by centrifugation (14,000 g, 10 min) and the nanoparticles were washed twice with HEPES buffer. Every supernatant was collected and stored for analysis. The amount of DOX in the supernatant was determined by UV-Vis spectrophotometry at 480 nm. The total DOX amount on the three supernatants was determined and subtracted to the DOX amount used during loading to obtain the DOX loaded amount per mg of NP.

Immobilization of human serum albumin (HSA).

After doxorubicin impregnation, the nanoparticles were coated with HSA. For this, 2.5 mg of drug-loaded nanocomposites were dispersed in 0.625 mL of an HSA solution in 100 mM HEPES pH 7.5 at 400 µg mL^{-1}. The dispersion was stirred on a mechanical wheel for 1 h at room temperature and in the dark, then centrifuged (12,000, 12 min) and washed twice with 2 mL HEPES buffer pH 7.5.

Quantification of HSA.

The three supernatants resulting after centrifugation and washings were kept and used to quantify the unbound HSA amount by means of the bicinchoninic acid (BCA) test. The principle of this assay relies on the reduction of copper ion Cu(II) into Cu(I) by the peptide bonds in proteins. Then, BCA forms a purple complex with Cu(I) specifically. The absorbance of the solution depends on the amount of reduced Cu(II) which is proportional to the amount of proteins in solution. As for the drug, the obtained amount was then subtracted to the amount employed during HSA incubation to obtain the protein amount bound to the NP. In the BCA reaction, the supernatant (100 µL) was mixed with the BCA reagent (20 µL) in a 96 well plate and left at 45 °C during 1 h. Afterwards, the absorbance at 562 nm was read. The obtained absorbance is compared with a calibration curve to obtain the HSA concentration per well.

III.1.2.3. Characterization techniques

Dosage of iron in the core shell NPs.

The concentration of nanoparticles was determined by drying a fixed volume of the dispersion (typically 100 µL) and weighing the powder. Then, to calculate the amount of iron, the dried powder was digested with nitric acid 65 wt% in order to dissolve the iron oxide core. The sample was then diluted to get a 2 wt% HNO_3 solution. The T_1 relaxation time of the solution was measured and, thanks to a pre-established calibration curve, the amount of iron was determined.

NIR laser irradiation and DOX release.

1 mL of DOX-loaded nanocomposite suspension at 3 $mg.mL^{-1}$ in 100 mM HEPES buffer at different pHs was added into a 1 mL plastic cuvette placed in a dedicated sample holder in front of the laser output. The laser was then switched on and the sample was irradiated for 45 min; then the laser was switched off. The power of the laser was fixed at 1 $W.cm^{-2}$ and the temperature elevation of the suspension is recorded by a thermocouple. Afterwards, the sample was centrifuged (10,000 g, 10 min) in order to collect the supernatant. The concentration of released DOX was determined by UV-Vis spectrophotometry as explained above. Fresh HEPES buffer was then added, the particles were redispersed by sonication and agitation, and a new irradiation cycle of 45 min was performed. In total, each sample was irradiated four times. The effect of the pH on the release was studied by adjusting the pH at 5.5, 6.5 or 7.5.

Fourier-transform infrared spectroscopy (FTIR).

FTIR spectra were recorded for wavenumbers between 4000 and 400 cm^{-1} on a Spectrum 100 from Perkin Elmer. Few drops of the dispersion were added to dry KBr. After grinding and pellet formation, FTIR transmittance spectra were measured.

Transmission electron microscopy (TEM).

The IO@STMS and STMS NPs were deposited on carbon-coated copper grids. TEM images were acquired with a JEOL 2100 TEM instrument operating at 200 kV. The software Image J was used to determine the size distribution of the NPs.

X-ray diffraction analysis (XRD).

X-ray diffraction (XRD) patterns were recorded at room temperature with a Brucker D8 Discover diffractometer equipped with a Lynx-Eye detector in the 20-70° (2θ) range with a scan step of 0.03° and the sample rotates at 30 rpm during the measure. Silicon powder was used as an internal standard. The diffraction peaks were compared to JCPDS database.

Thermogravimetric analysis (TGA).

The thermogravimetric analysis (TGA) was performed on a STD Q600 (TA Instruments). The runs were started from room temperature to 800 °C with a heating rate of 5 °C/min, under an air flow rate of 25 mL/min.

Dynamic light scattering (DLS).

Hydrodynamic size distributions and colloidal stability of the nanoparticles at different stages (i.e. with and without HSA, with and without DOX, and after storage at 4 °C during several days or weeks) were obtained in a Malvern Nanosizer instrument operating at room temperature. Prior measurements, samples were sonicated during 15 min and redispersed in a suitable buffer. Samples were measured in Milli-Q water (pH 5), 10 mM PBS (phosphate buffer saline), pH 7.4 and in 100 mM HEPES buffer, pH 7.5. Intensity and number distributions were obtained.

III.1.3. Results and Discussion

III.1.3.1. Photothermal properties of iron oxide@stellate mesoporous silica nanoparticles

First, IO NPs playing the role of NIR light-sensitive core materials were synthesized by the thermal decomposition method according to previously reported works.[59,60] TEM images indicated the formation of homogenous spherical iron oxide NPs with a mean diameter of 28 nm diameter (**Figure 3-2 A and B**)

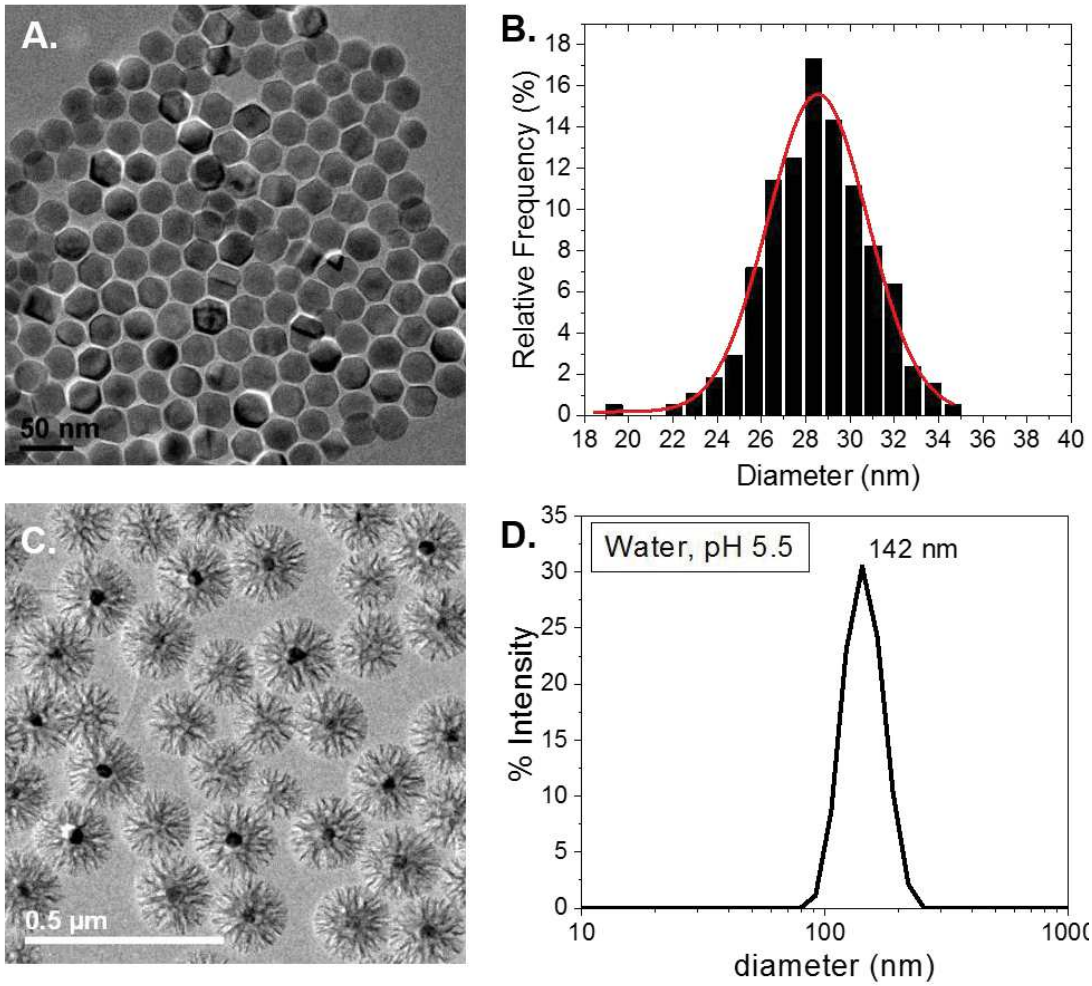

Figure 3-2. (A) TEM images and **(B)** size distribution of the synthesized IO NPs by thermal decomposition. **(C)** TEM images and **(D)** DLS in water of silica coated IO@STMS.

By analyzing the diffractogram of the synthesized iron oxide nanoparticles (**Figure 3-3.A**), the diffraction peaks corresponding to spinelle structure are clearly identified. No other crystalline structure of iron oxide is present. Some traces of NaCl are identified which is a residual salt coming from the reaction (*). Last peak identified comes from the silicon powder added as internal standard (**). After thermal decomposition reaction and following washing steps, the FTIR spectrum of the synthesized NPs is typical of iron oxide NPs coated with oleic acid (**Figure 3-3.B**). Narrow and intense bands at 2924 cm^{-1} and 2853 cm^{-1} are typical from CH_2 groups, respectively asymmetric and symmetric vibrations. They are due to the presence of oleic acid at the surface of NPs or some traces of reaction residues. The very weak band at 1706 cm^{-1} corresponds to the C=O carbonyl group of free oleic acid whereas the band at 1377 cm^{-1} is typical from the asymmetric vibration of grafted oleic acid on the NPs via a carboxylate function. 588 cm-1 band is characteristic of the Fe-O vibration. Magnetic properties of such iron oxide cores such as their paramagnetic behavior and suitable saturation magnetization values have been described in detail in previous works.[61,62]

Then, a stellate mesoporous silica (STMS) shell with controlled thickness and porosities was deposited around the iron oxide cores. CTATos was used as a porogenic surfactant yielding to stellate large pores after the sol gel reaction, as previously reported.[54,63] The surfactant was removed by extraction with ammonium nitrate in an ethanolic solution. TEM images showed the formation of individual and homogenous core shell NPs with large pore size (ca. 100 nm) (**Figure 3-2.C**) while DLS showed excellent colloidal dispersion in ethanol or aqueous buffer (**Figure 3-2.D**) as previously described.[51] Pore sizes of such STMS NPs were shown to be usually in the range of ca. 10-15 nm and specific areas in the range of 500-700 $m^2.g^{-1}$.[51,54]

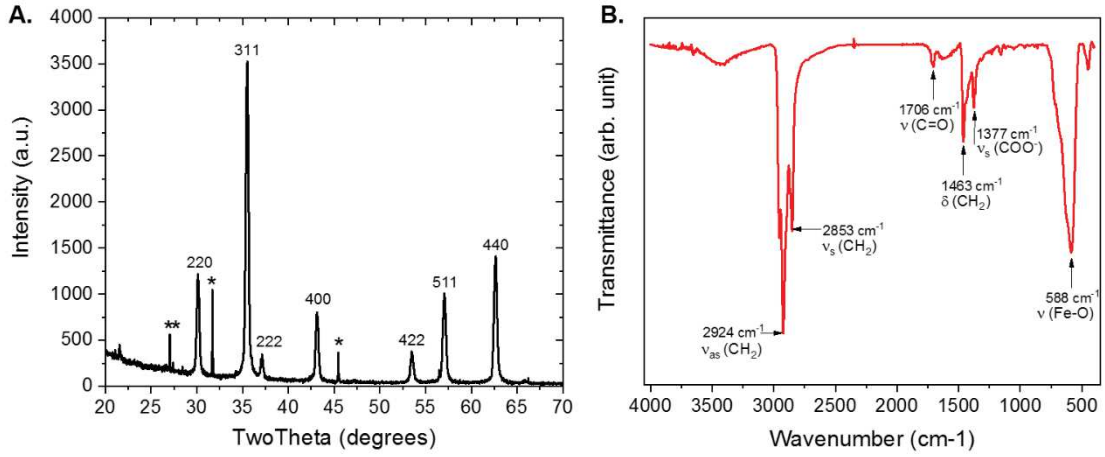

Figure 3-3. (A) X-ray diffractogram and **(B)** FTIR spectrum of IO NPs.

The photothermal properties of these core-shell NPs were evaluated by measuring the temperature elevation of aqueous dispersions when exposed to NIR light (1064 nm). This wavelength presents a good optical transparence in water and in biological tissues. Moreover, the YAG crystals, emitting at 1064 nm, are easy to process and allow to obtain high laser power which makes them frequently used in research but also in industry for their very competitive power to cost ratio. At this wavelength, it is reported that spinel phase iron oxide can absorb the radiation and, by a non-radiative decay, converts it into dissipated heat.[64] The influence of NPs concentration (**Figure 3-4.A**) and laser power (**Figure 3-4.B**) on temperature profiles was investigated. First, the data indicate that suspensions heat up quickly under irradiation by NIR light. Temperature elevations between 5 and 40 °C can be easily obtained as a function of the experimental conditions. This also indicates that it is possible to finely tune and control the amount of dissipated heat which is fundamental for medical applications where a precise temperature range has to be attained. In this non-adiabatic experimental set-up, temperature plateaus were reached rapidly after 5 to 10 min irradiation.

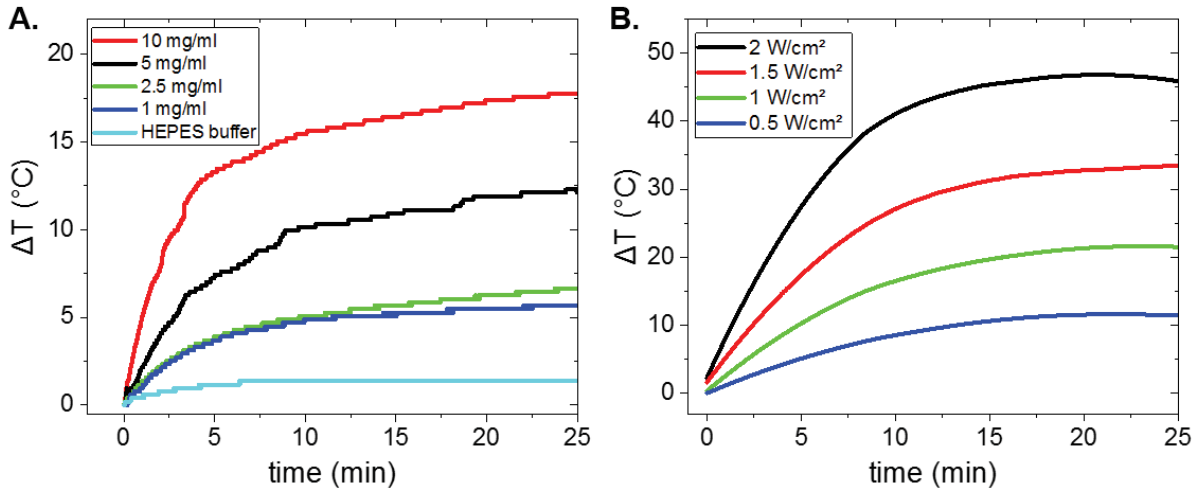

Figure 3-4. (A) Temperature elevations under NIR laser at 1 W.cm^{-2} for different NPs concentrations and **(B)** for different laser power, at a NPs concentration of 5 mg.mL^{-1}.

As an analogy to the magnetothermal transfer, the photothermal transfer can be calculated as the specific absorption rate (SAR) in watts per gram of iron oxide absorbing NIR light. This value was calculated by a calorimetric method. By plotting the temperature profiles of the NPs' suspensions subjected to NIR light and then adjusting the experimental curve with a polynomial function, the $[\mathrm{d}T/\mathrm{d}t]_{t=0,s}$ can be determined. Water and aqueous buffer solutions are almost transparent to the excitation light at 1064 nm and absorb very little the radiation. In order to perform precise calculations, the contribution of the solvent in the temperature elevation has to be removed. The calculation of the SAR is thus summed up as:

$$\mathrm{SAR} = C_s \cdot \frac{m_s}{m_{Fe}} \cdot \left(\left[\frac{dT}{dt} \right]_{t=0,s} - \left[\frac{dT}{dt} \right]_{t=0,buffer} \right)$$

where m_s and C_s are respectively the mass (g) and the heat capacity (J.g^{-1}.K^{-1}) of the sample, m_{Fe} (g) is the mass of iron oxide present in the sample, $(\mathrm{d}T/\mathrm{d}t)_{t=0,s}$ the derivative function of the temperature at $t = 0$ (K.s^{-1}) for the measured sample and $(\mathrm{d}T/\mathrm{d}t)_{t=0,\mathrm{buffer}}$ the derivative of the reference buffer.

It is worthy to note that when the NP concentration increases from 1 to 20 mg.mL^{-1} (from 0.013 to 0.26 mg[Fe_3O_4].mL^{-1} respectively), the SAR values (measured at fixed power of 1 W.cm^{-2}) decrease from 2014 to 453 W.g^{-1} (**Figure 3-5.A)**. An explanation is that at high concentrations, the penetration depth of the laser in the sample is limited due to light absorption by the dispersion.[65,66] Thus the incident light cannot be equally distributed in the whole sample, as the NPs in the front of the cuvette would absorb and scatter most of the light. This leads to a gradient of incident power in the sample and in average the NPs absorb less.[67] Furthermore, we investigated the effect of the laser power (at a fixed

concentration 5 mg.mL^{-1}) and an exponent-like growing evolution of SAR was obtained. This non-linear effect could be attributed to a better penetration of the laser beam into the sample (**Figure 3-5.B**).

Overall, it can be concluded that the NPs' concentration and the laser power influence considerably the photothermal SARs. In very recent reports, the effects of silica clustering or encapsulation around IO NPs, on the photothermal heating were investigated.[67,68] Photothermal SAR values (with laser power set at 0.3 W.cm^{-2}, at 808 nm) were shown to decrease from ca. 2000 to 200 W.g^{-1} when increasing NPs concentrations (iron concentration range of 10-150 mM) which is overall in agreement with our SAR results. These values obtained are also comparable to previously published magnetic SARs in usual conditions of frequency and fields (H = 500 G, f = 536 kHz). The SAR values obtained here with the photothermal approach are found of the same order of magnitude as the magnetothermal approach,[65] *i.e.* in the range of 1000-2000 W.g^{-1} with laser power compatible with biomedical applications (≤ 1W.cm^{-2}). For higher laser power (≥ 1 W.cm^{-2}) these SAR values can even be multiplied several times. This demonstrates the high feasibility of the iron oxide core@mesoporous silica for photothermal therapy applications.

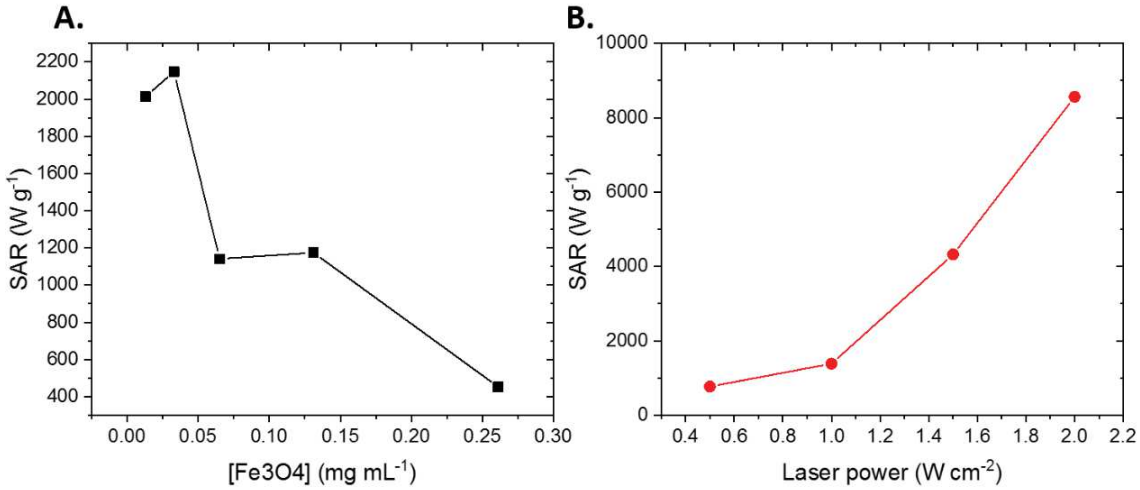

Figure 3-5. SAR values evolution (A) for different concentrations of core shell NPs and corresponding iron oxide amount and (B) for different laser powers at 5 mg mL^{-1}.

III.1.3.2. Drug loading study as a function of the pH and the surface chemistry

In this study, our aim was to produce a nanoplatform having two different antitumor effects: photothermal therapy and drug release. By modifying the surface chemistry of the IO@STMS core shell NPs, our aim was to engineer a suitable surface to i) load efficiently the IO@STMS NPs with a very high amount of antitumor drug, doxorubicin (DOX) and also ii) to ensure a suitable wrapping of the NPs with a tight serum albumin coating around the NPs to provide gate keeping (drug retention), and to afford a strategy limiting immune system clearance. This would ensure the production of a nano-object

able to perform tissue imaging (T_2 weighted-MRI due to the iron oxide core) as well as treatments by phototherapy and chemotherapy (drug delivery).

In previous works, we developed structurally equivalent functionalized mesoporous stellate silica nanoparticles without any iron oxide core.[57,69] In this section, the grafting of functional groups is compared between the stellate silica NPs with iron oxide core (IO@STMS) and without (STMS). The NPs without IO core were chosen to assess the relevance of the surface functional groups into the DOX loading capacity. They represent an alternative to the core-shell nanostructures for the assessment of these phenomena as they can be synthesized at a very large scale reproducing the same pore structures. These STMS NPs had similar size as the IO@STMS (**Figure 3-6**) but lack the IO core.

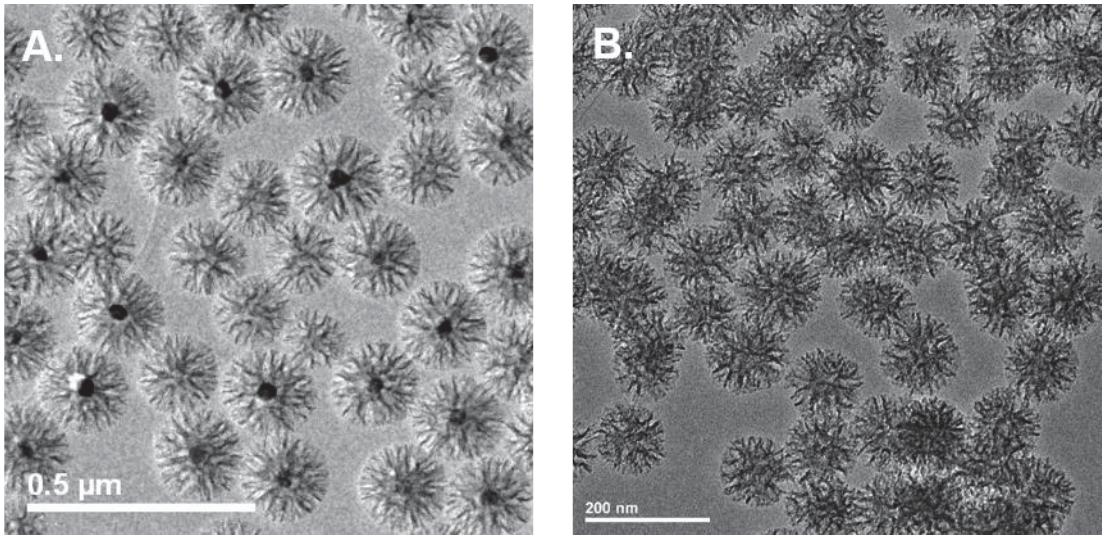

Figure 3-6. Comparison of TEM images showing the structure of **(A)** IO@STMS and **(B)** STMS.

To study the effect of the functionalization on the drug loading capacity of the NPs, the first step was to modify the BARE's surface with an aminosilane, 3-aminopropyltriethoxysilane (APTES). The reaction was performed in ethanol and catalyzed by the addition of ammonia. This leads to the APTES NPs. Then a further functionalization was carried out by reaction with isobutyrylchloride to get isobutyramide functional groups. These particles were denoted as IBAM NPs. **Figure 3-7.A** summarizes these reaction steps.

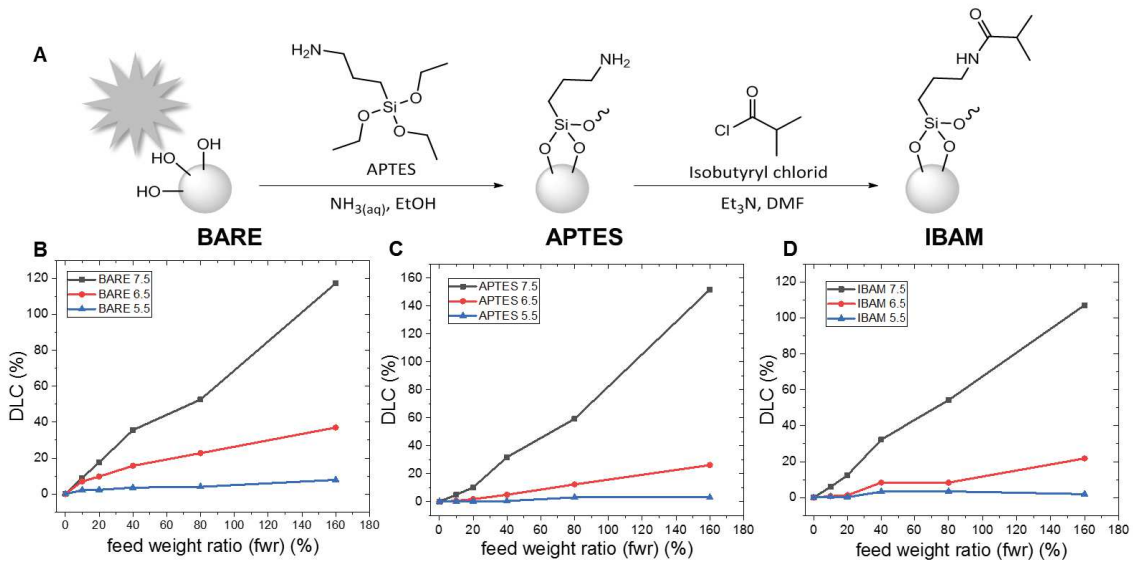

Figure 3-7. Chemical route to obtain the different surface chemistries (A) and the corresponding DLC of BARE (B), APTES (C) and IBAM (D) surfaces at the three evaluated pHs.

Once modified, we investigated the drug loading capacity (DLC) of each type of particle. The DLC is defined as the amount of DOX loaded onto and into the nanoparticle divided by the mass of NPs. Moreover, DOX is known to be sensitive to pH, in physiological aqueous solutions, especially due to the protonation of the osamine into ammonium groups (pKa_1= 8.2) (**Figure 3-8.A** for DOX chemical structure). DOX source itself is quite acidic as the soluble form of DOX used is doxorubicin hydrochloride. Thus, to ensure a good control of the loading conditions, HEPES buffer at 100 mM was used as loading dispersion medium and adjusted with HCl or NaOH to precisely set three different pH at 5.5; 6.5 or 7.5. These three pHs are known to be of biological relevance (endolysosomal vesicles, extratumoral tissues, *in vivo* blood, respectively). Here, the DLC is defined as the amount of loaded DOX, while the feed weight ratio (fwr) is used to characterize the amount of DOX given during the loading (**Figure 3-8.B**).

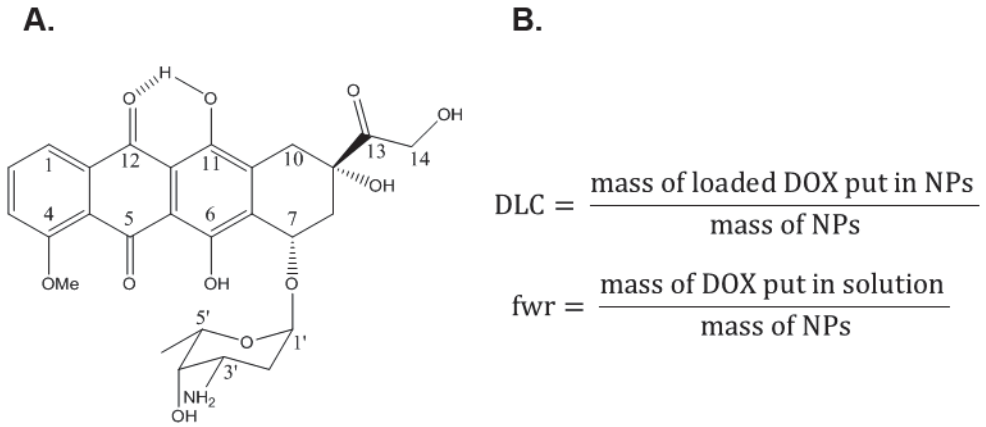

Figure 3-8. (A) Structure of DOX and **(B)** definition of DLC and fwr.

DOX payloads were thus evaluated by spectrophotometry analysis of the supernatant and using calibration curves (**Figure 3-9** for DOX calibration curves at the three pHs). The results show that for

all three surfaces, the pH of the DOX solution is a determinant factor of loading (**Figure 3-7.B-D.** for pH = 5.5; 6.5; 7.5). While for pH = 5.5, DOX shows almost no loading even at high feed weight ratios (for example on IBAM NPs, DLC = 2.0% at fwr = 160%), the DOX loading at pH = 6.5 showed slight increase of DLC (DLC = 21.8% at fwr = 160% for the same IBAM NPs) and the DOX loading considerably exploded at pH = 7.5 for the different fwr used (for example on IBAM NPs DLC = 107.1% at fwr = 160%). Thus, very high amounts of drug can be loaded on these NPs by selecting the most convenient loading buffer. By increasing the pH at 7.5 and using appropriate DOX concentrations, it is possible for these NPs to carry more than 100% of their own mass. Such high DLCs were previously obtained in our team on CNTs@MS@APTES[53] and IBAM[70] and here they are demonstrated for the first time on IO@STMS NPs. Worthy to note that such high DLCs are few reported in the literature on iron oxide@MS-based nanomaterials where usual DLCs are in the range 10-40%.[71,72]

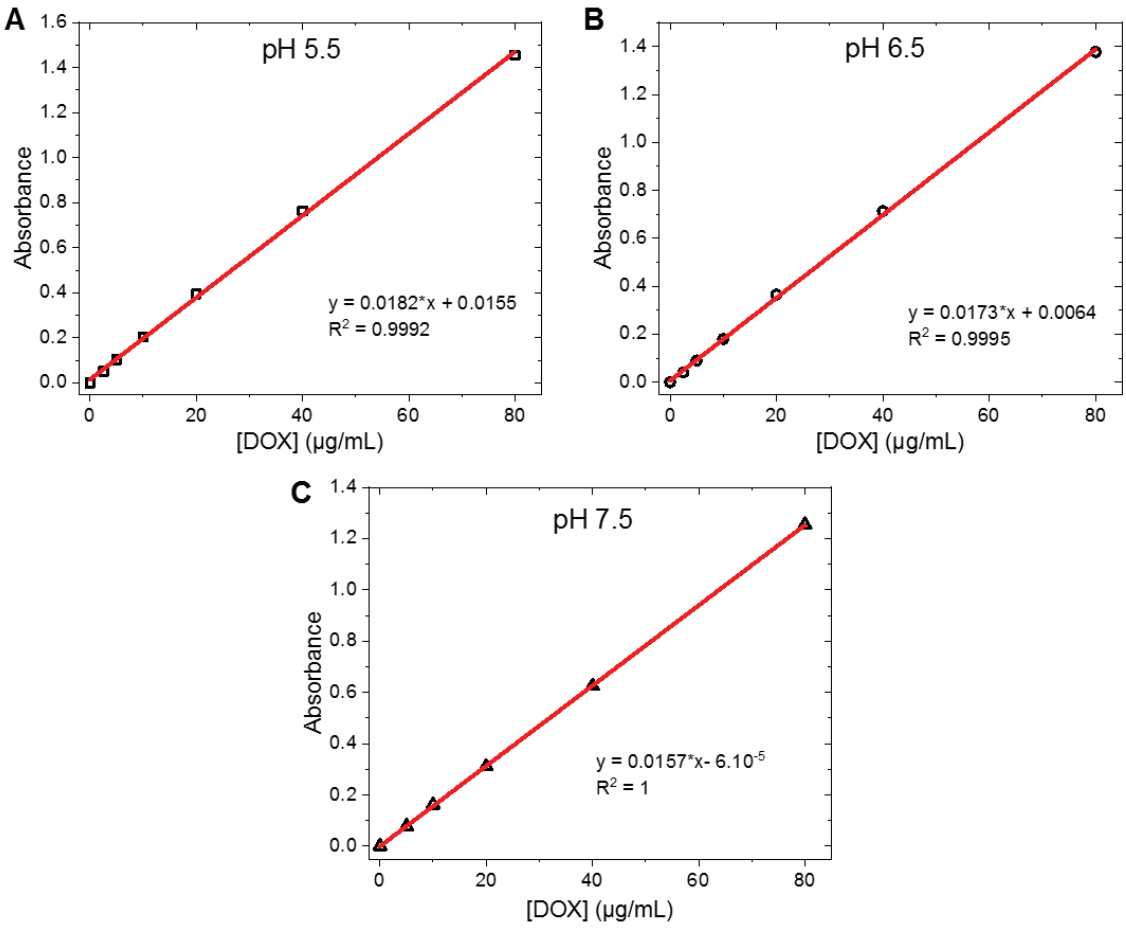

Figure 3-9. Calibration curves of the absorbance of DOX as a function of the concentration in the three buffer HEPES 100 mM at **(A)** pH 5.5, **(B)** pH 6.5 and **(C)** pH 7.5.

To explain this result, the behavior of DOX is influenced by several parameters, as the pH and the ionic strength of the medium. DOX contains two mild acid/base couples in its structure, one on the amine function of the osamine group with a pKa at 8.2 and the other one is carried by the hydroxyl group on the C11 with a pKa at 9.5. In the pH range used (5.5-7.5), it has technically one acidic proton

(NH_3^+/NH_2) group which is crucial to DOX solubility. Furthermore, in this pH range, it has been shown that DOX can auto-assemble into dimers like all anthracycline molecules but also into bigger structures, aggregates or gel which is more peculiar.[73–75] These self-assembly phenomena can be explained by the fact that when increasing the pH from 5.5 to 7.5, the proportion of neutral amine form grows, and electrostatic repulsions between DOX are decreased, limiting the fractions of individual molecules. A pH increase from 5.5 to 7.5 will thus increase the DOX self-aggregate sizes. This neutral form tends to build supramolecular polymer-like aggregates made of hundreds of units.[76] Weak interactions like dipolar interactions but especially stacking of π systems and numerous H-bonds may lead to these associations. It is thus assumed here that the very particular structure of DOX is responsible for such assembly behavior and may explain the achievements of such high DLCs.[75]

Once the behavior of the STMS NPs could be determined regarding their DOX loading capacity at different pHs and for various surface ligands, the same was carried out onto the core-shell IO@STMS. DOX was loaded in 100 mM HEPES buffer at pH = 7.5, the DLCs were calculated and compared to those obtained for NPs without an iron oxide core (**Figure 3-10**). On the BARE NPs, DLCs are relatively similar for STMS and IO@STMS from low to high fwr. However, a clear difference can be observed for the APTES and IBAM NPs: DLC on IO@STMS were half the ones obtained for STMS, especially for APTES and IBAM-functionalized NPs.

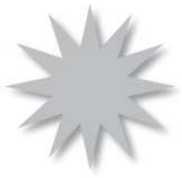

fwr %	BARE %	APTES %	IBAM %
20	17.6	10.1	12.4
80	52.5	59.2	54.2
160	117.3	151.7	107.1

fwr %	BARE %	APTES %	IBAM %
20	18.3	5.95	6.94
80	55.2	23.9	25.0
160	91.1	64.0	73.4

Figure 3-10. DLCs obtained for the three surfaces at pH 7.5 for STMS (left) and IO@STMS (right) NPs at various fwr.

To explain these differences, TGA was performed on STMS and IO@STMS and results indicate a better grafting of APTES on IO@STMS (18.9% wt) vs STMS (13.3% wt) respectively (**Figure 3-11**). STMS NPs are calcinated at 550 °C after synthesis to remove the surfactant whereas for IO@STMS the surfactant is chemically removed to preserve iron oxide core from phase transformation. This calcination may lead to more silica condensation of the STMS, which means less active hydroxyl groups at the surface (hydroxyl groups condense to form bridging oxygen bonds between two silicon). As a consequence, less APTES reacts with the STMS surface which allows more pore volume for DOX diffusion and this ensures that more DOX can be loaded in the STMS NPs. Additionally, as compared to the core-free STMS NPs, the large pore silica shell formed around the IO cores may have hindered

the interconnectivity of the pores which reduces also the pore volume available for the drug loading for these IO@STMS NPs.

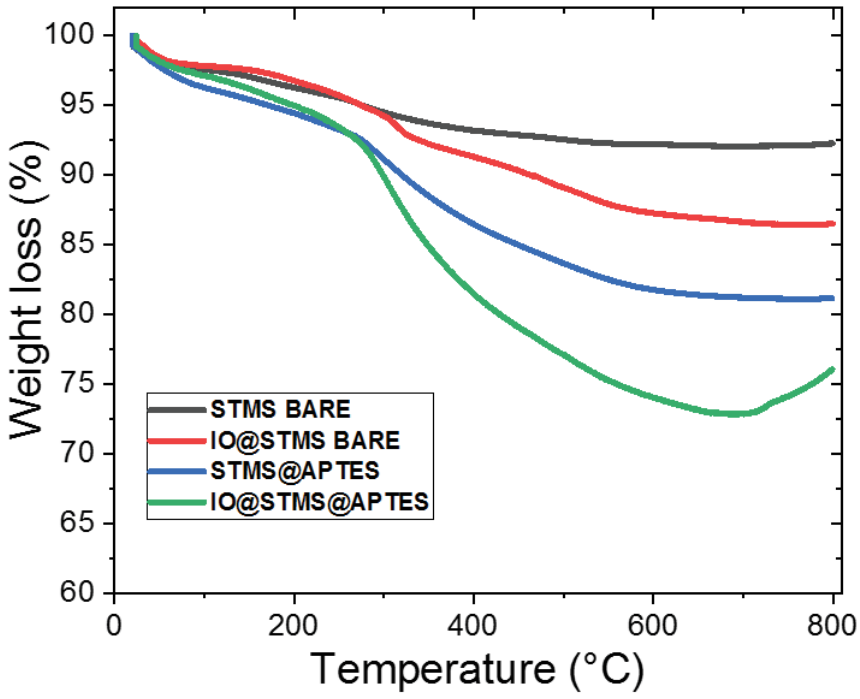

Figure 3-11. TGA curves of STMS, IO@STMS, STMS@APTES and IO@STMS@APTES.

III.1.3.3. Study of drug leaking effects and human serum albumin adsorption

Another crucial aspect for the design of this nanoformulation, is to ensure a limited leaking of the loaded DOX from the NPs, in order to handle and store the NPs before use. DOX loaded IO@STMS (BARE, APTES and IBAM-functionalized) NPs at the DLC in the range 20-45% as analyzed before, were consecutively washed with fresh loading buffer (HEPES 100 mM, pH = 7.5) and their supernatants were analyzed by UV-Vis spectrophotometry to determine the amount of DOX released during this washing process (**Figure 3-12.A**). Here, DOX loading was carried out at pH 7.5, as the releasing buffer. After one washing step (W1 in the figure), less than 10 % of the initially loaded DOX was leaked in all types of surfaces. Subsequent washings (W2 – W4 in the figure) induced a leaking ranging from 1 to 6 %. The spontaneous loss of DOX during these washings (at room temperature and at pH 7.5) is thus very limited. It is also noticeable that for higher fwr, i.e. high DLCs, the proportion of DOX that spontaneously leaks out is reduced. By promoting the supramolecular assembly of DOX, the pores are filled with the drug and both the surface area as well as the accessibility of the solvating aqueous solution to the DOX molecules may be reduced which may explain why less drug is leaking.

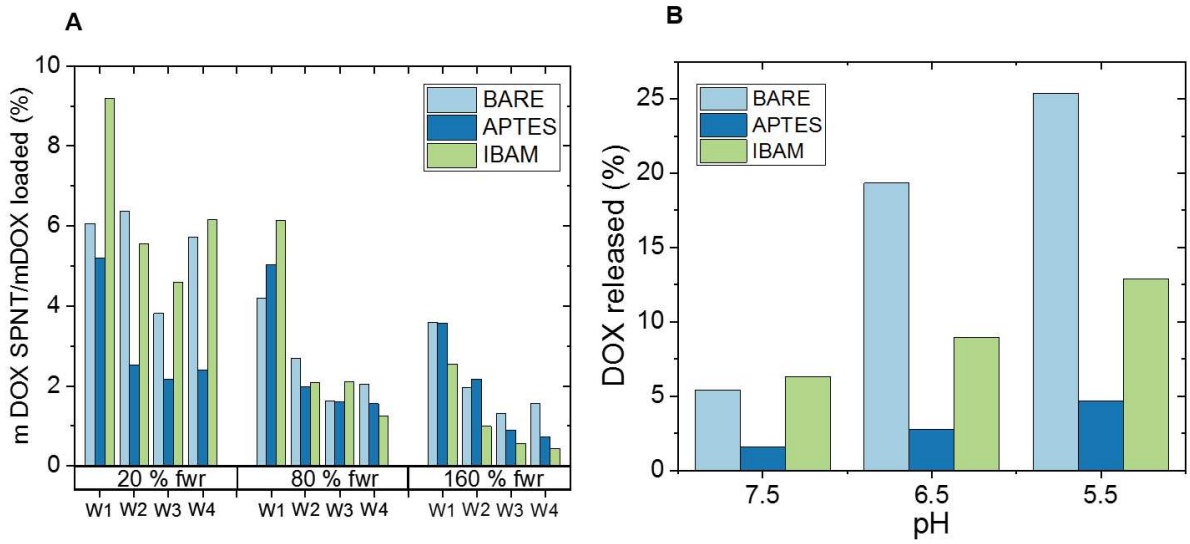

Figure 3-12. (A) DOX leaking due to consecutive washings immediately after drug loading. **(B)** Amount of DOX released by storage at 4 °C for different surface functionalization and different pH over one week.

The stability upon storage was also checked by leaving the same DOX loaded samples at 4 °C for one week. Here, the pH of the storage buffer was also adjusted and the fwr was fixed at 80%. After centrifugation, the amount of DOX leaked during this period was evaluated as compared to the initially loaded DOX. **Figure 3-12.B** clearly shows that by increasing the acidity of the storage liquid medium, more DOX was released from the NPs for each and all types of surface functionalization. The other interesting aspect is that BARE NPs were the most leaking formulation whereas APTES was the least one (ca. respectively 25 vs 5% at pH 7.5 over 1 week); IBAM leaks intermediately between these two.

Having evaluated the DOX release behavior after consecutive washings and upon storage at 4 °C during one week and at different pHs, it became clear that the nanosuspension slowly but steadily releases a rather small proportion of the DOX loaded to the medium. For further biological applications, this spontaneous DOX leaking has to be minimized. The addition of an external biocompatible coating would avoid this leaking and prevent the direct contact between the drug-loaded NP and the biological tissues. Human Serum Albumin (HSA) protein has been chosen in order to improve the biocompatibility of the NPs as well as to reduce opsonization of the nanoformulation. Before the HSA adsorption step, DLCs of DOX were previously calculated after DOX impregnation and two consecutive washings (**Table 3-1**).

Table 3-1. DLCs before and after washing with HEPES buffer.

Type of surface	DLC before washing (%)	DLC after washing (%)
BARE	41.8	38.2
APTES	8.23	7.39
IBAM	18.1	15.0

Then, at physiological pH, negatively charged HSA was adsorbed onto positively charged DOX-loaded NPs for the three surfaces (BARE, APTES and IBAM). The amount of coated HSA on the NPs

was determined by spectrophotometry using bicinchoninic acid (BCA) assay (see details in Materials and Methods section). The calibration curve is shown in **Figure 3-13.A**.

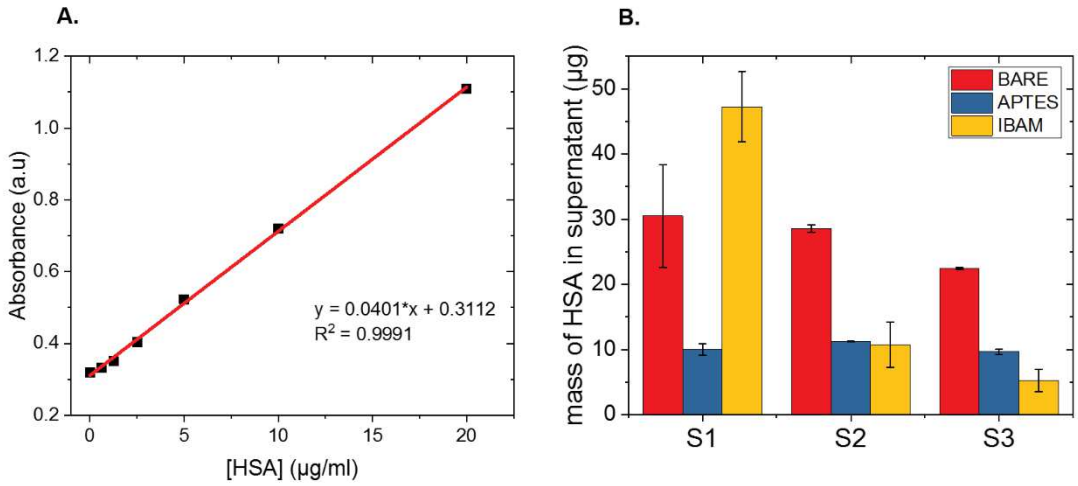

Figure 3-13. (A) BCA assay calibration curve for the dosage of HSA and **(B)** masses of HSA measured by the BCA assay allowing to quantify the HSA coatings after two washing steps. S1: HSA remaining in the loading supernatant, S2 and S3 are the two subsequent washings with buffer.

A feed weight ratio of 100 µg of HSA per mg of IO@STMS NPs was introduced during the HSA adsorption step. Analysis of the HSA amounts in the supernatants (after two washing steps) by the BCA assays (**Figure 3-13.B)** allowed to determine coatings in the range 51-81 µg(HSA).mg(NP)$^{-1}$. These results showed a quite effective HSA coverage (**Table 3-2**, top line) for the three surfaces used. Furthermore, the amount of DOX released during the protein coating and after two washings were measured for each surface (**Table 3-2**, bottom line). The lost quantities at this step were very low even if it can be noted that the BARE surface is the one that released the most. The final DLCs of the NPs correspond at this stage to the DLCs after HSA immobilization, taking into account the DOX leaked following washing steps.

Table 3-2. Amount of coated HSA and DOX released during the protein coating reaction.

	BARE	**APTES**	**IBAM**
HSA coating(µg/mg IO@STMS)	51.2	81.6	62.2
DOX leaking after HSA coating (% of DLC)	5.33	0.62	3.08

Overall, these characterizations have shown that the formulations described here are good candidates to combine photothermal therapy and drug delivery as it is possible to load them with high amounts of DOX as well as to induce significant heating upon NIR irradiation.

III.1.3.4. Drug release study as a function of pH, surface chemistry and NIR light applied

In a next step, we thus studied the drug release behavior of core-shell NPs loaded with DOX (obtained for equal DOX fwr), coated with HSA, and having intermediate DLCs (BARE: 45%, APTES: 18% and IBAM: 27%, all loaded in HEPES 100 mM, at pH 7.5). NIR light irradiation was also applied to the different surface-functionalized IO@STMS NPs (BARE, APTES, IBAM). As the pH played a major role in the DOX loading and leaking studies, we also investigated this parameter on the release, by using HEPES buffer 100 mM at three different values (pH= 5.5, 6.5, 7.5). 1 mL of DOX-loaded NPs were introduced into a plastic cuvette. Then the laser was switched on and the sample was irradiated at 1064 nm, from one side of the cuvette with a power of 1 $W.cm^{-2}$ **(Figure 3-14.A**). After 45 min, the laser was switched off and the supernatants were collected by centrifugation. Fresh buffer was added to the NPs and irradiation was repeated. In total four cycles were achieved on each sample.

For each functionalization (BARE, APTES and IBAM), and each pH, the amount of DOX released during the irradiation was measured and compared to the control sample which was not irradiated (**Figure 3-14.B-D, left)**. Associated heating curves showed that the temperature elevation profiles remain similar in every tested conditions (**Figure 3-14.B-D, right**). Indeed, the pH, the functionalization state of the silica shell and the repeated heating cycles did not degrade the heating performance of the iron oxide core. At higher pHs, some cooling can be seen after ten minutes laser irradiation. This may be due in some cases to sedimentation of the NPs at the bottom of the cuvette. pH 5.5 better stabilized the dispersion because in the core-shell NPs (IO@STMS@DOX@HSA), the charge of DOX governs the NP surface charge which is positively charged at pH 5.5. For instance, by decreasing the pH from 7.5 to 5.5, zeta potential values increased respectively for IO@STMS@DOX@HSA (BARE) from -7.8 to +14.4 mV and for IO@STMS@IBAM@DOX@HSA (IBAM) from -5.6 to +33.6 mV. This ensures better electrostatic repulsion between the NPs and thus a better colloidal stability.

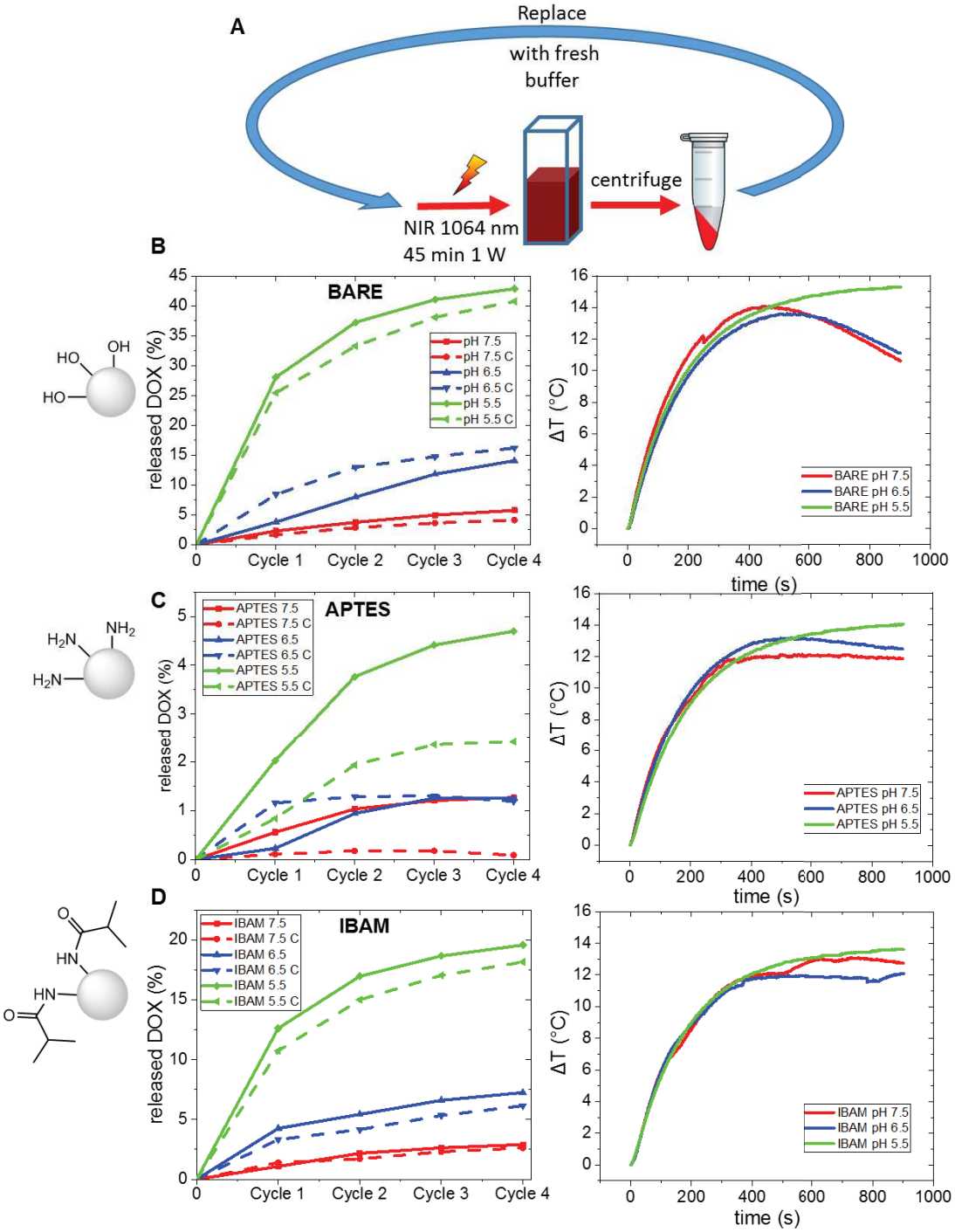

Figure 3-14. (A) Scheme of the NIR light irradiation protocol. Graphs on the left are the cumulative amounts of released DOX for the BARE **(B)**, APTES**(C)** and IBAM **(D)** surfaces. Bold lines correspond to NPs with NIR light and dotted lines without NIR light applied. Graphs on the right correspond to temperature elevation curves of the NP suspension upon NIR light. C means no NIR light applied.

Observations from **Figure 3-14.B-D** indicate that the temperature elevation, induced by the NIR laser, influenced very little the DOX delivery. Regarding the cumulative drug release curves, usually about half of the total DOX was delivered during the first cycle and the delivery was more sustained throughout the irradiation cycles. Furthermore, for each surface state, the main parameter to control the release was the pH of the buffered dispersion. At pH 7.5, a very limited amount of the total loaded DOX

was released for all three surfaces. These amounts were more than doubled at pH 6.5, and importantly increased at pH 5.5, which are suitable acidic pHs respectively for drug release in tumor tissues and in lysosomes. For example, in the case of BARE NPs, along the cumulative release, DOX release was of ca. 5.7, 14.0 and 42.8% when decreasing respectively the pH at 7.5, 6.5 and 5.5.

However, even if this trend (increasing DOX release by decreasing pH) was also found for the APTES and IBAM surfaces, it is worthy to remark the important influence of the surface chemistry on the % amount of drug released. **Figure 3-15** represents the evolution of the total % drug released (from the cumulative release study of **Figure 3-14**) as a function of the surface chemistry and the pH. This graph shows clearly that whatever the pH, the amount of DOX released from the chemically modified IO@STMS NPs follows this order: BARE ≥ IBAM≥ APTES. For instance, at pH = 5.5, DOX release from the three different surfaces was found to be ca. 40% for BARE, 17% for IBAM and only 2% for APTES (for no NIR light applied). The different DLCs (BARE: 45%, APTES: 18% and IBAM: 27%) do not explain this behavior as in the leaking study (**Figure 3-12.A**), it was observed that the %leaking were lowered when the DLCs were increased. If DLCs were rigorously the same, the obtained results in this release study would be even accentuated. These quite tricky results emphasize clearly the role of the surface chemistry over the drug release.

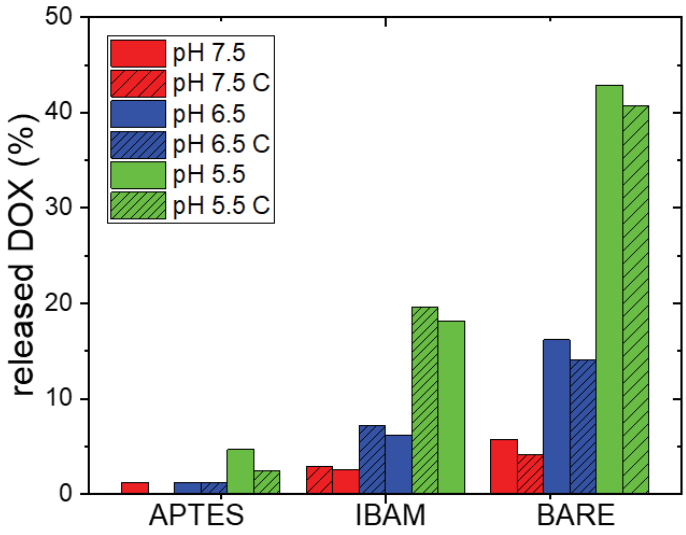

Figure 3-15. Representation of the total drug released over the 4 cycles (from **Figure 3-14**) as a function of the surface chemistry, pH and NIR light applied or not.

Regarding these results but also those from the drug leaking study described above, it appears that APTES and IBAM retain more DOX as compared to BARE whatever the pH. Our data indicate that the APTES polysiloxane which bears the amines, but also IBAM, plays a clear role in the DOX retention to the NPs as compared to the BARE surface. In our previous works, we reported that APTES polysiloxane layer at the surface of CNTs@MS is able to load an important amount of drugs (≥100 % wt) acting as a kind of organic sponge attracting DOX at the CNT@MS@APTES surface but the DOX release was found low (less than 5%). A combination of interactions was hypothesized through H-bonding and π-π stacking that are probably involved in ensuring retention of DOX at this surface.[53]

Thus at a fixed pH, the main parameter determining the release of drugs between the three modified surfaces is probably the kind of interactions involved between the modified surface and the drugs. It is assumed that:

-For BARE NPs, the release is increased importantly by decreasing pH because the electrostatic interactions DOX-surface becomes lower than the solvation forces of the protonated DOX. DOX can thus diffuse freely out of the silica.

-For APTES, it appears that the DOX is better retained to the aminosilane surface, despite the electrostatic repulsion involved between the two molecules. This result is not really intuitive. It may be possible that APTES act as kinds of surface primers able to favor non-electrostatic interactions such as H-bonds and π-stacking due to the underneath polysiloxane layer.

-For IBAM, the leaking effect is intermediate between these two situations.

III.1.4. Conclusion

In this work, we have addressed for the first time, the use of IO@STMS NPs for their NIR light-induced photothermal effect combined with drug release. The main points of the article are the following:

i) We showed first, by tracing temperature profiles upon NIR light and evaluating SAR, that the NPs concentration, and the laser power are key parameters of the photothermal properties. Photothermal SAR which can reach values up to 2000 $W.g^{-1}$ (at 1 $W.cm^{-2}$) appear as particularly competing with the magnetothermal values published previously.

ii) Regarding the drug loading study of these core shell NPs with DOX, the pH of the drug impregnation aqueous solution was found to be the critical parameter determining the drug payload while the surface chemistry used: BARE, APTES or IBAM had a limited influence. Indeed, for instance, with IO@STMS@IBAM we have shown that a loading at pH = 7.5, allowed to reach DLC up to 73%, a high DLC as compared to the literature, while at pH = 5.5, DLC reached only 7%. Further, a coating of HSA wrapped around such core-shell NPs estimated at ca. 50-80 µg/mg IO@STMS (depending on the surface functionalization considered) was found to ensure limited drug leaking before the intended application.

iii) At last, to assess both the possibility of NIR-induced photothermia combined with drug release from these IO@STMS@DOX@HSA core-shell systems, a cumulative release study was achieved upon 4 daily cycles in the presence or absence of NIR light. Even if the NIR light does not trigger the drug release, the combination of local photo-induced hyperthermia along with pH-induced drug delivery has been demonstrated, with a final amount released depending strongly here on the surface chemistry used. This low pH-induced drug delivery (pH 5.5) may be beneficial for intracellular drug release in lysosomal cell compartment. In next works, a biological study with cancer cells is

expected to evaluate the interactions of the NPs with the cells and the combined effect of photothermia and drug delivery for synergistic anti-tumor treatments.

III.2. Biological studies

Multifunctional nanoplatforms combining imaging, therapy and targeting properties are highly promising for customized treatments, reducing side effects and improving the treatment efficiency. Previously in this chapter, we described and characterized a nanoplatform IO@STMS whose surface has been chemically engineered, then loaded with DOX and coated with HSA. The next step consists in the evaluation and validation of this nanoplatform as an effective system for PTT and drug delivery. For this, we collaborated with biologists from INSERM (U1109 *Tumor Biomechanics* team) to evaluate the antitumor efficacy and the biocompatibility of these nanoplatforms. Preliminary *in vitro* and *in vivo* studies have been performed. Zebrafish melanoma cells (ZMEL-1) have been chosen as our reference cell line model. It is a syngeneic tumor cell line coming from the zebrafish which allows to follow the metastatic progression of melanoma.[77] In the light of the results of the previous section (III.1) where we studied three different surface chemistries, we were able to choose the most appropriate one. Modification with IBAM groups provided the best compromise for maximized drug delivery with the lowest spontaneous drug leaking. It also stabilized the best the HSA protein coating. Thus, the following biological tests have been conducted with IO@STMS@IBAM@DOX@HSA. Thus the efficacy of our nanoplatforms on these *in vitro* cancer cells was studied and the most appropriate conditions for combined therapies (NPs' concentration, laser power and duration) were defined. Then, the same cell line can be studied *in vivo* after intravenous transplantation in zebrafish to mimic metastatic tumors. Zebrafish (ZF) embryos are particular suited models for *in vivo* studies. They present the advantages of having a short generation time, rapid development and being optically transparent. This latter allows to follow fluorescent NPs by confocal microscopy.

III.2.1. *In vitro* cytotoxicity tests: PTT and drug delivery

III.2.1.1. *In vitro* drug release after NIR illumination

A first experiment consisted in observing by optical (transmission) and confocal microscopies, the effect of NIR light irradiation on ZMEL-1 tumor cells incubated with core-shell NPs IO@STMS@IBAM@DOX@HSA-FITC. Here the protein layer of native HSA was replaced by a HSA labeled with fluorescein isothiocyanate (HSA-FITC) for additional fluorescence visualization. FITC allows a green labeling whereas the DOX is naturally red fluorescent.

ZMEL cells were grown at 28 °C – 4% CO_2 in the proper cell culture medium until reaching confluency in a 10 cm petri dish. These cells were, then, tripsinized and seeded in a new Maptek dish at a concentration c/10 for 24 h. Then the NPs were added at a concentration of 1 mg/ml and the luminescence coming from the DOX in the cells when these ones were exposed or not to a 15-minute NIR laser at 1 W/cm^2 was followed.

The Maptek dish was taken under the confocal microscope and the sum of intensity of light coming from the DOX inside the cells was followed over one hour. To do so, the cytoplasm of the cell was segmented and this mask was applied to our image to obtain only the intensity coming from the defined region. Intracellular fluorescence intensities were measured as a function of time in order to study the accumulation and diffusion of DOX inside the cells on wide shots containing dozens of cells. The results obtained are shown in **Figure 3-16**. Upon NIR light irradiation, the level of DOX fluorescence is very high compared to the non-irradiated systems which showed only a comparative very low level of leaking. Thus, NIR irradiation seems to trigger the DOX release. This result is very promising and tends to show that the system can be activated by light in cell cultures, which was not the case when it was tested as dispersion in cuvettes in the previous section (III.1).

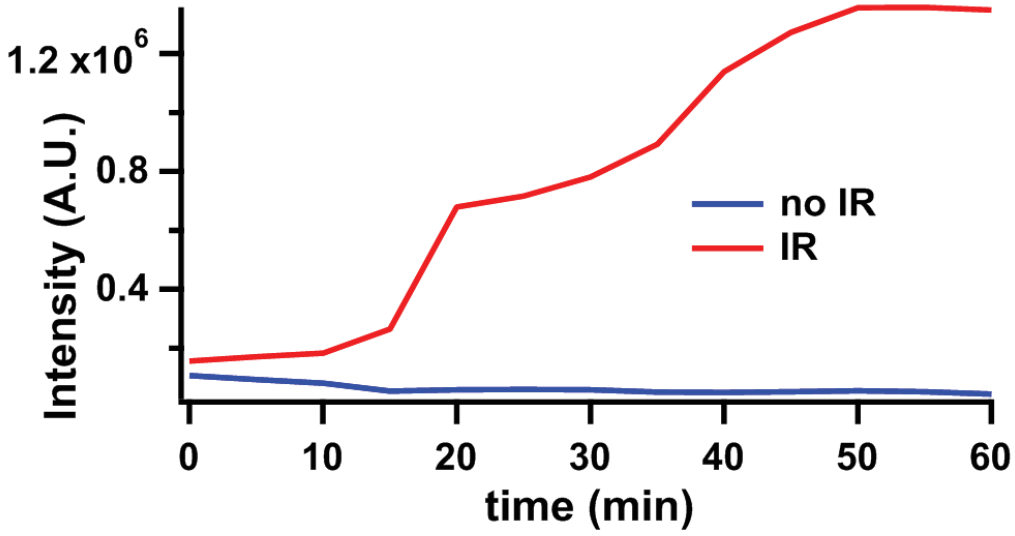

Figure 3-16. Temporal evolution of DOX luminescence coming from wide shots as a function of time, averaged on three different experiments.

III.2.1.2. *In vitro* drug accumulation in the cell one hour after NIR illumination

We also wanted to understand how the NPs and the loaded drug interact with the cells and accumulate within them. For this, ZMEL cells were seeded in the same conditions as described previously. The NPs were added to a final concentration of 1 mg/mL before the sample was irradiated for 15 min with the NIR laser at a power density of 1 W/cm^2. These irradiated cells were put back in the

incubator for 1 h at 28 °C - 4% CO_2. Then these cells were incubated with NuncBlue for 15 min in order to stain their nucleus, before placing the Maptek under the confocal microscope to follow more precisely the distribution of DOX in the cells.

On the pictures, accumulation of the NPs on the cell walls and inside the cytoplasm can be observed (more intense fluorescent spots). DOX which is releasing from the NPs diffuses and progressively accumulates inside the cell nuclei which is the expected to be the mode of DOX action (**Figure 3-17**).

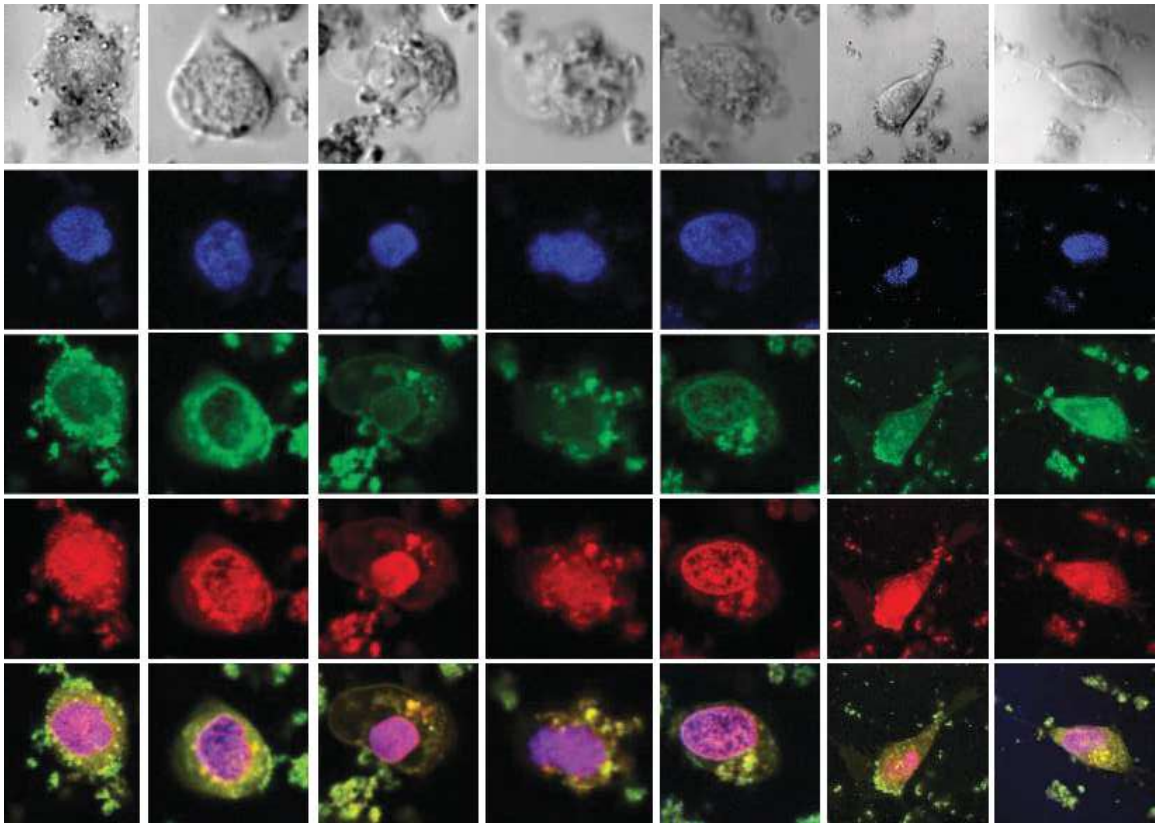

Figure 3-17. First line, transmission optical microscopy of individual cells after incubation with IO@STMS@IBAM@DOX@HSA-FITC. From second line to the bottom, the same cells in fluorescence microscopy: blue (nucleus), green (HSA-FITC), red (DOX) and bottom line, merged.

III.2.1.3. *In vitro* cell viability

A cellular MTT cytotoxicity test has also been conducted on ZMEL-1 cells. It is a colorimetric assay used to monitor the cellular metabolic activity. 3-(4,5-dimethylthiazol-2-yl)-2,5-diphenyltetrazolium bromide (MTT) is a yellow tetrazolium salt which is reduced to insoluble purple formazan in presence of active living cells. Then a solubilization solution is added to dissolve the product in a colored solution whose absorbance is then measured by a spectrophotometer. Absorbance is thus proportional to the amount of living and metabolically active cells.

To do this test, ZMEL-1 cells were seeded (50,000 cells per well in 50 µl of medium) in each well of the opaque 96 well plate and incubated at 28 °C in 5% CO_2 for 45 min to an hour to allow the cells to adhere. Then, additional medium (150 µL) supplemented with the final concentration of NPs suspensions were introduced and incubated at 28 °C, 5% of CO_2 for 24 h. NIR irradiation (at 1 W/cm^2 for 15 min) was applied and the cells were further incubated at 28 °C in 5% CO_2 for 24 h. NIR irradiation was performed with a homemade setup. The illumination was performed from the top cover towards the well. Cell Titer Glo (Promega) reagent was then added to each well (20 µL) followed by one-hour incubation at room temperature, allowing cell lysis to be completed and luciferin to be oxidized by the cellular ATP. The 96 well plate was introduced into a plate cell reader (SpectraMaxID5 from MolecularDevices) and luminescence was collected.

The intensity of control wells (cells without NPs called Luminescence Control) was used to normalize the luminescence values (all values are between 0 and 1, value of the control wells). The luminescence values from wells filled with medium were measured. The obtained values were at the noise level, therefore it has been decided to not correct the next samples with these values. Nevertheless, NPs have a dark aspect and therefore could absorb part of the emitted light from the viability experiments. Thus the amount of light absorbed by the NPs in the wells was characterized. For this, different wells were cultured with 50,000 cells per well for 48 h in normal cell growth conditions. Before running the Cell Titer Glo experiment, we first added the 4 studied concentrations of NP in different wells. This short time, when the NPs were in contact with the cells, is assumed to only affect the emitted light. We used the average absorption values obtained for each concentration of NPs to correct all the signals measured in presence of NPs. Using the mathematical formulation, we can write:

$$Relative\ Viability = \frac{Measured\ luminescence}{Luminescence\ Control} X \frac{1}{Absorption}$$

The influence of the concentration of NPs (loaded or not with DOX) was studied and the antitumor action with or without NIR light irradiation was compared. First of all, these experiments showed that without NIR irradiation, the cytotoxicity is relatively moderated, regardless of the concentration of NPs and the DOX loading. This toxicity certainly comes from a slightly too high NPs concentration **(Figure 3-18, black bars)** which thus will need to be adjusted for future experiments. Then, the NIR laser running at 1064 nm was turned on at a power of 1 W/cm^2. Without NPs, NIR irradiation has no measurable effect on the cell viability which shows that cells do not absorb this wavelength and the temperature did not significantly increase in the cell culture. However, with our core-shell IO@STMS NPs, in absence of DOX, the photothermal action increased significantly the cell death. This demonstrated the importance of the photo-induced hyperthermia treatment. Moreover, this effect was very dependent on the concentration of the NPs. By increasing the concentration from 0.5 to

2 mg/mL, the ZMEL-1 cells are even more killed **(Figure 3-18, red bars No DOX)**. Finally, DOX-loaded NPs were incubated with the tumor cells and under NIR laser, the highest cytotoxic effect was observed **(Figure 3-18, red bars DOX)**. This demonstrates a synergetic effect of both photothermal treatment and DOX release. This combined action is further supported by the visualization of the intracellular DOX diffusion in **Figure 3-17**. Under NIR light, the comparison of NPs loaded with or without DOX, clearly highlights the cytotoxic effect of DOX in addition to PTT **(Figure 3-19)**.

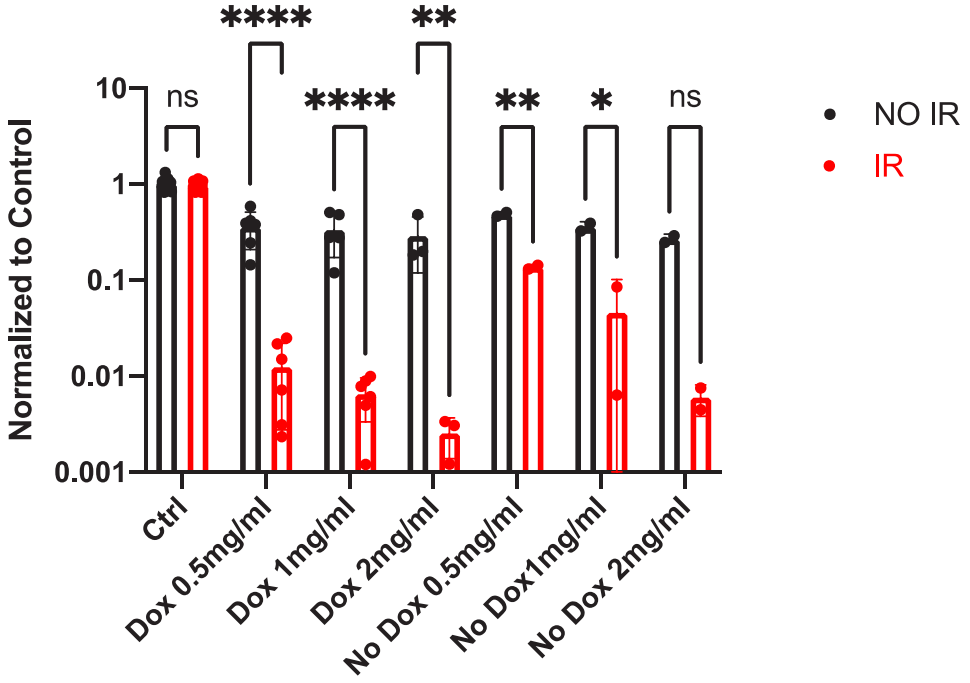

Figure 3-18. Cell toxicity assay with (red bars) and without (black bars) NIR irradiation. NPs loaded with DOX (Dox) and non-loaded (No Dox) at three different concentrations were tested.

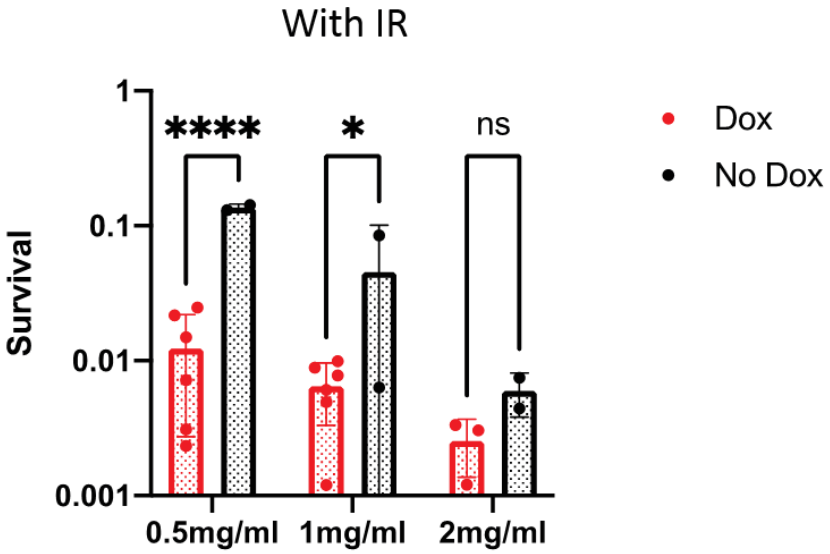

Figure 3-19. Cytotoxic effect of DOX on cells exposed to NIR by comparing NPs loaded with DOX (red bars) and non-loaded NPs (black bars) at three concentrations.

Future *in vitro* experiments will consist in refining and repeating these cytotoxicity tests to define the more adapted concentrations which should have no toxicity without NIR and maintaining a high antitumor activity with infrared irradiation. The melanoma model will be further studied by implementing MTT assays on a murine melanoma cell line B16F10 and a human melanoma cell line A375. This should allow us to show the efficacy of the nanoformulation on a coherent panel of cell lines.

III.2.2. *In vivo* study on ZF embryos

III.2.2.1. *In vivo* toxicity

A preliminary *in vivo* study on ZF embryos has been conducted in order to evaluate the toxicity, the development of these embryos and the biodistribution of the NPs. LifeAct-fli GFP Zebrafish were breeded, and the eggs were kept for 48 h at 28 °C. At 48 HPF (hours post fecundation) the embryos were dechorionated and embedded in 0.7% agarose on a Maptek petri dish. Half of the ZFs population were injected in the Duct of Cuvier with 32 nL at 5 mg/mL of core-shell NPs suspension IO@STMS@IBAM@DOX@HSA with a DLC of DOX of 25%. After 3 HPI (hours post injection) the embryos were imaged and from the images their sizes and heartbeats were determined. After the imaging session, the embryos were released from the agarose and kept in Danio breeding water at 28 °C to repeat these same experiments at 24, 48, 72 and 96 h.

Intravenous injection is performed in Duct of Cuvier of 14 embryos. The experiments, conducted on 4 days, showed that the development of embryos was not modified or hampered compared to the control group without NPs: they did not exhibit any significant differences in terms of size or malformations. A complementary experiment measuring the heartbeat of 48 h and 72 h old fish did not show any significant modification compared to the non-injected embryos, thus bringing one more clue of the non-toxicity of our formulation **(Figure 3-20)**.

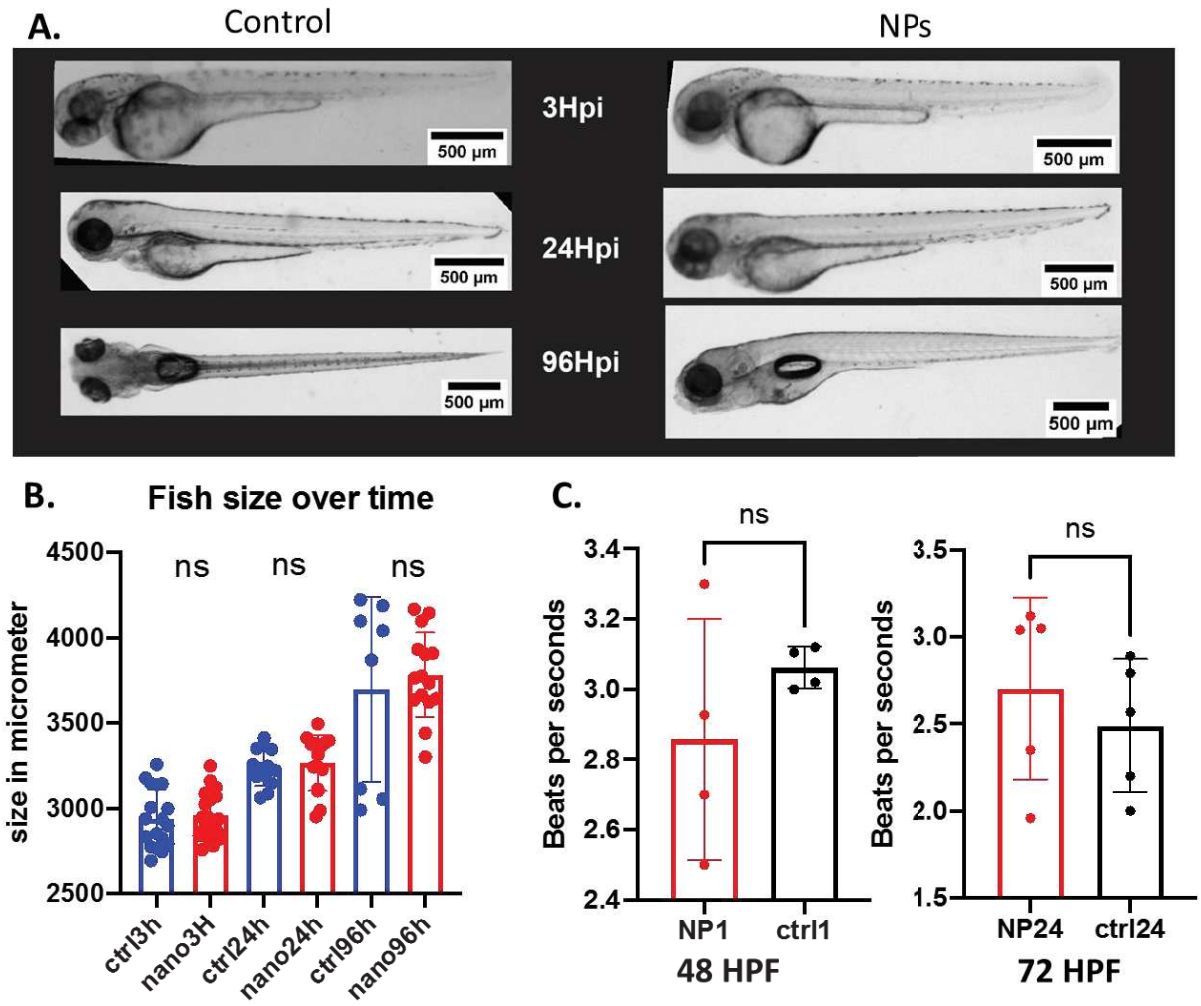

Figure 3-20. (A) Photographs of ZF embryos 3 h (first line), 24 h (second line), 96 h (third line) after NPs injection (right column) and without injection (left). **(B)** Size evolution over time of injected (red) and non-injected (blue) ZF. **(C)** Measured heartbeats of injected (red) and non-injected (black) of 48 h old (left) and 72 h old (right) ZF embryos. Hpi means "hours post injection". HPF means "hours post fecundation".

III.2.2.2. *In vivo* localization of the nanoparticles.

To observe the biodistribution inside the ZF embryos, they were injected with FITC-labeled IO@STMS@IBAM@DOX@HSA-FITC. We took advantage of the fluorescence of the DOX (excitation at 488 nm, emission at 600 nm) and the FITC-labeled HSA to follow and track the NPs in the embryo. Wild-type ZF were breeded and the eggs were kept 48 h at 28 °C. At 48 HPF the embryos were dechorionated and embedded in 0.7% agarose on a Maptek petri dish. We injected the embryos with the NP suspension (32 nL - 5mg/mL) in the Duct of Cuvier. After 3 HPI the embryos were imaged on the confocal microscope. The entire embryo was reconstructed by stitching the different camera shots (**Figure 3-21**). A homogeneous NP distribution in the whole fish body can be observed by a strong labeling of the vasculature. These data highlight the good circulation of the NPs.

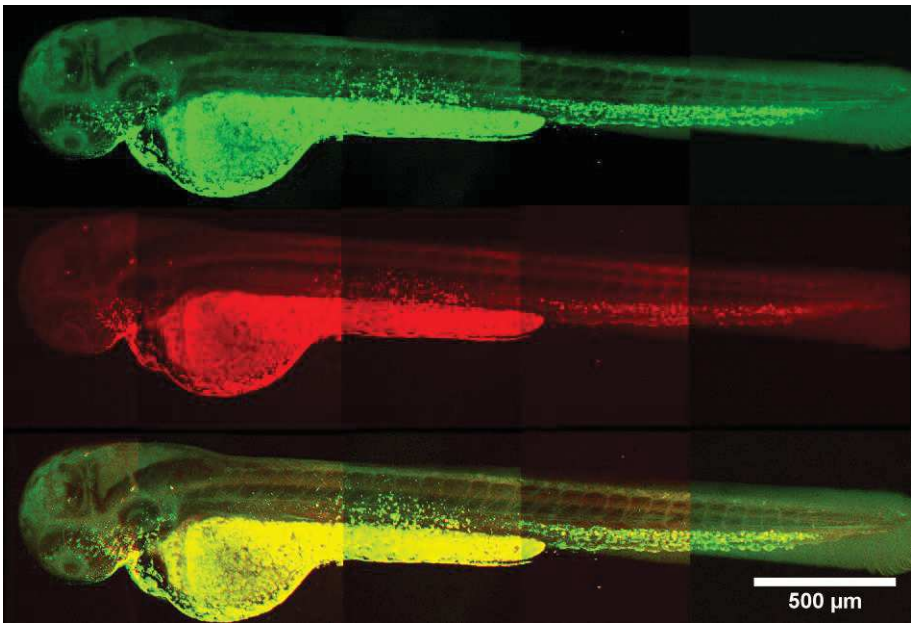

Figure 3-21. Fluorescence microscopy of ZF embryos 3 h after injection with DOX-loaded NPs; from top to bottom, green from FITC, red from DOX and merged pictures.

Some aggregates can be detected in the tail and the head of the fish. Zooming on regions where a high density of nanoparticles was observed led us to think that these nanoparticles are taken over by the macrophages (**Figure 3-22**). The colocation of both red fluorescence from DOX and green fluorescence from HSA-FITC suggests that these two molecules are still on the NPs when the pictures were taken, thus indicating a good stability of the formulation. Additional experiments to colocalize the NPs with the DOX and HSA will be conducted. Several methods can be used to localize the IO-based NPs such as *in vivo* MRI, TEM on thin tissue section, magnetic particle spectroscopy (MPS)[78] or Prussian blue staining[79].

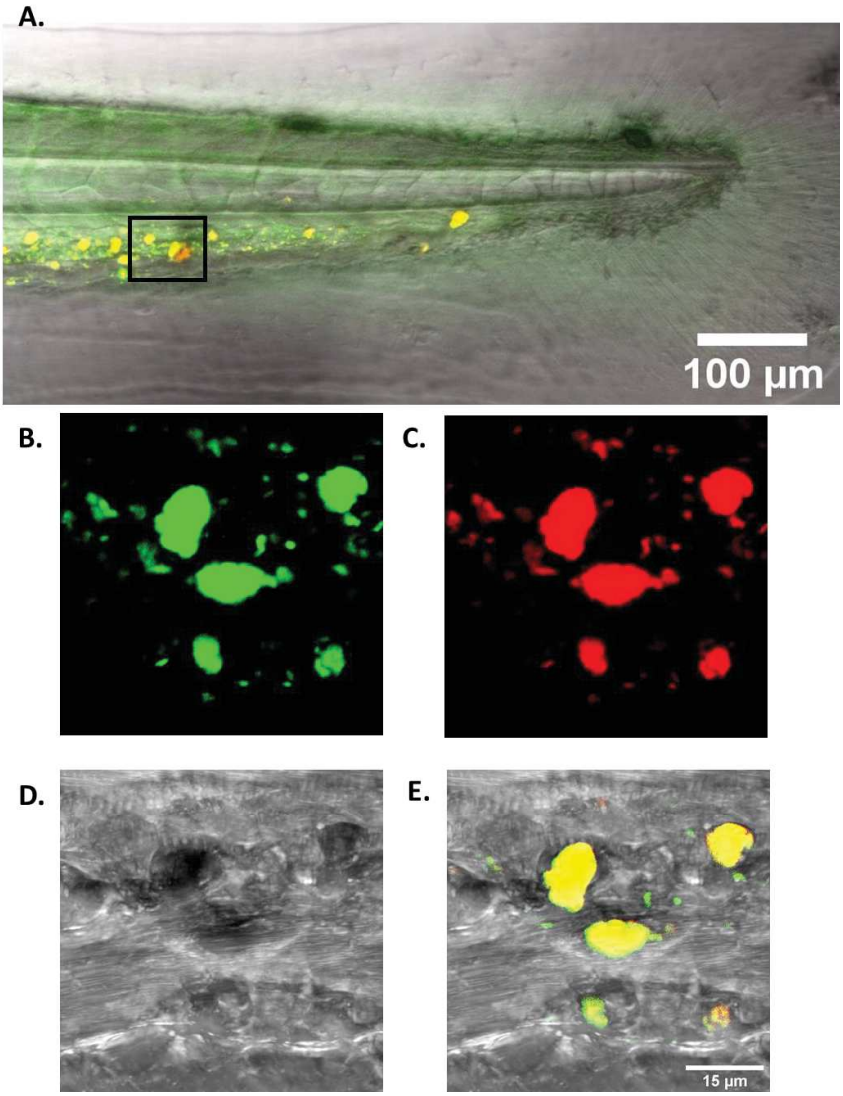

Figure 3-22. (A) Merged images of transmission and green fluorescence (FITC) microscopy of a ZF tail. The black rectangle represents the zoomed region shown in B to E. (B) green fluorescence of FITC, (C) red fluorescence of DOX, (D) transmission image, (E) merged images.

III.2.2.3. *In vivo* tumor growth and nanoparticle localization

As an example to illustrate the future *in vivo* experiments on ZFs envisioned with our NPs, very preliminary studies were performed by the INSERM team on ZF embryos transplanted with ZMEL-1 cells to mimic metastatic tumor models. Tumor cells are genetically modified to be red fluorescent and FITC has a green fluorescence which should indicate the localization of the NPs (coated HSA-FITC). Wild-type ZF were breeded and the eggs were kept 48 h hat 28 °C. At 48 HPF the embryos were dechorionated and embedded in 0.7% agarose on a Maptek petri dish. The embryos were injected with 32 nL of ZMEL-LifeAct TdTomato cells in the Duct of Cuvier. After the injection the embryos were freed from the agarose and were left in the Danio breeding water for 24 h. This time allows the cells to

adhere to the endothelial walls and to start their metastatic progression. At 72 HPF these embryos were embedded again in agarose and were injected with core-shell suspension IO@STMS@IBAM@DOX@HSA-FITC (32 nL – 5 mg/mL).

These embryos were then kept at 28 °C for 4 more days before being imaged under the confocal microscope. From the different images we can clearly see situations were the tumor cell aggregates and HSA-FITC are colocalized. In **Figure 3-23**. **A to I** the colocation of green (FITC) and red (tumor cells) demonstrates that there is an accumulation of the NPs in or on the tumors. From **A to C** in **Figure 3-23**, the images show that the NPs can target an aggregate of tumor cells. **D to F** and **G to I** show how the FITC labeled the whole vasculature but a more important contrast is seen in tumor cells location, suggesting an enhanced accumulation. **Figure 3-23. J and K** prove the formation of metastases dispersed in different parts of the ZF body and the clear labeling of FITC of the endothelium. Next studies will monitor the circulation of the NPs in the body and should bring new clues for their accumulation in tumors.

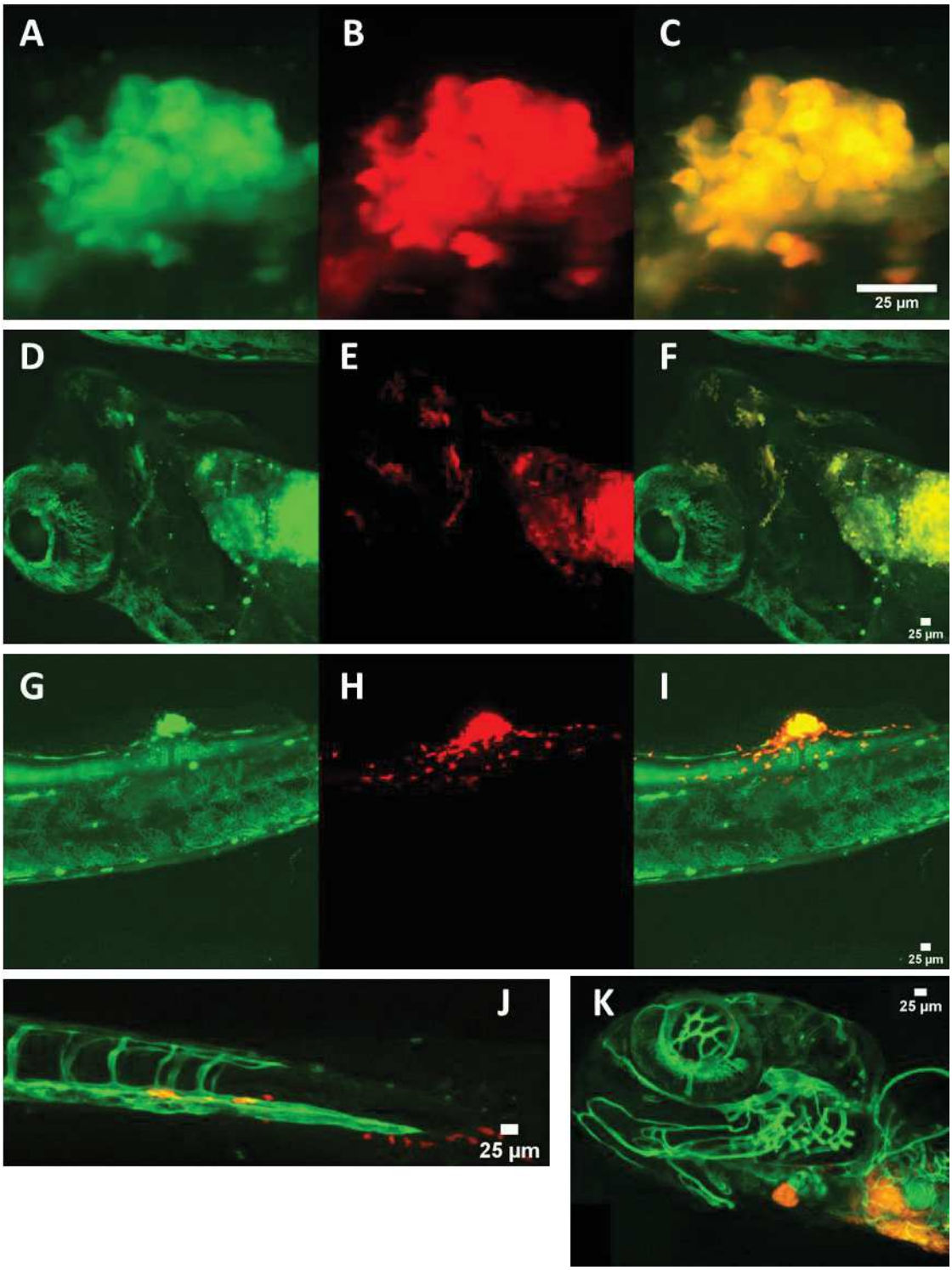

Figure 3-23. Confocal images showing the fluorescence distribution of green fluorescein (A, D, G), of red tumor cells (B, E, H) and merged images of both (C, F, I, J, K).

III.3. Conclusion of Chapter III

In this chapter, an innovative nanoplatform for PTT and drug delivery has been developed. The system based on core-shell IO@STMS was synthesized and the photothermal properties were deeply characterized. Concentration of NPs and laser power are key parameters to control the heat elevation and the SAR obtained at 1 W/cm^2 are particularly competing with the other reported nanosystems. To load high amounts of drugs, we demonstrated that the pH of the impregnation solution is the critical parameter to maximize the loading. In the case of DOX, pH=7.5 was a lot more efficient than pH=5.5 whatever the surface chemistry of the NP. However, the surface chemistry, concomitantly with the pH buffer, appeared to be of very high importance to tune the drug delivery, certainly because of modified drug-surface interaction. The application of NIR light on DOX-loaded NPs indicated that a dual-mode therapy is achievable for synergetic antitumor application. The drug delivery being particularly enhanced when pH is lowered to 5.5, this perfectly fits with drug release in lysosomal or intra-tumoral compartments as they are known as relatively acidic.

Then, preliminary biological assays have been conducted and they evidenced that the intracellular DOX diffusion is triggered by NIR light. Cytotoxicity tests highlighted the potential of IO@STMS@IBAM@DOX@HSA to induce cell death by photothermia and which is enhanced by DOX delivery under NIR light. *In vivo* tests showed no toxicity of the nanoformulation on ZF when no NIR light is used. The system has an excellent circulation in the whole blood stream which is shown by the labeling of the vasculature. Furthermore, in very preliminary experiments, when melanoma ZMEL-1 cells were transplanted in the fish, the NPs displayed an accumulation in the tumor sites. These appealing results will need to be reproduced and validated through more detailed investigations in the future. The system IO@STMS@IBAM@DOX@HSA that we developed is now very well understood from a physicochemical point of view. It is now mature for biological tests which is an ongoing process.

III.4. References

(1) Lammers, T.; Aime, S.; Hennink, W. E.; Storm, G.; Kiessling, F. Theranostic Nanomedicine. *Acc. Chem. Res.* **2011**, *44* (10), 1029–1038.

(2) Janib, S. M.; Moses, A. S.; MacKay, J. A. Imaging and Drug Delivery Using Theranostic Nanoparticles. *Adv. Drug Deliv. Rev.* **2010**, *62* (11), 1052–1063.

(3) Choi, K. Y.; Liu, G.; Lee, S.; Chen, X. Theranostic Nanoplatforms for Simultaneous Cancer Imaging and Therapy: Current Approaches and Future Perspectives. *Nanoscale* **2012**, *4* (2), 330–342.

(4) Mura, S.; Couvreur, P. Nanotheranostics for Personalized Medicine. *Adv. Drug Deliv. Rev.* **2012**, *64* (13), 1394–1416.

(5) Lammers, T.; Rizzo, L. Y.; Storm, G.; Kiessling, F. Personalized Nanomedicine. *Clin. Cancer Res.* **2012**, *18* (18), 4889–4894.

(6) Laurent, S.; Forge, D.; Port, M.; Roch, A.; Robic, C.; Vander Elst, L.; Muller, R. N. Magnetic Iron Oxide Nanoparticles: Synthesis, Stabilization, Vectorization, Physicochemical Characterizations, and Biological Applications. *Chem. Rev.* **2008**, *108* (6), 2064–2110.

(7) Mahmoudi, M.; Sant, S.; Wang, B.; Laurent, S.; Sen, T. Superparamagnetic Iron Oxide Nanoparticles (SPIONs): Development, Surface Modification and Applications in Chemotherapy. *Adv. Drug Deliv. Rev.* **2011**, *63* (1–2), 24–46.

(8) Stanicki, D.; Vander Elst, L.; Muller, R. N.; Laurent, S.; Felder-Flesch, D.; Mertz, D.; Parat, A.; Begin-Colin, S.; Cotin, G.; Greneche, J.-M. Iron-Oxide Nanoparticle-Based Contrast Agents. In *Contrast Agents for MRI*; 2017; pp 318–447.

(9) Hachani, R.; Lowdell, M.; Birchall, M.; Hervault, A.; Mertz, D.; Begin-Colin, S.; Thanh, N. T. K. Polyol Synthesis, Functionalisation, and Biocompatibility Studies of Superparamagnetic Iron Oxide Nanoparticles as Potential MRI Contrast Agents. *Nanoscale* **2016**, *8* (6), 3278–3287.

(10) Na, H. B.; Song, I. C.; Hyeon, T. Inorganic Nanoparticles for MRI Contrast Agents. *Adv. Mater.* **2009**, *21* (21), 2133–2148.

(11) Mazuel, F.; Espinosa, A.; Luciani, N.; Reffay, M.; Le Borgne, R.; Motte, L.; Desboeufs, K.; Michel, A.; Pellegrino, T.; Lalatonne, Y.; Wilhelm, C. Massive Intracellular Biodegradation of Iron Oxide Nanoparticles Evidenced Magnetically at Single-Endosome and Tissue Levels. *ACS Nano* **2016**, *10* (8), 7627–7638.

(12) Lartigue, L.; Alloyeau, D.; Kolosnjaj-Tabi, J.; Javed, Y.; Guardia, P.; Riedinger, A.; Péchoux, C.; Pellegrino, T.; Wilhelm, C.; Gazeau, F. Biodegradation of Iron Oxide Nanocubes: High-Resolution In Situ Monitoring. *ACS Nano* **2013**, *7* (5), 3939–3952.

(13) Blanco-Andujar, C.; Walter, A.; Cotin, G.; Bordeianu, C.; Mertz, D.; Felder-Flesch, D.; Begin-Colin, S. Design of Iron Oxide-Based Nanoparticles for MRI and Magnetic Hyperthermia. *Nanomed.* **2016**, *11* (14), 1889–1910.

(14) Lee, N.; Yoo, D.; Ling, D.; Cho, M. H.; Hyeon, T.; Cheon, J. Iron Oxide Based Nanoparticles for Multimodal Imaging and Magnetoresponsive Therapy. *Chem. Rev.* **2015**, *115* (19), 10637–10689.

(15) Perigo, E. A.; Hemery, G.; Sandre, O.; Ortega, D.; Garaio, E.; Plazaola, F.; Teran, F. J. Fundamentals and Advances in Magnetic Hyperthermia. *Appl. Phys. Rev.* **2015**, *2* (4), 041302.

(16) Hugounenq, P.; Levy, M.; Alloyeau, D.; Lartigue, L.; Dubois, E.; Cabuil, V.; Ricolleau, C.; Roux, S.; Wilhelm, C.; Gazeau, F. Iron Oxide Monocrystalline Nanoflowers for Highly Efficient Magnetic Hyperthermia. *J. Phys. Chem. C* **2012**, *116* (29), 15702–15712.

(17) Thiesen, B.; Jordan, A. Clinical Applications of Magnetic Nanoparticles for Hyperthermia. *Int. J. Hyperthermia* **2008**, *24* (6), 467–474.

(18) Maier-Hauff, K.; Ulrich, F.; Nestler, D.; Niehoff, H.; Wust, P.; Thiesen, B.; Orawa, H.; Budach, V.; Jordan, A. Efficacy and Safety of Intratumoral Thermotherapy Using Magnetic Iron-Oxide Nanoparticles Combined with External Beam Radiotherapy on Patients with Recurrent Glioblastoma Multiforme. *J. Neurooncol.* **2011**, *103* (2), 317–324.

(19) Maier-Hauff, K.; Rothe, R.; Scholz, R.; Gneveckow, U.; Wust, P.; Thiesen, B.; Feussner, A.; von Deimling, A.; Waldoefner, N.; Felix, R. Intracranial Thermotherapy Using Magnetic Nanoparticles Combined with External Beam Radiotherapy: Results of a Feasibility Study on Patients with Glioblastoma Multiforme. *J. Neurooncol.* **2007**, *81* (1), 53–60.

(20) Stolik, S.; Delgado, J. A.; Pérez, A.; Anasagasti, L. Measurement of the Penetration Depths of Red and near Infrared Light in Human "Ex Vivo" Tissues. *J. Photochem. Photobiol. B* **2000**, *57* (2), 90–93.

(21) Henderson, T. A.; Morries, L. D. Near-Infrared Photonic Energy Penetration: Can Infrared Phototherapy Effectively Reach the Human Brain? *Neuropsychiatr. Dis. Treat.* **2015**, *11*, 2191–2208.

(22) Wang, Y.; Wang, K.; Zhao, J.; Liu, X.; Bu, J.; Yan, X.; Huang, R. Multifunctional Mesoporous Silica-Coated Graphene Nanosheet Used for Chemo-Photothermal Synergistic Targeted Therapy of Glioma. *J. Am. Chem. Soc.* **2013**, *135* (12), 4799–4804.
(23) Choi, W. I.; Sahu, A.; Kim, Y. H.; Tae, G. Photothermal Cancer Therapy and Imaging Based on Gold Nanorods. *Ann. Biomed. Eng.* **2012**, *40* (2), 534–546.
(24) Dickerson, E. B.; Dreaden, E. C.; Huang, X.; El-Sayed, I. H.; Chu, H.; Pushpanketh, S.; McDonald, J. F.; El-Sayed, M. A. Gold Nanorod Assisted Near-Infrared Plasmonic Photothermal Therapy (PPTT) of Squamous Cell Carcinoma in Mice. *Cancer Lett.* **2008**, *269* (1), 57–66.
(25) Croissant, J.; Maynadier, M.; Mongin, O.; Hugues, V.; Blanchard-Desce, M.; Chaix, A.; Cattoën, X.; Wong Chi Man, M.; Gallud, A.; Gary-Bobo, M. Enhanced Two-Photon Fluorescence Imaging and Therapy of Cancer Cells via Gold@ Bridged Silsesquioxane Nanoparticles. *Small* **2015**, *11* (3), 295–299.
(26) Chitgupi, U.; Qin, Y.; Lovell, J. F. Targeted Nanomaterials for Phototherapy. *Nanotheranostics* **2017**, *1* (1), 38–58.
(27) Nanospectra | Leveraging Nanoshells in the First True Focal Therapy.
(28) Estelrich, J.; Busquets, M. A. Iron Oxide Nanoparticles in Photothermal Therapy. *Molecules* **2018**, *23* (7), 1567.
(29) Shen, S.; Wang, S.; Zheng, R.; Zhu, X.; Jiang, X.; Fu, D.; Yang, W. Magnetic Nanoparticle Clusters for Photothermal Therapy with Near-Infrared Irradiation. *Biomaterials* **2015**, *39*, 67–74.
(30) Espinosa, A.; Di Corato, R.; Kolosnjaj-Tabi, J.; Flaud, P.; Pellegrino, T.; Wilhelm, C. Duality of Iron Oxide Nanoparticles in Cancer Therapy: Amplification of Heating Efficiency by Magnetic Hyperthermia and Photothermal Bimodal Treatment. *ACS Nano* **2016**, *10* (2), 2436–2446.
(31) Cabana, S.; Curcio, A.; Michel, A.; Wilhelm, C.; Abou-Hassan, A. Iron Oxide Mediated Photothermal Therapy in the Second Biological Window: A Comparative Study between Magnetite/Maghemite Nanospheres and Nanoflowers. *Nanomaterials* **2020**, *10* (8), 1548.
(32) Saint-Cricq, P.; Deshayes, S.; Zink, J. I.; Kasko, A. M. Magnetic Field Activated Drug Delivery Using Thermodegradable Azo-Functionalised PEG-Coated Core–Shell Mesoporous Silica Nanoparticles. *Nanoscale* **2015**, *7* (31), 13168–13172.
(33) Hu, S.-H.; Chen, S.-Y.; Liu, D.-M.; Hsiao, C.-S. Core/Single-Crystal-Shell Nanospheres for Controlled Drug Release via a Magnetically Triggered Rupturing Mechanism. *Adv. Mater.* **2008**, *20* (14), 2690–2695.
(34) Griffete, N.; Fresnais, J.; Espinosa, A.; Wilhelm, C.; Bée, A.; Ménager, C. Design of Magnetic Molecularly Imprinted Polymer Nanoparticles for Controlled Release of Doxorubicin under an Alternative Magnetic Field in Athermal Conditions. *Nanoscale* **2015**, *7* (45), 18891–18896.
(35) N'Guyen, T. T. T.; Duong, H. T. T.; Basuki, J.; Montembault, V.; Pascual, S.; Guibert, C.; Fresnais, J.; Boyer, C.; Whittaker, M. R.; Davis, T. P.; Fontaine, L. Functional Iron Oxide Magnetic Nanoparticles with Hyperthermia-Induced Drug Release Ability by Using a Combination of Orthogonal Click Reactions. *Angew. Chem. Int. Ed.* **2013**, *52* (52), 14152–14156.
(36) Knežević, N. Ž.; Slowing, I. I.; Lin, V. S.-Y. Tuning the Release of Anticancer Drugs from Magnetic Iron Oxide/Mesoporous Silica Core/Shell Nanoparticles. *ChemPlusChem* **2012**, *77* (1), 48–55.
(37) Yue, Q.; Li, J.; Luo, W.; Zhang, Y.; Elzatahry, A. A.; Wang, X.; Wang, C.; Li, W.; Cheng, X.; Alghamdi, A. An Interface Coassembly in Biliquid Phase: Toward Core–Shell Magnetic Mesoporous Silica Microspheres with Tunable Pore Size. *J Am Chem Soc* **2015**, *137* (41), 13282–13289.
(38) Kim, J.; Kim, H. S.; Lee, N.; Kim, T.; Kim, H.; Yu, T.; Song, I. C.; Moon, W. K.; Hyeon, T. Multifunctional Uniform Nanoparticles Composed of a Magnetite Nanocrystal Core and a Mesoporous Silica Shell for Magnetic Resonance and Fluorescence Imaging and for Drug Delivery. *Angew. Chem. Int. Ed.* **2008**, *47* (44), 8438–8441.
(39) Baeza, A.; Guisasola, E.; Ruiz-Hernández, E.; Vallet-Regí, M. Magnetically Triggered Multidrug Release by Hybrid Mesoporous Silica Nanoparticles. *Chem. Mater.* **2012**, *24* (3), 517–524.
(40) Mertz, D.; Sandre, O.; Bégin-Colin, S. Drug Releasing Nanoplatforms Activated by Alternating Magnetic Fields. *Biochim. Biophys. Acta BBA - Gen. Subj.* **2017**, *1861* (6), 1617–1641.
(41) Hervault, A.; Thanh, N. T. K. Magnetic Nanoparticle-Based Therapeutic Agents for Thermo-Chemotherapy Treatment of Cancer. *Nanoscale* **2014**, *6* (20), 11553–11573.
(42) Mertz, D.; Harlepp, S.; Goetz, J.; Bégin, D.; Schlatter, G.; Bégin-Colin, S.; Hébraud, A. Nanocomposite Polymer Scaffolds Responding under External Stimuli for Drug Delivery and Tissue Engineering Applications. *Adv. Ther.* **2020**, *3* (2), 1900143.
(43) Cazares-Cortes, E.; Cabana-Montenegro, S.; Boitard, C.; Nehling, E.; Griffete, N.; Fresnais, J.; Wilhelm, C.; Abou-Hassan, A.; Ménager, C. Recent Insights in Magnetic Hyperthermia: From the "Hot-Spot" Effect for Local Delivery to Combined Magneto-Photo-Thermia Using Magneto-Plasmonic Hybrids. *Adv. Drug Deliv. Rev.* **2019**, *138*, 233–246.

(44) Narayan, R.; Nayak, U. Y.; Raichur, A. M.; Garg, S. Mesoporous Silica Nanoparticles: A Comprehensive Review on Synthesis and Recent Advances. *Pharmaceutics* **2018**, *10* (3), 118.
(45) Wang, Y.; Gu, H. Core–Shell-Type Magnetic Mesoporous Silica Nanocomposites for Bioimaging and Therapeutic Agent Delivery. *Adv. Mater.* **2015**, *27* (3), 576–585.
(46) Sun, Z.; Zhou, X.; Luo, W.; Yue, Q.; Zhang, Y.; Cheng, X.; Li, W.; Kong, B.; Deng, Y.; Zhao, D. Interfacial Engineering of Magnetic Particles with Porous Shells: Towards Magnetic Core–Porous Shell Microparticles. *Nano Today* **2016**, *11* (4), 464–482.
(47) Croissant, J.; Salles, D.; Maynadier, M.; Mongin, O.; Hugues, V.; Blanchard-Desce, M.; Cattoën, X.; Wong Chi Man, M.; Gallud, A.; Garcia, M. Mixed Periodic Mesoporous Organosilica Nanoparticles and Core–Shell Systems, Application to in Vitro Two-Photon Imaging, Therapy, and Drug Delivery. *Chem. Mater.* **2014**, *26* (24), 7214–7220.
(48) Zhao, W.; Wang, H.; Wang, H.; Han, Y.; Zheng, Z.; Liu, X.; Feng, B.; Zhang, H. Light-Responsive Dual-Functional Biodegradable Mesoporous Silica Nanoparticles with Drug Delivery and Lubrication Enhancement for the Treatment of Osteoarthritis. *Nanoscale* **2021**, *13* (13), 6394–6399.
(49) Zhou, S.; Zhong, Q.; Wang, Y.; Hu, P.; Zhong, W.; Huang, C.-B.; Yu, Z.-Q.; Ding, C.-D.; Liu, H.; Fu, J. Chemically Engineered Mesoporous Silica Nanoparticles-Based Intelligent Delivery Systems for Theranostic Applications in Multiple Cancerous/Non-Cancerous Diseases. *Coord. Chem. Rev.* **2022**, *452*, 214309.
(50) He, Y.; Shao, L.; Usman, I.; Hu, Y.; Pan, A.; Liang, S.; Xu, H. A PH-Responsive Dissociable Mesoporous Silica-Based Nanoplatform Enabling Efficient Dual-Drug Co-Delivery and Rapid Clearance for Cancer Therapy. *Biomater. Sci.* **2020**, *8* (12), 3418–3429.
(51) Perton, F.; Tasso, M.; Muñoz Medina, G. A.; Ménard, M.; Blanco-Andujar, C.; Portiansky, E.; van Raap, M. B. F.; Bégin, D.; Meyer, F.; Begin-Colin, S.; Mertz, D. Fluorescent and Magnetic Stellate Mesoporous Silica for Bimodal Imaging and Magnetic Hyperthermia. *Appl. Mater. Today* **2019**, *16*, 301–314.
(52) Ménard, M.; Meyer, F.; Affolter-Zbaraszczuk, C.; Rabineau, M.; Adam, A.; Ramirez, P. D.; Bégin-Colin, S.; Mertz, D. Design of Hybrid Protein-Coated Magnetic Core-Mesoporous Silica Shell Nanocomposites for MRI and Drug Release Assessed in a 3D Tumor Cell Model. *Nanotechnology* **2019**, *30* (17), 174001.
(53) Wells, C.; Vollin-Bringel, O.; Fiegel, V.; Harlepp, S.; Schueren, B. V. der; Bégin-Colin, S.; Bégin, D.; Mertz, D. Engineering of Mesoporous Silica Coated Carbon-Based Materials Optimized for an Ultrahigh Doxorubicin Payload and a Drug Release Activated by PH, T, and NIR-Light. *Adv. Funct. Mater.* **2018**, *28* (17), 1706996.
(54) Adam, A.; Parkhomenko, K.; Duenas-Ramirez, P.; Nadal, C.; Cotin, G.; Zorn, P.-E.; Choquet, P.; Bégin-Colin, S.; Mertz, D. Orienting the Pore Morphology of Core-Shell Magnetic Mesoporous Silica with the Sol-Gel Temperature. Influence on MRI and Magnetic Hyperthermia Properties. *Molecules* **2021**, *26* (4), 971.
(55) Wang, Y.; Sun, Y.; Wang, J.; Yang, Y.; Li, Y.; Yuan, Y.; Liu, C. Charge-Reversal APTES-Modified Mesoporous Silica Nanoparticles with High Drug Loading and Release Controllability. *ACS Appl. Mater. Interfaces* **2016**, *8* (27), 17166–17175.
(56) Mehmood, Y.; Khan, I. U.; Shahzad, Y.; Khan, R. U.; Khalid, S. H.; Yousaf, A. M.; Hussain, T.; Asghar, S.; Khalid, I.; Asif, M.; Shah, S. U. Amino-Decorated Mesoporous Silica Nanoparticles for Controlled Sofosbuvir Delivery. *Eur. J. Pharm. Sci.* **2020**, *143*, 105184.
(57) Perton, F.; Harlepp, S.; Follain, G.; Parkhomenko, K.; Goetz, J. G.; Bégin-Colin, S.; Mertz, D. Wrapped Stellate Silica Nanocomposites as Biocompatible Luminescent Nanoplatforms Assessed in Vivo. *J. Colloid Interface Sci.* **2019**, *542*, 469–482.
(58) Mertz, D.; Tan, P.; Wang, Y.; Goh, T. K.; Blencowe, A.; Caruso, F. Bromoisobutyramide as an Intermolecular Surface Binder for the Preparation of Free-Standing Biopolymer Assemblies. *Adv. Mater.* **2011**, *23* (47), 5668–5673.
(59) Walter, A.; Billotey, C.; Garofalo, A.; Ulhaq-Bouillet, C.; Lefèvre, C.; Taleb, J.; Laurent, S.; Vander Elst, L.; Muller, R. N.; Lartigue, L. Mastering the Shape and Composition of Dendronized Iron Oxide Nanoparticles to Tailor Magnetic Resonance Imaging and Hyperthermia. *Chem. Mater.* **2014**, *26* (18), 5252–5264.
(60) Baaziz, W.; Pichon, B. P.; Fleutot, S.; Liu, Y.; Lefevre, C.; Greneche, J.-M.; Toumi, M.; Mhiri, T.; Begin-Colin, S. Magnetic Iron Oxide Nanoparticles: Reproducible Tuning of the Size and Nanosized-Dependent Composition, Defects, and Spin Canting. *J. Phys. Chem. C* **2014**, *118* (7), 3795–3810.
(61) Cotin, G.; Blanco-Andujar, C.; Nguyen, D.-V.; Affolter, C.; Boutry, S.; Boos, A.; Ronot, P.; Uring-Lambert, B.; Choquet, P.; Zorn, P. E.; Mertz, D.; Laurent, S.; Muller, R. N.; Meyer, F.; Flesch, D. F.; Begin-Colin, S. Dendron Based Antifouling, MRI and Magnetic Hyperthermia Properties of Different Shaped Iron Oxide Nanoparticles. *Nanotechnology* **2019**, *30* (37), 374002.
(62) Cotin, G.; Blanco-Andujar, C.; Perton, F.; Asín, L.; Fuente, J. M. de la; Reichardt, W.; Schaffner, D.; Ngyen, D.-V.; Mertz, D.; Kiefer, C.; Meyer, F.; Spassov, S.; Ersen, O.; Chatzidakis, M.; Botton, G. A.;

Hénoumont, C.; Laurent, S.; Greneche, J.-M.; Teran, F. J.; Ortega, D.; Felder-Flesch, D.; Begin-Colin, S. Unveiling the Role of Surface, Size, Shape and Defects of Iron Oxide Nanoparticles for Theranostic Applications. *Nanoscale* **2021**, *13* (34), 14552–14571.

(63) Zhang, K.; Xu, L.-L.; Jiang, J.-G.; Calin, N.; Lam, K.-F.; Zhang, S.-J.; Wu, H.-H.; Wu, G.-D.; Albela, B.; Bonneviot, L. Facile Large-Scale Synthesis of Monodisperse Mesoporous Silica Nanospheres with Tunable Pore Structure. *J. Am. Chem. Soc.* **2013**, *135* (7), 2427–2430.

(64) Hai, J.; Piraux, H.; Mazarío, E.; Volatron, J.; Ha-Duong, N. T.; Decorse, P.; Lomas, J. S.; Verbeke, P.; Ammar, S.; Wilhelm, C.; Chahine, J.-M. E. H.; Hémadi, M. Maghemite Nanoparticles Coated with Human Serum Albumin: Combining Targeting by the Iron-Acquisition Pathway and Potential in Photothermal Therapies. *J. Mater. Chem. B* **2017**, *5* (17), 3154–3162.

(65) Cabana, S.; Curcio, A.; Michel, A.; Wilhelm, C.; Abou-Hassan, A. Iron Oxide Mediated Photothermal Therapy in the Second Biological Window: A Comparative Study between Magnetite/Maghemite Nanospheres and Nanoflowers. *Nanomaterials* **2020**, *10* (8), 1548.

(66) Lozano-Pedraza, C.; Plaza-Mayoral, E.; Espinosa, A.; Sot, B.; Serrano, A.; Salas, G.; Blanco-Andujar, C.; Cotin, G.; Felder-Flesch, D.; Begin-Colin, S.; J. Teran, F. Assessing the Parameters Modulating Optical Losses of Iron Oxide Nanoparticles under near Infrared Irradiation. *Nanoscale Adv.* **2021**, *3* (22), 6490–6502.

(67) Nemec, S.; Kralj, S.; Wilhelm, C.; Abou-Hassan, A.; Rols, M.-P.; Kolosnjaj-Tabi, J. Comparison of Iron Oxide Nanoparticles in Photothermia and Magnetic Hyperthermia: Effects of Clustering and Silica Encapsulation on Nanoparticles' Heating Yield. *Appl. Sci.* **2020**, *10* (20), 7322.

(68) Kolosnjaj-Tabi, J.; Kralj, S.; Griseti, E.; Nemec, S.; Wilhelm, C.; Plan Sangnier, A.; Bellard, E.; Fourquaux, I.; Golzio, M.; Rols, M.-P. Magnetic Silica-Coated Iron Oxide Nanochains as Photothermal Agents, Disrupting the Extracellular Matrix, and Eradicating Cancer Cells. *Cancers* **2019**, *11* (12), 2040.

(69) Duenas-Ramirez, P.; Bertagnolli, C.; Müller, R.; Sartori, K.; Boos, A.; Elhabiri, M.; Bégin-Colin, S.; Mertz, D. Highly Chelating Stellate Mesoporous Silica Nanoparticles for Specific Iron Removal from Biological Media. *J. Colloid Interface Sci.* **2020**, *579*, 140–151.

(70) Li, B.; Harlepp, S.; Gensbittel, V.; Wells, C. J. R.; Bringel, O.; Goetz, J. G.; Begin-Colin, S.; Tasso, M.; Begin, D.; Mertz, D. Near Infra-Red Light Responsive Carbon Nanotubes@mesoporous Silica for Photothermia and Drug Delivery to Cancer Cells. *Mater. Today Chem.* **2020**, *17*, 100308.

(71) Liu, J.; Detrembleur, C.; De Pauw-Gillet, M.-C.; Mornet, S.; Vander Elst, L.; Laurent, S.; Jérôme, C.; Duguet, E. Heat-Triggered Drug Release Systems Based on Mesoporous Silica Nanoparticles Filled with a Maghemite Core and Phase-Change Molecules as Gatekeepers. *J. Mater. Chem. B* **2014**, *2* (1), 59–70.

(72) Chang, B.; Guo, J.; Liu, C.; Qian, J.; Yang, W. Surface Functionalization of Magnetic Mesoporous Silica Nanoparticles for Controlled Drug Release. *J. Mater. Chem.* **2010**, *20* (44), 9941–9947.

(73) Hayakawa, E.; Furuya, K.; Ueno, H.; Kuroda, T.; Moriyama, M.; Konda, A., Visible Absorption and Proton Nuclear Magnetic Resonance Studies on the Self-Association of Doxorubicin in Aqueous Solution. *Chem. Pharm. Bull. (Tokyo)* **1991**, *39* (4), 1009–1012.

(74) Menozzi, M.; Valentini, L.; Vannini, E.; Arcamone, F. Self-Association of Doxorubicin and Related Compounds in Aqueous Solution. *J. Pharm. Sci.* **1984**, *73* (6), 766–770.

(75) Tasca, E.; Alba, J.; Galantini, L.; D'Abramo, M.; Giuliani, A. M.; Amadei, A.; Palazzo, G.; Giustini, M. The Self-Association Equilibria of Doxorubicin at High Concentration and Ionic Strength Characterized by Fluorescence Spectroscopy and Molecular Dynamics Simulations. *Colloids Surf. Physicochem. Eng. Asp.* **2019**, *577*, 517–522.

(76) Tasca, E.; D'Abramo, M.; Galantini, L.; Giuliani, A. M.; Pavel, N. V.; Palazzo, G.; Giustini, M. A Stereochemically Driven Supramolecular Polymerisation. *Chem. – Eur. J.* **2018**, *24* (32), 8195–8204.

(77) Osmani, N.; Goetz, J. G. Multiscale Imaging of Metastasis in Zebrafish. *Trends Cancer* **2019**, *5* (12), 766–778.

(78) Scharlach, C.; Kratz, H.; Wiekhorst, F.; Warmuth, C.; Schnorr, J.; Genter, G.; Ebert, M.; Mueller, S.; Schellenberger, E. Synthesis of Acid-Stabilized Iron Oxide Nanoparticles and Comparison for Targeting Atherosclerotic Plaques: Evaluation by MRI, Quantitative MPS, and TEM Alternative to Ambiguous Prussian Blue Iron Staining. *Nanomedicine Nanotechnol. Biol. Med.* **2015**, *11* (5), 1085–1095.

(79) Millward, J. M.; Schnorr, J.; Taupitz, M.; Wagner, S.; Wuerfel, J. T.; Infante-Duarte, C. Iron Oxide Magnetic Nanoparticles Highlight Early Involvement of the Choroid Plexus in Central Nervous System Inflammation. *ASN Neuro* **2013**, *5* (2), AN20120081.

Chapter IV

Design of innovative implantable photoresponsive hydrogel build up from enzyme-coated carbon nanotubes

Chapter IV. Design of innovative implantable photoresponsive hydrogel build up from enzyme-coated carbon nanotubes

Context

In the previous chapter, we demonstrated that IO@STMS NPs can be an adapted nanosystems for new applications combining PTT and drug delivery applications. Preliminary biological tests showed an efficient antitumor activity and a synergetic effect of the dual therapy mode on the cell death. However, in some cancer cases, it can be very difficult to target the tumor sites by using circulating NPs or drugs injected in the blood stream. Either by renal clearance or uptake by macrophages, the drug can be eliminated resulting in an ineffective treatment. But it can also accumulate in healthy tissues, usually filtering organs such as liver, bladder, spleen and causing unwanted toxicity.

Implantable local drug delivery systems are now designed to address these shortcomings. By being implanted around or inside the tumor, they should allow to deliver drugs locally, to present controlled drug release profile to maintain therapeutic concentration over time and to prevent the drug clearance.[1] Smart implants that could be remotely activated by external fields such as NIR light are thus particularly needed. These could be obtained by the combination of smart NPs as we described above and a biocompatible implantable matrix. Polymer scaffolds and especially hydrogels are emerging as power tools to design this new generation of materials.[2] The incorporation of NPs also has the advantage to increase the mechanical stability of the hydrogel. As we detailed in Chapter 1, CNTs are among the mechanically strongest materials and have shown excellent photothermal properties; thus they appear as particularly suited materials to be used a fillers in hydrogels to create smart implantable scaffolds (**Figure 4-1**). Moreover, incorporation of CNTs in an enough stable polymer matrix would prevent any risk of dissemination of the particles in body.

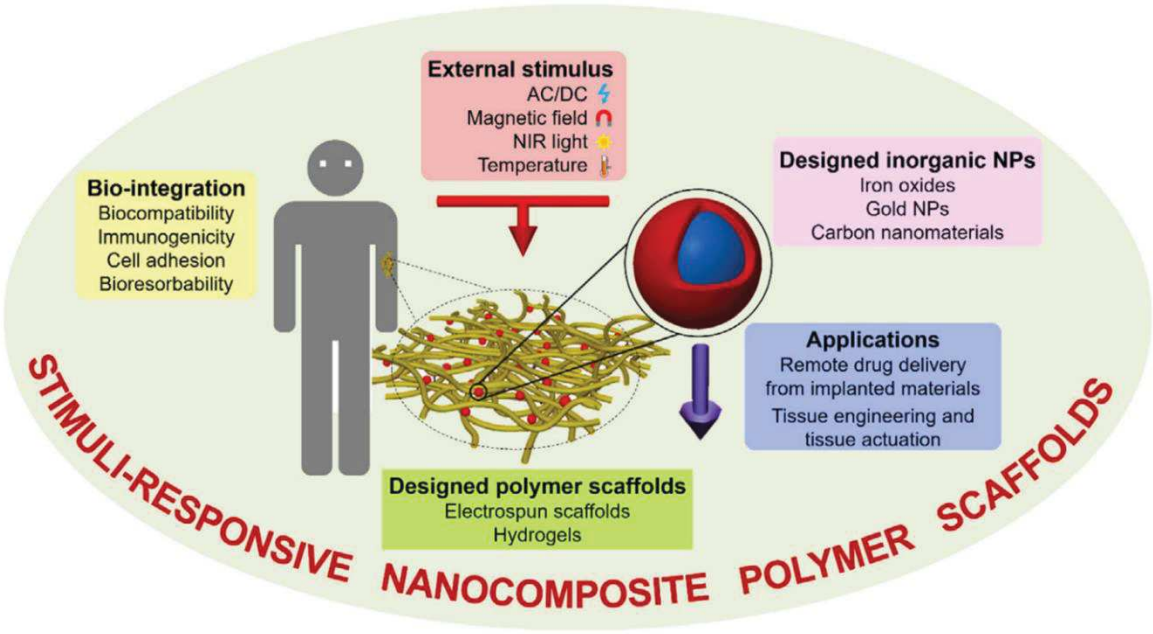

Figure 4-1. Scheme illustrating the components for the design of smart stimuli-responsive nanocomposite polymer scaffolds and their challenges for drug delivery applications.[2]

Thus, the strategy developed in the previous chapters was also transposed to CNTs. This study was initiated and described in the frame of the PhD thesis of Bing Li ((2017-2020), University of Strasbourg, thesis directors: D. Begin and D. Mertz, chapter 3). During the last year of my PhD thesis, I have been importantly involved in this work, to reproduce, complete and finalize various investigations, especially synthesizing drug-loaded nanocomposite hydrogels and setting up NIR light irradiation studies to evaluate SAR measurements and implement drug release studies. This collaborative work is currently submitted to the journal *Materalia, (Elsevier)*: **"Near-infrared Responsive Nanocomposite Hydrogels Made from Enzyme-Coated Carbon Nanotubes@ Large Pore Mesoporous Silica for Remotely Triggered Drug Delivery"** from Bing Li, Alexandre Adam, Miryam Criado-Gonzalez, Loïc Jierry, Joëlle Bizeau, Alain Chaumont, Sebastien Harlepp, Christophe Mélart, Sylvie Begin-Colin, Dominique Begin, Damien Mertz.

Hence, the next pages provide first a description of my contributions to this work and then the submitted manuscript to *Materialia* by B. Li et al.

In this work, we showed how to coat CNTs with large pore MS to synthesize innovative CNT-core@MS-shell NPs. Then, an original method to produce a self-assembled hydrogel from the CNT@MS was proposed. By immobilization of an enzyme on CNT@MS, we were able to trigger the formation of a supramolecular peptide hydrogel. During the gelification, DOX was added to the formulation. Afterwards, the photothermal activity of the gel was studied. The main goal here was to produce a smart hydrogel which is able to release DOX by using NIR light as the delivery trigger.

- First, I have been involved in the synthesis and functionalization of the large pore mesoporous silica shell around sliced CNTs (CNTs@LPMS). By using strong acidic conditions and sonication, the

commercial CNTs which are very long (size of several microns) were cut into smaller sections (*ca.* hundreds nm). This process also allows the purification of CNTs which can be contaminated with metallic species. These strong conditions can also oxidize their surface and thus they are reduced in the oven under inter atmosphere before use. CTAB surfactant is then added. Its hydrophobic alkyl chain interacts with the surface of CNT which results in well-dispersed CNTs in aqueous phase. Then, swelling agents are added (decane and 1,3,5-triisopropylbenzene) and play a key role in the growth of a silica shell having large pores. These agents are not soluble in water and thus enter the CTAB micelles to join their hydrophobic core. Consequently, the micelles swell and the condensing silicate species organize around larger domains which produce large pore in silica (CNTs@LPMS). The large pore silica shell was then functionalized by using the same method as previously described in Chapter III. First, the surface is modified by APTES to bring amine groups which then are converted into isobutyramide functions (IBAM) by using an acyl chloride (isobutyryl chloride). As we saw above, IBAM functions allow to load a broad variety of molecules and in particular it can carry proteins such as enzymes. Here, bovine alkaline phosphatase (AP) is immobilized on CNTs@LPMS@IBAM.This immobilized enzyme is thus used as an initiator for peptide hydrogelation as described in the following manuscript.

- Then, I have been involved in producing hydrogels assembled from dissolved tripeptides. Indeed, the peptide was properly selected in order that, by the reaction of the enzyme on the peptide, the obtained product is able to self-assemble into large structures. To react with alkaline phosphatase enzyme, a phosphated tripeptide (Fmoc-FF*p*Y) whose phosphate group is removed by the enzyme in alkaline conditions, was chosen. This dephosphated peptide is known to be prone to self-assembly in defined conditions. In this frame, I synthesized and optimized the production of supramolecular hydrogels which were additionally loaded with DOX. TEM and cryo-SEM images showed that the peptide self-assemble into a dense network of nanofibers. As the enzyme is only presented at the surface of the nanocomposite, the CNT@LPMS@IBAM@AP act as the starting point of the fibers growth and thus cross-linking objects in the gel. The DOX is also shown to be incorporated in and in between the fibers such as detailed below.
- Lastly, I investigated the possibility of triggering the release of DOX from the gels when they are heated either in a thermostated oil bath or by the intermediate of light-irradiation with a NIR laser. First, the DOX release upon heating in hot bath at different temperatures were evaluated and the influence of the temperature on the drug release was shown. Moreover, CNTs present an excellent conversion of NIR light into heat and this property is promising to build biomedical implants that can be remotely activated. I have implemented a setup to irradiate properly gels with a NIR laser. Then, SAR and the heating profiles of gels containing different concentrations of CNT composites were measured. This led us to highlight the potential of remotely triggered drug delivery from supramolecular self-assembled hydrogel by using NIR light.
- This full work submitted to *Materialia* is presented in the following pages.

Near-infrared Responsive Nanocomposite Hydrogels Made from Enzyme-Coated Carbon Nanotubes@ Large Pore Mesoporous Silica for Remotely Triggered Drug Delivery

Bing Li[1,2], **Alexandre Adam[1]**, Miryam Criado-Gonzalez[3], Loïc Jierry[3], Joëlle Bizeau[1], Alain Chaumont[4], Sebastien Harlepp[5-7], Christophe Mélart[2], Sylvie Bégin-Colin[1], Dominique Bégin[2], Damien Mertz[1]

[1]Institut de Physique et Chimie des Matériaux de Strasbourg (IPCMS), UMR-7504 CNRS-Université de Strasbourg, 23 rue du Lœss, BP 34 67034, Strasbourg Cedex 2, France

[2]Institut de Chimie et Procédés pour l'Energie, l'Environnement et la Santé (ICPEES), UMR-7515 CNRS-Université de Strasbourg, 25 rue Becquerel, 67087 Strasbourg, Cedex 2, France

[3] Institut Charles Sadron (ICS) CNRS UPR 22, 23 rue du Loess BP 84407, 67034 Strasbourg cedex

[4]UMR 7140 - Chimie de la Matière Complexe, 4 rue Blaise Pascal, 67081 Strasbourg Cedex

[5] Tumor Biomechanics, INSERM UMR_S1109, Strasbourg, France,

[6] Université de Strasbourg, Strasbourg, France.

[7] Fédération de Médecine Translationnelle de Strasbourg (FMTS), Strasbourg, France.

ABSTRACT. The design of smart nanocomposite supramolecular scaffolds for tissue engineering or anticancer applications, able to release drugs under external fields is currently a challenge. Such architectures require not only strong interactions between the polymer matrix and externally responsive nanomaterials, but also an efficient strategy for the loading and release of drugs. Herein, we address an original approach to trigger the self-assembly of peptide hydrogel from enzyme-coated carbon-based nanocomposites which act as initiators and cross-linking points of the resulting nanocomposite hydrogel. Carbon nanotubes (CNTs), chosen given their photothermal behavior under near infra-red (NIR) light, were coated with large pore (>10 nm) mesoporous silica (CNT@LPMS) which are very suitable for a high loading of enzymes. Then, based on an original isobutyramide (IBAM)-mediated coating, a huge amount of alkaline phosphatase (AP) (>100% wt) was immobilized within the large pores allowing the localized growth of peptide nanofibrous network resulting in supramolecular hydrogel. The incorporation of Doxorubicin (DOX) during the hydrogelation process leads to a reservoir material of anti-cancer agents whose release is photothermally triggered by the NIR light-induced hyperthermia temperature. Combination of rheological studies and molecular simulations indicate an original mechanism in which DOX is included within the peptide nanofibers.

Graphical Abstract.

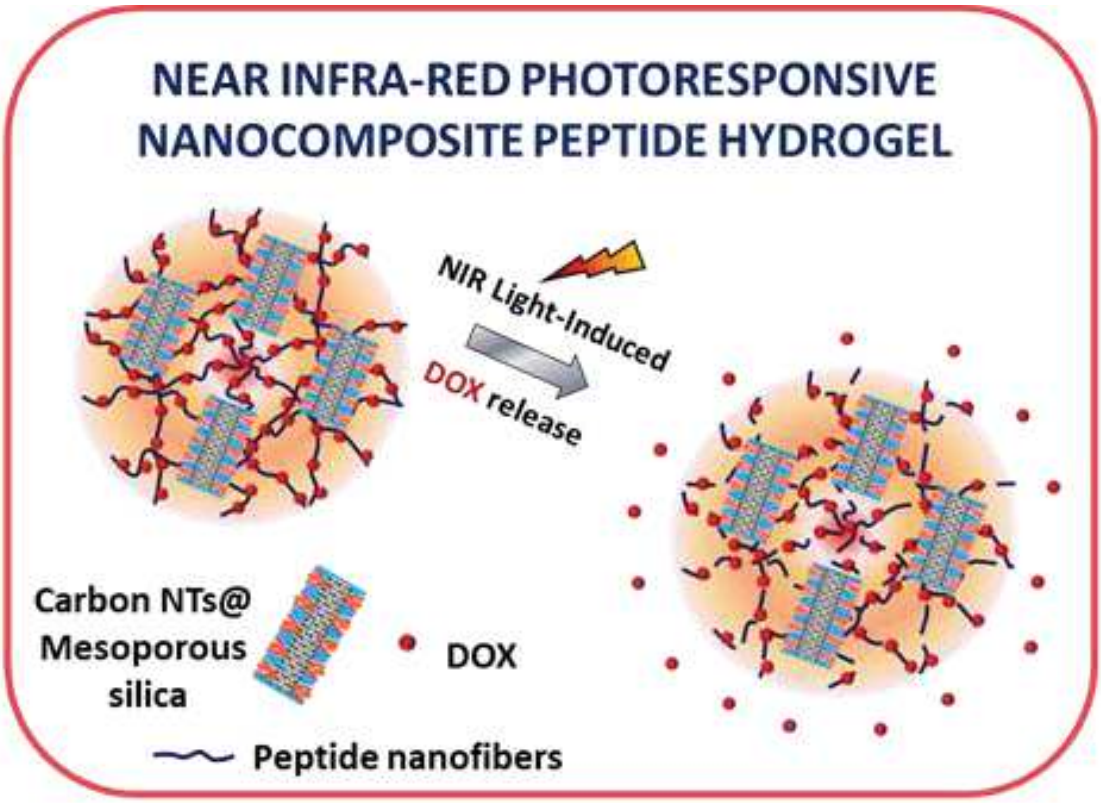

IV.1. Introduction

Today, the meeting between macromolecular science and nanomaterial synthesis lets envisioning the development of new and powerful stimuli-responsive advanced composite materials[3,4] for a wide range of technological applications such as energy storage,[5] self-repairing materials,[6] catalysis[7] or sensing.[8] In particular, in the field of nanomedicine and tissue engineering, the development of such nano-engineered smart composite materials combining nanomaterials in a supramolecular matrix has become blossoming these last years.[2,9,10] The polymer matrix of such nanocomposite assemblies ensures features such as reinforced controlled mechanical properties, biocompatibility, and a suitable macroscopic support for cell adhesion/interaction, and the nanomaterials ensure the role of mechanical fillers, anchoring local points and eventually, response under external fields. Usual nanomaterials such as gold or iron oxide nanoparticles (NPs) are particularly attractive nanocomponents of smart remotely responsive polymer scaffold materials given respectively their response to external fields such as near infra-red (NIR) light[11,12] or magnetic fields[13–15] due to their plasmonic or magnetization properties. One main challenge today of such stimuli responsive nanocomposite scaffolds is the need of a specific design favoring suitable drug loading and release as standard polymer matrix may load low amount of drugs or retain the drug with limited release respectively due to either too weak or too strong interactions between the matrix and the nanomaterials.

Hence, designing such smart functional scaffolds is currently an important challenge since their internal architecture needs to be built on a very controlled fashion. To achieve this aim, a fine engineering of the surface of nanomaterials is highly required which is addressed in this work. An ideal surface should have a high surface area to ensure high linker surface grafting and multiple connection points with the network polymer. Moreover, the surface should be easily chemically modified with suitable surface binders ensuring tight and strong contacts with the polymer network. Indeed, though many studies report the insertion of nanoparticles within a polymer matrix, there is still few studies reporting the use of surface engineered nanoparticles to finely crosslink the polymer network which is the challenge addressed here.

Among the possible nanomaterials choices, carbon nanotubes (CNTs) are particularly attractive to design nanocomposite scaffolds because they bring high mechanical properties, high electrical conductivity and NIR light induced thermal activation properties.[16,17] However, for biomedical applications, given their intrinsic surface hydrophobicity, the capping of such carbon materials with hydrophilic coating is necessary.[18,19] Among the various capping possibilities described in the literature, which encompasses molecules or polymer coatings[20,21], mesoporous silica (MS) is a particularly suitable coating of CNTs[22–24]. Indeed, in addition to providing a great dispersion in aqueous buffers, the silanol groups can be easily chemically modified with a range of silane precursors and the high surface area allows the loading with various types of drugs.[25–27] Besides, the vast majority of such design concern

small pore silica and the design of large pore silica around CNTs (or other nanomaterial) is very few reported.[28] Especially such large pore mesoporous silica (LPMS) design is particularly suitable for the immobilization of high molecular weight biomolecules such as enzyme, DNA or other biopolymer of therapeutic interest. As compared to strategies to anchor polymers or molecules, the advantages of MS rely on better grafting density and better colloidal stability. Some works have reported different ways allow to immobilize biofunctional proteins such as enzymes in CNTs by chemical strategies[29,30], however a better coverage density is currently needed and the chemical crosslinking/coupling may induce loss of the enzymatic activity.

Among the polymer matrix possibilities, hydrogels are particularly interesting systems as their chemistry and their physicochemical features can be easily controlled by the polymer chemistry and the gel formation process. Even if main hydrogel development concerns synthetic polymers such as polyethyleneglycol, Pluronics™ etc., there are important developments towards natural polymer building blocks such as peptides to constitute a biocompatible/biologically favorable hydrogel. Recently, a new biocompatible and effective approach has been developed to initiate locally the formation of hydrogel exclusively from any kind of surface[31], in particular from nano-objects.[32–34] It is based on the concept of enzyme-assisted self-assembly[35] of peptides where the enzyme is immobilized onto the surface of a nano-object and transforms the precursor peptides into hydrogelators. This strategy ensures the growth of a fibrous network of self-assembled peptide nanofibers from the surface of the enzyme-modified nano-objects. Thus, it allows the generation of a composite nanomaterial, where the nano-objects are specifically located at the nodes of its internal architecture. Herein, the assembly chosen is based on a tripeptide, *i.e.* Fmoc-FFY. [36]

In this work, as we have recently shown on stellate silica nanoparticles in a short letter[37], we propose a powerful and facile strategy to trigger the self-assembly of a peptide hydrogel from enzyme-coated CNT@LPMS composites, which act as initiators of the peptide self-assembly and cross-linking points of the resulting nanocomposite hydrogel (**Figure 4-2**). The association of CNT@LPMS with the self-assembled peptide hydrogel as a polymer scaffold appears as an innovative strategy for the development of a new generation of stimuli responsive hydrogel nanocomposites having suitable and innovative features for nanomedecine applications. In this work, we address several originality as compared to the literature. Firstly, the design of new carbon-based nanocomposites made of large pore MS surrounding CNTs is achieved which is few reported in the literature. The LPMS design is well adapted for loading high molecular weight molecules such as enzymes with suitable surface binders. Secondly, the immobilization of enzyme alkaline phosphatase (AP) with very high loading capacity (sup 100%) within the porous shell thanks to the use of isobutyramide (IBAM) grafts is demonstrated. Previously, IBAM binders grafted at silica surface were already shown efficient to immobilize range of biopolymers of therapeutic interest including: nucleic acids[38], polysaccharides[39], or serum albumin[40,41], and their use to immobilize enzymes on non-porous silica was shown with preservation of their enzymatic catalysis functionality.[42,43] Here, the biocatalytic activity of such AP-coated CNT@LPMS is

then assessed by following the conversion of AP enzymatic substrate paranitrophenylphosphate (pNPP) into paranitrophenol (pNP). Thirdly, with the aim to create new and powerful self-assembled peptide hydrogel nanocomposites whose assembly is triggered by the dephosphorylation catalytic activity of AP, the self-assembly of Fmoc−FFY peptide (Fmoc: fluorenylmethyloxycarbonyl; F: phenylalanine; Y: tyrosine) is assessed in the presence of AP-coated CNT@LPMS. The mechanical properties of such nanocomposite hydrogels are investigated through rheological studies and without/with the loading of doxorubicin (DOX), an antitumor drug. The ability to release DOX upon NIR light–induced hyperthermia is then investigated. Finally, to decipher the mechanism of the nanocomposite hydrogel assembly, a molecular simulation study is proposed to provide a model of drug binding within the peptide architecture and its releasing mechanism.

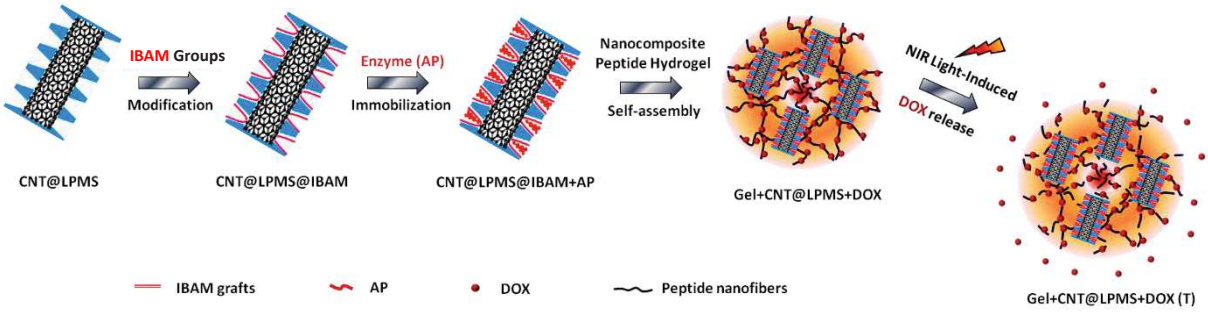

Figure 4-2. Schematic representation yielding to nanocomposite supramolecular hydrogels self-assembled from AP-immobilized CNT@LPMS composites and the NIR light photothermally induced DOX release.

IV.2. Experimental section

IV.2.1. Chemicals

Carbon nanotubes PR-24-XT-PS (CNTs) were purchased from Pyrograf-III. Cetyltrimethylammonium bromide (CTAB) was purchased from Roth (France). Nitric acid (HNO_3), sulfuric acid (H_2SO_4), ethanol (EtOH), tetraethyl orthosilicate (TEOS), sodium hydroxide (NaOH), ammonium nitrate (NH_4NO_3, >99%), 3-aminopropyltriethoxysilane (APTES), isobutyryl chloride (IBC), triethylamine (Et_3N), dimethylformamide (DMF), dimethylsulfoxide (DMSO), sodium bicarbonate ($NaHCO_3$), fluorescein isothiocyanate (FITC), ethylene glycol (EG, 99.8%), decane (≥99%), bovine alkaline phosphatase (AP) and 4-Nitrophenyl phosphate disodium hexahydrate (pNPP-Na) were purchased from Sigma-Aldrich (France). Ammonium hydroxide solution (25% in H_2O) was purchased from Fluka. Doxorubicin hydrochloride (DOX, purity 99%) was purchased from OChem Incorporation (USA). Sodium tetraborate anhydrous (borax) and 1, 3, 5-Triisopropylbenzene (TIB, 95%) were supplied by Acros Organics. Fmoc−FF*p*Y peptide (Fmoc: fluorenylmethyloxycarbonyl; F: phenylalanine; Y: tyrosine; p: phosphate group) was purchased from PepMic company.

IV.2.2. Procedures

Synthesis of large pore mesoporous silica coated CNTs (CNT@LPMS).

First, the pristine CNTs were cleaved in a better-suited length. Typically, 0.75 g of pristine CNTs was added into 108 mL mixture of H_2SO_4/HNO_3 (Volume ratio = 3 : 1,) and sonicated at 0 °C for 24 h. The mixture was then monitored to neutrality with NaOH (1 M) solution. The sliced CNTs were washed with distilled water (3 x 25 mL), dried at room temperature, and then reduced at 900°C for 2 h under argon. The resulting sliced CNTs were used as the initial material for the following silica layer coating step.

100 mg of sliced CNTs was well dispersed in 120 mL distilled water by ultrasonication (Vibracell 75043 from Bioblock Scientific, 2 x 10 min, Power = 750 W, Amplitude = 40%, Temperature = 30°C, runs: 50" ON, 50" OFF). 684 mg of CTAB was dissolved in 60 mL of distilled water and stirred at room temperature for 40 min at 250 rpm. Then, the CNTs solution was mixed with the CTAB solution, and the mixture was sonicated for 30 min. After that, 45 mL of ethylene glycol and 456 µL of NaOH (1 M) solution were added, and the mixture was stirred at 250 rpm at 70 °C. After 1 h, 1.095 mL of decane was added and kept stirring at 250 rpm at 70 °C. After continuous stirring for 2 h, 1.35 mL of TIB was added. Then, stirring was continued at 70 °C at 250 rpm for another 2 h, and finally 684 µL of TEOS was added, and stirring was continued for 3 h under the same conditions. After the sol gel reaction, LPMS coated CNTs product was obtained, followed by centrifugation (8000 g x 10 min) and washing with EtOH (2 x 20 mL).

Surfactant extraction from the LPMS coated composite.

The removal of CTAB template agent from the silica pores was achieved by redispersing the composite in 25 mL of NH_4NO_3 (20 mg/mL in EtOH), and extracting with stirring at 60°C for 1 h. Then 10 µL of the mixture was diluted in 1 mL of water and measured its Zeta potential. The surface charge of the composite measured by ZP allows determining when all the CTAB templates were removed. The procedure was repeated until almost all the CTAB templates were extracted from the composite (approximately 5 extractions were required). At this point, the composite was denoted as CNT@LPMS.

FITC labeling.

AP was fluorescently labeled with FITC using a stoichiometry of 2 moles of fluorescent dye per mole of enzyme. 100 mg of AP was first dissolved in 10 mL of sodium bicarbonate buffer ($NaHCO_3$ 50 mM, pH 8.5) and then 212 µL of FITC (10 mg/mL in DMSO) was added into the AP solution. The mixture was stirred on the wheel for 24 h and then dialyzed for 2 days (membrane pore size: 10 kDa) in distilled water at room temperature to remove the free FITC. The water was changed every 2 h. Finally, the resulting AP^{FITC} was adjusted to a concentration of 10 mg/mL for further use.

APTES functionalization of silica surface.

Firstly, 20 mg of CNT@LPMS composites were dispersed in 6 mL of EtOH. Then 0.3 mL of ammonium hydroxide (25%) was added and the mixture was vortexed for 10 s, followed with the addition of 1.25 mL of APTES. After 2 h of stirring on the wheel at room temperature, the amino modified composites were centrifuged (13 000g x 10 min) and washed with EtOH (1 x 10 mL) and DMF (2 x 10 mL).

IBAM modification.

The resulting amino-modified composites were firstly dispersed in a mixed solution of 0.24 mL of Et_3N and 3 mL of DMF, and vortexed for 10 s. After that, a solution containing of 0.55 mL of IBC and 3 mL of DMF was added. After stirring on the wheel for 2 h at room temperature, about 1 mL of distilled water was added to dissolve the inorganic salt formed from the reaction, and finally a clear orange solution was obtained. The resulting IBAM-modified composites were separated via centrifugation (13 000g x 10 min) and then washed with DMF (1 x 5 mL). Finally, the IBAM moieties functionalized composites were dispersed in DMF and stored on the wheel with stirring at room temperature.

AP immobilization on the CNT@LPMS@IBAM composites.

4 mg of chemically modified CNT@LPMS@IBAM was isolated by centrifugation (13 000g x 10 min) to remove the DMF, then washed with distilled water (1 x 1 mL). After that, the composite was dispersed in 1 mL of a certain concentration (from 100 µg/mL to 25 000 µg/mL) of AP^{FITC} aqueous solution and sonicated for 10 s. The mixture was stirred on the wheel for 1 h at room temperature and then centrifuged (13 000g x 10 min). The supernatant was collected and diluted with water to a certain multiple in order to quantify AP^{FITC} remaining in the supernatant through the calibration curve of AP^{FITC} (e.g. the supernatant of 500 µg/mL impregnating solution is diluted by 2 times, and the supernatant of 25 000 µg/mL impregnating solution is diluted by 160 times). The diluted supernatant was measured by spectrofluorimetry. By recording the maximum fluorescence intensity at 520 nm, the AP^{FITC} remaining in the supernatant could be calculated, which allow us determining the mass of AP^{FITC} adsorbed on the chemically modified CNT@LPMS@IBAM composites. The AP^{FITC} immobilized composites were washed with water (1 mL) to remove the loosely bound enzyme, centrifuged (13 000g x 10 min) and then dried at 40 °C for 3 days. The dry AP^{FITC} immobilized composites were analyzed by TGA to confirm the actual immobilization amount of AP^{FITC}.

Enzymatic activity measurement of the immobilized AP.

The enzymatic activity of the immobilized AP was performed on the composites loaded with 100 wt% AP relative to CNT@LPMS, which were denoted as CNT@LPMS@IBAM+AP (100 wt%). The assay was performed using p-Nitrophenyl phosphate disodium hexahydrate (pNPP-Na) as the substrate. Firstly, 20 µL of AP immobilized-composites (0.1 mg/mL in 50 mM $NaHCO_3$ buffer) was

dispersed in 0.98 mL $NaHCO_3$ buffer (50 mM, pH = 8.5) and sonicated for 10 s. Then 1 mL of pNPP-Na substrate solution (0.1 mg/mL in 50 mM $NaHCO_3$ buffer) was added and the mixture was vortexed for 10 s. That is, the final concentration of pNPP-Na substrate was 0.05 mg/mL. After that, the mixture was covered with aluminum foil and placed in the 25, 37 and 42 °C water baths. The subsequent conversion of pNPP-Na into p-nitrophenol (pPN) and disodium phosphate was catalyzed by the immobilized AP. The enzymatic hydrolysis of pNPP-Na was detected by the presence of the yellow color product pNP using a UV-vis spectrometry. After reacting for 10, 20, 30, 40, 60, 90 and 120 min, the mixture was transferred to a 1 cm path length cell. The hydrolysis product pNP was monitored by the UV-vis spectroscopy, and the maximum absorbance at λ = 405 nm was recorded.

Formation of nanocomposite supramolecular hydrogels.

The peptide self-assembly process was synthesized according to the reported procedure.[44] Firstly, 1 mg of Fmoc-FF*p*Y peptide was dissolved in 155 µL borax buffer (25 mM, pH = 9.5) by vortex for 60 s. Then, 25 µL of DOX aqueous solution at 4 mg/mL was added into the peptide solution and the mixture was vortexed for 20 s. Finally, 20 µL of CNT@LPMS@IBAM+AP (100 wt%) composites (1 mg/mL) was added into the mixture of peptide and DOX. The mixture was vortexed for 20 s, and then allowed to stand at room temperature for 24 h to self-assemble to form hydrogel. The same procedure was used to prepare hydrogels without DOX, except that 1 mg of Fmoc-FF*p*Y peptide was dissolved in 180 µL borax buffer (25 mM, pH = 9.5). The hydrogels with and without DOX assembly formed from CNT@LPMS@IBAM+AP composites are denoted as: Gel+CNT@LPMS+DOX, and Gel+CNT@LPMS, respectively. The gel prepared from free AP is denoted as Gel, which was obtained by dissolving 1 mg of Fmoc-FF*p*Y peptide in 180 µL of borax buffer and contacting with 20 µL of AP solution in 1 mg/mL for 24 h. The final concentrations of Fmoc-FF*p*Y, CNT@LPMS@IBAM+AP composite or free AP, and DOX in the hydrogel were maintained respectively 5 mg/mL, 0.1 mg/mL and 0.5 mg/mL.

DOX release from nanocomposite hydrogel with heated water baths.

After the hydrogel formation, 1 mL of distilled water was added slowly along the tube wall. The tubes were then covered with aluminum foil and placed in the water baths for 24 h. Thereafter, the supernatant containing the released DOX was collected and then measured by UV-vis spectrometry. The amount of DOX released in the supernatant was then calculated by the DOX calibration curve. The calibration curve of DOX aqueous solution was obtained by measuring the absorbance of different DOX concentrations at 480 nm. An inverted tube test was conducted after to detect the stability of the hydrogel.

DOX release from nanocomposite hydrogel by NIR laser stimulation.

In the vial containing the hydrogel, 1 mL of distilled water was added. The vial was then placed in the sample holder and exposed to the 1064 nm NIR laser with a power density of 1 W/cm² for 2 hours.

The temperature elevation was recorded as a function of time with a probe immersed in the aqueous phase. Right after the irradiation, the supernatant was collected and measured by UV-Vis spectrometry in order to calculate the amount of DOX released.

IV.2.3. Characterization Methods

Nitrogen adsorption-desorption analysis.

The Nitrogen adsorption-desorption isotherms were measured on a Tristar 3000 Gas Adsorption Analyzer (Micromeritics). Before each measurement, the sample was outgassed under vacuum at 150 °C for 4 h. The specific surface area was calculated by Brunauer-Emmett-Teller (BET) method, the pore size and pore volume were calculated by Barrett-Joyner-Halenda model (BJH).

Zeta potential and dynamic light scattering measurements.

Zeta potential (ZP) and dynamic light scattering (DLS) measurements were carried out using Zetasizer nano ZS manufactured by Malvern Instruments. Zeta potential measurements were performed by diluting 10 µL of the stock suspensions in 1 mL of water using a DTS1070 folded capillary cell. The measurements were carried out at 25 °C in triplicate. The DLS measurements were carried out by measuring the particle size distribution at concentration of 0.5 mg/mL in water in triplicate.

Thermal gravimetric analysis.

The thermogravimetric analysis (TGA) was performed on a Q5000 Automatic Sample Processor (TA Instruments). The runs were started from room temperature to 800 °C with a heating rate of 10 °C/min, under an air flow rate of 25 mL/min.

Scanning electron microscopy.

The morphology of CNT@LPMS composites were characterized by scanning electron microscopy (SEM) on the JEOL F2600 microscope equipped with a CCD camera. The tested composites were firstly dispersed in EtOH and a drop of the suspension was dropped on a copper grid for observation.

Transmission electron microscopy.

Transmission electron microscopy (TEM) images were taken via a JEOL 2100 apparatus with high resolution operating at an acceleration voltage of 200 kV. The CNT@LPMS composites were firstly dispersed in EtOH, then a few drops of the suspension were deposited on a carbon-coated copper grid and then dried at room temperature before observation.

Fluorescence spectroscopy.

The fluorescence spectra of AP^{FITC} were obtained on a Horiba scientific Fluorolog spectrophotometer using a 1 cm path length cell. The emission spectra were recorded from 505 to 600 nm upon an excitation wavelength of 495 nm.

UV-Vis spectroscopy.

UV-vis spectroscopy was used to determine the enzymatic activity of the immobilized AP and the amount of drug released in the supernatant. The UV-vis spectra were recorded by a Lambda 950 UV/vis Spectrometer (Perkin Elmer). The colorless substrate pNPP-Na resulted in a yellow product by enzymatic hydrolysis of pNPP-Na in the presence of AP, with absorbance at $\lambda = 405$ nm. The relative enzymatic activity of immobilized AP was determined by recording the absorbance of pNPP-Na solution at $\lambda = 405$ nm. The concentration of DOX was obtained by measuring the absorbance at 480 nm.

NIR laser irradiation.

A 1064 nm laser was used to induce the heating of the hydrogels. The samples were exposed to the light for 2 h. The temperature monitoring allows to calculate the specific absorption rate (SAR) of the samples. The temperature elevation curves were fitted over the first 200 seconds with a second order polynomial function in order to determine $[dT/dt]_{t=0}$ as described by Perigo et al.[13] The control sample with only water also slightly heats when exposed to NIR laser. This contribution has to be removed to calculate precisely the contribution of the carbon material. Finally, the SAR (W g^{-1}) values are obtained by using the following equation:

$$\mathrm{SAR} = C_s \cdot \frac{m_s}{m_{CNT}} \cdot \left(\left[\frac{dT}{dt} \right]_{t=0,s} - \left[\frac{dT}{dt} \right]_{t=0,water} \right)$$

where m_s and C_s are respectively the mass (kg) and the heat capacity (J kg^{-1} K^{-1}) of the sample, m_{CNT} (kg) is the mass of carbon nanotubes present in the sample $(dT/dt)_{t=0,s}$ the derivative function of the temperature at $t = 0$ s (K s^{-1}) of the sample containing CNT and $(dT/dt)_{t=0,water}$ the one of distilled water exposed to NIR.

Cryo-SEM.

The morphology of the obtained peptide fibers was observed through a Cryo-SEM designed and manufactured by the mechanical facility of the *Charles Sadron Institute*. The supramolecular hydrogel was plunged quickly into liquid ethane and then fixed vertically into a cryo-holder which was previously placed inside a nitrogen bath. During the plunging, the sample is rapidly frozen by direct contact with the liquid ethane. The specific cryo-holder was designed and manufactured by the mechanical facility of the *Charles Sadron Institute*. The cryo-holder was then placed under vacuum into the cryo preparation chamber of the Quorum PT 3010 machine attached to the microscope. The sample was fractured with a razor blade and a slight etching at -90 °C for 3 min was performed to render the fibers more visible. The

sample was eventually transferred in the FEG-cryoSEM (Hitachi SU8010) and observed at 1 kV at -150 °C.

Rheological measurements.

Rheological properties were measured in a Kinexus Malvern rheometer using a Peltier plate aluminium geometry of 10 mm diameter and a gap of 1.2 mm. Strain measurements were performed from 1% to 100% at a fixed frequency of 1 Hz at 25 °C. Frequency sweeps were carried out from 1 Hz to 10 Hz at a fixed strain of 1% at 25 °C. Gels were previously prepared in teflon molds of 10 mm diameter before the measurements.

Molecular dynamics (MD).

Classical molecular dynamics "MD" were performed using the AMBER.18 GPU[45] software in which the potential energy U is empirically described by a sum of bond, angle and dihedral deformation energies and a pairwise additive 1-6-12 potential (electrostatic + van der Waals) between non-bonded atoms **(Eq 1)**.

$$U = \sum_{bonds} k_b \left(r - r_0\right)^2 + \sum_{angles} k_\theta \left(\theta - \theta_0\right)^2 + \sum_{dihedrals} \sum_{n} V_n \left(1 + \cos\left(n\varphi - \gamma\right)\right) + \sum_{i<j} \left[\frac{q_i q_j}{R_{ij}} - 2\varepsilon_{ij} \left(\frac{R_{ij}^*}{R_{ij}} \right)^6 + \varepsilon_{ij} \left(\frac{R_{ij}^*}{R_{ij}} \right)^{12} \right] \quad \textbf{Eq(1)}$$

The simulated system was composed of 16 Fmoc-FFY peptides and 8729 water molecules. Furthermore 16 Na^+ ions were added in order to neutralize the system. Force field parameters for the different amino acids were taken from the AMBER ff14SB force field[46], those of the Fmoc fragment as well as those for the Doxorubicin molecule stem from GAFF[47] while for Na^+ cations we used the ones reported by Cheatham et al.[48] Atomic charges of the Fmoc fragment as well as those for the Doxorubicin were obtained using the RESP procedure.[49] Water molecules were represented using the TIP3P.[50] Cross terms in van der Waals interactions were constructed using the Lorentz−Berthelot rules. 1-4 van der Waals and 1-4 electrostatic interactions were scaled by a factor of 2 and 1.2, respectively. Simulations were performed using a cubic box and 3D periodic conditions were applied. An atom-based cutoff of 9 Å for electrostatic and vdW interactions was applied, while long-range electrostatic interactions were calculated using the particle mesh Ewald method. Simulation started either from a randomly mixed solution or with a preformed peptide assembly and the Doxorubicin molecule was initially placed at about 15 Å from the surface of this assembly. After equilibration an MD simulation of a total of 1 μs at 298.15K in the NVT ensemble was performed for each system. We then increased the temperature of the system to 333.15 K and an additional MD run of 1 μs was performed. During the various simulations,

the temperature of the system was maintained constant using a Berendsen thermostat[51] with a relaxation time of 1.0 ps. A time step of 2 fs was used to integrate the equations of motion via the Verlet leapfrog algorithm. Snapshots along the trajectory were taken using the VMD software.[52]

IV.3. Results and Discussion

IV.3.1. Synthesis and characterization of CNT@LPMS

The pristine CNTs were firstly cleaved through acid treatment and a sol-gel procedure (**Figure 4-3. A**) was performed to coat the sliced CNTs with a homogeneous MS shell. **Figure 4-3. B-D** shows the TEM and SEM images of LPMS layer coated CNTs. It can be seen that the MS layer is composed of numerous large pore channels, which are uniformly surrounded on the outer surface of the CNTs. TEM image reveals that the silica layer surrounding the CNTs was characterized with a shell thickness of ca. 50 nm. The silica content and the CNT content of CNT@LPMS composite were evaluated by a TGA measurement. As shown in **Figure 4-5. A** (black curve), based on the combustion of CNT at about 500 °C, the proportion of silica is estimated to 56 wt%. After CTAB extraction, the CNT@LPMS composite was characterized by N_2 adsorption-desorption isotherms. The isotherms of CNT@LPMS are classified as a type IV-like with a type H3 hysteresis loop, which indicates the mesoporous structure of the silica layer. The BET surface area of CNT@LPMS shows a high value of specific surface area (672 m^2/g), which is much larger than that of the pristine CNT (80 m^2/g) (in **Figure 4-4**). The pore volume of pristine CNTs is 0.14 cm^3/g, which is increased to 2.12 cm^3/g after LPMS layer coating. The pore size distribution of CNT@LPMS shows a peak near 12 nm, which again indicates the formation of a LPMS layer on the CNTs surface. The formation of mesoporous structure of the MS layer greatly improved the specific surface area and the pore volume, making these nanocomposites as ideal supports to host guest molecules.

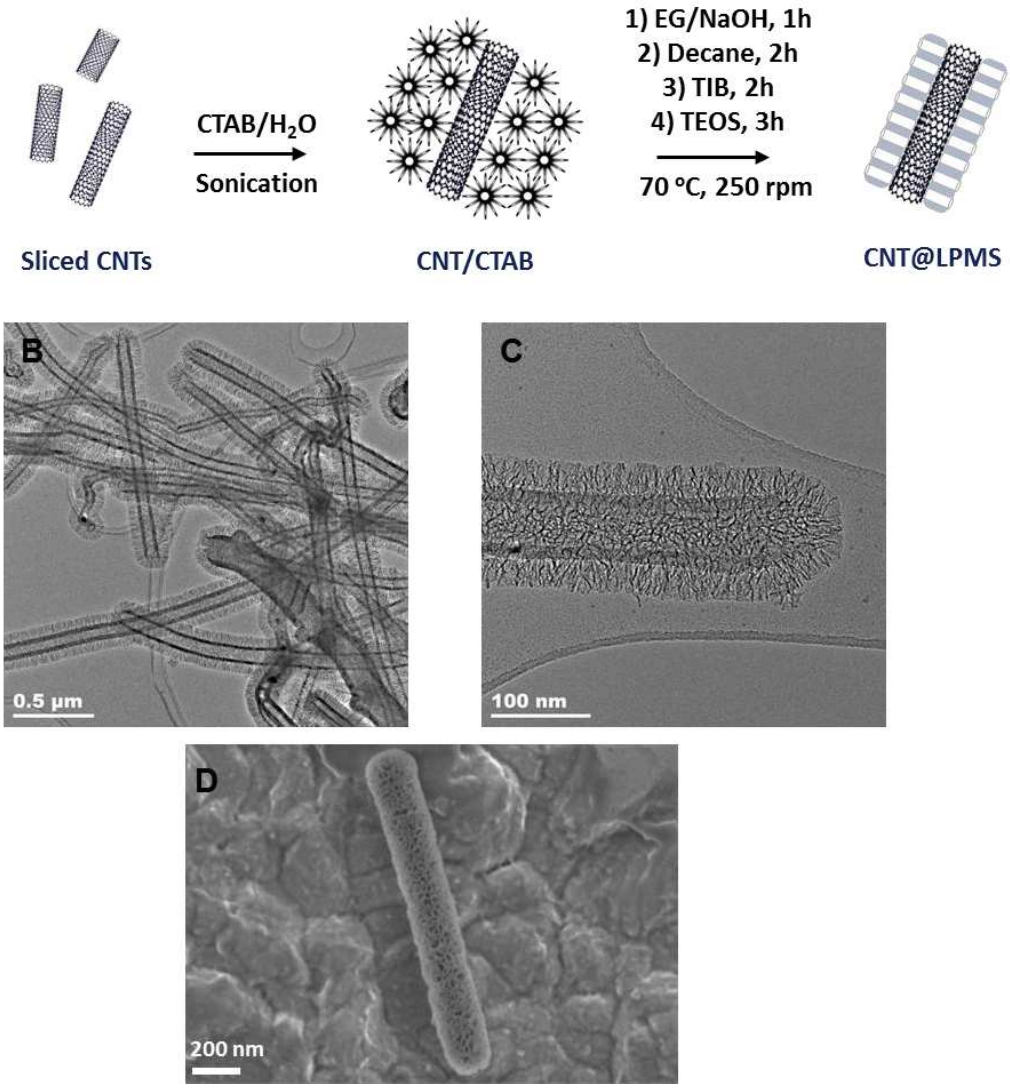

Figure 4-3. (A) A schematic illustration for the synthesis of CNT@LPMS. **(B, C)** TEM and **(D)** SEM images of CNT@LPMS.

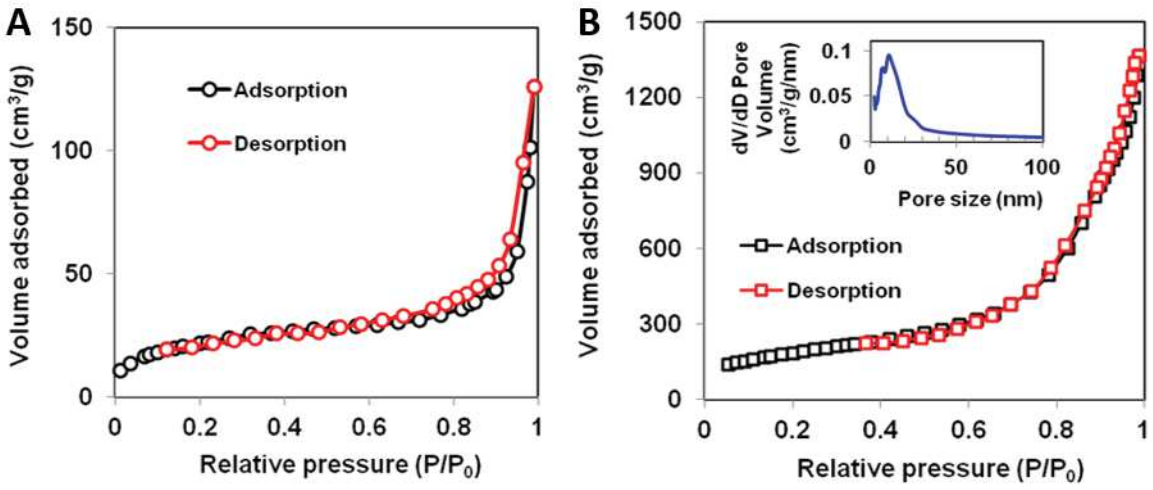

Figure 4-4. (A) N2 adsorption-desorption isotherms of CNT@LPMS associated with the pore size distribution and **(B)** isotherms of pristine CNTs.

IV.3.2. Functionalization of silica surface

Surface functionalization of CNT@LPMS was carried out before enzyme immobilization. Firstly, the silica shell surface was "silanized" by NH_4OH catalyzing 3-aminopropyltriethoxysilane (APTES) condensation on their surface. Therefore, the amine-modified silica surface was further functionalized by isobutyryl chloride (IBC), and finally, isobutyramide (IBAM) terminal functional groups were formed on the LPMS shell surface. The extent of APTES and IBAM functional groups was studied using thermogravimetric analysis. TGA experiments were performed on the pristine CNTs and functionalized samples: CNT@LPMS, CNT@LPMS@APTES and CNT@LPMS@IBAM from 50 °C to 800 °C under airflow, as shown in **Figure 4-5**. The pristine CNTs remained fairly stable at temperatures up to 500 ° C, after which they quickly began to oxidize and burn. It is worth noting that the decomposition of carbon in CNT@LPMS started from 400 °C, which was lower than the combustion of pristine CNT. This is most likely due to more defects generated on the sliced CNTs during acid treatment. The TGA curves of the functionalized CNT@LPMS are significantly different from that of bare CNT@LPMS. The TGA curves of CNT@LPMS@APTES and CNT@LPMS@IBAM show two distinct weight loss regions. The functional groups started to decompose at 250 °C due to the elimination of APTES and IBAM groups, from which the approximate number of functional groups grafted on the LPMS surface could be determined. The second region weight loss in the temperature range of 400°C to 600°C corresponds to the combustion of carbon. It was calculated that the fixed APTES and IBAM functional groups were respectively ca. 10.4 wt% and 9.2 wt% of CNT@LPMS. This allowed estimating the grafting density of APTES and IBAM groups on the silica surface. to 3.5 per nm^2 and 2.7 per nm^2, respectively.

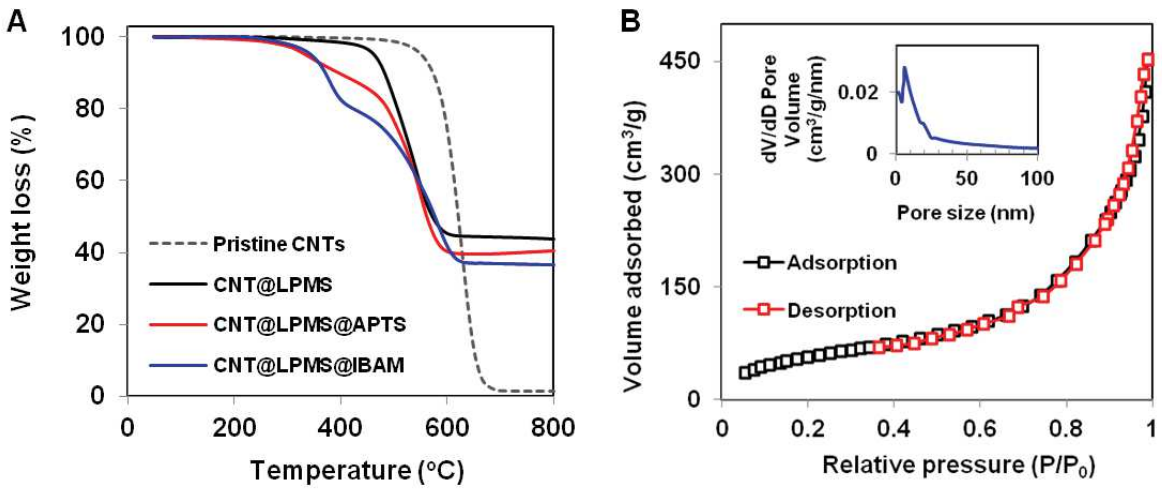

Figure 4-5. (A) TGA curves of pristine CNT, CNT@LPMS, CNT@LPMS@APTES and CNT@LPMS@IBAM. **(B)** N_2 adsorption-desorption isotherms associated with the pore size distribution of CNT@LPMS@IBAM.

The characteristics of the porous structure of the functionalized CNT@LPMS@IBAM were also studied by N_2 adsorption-desorption analysis, the results are shown in **Figure 4-5.B** and **Table 4-1**. As expected, the introduction of the IBAM moieties resulted in the reduction in specific surface area, pore volume and average pore size. The changes of the structural properties of CNT@LPMS@IBAM composites indicate that the functional groups are partially located in the pore channels of the silica matrix, resulting in a reduction of these textural structure parameter values, which can also indirectly confirm the effectiveness of the modification process.

Table 4-1. Relevant parameters characterizing the textural features of supports and after surface functionalization.

Sample	BET surface area (m^2/g)	Pore volume (cm^3/g)	Pore size (nm)
CNT@LPMS	672	2.12	12.0
CNT@LPMS@IBAM	218	0.70	7.7

ZP were measured in water at pH=6.5 to characterize the surface charge of the prepared samples. **Figure 4-6** shows the zeta potentials of the naked CNT@LPMS, and IBAM-functionalized CNT@LPMS dispersed in pure water (pH 6.5) (and later on after enzyme adsorption). The ZP value, which corresponds theoretically to the electrostatic potential at the sliding plane of the double ion layer on the coated surface, indicates the surface charge of the nanocomposite. ZP measurement results show that for bare CNT@LPMS, negatively charged surfaces with zeta potential of -14.2±1.2 mV. As IBAM groups are introduced on the silica surface, the ZP value recorded for the modified CNT@LPMS@IBAM is significantly different. ZP values of +24.3±0.9 mV corresponding to CNT@LPMS@IBAM is found. There are still remaining APTES groups exposed after the IBAM modification which probably result in this positive ZP value. The successful functionalization with IBAM on the silica surface of CNT@LPMS@IBAM is beneficial to the high loading capacity for enzyme immobilization.

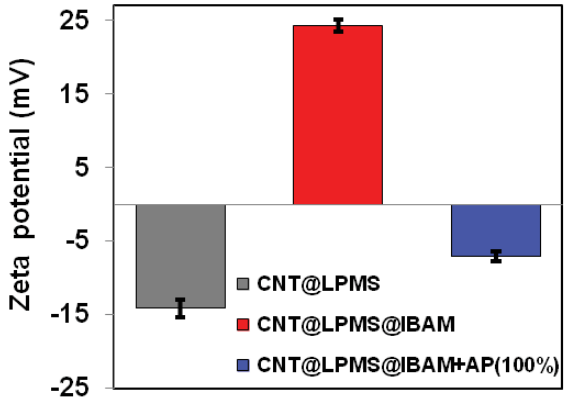

Figure 4-6. Zeta potential of CNT@LPMS, CNT@LPMS@IBAM and CNT@LPMS@IBAM+AP (100 wt%) in water at pH 6.5.

IV.3.3. Immobilization of AP on functionalized composites

In order to study the ability and efficiency of the functionalized composites for enzyme immobilization and to determine the maximum immobilization capacity, AP adsorption tests at various concentrations were investigated. The enzyme immobilization capacity q represents the mass of the adsorbed AP (mg) versus the mass of composite (mg), and the enzyme loading efficiency represents the mass of the absorbed AP versus the initial mass of AP introduced. AP was firstly labeled with fluorescent FITC for subsequent quantitative measurements. For the enzyme adsorption process, AP^{FITC} was firstly incubated with the composite under continuous stirring for 1 hour, then the AP-immobilized composites were separated by centrifugation. The supernatant was collected and measured after dilution with water by spectrofluorimetry. Thereafter, the mass of AP^{FITC} remaining in the supernatant (ie, AP^{FITC} that has not yet been adsorbed) could be determined using the calibration curve of AP^{FITC} (**Figure 4-7.D**), which allows us calculating the actual amount of adsorbed enzyme. The immobilization and efficiency capacities of AP on the functionalized CNT@LPMS@IBAM were traced as a function of the initial enzyme concentration and compared with the naked CNT@LPMS (**Figure 4-7.A,** black curves). The results show that for the CNT@LPMS, the immobilization capacities of AP increase with increasing initial enzyme concentration ranging from 0.1 to 1 mg/mL and reach maximum loading capacity at ca. 127 µg AP per mg of CNT@LPMS (at concentration of 1 mg/mL). Although the immobilization capacity increased with increasing AP concentration, the loading efficiency decreased as the AP concentration increased (**Figure 4-7.A**, blue curves).

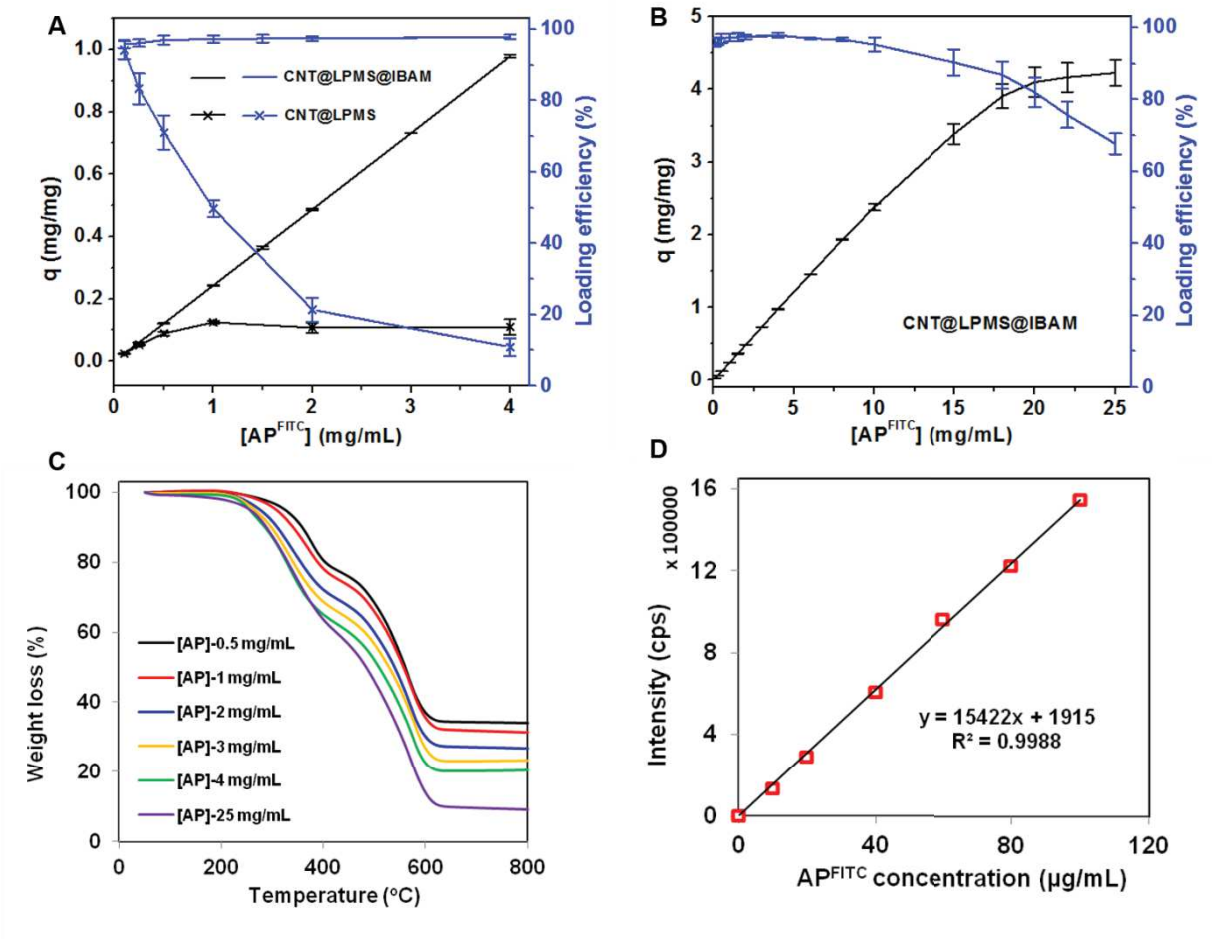

Figure 4-7. (A) Enzyme immobilization capacity q (mg of AP adsorbed per mg of composite, black curves) and loading efficiency (in %, blue curves) on bare CNT@LPMS and CNT@LPMS@IBAM, as a function of the initial enzyme concentration (until 4 mg/mL) and **(B)** on CNT@LPMS@IBAM (until 25 mg/mL). **(C)** TGA profiles of CNT@LPMS@IBAM immobilized with different amount of AP^{FITC} at different initial concentrations. **(D)** Calibration curve of AP^{FITC} in water representing fluorescence intensity at 520 nm vs [AP^{FITC}] by spectrofluorimetry.

The immobilization capacity and loading efficiency of AP were then investigated on the functional CNT@LPMS@IBAM composites as a function of the initial AP concentration from 0.1 to 4 mg/mL (increasing initial AP concentration up to 25 mg/mL are shown in **Figure 4-7.B**. The results in **Figure 4-7.A** indicate that the immobilization capacities of AP on CNT@LPMS@IBAM composites are greatly improved and the maximum immobilization plateau was reached at the concentration of AP ca. 22 mg/mL. The maximum immobilization capacity of AP on the CNT@LPMS@IBAM composites was calculated to be 4.3 mg of AP adsorbed per mg of CNT@LPMS@IBAM composite (i.e.) 430 wt% (or 4.3 times more the carrier mass). The CNT@LPMS@IBAM composites after AP adsorption were washed with water and then TGA measurements were performed to confirm the amount of immobilized AP (**Figure 4-7.C**). TGA profiles show that the amounts of AP^{FITC} immobilized on the composites are consistent with the values obtained by fluorescence spectrometry.

These data also indicate that the loading efficiency remains ca. 97% at the studied concentration below 8 mg/mL. A continuous decrease in the loading efficiency was observed with the continuous increase

of the impregnation concentration of AP. Whatever their concentration, the immobilization capacities of AP on functionalized CNT@LPMS@IBAM are far higher than in the case of naked CNT@LPMS. The high loading capacity of AP on the IBAM-modified composites could be attributed to the high density of IBAM functional groups establishing strong non-covalent bonding interactions with AP, and providing abundant binding sites for AP adsorption. These results reveal that IBAM-modified composites are promising candidates for AP immobilization with high loading capacity. After immobilization of AP, ZP measurement was performed on CNT@LPMS@IBAM+AP(100 wt%) composites in water at pH 6.5 (**Figure 4-6**), and it was found that the ZP value changed from positive to negative at ca. –7.1±0.8 mV. The decrease in zeta potential value was likely due to the introduction of AP on the outer surface, which confirmed the effective immobilization of AP on the functionalized composites.

IV.3.4. Biocatalytic performance of the immobilized AP

The biological functionality of the immobilized enzyme was assessed by investigating the biocatalytic property of the AP loaded composites meaning their enzymatic activity to turn a molecular substrate to its product. The enzymatic activity measurements were performed using a conventional spectrophotometric method based on the ability of phosphatase enzymes to hydrolyze the p-nitrophenyl phosphate disodium hexahydrate (pNPP-Na) into p-nitrophenol (pNP), a chromogenic product with a maximum absorbance at 405 nm. In the presence of AP, the hydrolysis of pNPP-Na substrate was quickly catalyzed to obtain the pNP with a yellow color, which was recorded by the UV-visible spectrum. The auto-hydrolysis process of pNPP-Na (in the absence of AP) was found extremely slow at room temperature (**Figure 4-8.C**), which was assumed negligible. Furthermore, given that the contribution of the composites on the absorbance was shown to be negligible because of their low concentration, the AP-immobilized composites and pNPP substrates were directly subjected to UV-visible spectrometry detection without centrifugation **(Figure 4-8.A)**.

In order to study the enzymatic activity of the immobilized AP, 2 mL of pNPP-Na (0.05 mg/mL in 50 mM $NaHCO_3$ buffer) was brought in contact with 2 µg of AP immobilized nanocomposites in water baths set at different temperatures: 25 and 37 °C for 2 h. **Figure 4-8.B** shows the absorbance of the suspension versus time, revealing the conversion of pNPP into pNP catalyzed by the immobilized AP. The results show that under the temperature conditions studied, the immobilized AP continuously catalyzed the hydrolysis of pNPP-Na into the pNP product over 2 hours. No conversion was observed in the absence of immobilized AP (control, black curve). The higher activity of the immobilized enzyme was observed at the temperature of 37 °C which is consistent with its biological role. Similar results have been reported in other literature, showing that the optimal enzymatic activity of AP is around 40 °C.[53,54]

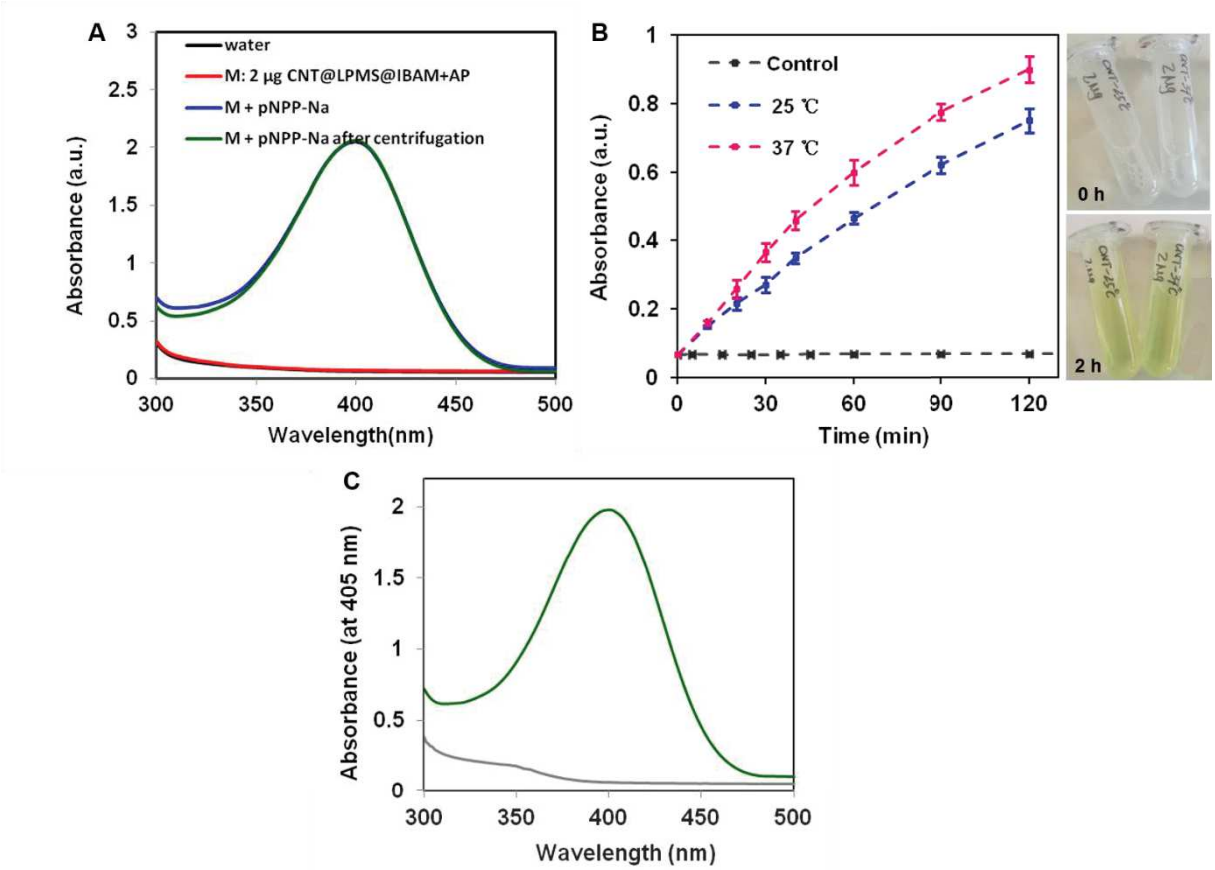

Figure 4-8. (A) UV-visible spectra of 2 mL of pNPP-Na solution after 24 h contact with CNT@LPMS@IBAM+AP (100 wt%). The results show that 2 µg CNT@LPMS@IBAM+AP did not change the maximum absorbance of the solution, which was almost the same as the absorbance of the solution after removing the composites by centrifugation. **(B)** Absorbance of p-nitrophenol (pNP) as a function of time, converted from 2 mL of p-nitrophenyl phosphate disodium hexahydrate (pNPP-Na) in the presence of 2 µg of CNT@LPMS@IBAM+AP(100 wt%). The absorbance was measured at λ= 405 nm by UV-visible spectrometry. The related photographs show that immobilized AP catalyzed the hydrolysis of pNPP-Na to the yellow product pPN. **(C)** UV-visible spectra of pNPP-Na solution in the absence of immobilized AP (grey) and in the presence of immobilized AP (green) after 24 h at room temperature.

A faster catalytic effect was obtained when 5 µg of AP immobilized composites were used to catalyze the hydrolysis of pNPP-Na. Photographs of different amounts of immobilized AP catalyzed the hydrolysis of pNPP-Na to the yellow product pNP are also shown (**Figure 4-9**).

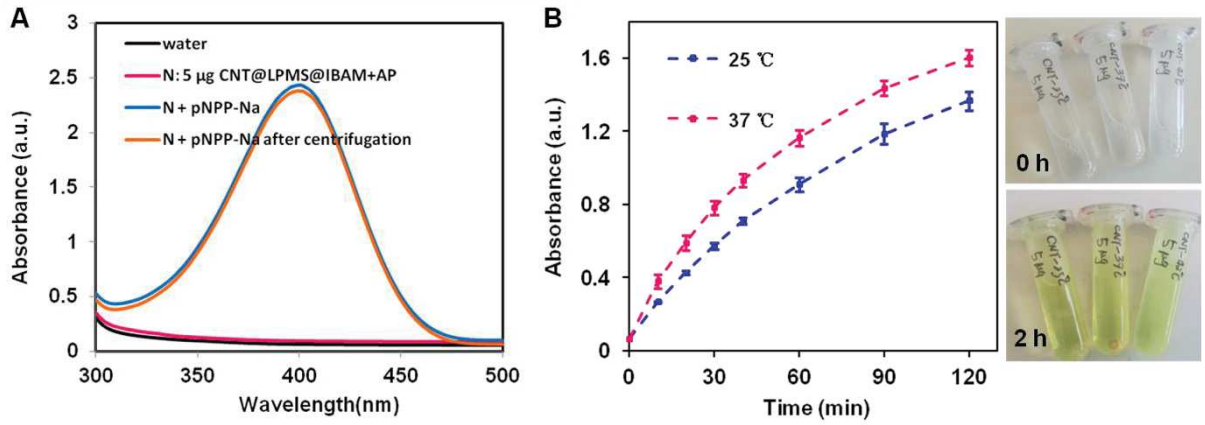

Figure 4-9. (A) The UV visible spectra of 2 mL of pNPP-Na solution after 24 h of contact with CNT@LPMS@IBAM+AP (100 wt%). The results show that the existence of 5 µg CNT@LPMS@IBAM+AP hardly changed the maximum absorbance of the solution, which was almost the same as the absorbance of the solution after removing the composites by centrifugation. **(B)** The absorbance of pNP as a function of time, converted from 2 mL of p-Nitrophenyl phosphate disodium hexahydrate (pNPP-Na) in the presence of 5 µg CNT@LPMS@IBAM+AP(100 wt%). The absorbance was measured at λ= 405 nm by UV-visible spectrometry. The related photographs showing the hydrolysis of pNPP-Na to the yellow product pNP.

IV.3.5. Hydrogel formation and DOX loading - rheology study

In this paragraph, we describe the driven assembly of the peptide hydrogel mediated by the enzyme immobilized on CNT@LPMS nanocomposites to yield a novel generation of responsive nanocomposite hydrogel. The hybrid supramolecular hydrogel is prepared from the Fmoc-FF*p*Y tripeptide, which is dephosphorylated into Fmoc-FFY by the catalytic action of immobilized alkaline phosphatase (AP). This mechanism induces the localized growth of self-assembled Fmoc-FFY peptide nanofibers from the silica shell surface of CNT@LPMS, leading to the formation of hydrogels with fibrillary nanoarchitecture (**Figure 4-10.A**, reactional scheme). Hence, the self-assembled peptide nanofibers network is cross-linked with the AP-immobilized CNT@LPMS as the intersection points. The drug-loaded hydrogel was simply prepared by pre-mixing the Fmoc-FF*p*Y peptide precursor solution and the anticancer drug (DOX) aqueous solution to yield a suitable hydrogel system for drug delivery. The Fmoc-FFY self-assembled hydrogels with and without DOX obtained from CNT@LPMS@IBAM+AP(100 wt%) were obtained by mixing the AP-immobilized nanocomposites with Fmoc−FF*p*Y peptide for 24 h at room temperature.

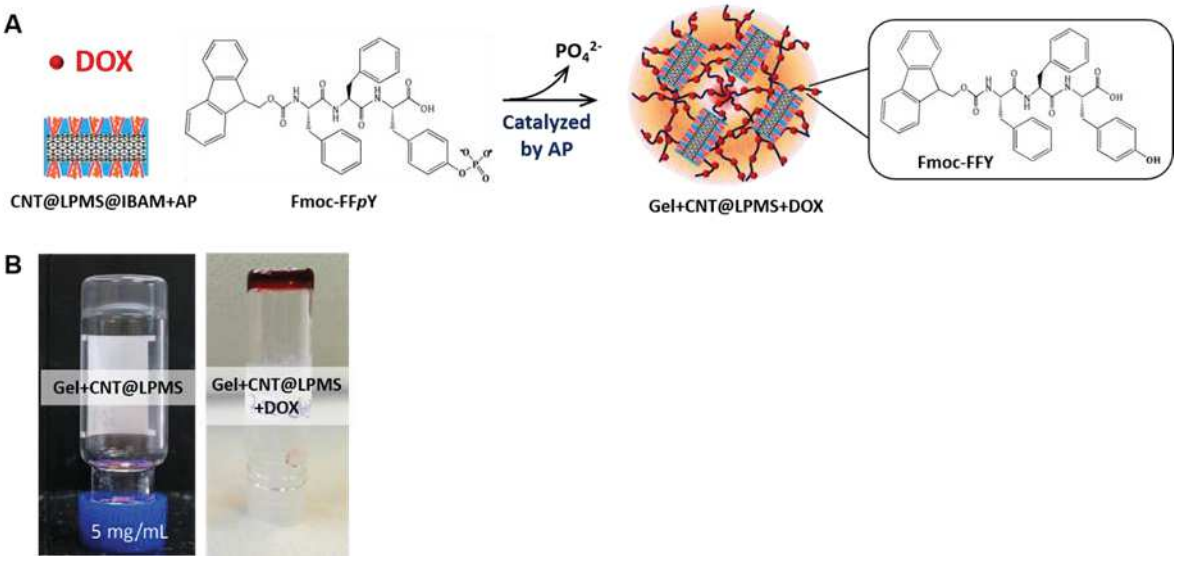

Figure 4-10. (A) Scheme showing the dephosphorylation of Fmoc-FFpY peptide into Fmoc−FFY by AP immobilized CNTs@LPMS@IBAM. (B) Inverted tube tests of self-assembled hydrogels from AP-immobilized composites: (left) without and (right) with DOX.

The concentrations of Fmoc-FF*p*Y, CNT@LPMS@IBAM+AP and DOX components in the hydrogel were set at 5 mg/mL, 0.1 mg/mL, and 0.5 mg/mL, respectively. As can be seen from **Figure**

4-10.B, (test of inverted tubes without loaded DOX) homogeneous, opaque and dense hydrogel with a dark gray color due to the blackness of CNTs, was obtained from the AP-immobilized composites. In the presence of DOX, the resulting hydrogel displayed a uniform dark red color and adhered stably monolithically on the wall of the tubes (**Figure 4-10.B**), indicating that the DOX was uniformly distributed in the hydrogel.

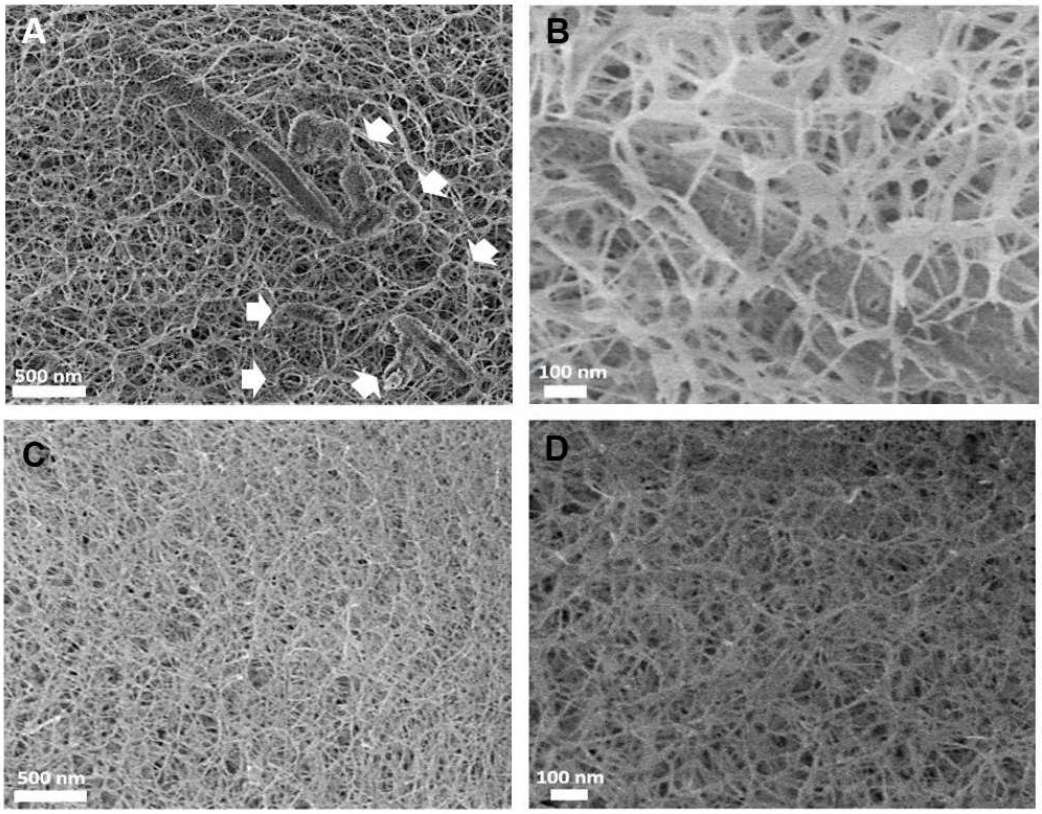

Figure 4-11. (A, B) Typical Cryo-SEM images taken from supramolecular hydrogel prepared from CNT@LPMS@IBAM+AP(100 wt%). White arrows show CNT@LPMS perpendicular to the image section. **(C, D)** Cryo-SEM images of the supramolecular hydrogel prepared from free AP in solution in the presence of Fmoc-FF*p*Y.

The internal nanoarchitecture of the composite supramolecular hydrogel generated from AP immobilized nanocomposites: CNT@LPMS@IBAM+AP(100 wt%), as well as free AP (equivalent to the immobilized AP) were visualized by Cryo-SEM in **Figure 4-11.A, B** and **C, D** respectively. The images confirmed the formation of nanofibrous architecture in both cases. Because the AP is localized on LPMS through the interaction with IBAM, the self-assembly process is initiated specifically from the surface of the nano-objects. The diameter of the self-assembled nanofibers is around ~15 nm, close to those observed when the hydrogel is formed using free AP. Cryo-SEM images taken from the composite supramolecular hydrogel formed from AP-immobilized CNT@LPMS (**Figure 4-11.A, B**), show equivalent fibrous network as the one observed with free AP **(Figure 4-11.C, D**). It can be clearly observed that the self-assembled peptide nanofibers grew from the surface of CNT@LPMS nanotubes which results in embedding them within the peptide hydrogel fibrous network. The AP-immobilized CNT@LPMS act thus as a cross-linking points in the 3D nanofibrous network, which confirms that the

immobilized enzyme maintains a good biocatalytic activity to convert Fmoc-FF*p*Y into Fmoc-FFY nanofibers. Then, we investigated such approach had the potential to enhance the mechanical properties of the hydrogel network.

The mechanical properties of the studied nanocomposite hydrogels (and the bare gel formed by dephosphorylation of Fmoc-FF*p*Y peptide in contact with free AP as a control) were determined by dynamic oscillatory rheology providing information about the storage modulus (G') and loss modulus (G''). G' is an indicator of the elastic behavior of the material by measuring the ability to store deformation energy which can be recovered after removing the applied load. G" measures the deformation energy that is dissipated as heat and friction during the shearing process. Strain sweeps from 0.1-100 % at a fixed frequency of 1 Hz were carried out in order to determine the linear viscoelastic region, defined as the region where the elastic modulus (G') and loss modulus (G'') are parallel and independent of the strain amplitude. As shown in **Figure 4-12.A**, G' and G'' remained constant up to 10% of the strain was applied and then decreased when strain was further increased. In order to get further insight on the elastic properties of the formed hydrogels, G' and G'' were measured as a function of frequency (0.01-10 Hz) and the results are depicted in **Figure 4-12.B**.

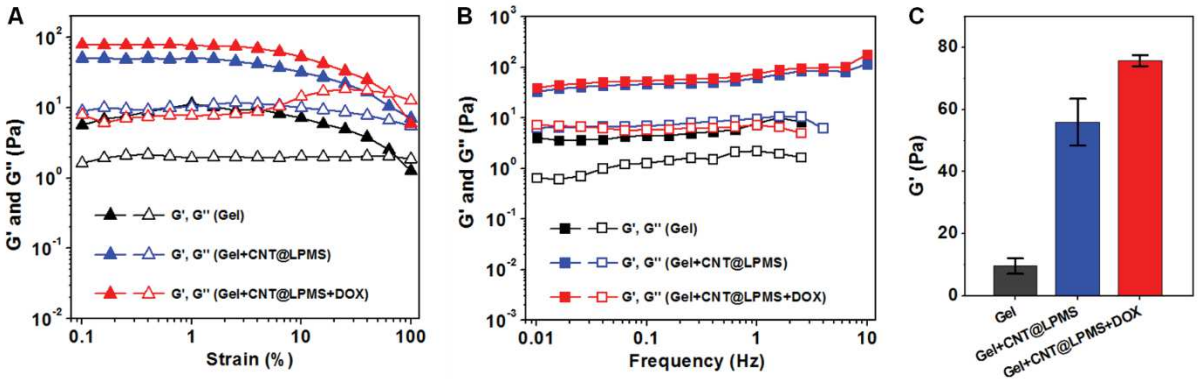

Figure 4-12. Storage modulus (G' –solid symbols) and loss modulus (G'' – hollow symbols) of bare hydrogel (Gel), Gel+CNT@LPMS(@AP), and Gel+CNT@LPMS(@AP)+DOX on: **(A)** strain sweeps and **(B)** frequency sweeps. **(C)** Storage modulus values (G') at 1 Hz, 1% of the studied samples.

Over all the frequency range, and for all gels, the values of the elastic modulus were higher than the corresponding to the viscous modulus (G' > G'') indicating the gel-like behavior for all samples under study. At a frequency of 1 Hz and a strain of 1%, G' (resp. G'') of the bare control gel (Gel) reached a value of 9.5 ± 2.5 Pa (resp. 2.0 ± 0.2 Pa) while the formation of nanocomposite hydrogels by the action of AP-immobilized CNT@LPMS, resulted in the increase of G' up 55.9 ± 7.5 Pa (G'' resp. 10.0 ± 0.4 Pa) (**Figure 4-12.C**). The CNT@LPMS composites, employed as supports for the immobilization of a larger number of enzymes ensured thus enrichment of the interaction points for Fmoc-FF*p*Y peptide self-assembly and cross-linked fiber network, which gave rise to enhance shear stiffness of the self-assembled hydrogels. The increase in the elastic modulus was even higher when DOX was introduced in those hydrogels, resulting in 75.8 ± 1.8 Pa (resp. 7.5 ± 0.4 Pa) for

Gel+CNT@LPMS(@AP)+DOX. This effect suggests the contribution of the therapeutic agent in the hydrogel architecture which is discussed later on in section 8 dealing with the molecular model used to explain interactions of the peptide gel with DOX.

IV.3.6. Thermally and NIR-photothermally-induced DOX release from hydrogels

We thus studied the possibility to thermally trigger DOX release from such nanocomposite hydrogel whether by macroscopic T increase or by NIR light photo-induced hyperthermia. Regarding the thermal drug release study, after the formation of the NC hydrogel loaded with DOX (at 0.5 mg/mL), 1 mL of water was added along the tube wall and the release of DOX was followed out at 25, 37 and 42 °C for 24 h. After 24 h of treatment, the supernatant was removed and the amount of DOX released in the solution was calculated by UV-Vis spectrometry using the DOX calibration curve (**Figure 4-13**).

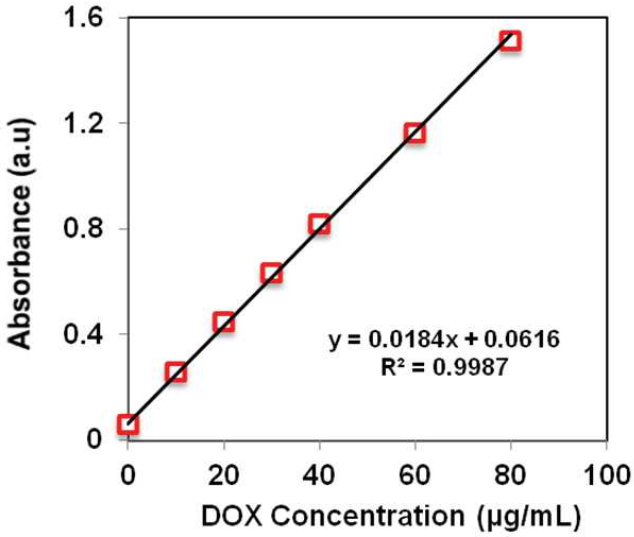

Figure 4-13. Calibration curve of DOX in water representing the maximum absorbance at 480 nm vs [DOX] by UV-visible spectrophotometry.

Figure 4-14.A shows the release of DOX from hydrogels after 24 h of treatment at 25, 37 and 42°C. These three temperatures mimic respectively the preparation, in vivo and hyperthermia temperatures. In the case of the hydrogels treated at 25 °C, a small amount of DOX (ca. 5.6 %) was found released from the hydrogel systems. This suggests that DOX was not simply retained in water pockets of the hydrogel, (as it does not diffuse spontaneously), but interacts with its nanofibrous structure. Conversely, the amount of DOX released from Gel+CNT@LPMS+DOX hydrogel systems was gradually increased when the gels were heated at 37 and 42 °C for 24 h, with the release reaching ca. 10.5 % and 15.1 %, respectively. The associated photographs show a significant difference in the contrast of DOX released in the supernatants between 25 and 42 °C. The drug release of these DOX-

encapsulated hydrogels was also investigated over a longer period of 48 h at 42 °C and at a higher stimulation temperature (50 °C) mimicking ablation temperature (**Figure 4-14.B**). As expected, it was found that the DOX-gel systems released more DOX over extended treatment time and temperature. The % DOX release from Gel+CNT@LPMS+DOX systems reached 17.6% at 42°C and 23.2% at 50°C, over 48 h. Associated photographs show DOX released into the aqueous solution after being treated at 42 °C and 50 °C for 48 h.

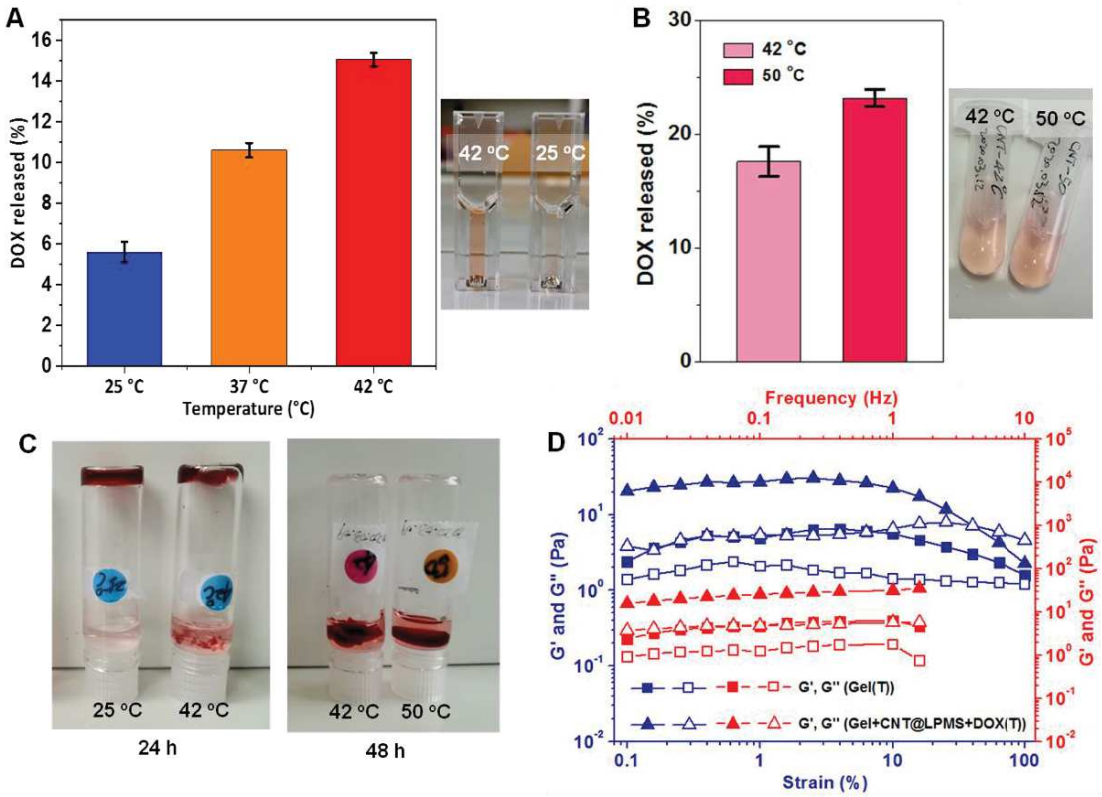

Figure 4-14. DOX release from Gel+CNT@LPMS+DOX hydrogels stimulated at (A) 25, 37 and 42 °C for 24 h and (B) 42 and 50 °C for 48 h. The associated photographs show the DOX released into the aqueous solution after treatment at these different temperatures. (C) Photographs of hydrogels after the temperature treatment. (D) Storage modulus (G' –solid symbols) and loss modulus (G'' – hollow symbols) of Gel+CNT@LPMS+DOX(T) after heating at 42 °C for 24 h and return at 25°C. Strain sweep study corresponds to the blue curves while frequency sweeps study corresponds to the red curves. Log scales are set differently between the two studies to facilitate graph reading.

Regarding the effect on the hydrogel structure upon heat treatment, photos in **Figure 4-14.C** show that these nanocomposite hydrogels were somewhat more fragile after treatment under 42 °C and 50 °C (see reddish gels in inverted tubes). Indeed, while the hydrogels treated at 25 °C remained stuck to the vials, we observed that the DOX-containing hydrogels after treatment at 42 and 50 °C keep overall their integrity and unstick from the glass vial. By falling off from the bottom of the tube, they even break into small pieces indicating their brittleness upon heat treatment. Interestingly, the corresponding free DOX nanocomposite hydrogels treated at 42 °C for 24 h stayed intact. The hydrogel might fall off from the bottom as a whole but it still maintained good integrity. (**Figure 4-15**).

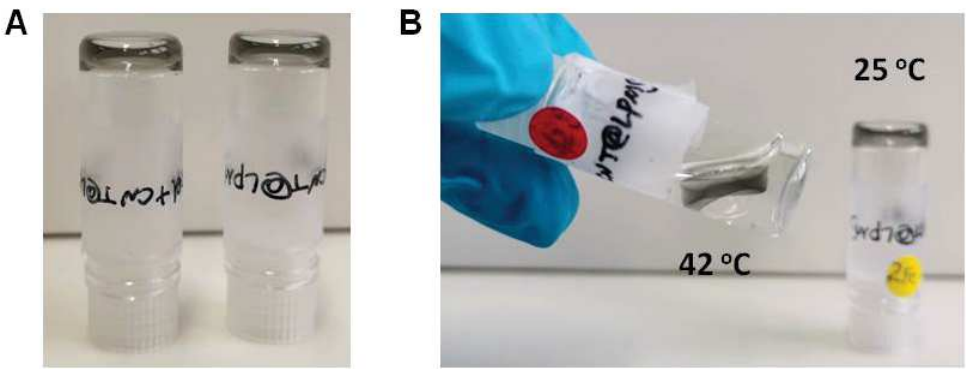

Figure 4-15. Photographs of DOX-free nanocomposite hydrogels (A) before heating and (B) after temperature treatment at 25 and 42 °C for 24 h.

With the aim to gain insight into the properties of the nanocomposite hydrogels after heat treatment, DOX-loaded hydrogels (Gel+CNT@LPMS+DOX), treated at 42 °C for 24 h, were then characterized by rheological measurements (**Figure 4-14.D**). It is obviously seen that the G' value of the heated hydrogel Gel+CNT@LPMS+DOX(T) was considerably lower than that of Gel+CNT@LPMS+DOX samples. Storage modulus G' (resp. G'') of heated hydrogels were measured to be 31.5±6.1 Pa (resp. 5.6±0.2 Pa) for Gel+CNT@LPMS+DOX(T), which was highly reduced of 58% as compared to the gel at 25°C being of 75.8±1.8 Pa (**Figure 4-12.C**). These results indicate that the thermal treatment (42 °C) results in appreciable loss of the storage modulus of the hydrogels. This would mean that the DOX is influencing the peptide self-assembled nanoarchitecture, and the release of DOX, caused by temperature increase, had an impact on the hydrogel structure. It must be noticed that the mechanical features of supramolecular hydrogels containing drugs prepared in bulk conditions have been recently shown behaving similarly once drug is loaded and released.[55–57] These DOX-loaded hydrogel systems show thus a great interest for thermally induced drug release from smart implantable systems.

Regarding the potential for photothermal drug release, the strong absorbance characteristics of CNTs in the NIR region (750-1400 nm), allow them to convert NIR light into local heat, which would be a way to generate heat locally by external stimulation. As we have previously confirmed above that such nanocomposite peptide hydrogels release DOX in response to external thermal stimulation, we then studied the possibility of these nanocomposite peptide hydrogels to release DOX under NIR light irradiation. The test was performed by adding 1 mL of distilled water in the cuvette containing the nanocomposite hydrogel at the bottom and then exposed to the 1064 nm NIR laser with a power density of 1 W/cm² for 2 h (**Figure 4-16.A**). The temperature elevation was recorded as a function of time through a T-probe immersed in the aqueous phase. The amount of DOX released in the aqueous solution was calculated by collecting the supernatant and measuring by UV-vis spectrometry. As shown in **Figure 4-16.B**, obvious CNT@LPMS concentration-dependent photothermal heating effects were observed. The effect of NIR light in water (without CNT@LPMS composites) showed a slight increase in T by 4°C. The temperature of the CNT@LPMS solution increased rapidly in the early stage, and then

slowed down with the extension of the NIR light stimulation. As the mass of CNT@LPMS increased to 200 µg, the increase in T could reach ca. 11 °C. The remarkable photothermal performances of CNT@LPMS make them thusly an effective photothermal agent for stimulating drug release.

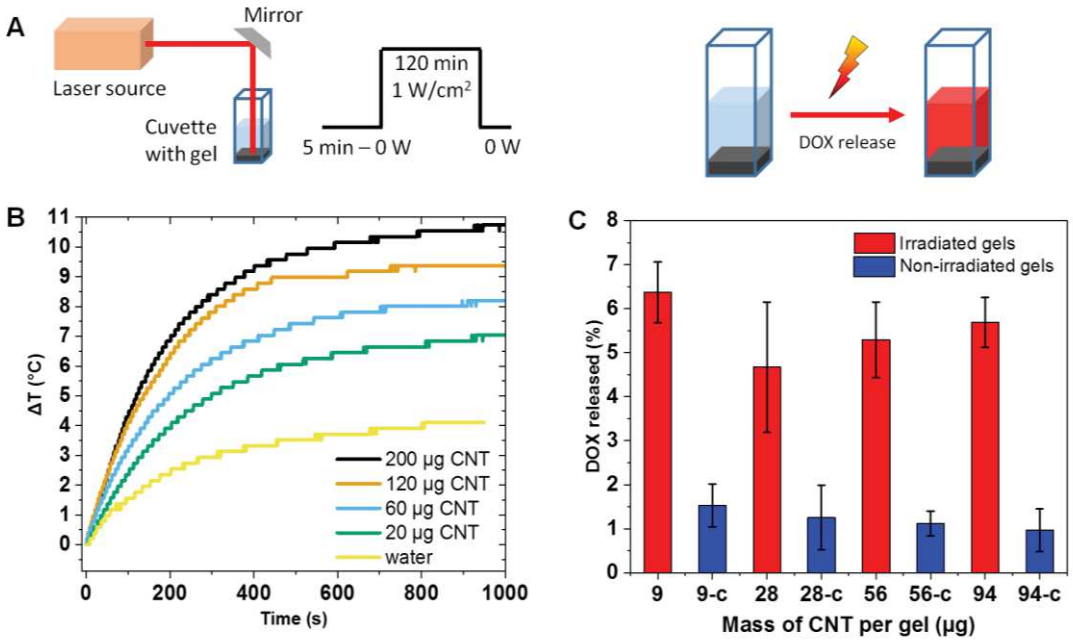

Figure 4-16. (A) Scheme of the setup to ensure NIR light irradiation and principle of the NIR light-induced drug release. (B) Temperature elevation profiles as a function of the mass of CNT@LPMS composites. (C) DOX released (% vs initial loading) upon NIR light irradiation for 2 h at 1W/cm^2.

Then, the NIR-light photothermal induced drug release from nanocomposite peptide hydrogels was investigated by exposing the hydrogel with various mass of CNT@LPMS (9 – 94 µg) to the NIR laser for 2 h **(Figure 4-16.C)**. Corresponding control samples containing the same mass of CNT@LPMS were also considered to confirm drug natural leakage at room temperature without NIR stimulation (blue bars). The results (red bars) indicate that the increase of CNT@LPMS mass in hydrogel led to similar levels of DOX release under the stimulation of NIR light. Approximately 6% of DOX over 2 hours was released from the hydrogel under NIR laser stimulation, which was almost four times that of control sample (*ca.* 1.5%) Evaluation of the specific absorption rates (SAR) corresponding to the photothermal powers (W/g) dissipated by the CNTs@LPMS was performed as a function of the concentration. The temperature profiles allow to calculate the specific absorption rate (SAR) of the samples by fitting these curves over the first 200 seconds with a second order polynomial function in order to determine $[dT/dt]_{t=0}$. As water also moderately heats when exposed to NIR laser, its heating contribution is deduced to calculate more precisely the contribution of the CNTs@MS material. The SAR (W g^{-1}) values are calculated with the following equation:

$$\mathrm{SAR} = C_s \cdot \frac{m_s}{m_{CNT}} \cdot \left(\left[\frac{dT}{dt}\right]_{t=0,s} - \left[\frac{dT}{dt}\right]_{t=0,water} \right)$$

where m_s and C_s are the mass (g) and the heat capacity (J g^{-1} K^{-1}) of the NC gel + aqueous phase sample respectively, m_{CNT} (g) is the mass of carbon nanotubes present in the sample as heat mediator,

$(dT/dt)_{t=0,s}$ (K s^{-1}) is the temperature derivative function at $t = 0$ of the aqueous phase and $(dT/dt)_{t=0,water}$ the one of distilled water exposed to NIR. The results indicate that even if the T increases with the concentration of the CNTs@LPMS, the SAR value decreases by ca. three times from 3867 to 1436 W/g when the concentration is increased from 100 to 1000 µg.mL^{-1} (**Table 4-2**). This would eventually explain why the DOX release is not really improved with CNTs concentration.

Table 4-2. Explanation table for evaluating SAR (W/gCNT). The contribution of water in ΔT is taken into account to accurately calculate the contribution of CNT@LPMS.

CNT@LPMS@IBAM µg/ml gel	Calculated mCNT (µg)	Raw b1 (°C/s)	Adjusted b1 (°C/s)	SAR (W/g CNT)
100	9,36	0,0280	0,0087	3867
300	28,1	0,0400	0,0207	3083
600	56,2	0,0506	0,0313	2327
1000	93,6	0,0515	0,0322	1436

IV.3.7. Deciphering DOX assembly in peptide structures at molecular scale - Molecular Dynamics Simulation

As previously observed, it seems that DOX is not simply embedded within the supramolecular hydrogel, as quite a small amount of DOX was found diffusing out from the material at room temperature when brought in contact with aqueous solution. Thermal energy is required to start and control the releasing process of DOX over 48 h. This means that DOX is robustly entrapped in the supramolecular hydrogel. In addition, the mechanical properties of DOX-containing hydrogels **(Figure 4-12.** Storage modulus (G' –solid symbols) and loss modulus (G'' – hollow symbols) of bare hydrogel (Gel), Gel+CNT@LPMS(@AP), and Gel+CNT@LPMS(@AP)+DOX on: (**A)** strain sweeps and (**B)** frequency sweeps. (**C)** Storage modulus values (G') at 1 Hz, 1% of the studied samples.**Figure 4-12**) show that this therapeutic agent reinforces the structure of the material leading to a stronger hydrogel. Finally, heated beyond 48 h at 42 °C would result in a maximum of DOX released as well as a decrease in mechanical properties of the hydrogel. All these observations bring to light that DOX behaves as a building block of the nanofibrous structure of the gel. This compound is added to the precursor tripeptide Fmoc-FF*p*Y solution before the enzymatic triggering of AP. Thus, we can envisage the incorporation of DOX into the peptide nanofibers in two possible ways: (*i*) concomitantly with Fmoc-FFY during the self-assembly of nanofibers or (*ii*) interacted on Fmoc-FFY-assembled nanofibers once formed through electrostatic interaction, an expected loading mechanism put forward in the literature.[55–60] In its chemical

structure, DOX contains a large aromatic anthraquinone ring and a primary amine which is positively charged in physiological conditions, both involved in the DNA intercalating feature responsible of its anticancer activity.[61] Therefore, we expect an ability of DOX to intercalate similarly in the Fmoc-FFY assembly.

To tackle this question, we have performed molecular dynamics simulation (MD) of 16 Fmoc-FFY peptides in aqueous solution and in presence of a single DOX molecule starting either from a randomly mixed solution or with an already preformed peptide assembly. In the simulation which started from a random configuration, we observed that Fmoc-FFY and DOX self-assembled spontaneously (within 20 ns) together to generate a single assembled structure centered around the DOX (**Figure 4-17**). After 1 μs, the DOX was found to be completely buried inside the peptides assembly. Aromatic rings such as those from the different Fmoc groups as well as those of the anthraquinone of DOX were found to interact via π-π stacking, constituting the backbone of the assembly. Furthermore, the ammonium group as well as the hydroxyl group of the DOX was found to interact via hydrogen bonding with two different peptides. As expected, Fmoc-FFY peptides are assembled in a pseudo β-sheet structure[42], mainly pointing their negatively charged carboxylate groups towards the aqueous phase.

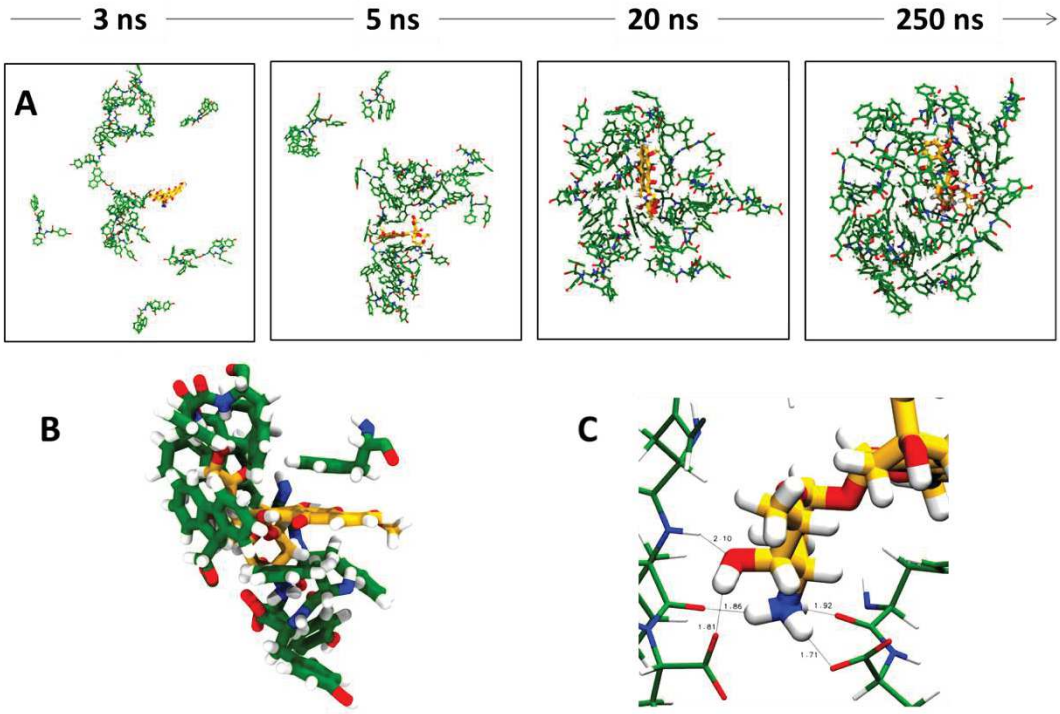

Figure 4-17. (A) Snapshots taken along the trajectory of an initially mixed aqueous solution of DOX + 16 Fmoc-FFY peptides at 298.15 K at 3, 5, 20 and 250 ns. **(B)** View of the DOX – peptides π-π stacking interactions between the anthraquinone group of DOX and a phenylalanine residue of Fmoc-FFY. For the sake of clarity, some Fmoc-FFY peptides are not shown. **(C)** Electrostatic interaction between the ammonium group of DOX and the C-terminal carboxylate group of Fmoc-FFY, and hydrogen bonds between N-H from the ammonium and C=O from the amide group.

By increasing the temperature to 333.15 K, we observe that the DOX is pushed out from the center of peptide assembly towards the surface of the peptide assembly where it is then accessible to the

solvent and can be released. (**Figure 4-18**) Based on these observations, it appears obvious that releasing too much DOX triggered by the temperature rise stimulus leads to a weakening in the hydrogel nanoarchitecture, as observed experimentally by rheology.

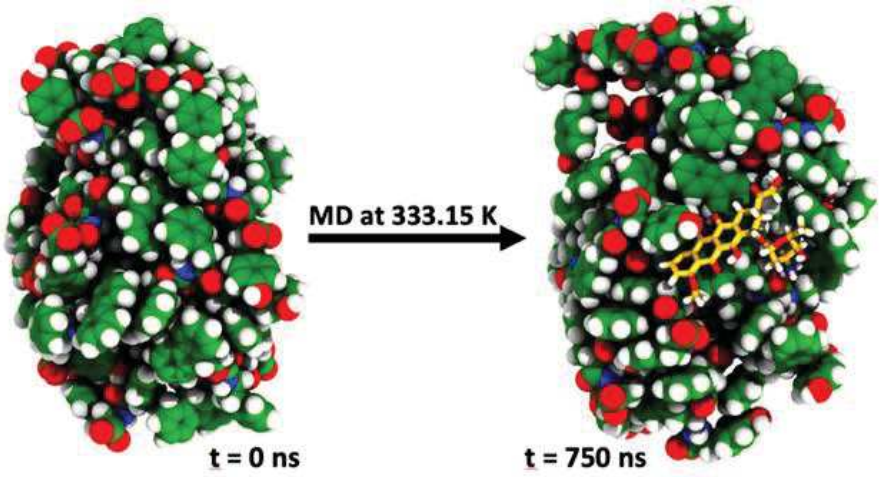

Figure 4-18. Space filling views of the DOX-peptides assembly at 0 and 750 ns at 333.15K. At 0 ns, DOX molecule is buried inside the peptide assembly while at 750 ns it is pushed outside.

Additionally, MD studies starting with a preformed peptide assembly do not lead to the penetration of the DOX inside the Fmoc-FFY assembly but the DOX rather intercalates between two peptides remaining, however, largely accessible to the solvent and hence easier to be released from the peptide assembly (**Figure 4-19**). Based on these results, the first way of DOX incorporation seems far more likely, as already observed with the mixture of peptides.[62]

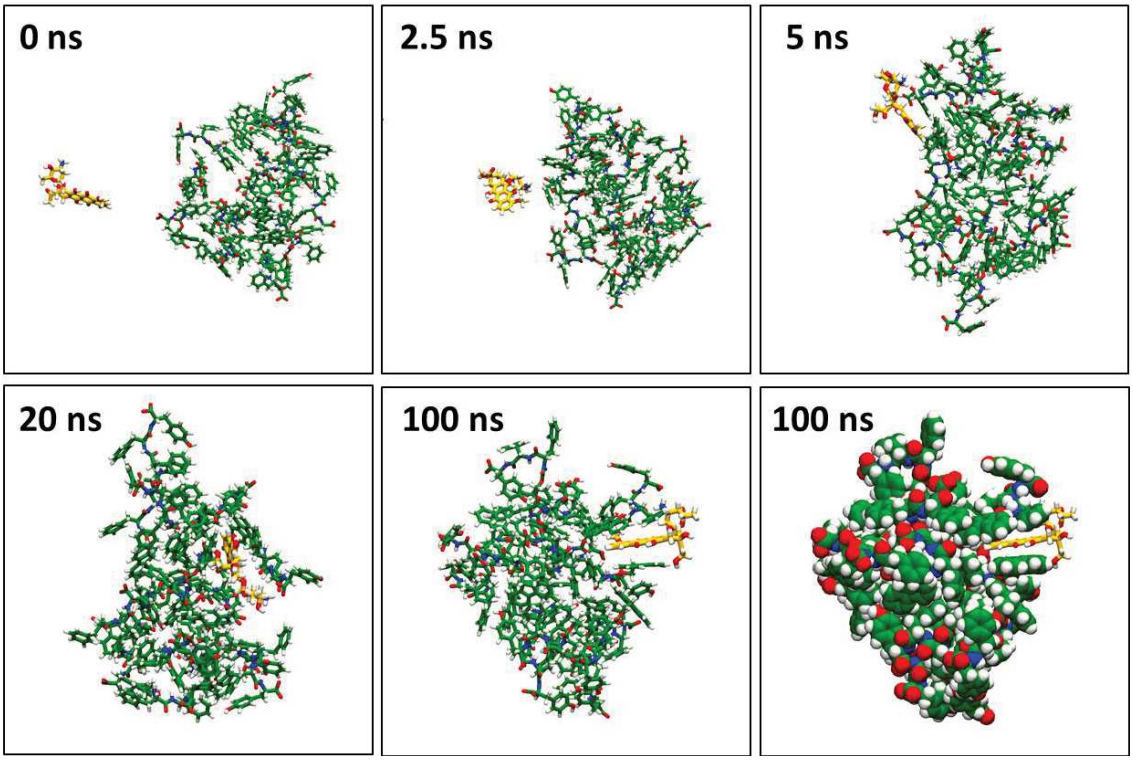

Figure 4-19. Time laps simulations in the case of DOX adsorbing on 16 preformed aggregate Fmoc-FFY peptides at 298.15 K.

IV.4. Conclusion of Chapter IV

In summary, a novel strategy to trigger the self-assembly of a peptide hydrogel from enzyme-coated CNT@LPMS composites has been designed for photothermally-induced drug delivery. First, CNTs were coated with a large homogeneous pore mesoporous silica layer, making them particularly suitable for loading high MW biomacromolecules. It was found that an ultra-high AP loading capacity (≥ 100 wt%) was achieved in the porous inorganic layer with the IBAM binders grafted on the silica surface. The excellent AP loading capacity of CNT@LPMS@IBAM composites enabled them to act as initiators of the peptide self-assembly and cross-linking points of the resulting nanocomposite supramolecular hydrogel, allowing localized growth of peptide self-assembled nanofibers architecture from the silica surface. Furthermore, significant DOX release from these hydrogels was obtained when the DOX-loaded hydrogels were submitted to external high temperature (42 °C) stimulation (about three times more as compared to the samples at 25 °C).

Regarding the NIR light–induced photo-thermal response, it was shown that such nanocomposite hydrogels are able to heat locally when they are irradiated remotely with NIR light, with temperature profiles and SAR values suitable for hyperthermia biomedical applications. Furthermore, we also show that the drug release can be activated by NIR light applied, with a DOX release found to be four times increased as compared to the control without NIR light stimulation.

Rheological studies showed that the elastic (storage) modulus of these hydrogels increased with the CNTs@MS but also with the introduction of DOX, while it is decreased significantly after thermal treatment (42 °C). Molecular dynamic simulation MD simulation suggests an original mechanism of drug encapsulation in supramolecular hydrogel structure which explains the rheological features of the material when loaded and after the drug release.

Overall, these results indicate that these nanocomposite supramolecular hydrogels assembled from enzyme-coated large pore mesoporous materials can be used as photothermally responsive controlled release nanoplatforms. The association of CNT@LPMS nanocomposites and self-assembled peptide supramolecular hydrogel as scaffold is an innovative strategy, which is expected to be used to develop a new generation of stimuli-responsive drug delivery systems suitable for biomedical applications.

IV.5. References

(1) Talebian, S.; Foroughi, J.; Wade, S. J.; Vine, K. L.; Dolatshahi-Pirouz, A.; Mehrali, M.; Conde, J.; Wallace, G. G. Biopolymers for Antitumor Implantable Drug Delivery Systems: Recent Advances and Future Outlook. *Adv. Mater.* **2018**, *30* (31), 1706665.

(2) Mertz, D.; Harlepp, S.; Goetz, J.; Bégin, D.; Schlatter, G.; Bégin-Colin, S.; Hébraud, A. Nanocomposite Polymer Scaffolds Responding under External Stimuli for Drug Delivery and Tissue Engineering Applications. *Adv. Ther.* **2020**, *3* (2), 1900143.

(3) Stuart, M. A. C.; Huck, W. T. S.; Genzer, J.; Müller, M.; Ober, C.; Stamm, M.; Sukhorukov, G. B.; Szleifer, I.; Tsukruk, V. V.; Urban, M.; Winnik, F.; Zauscher, S.; Luzinov, I.; Minko, S. Emerging Applications of Stimuli-Responsive Polymer Materials. *Nat. Mater.* **2010**, *9* (2), 101–113.

(4) Roy, D.; Cambre, J. N.; Sumerlin, B. S. Future Perspectives and Recent Advances in Stimuli-Responsive Materials. *Prog. Polym. Sci.* **2010**, *35* (1), 278–301.

(5) Alvi, F.; Ram, M. K.; Basnayaka, P. A.; Stefanakos, E.; Goswami, Y.; Kumar, A. Graphene–Polyethylenedioxythiophene Conducting Polymer Nanocomposite Based Supercapacitor. *Electrochimica Acta* **2011**, *56* (25), 9406–9412.

(6) Thakur, V. K.; Kessler, M. R. Self-Healing Polymer Nanocomposite Materials: A Review. *Polymer* **2015**, *69*, 369–383.

(7) Döring, A.; Birnbaum, W.; Kuckling, D. Responsive Hydrogels – Structurally and Dimensionally Optimized Smart Frameworks for Applications in Catalysis, Micro-System Technology and Material Science. *Chem. Soc. Rev.* **2013**, *42* (17), 7391–7420.

(8) Alamusi; Hu, N.; Fukunaga, H.; Atobe, S.; Liu, Y.; Li, J. Piezoresistive Strain Sensors Made from Carbon Nanotubes Based Polymer Nanocomposites. *Sensors* **2011**, *11* (11), 10691–10723.

(9) Merino, S.; Martín, C.; Kostarelos, K.; Prato, M.; Vázquez, E. Nanocomposite Hydrogels: 3D Polymer–Nanoparticle Synergies for On-Demand Drug Delivery. *ACS Nano* **2015**, *9* (5), 4686–4697.

(10) Adedoyin, A. A.; Ekenseair, A. K. Biomedical Applications of Magneto-Responsive Scaffolds. *Nano Res.* **2018**, *11* (10), 5049–5064.

(11) Bendix, P. M.; Reihani, S. N. S.; Oddershede, L. B. Direct Measurements of Heating by Electromagnetically Trapped Gold Nanoparticles on Supported Lipid Bilayers. *ACS Nano* **2010**, *4* (4), 2256–2262.

(12) Dreaden, E. C.; Alkilany, A. M.; Huang, X.; Murphy, C. J.; El-Sayed, M. A. The Golden Age: Gold Nanoparticles for Biomedicine. *Chem. Soc. Rev.* **2012**, *41* (7), 2740–2779.

(13) Perigo, E. A.; Hemery, G.; Sandre, O.; Ortega, D.; Garaio, E.; Plazaola, F.; Teran, F. J. Fundamentals and Advances in Magnetic Hyperthermia. *Appl. Phys. Rev.* **2015**, *2* (4), 041302.

(14) Mertz, D.; Sandre, O.; Bégin-Colin, S. Drug Releasing Nanoplatforms Activated by Alternating Magnetic Fields. *Biochim. Biophys. Acta BBA - Gen. Subj.* **2017**, *1861* (6), 1617–1641.

(15) Dutz, S.; Hergt, R. Magnetic Particle Hyperthermia—a Promising Tumour Therapy? *Nanotechnology* **2014**, *25* (45), 452001.

(16) Geim, A. K.; Novoselov, K. S. The Rise of Graphene. *Nat. Mater.* **2007**, *6* (3), 183–191.

(17) Dai, H. Carbon Nanotubes: Synthesis, Integration, and Properties. *Acc. Chem. Res.* **2002**, *35* (12), 1035–1044.

(18) Kostarelos, K.; Bianco, A.; Prato, M. Promises, Facts and Challenges for Carbon Nanotubes in Imaging and Therapeutics. *Nat. Nanotechnol.* **2009**, *4* (10), 627–633.

(19) Bianco, A.; Kostarelos, K.; Partidos, C. D.; Prato, M. Biomedical Applications of Functionalised Carbon Nanotubes. *Chem. Commun.* **2005**, No. 5, 571–577.

(20) Liu, Z.; Sun, X.; Nakayama-Ratchford, N.; Dai, H. Supramolecular Chemistry on Water-Soluble Carbon Nanotubes for Drug Loading and Delivery. *ACS Nano* **2007**, *1* (1), 50–56.

(21) Samorì, C.; Ali-Boucetta, H.; Sainz, R.; Guo, C.; Toma, F. M.; Fabbro, C.; Da Ros, T.; Prato, M.; Kostarelos, K.; Bianco, A. Enhanced Anticancer Activity of Multi-Walled Carbon Nanotube–Methotrexate Conjugates Using Cleavable Linkers. *Chem. Commun.* **2010**, *46* (9), 1494–1496.

(22) Zhang, M.; Zhang, X.; He, X.; Chen, L.; Zhang, Y. A Facile Method to Coat Mesoporous Silica Layer on Carbon Nanotubes by Anionic Surfactant. *Mater. Lett.* **2010**, *64* (12), 1383–1386.

(23) Bian, S.-W.; Ma, Z.; Zhang, L.-S.; Niu, F.; Song, W.-G. Silica Nanotubes with Mesoporous Walls and Various Internal Morphologies Using Hard/Soft Dual Templates. *Chem. Commun.* **2009**, No. 10, 1261–1263.

(24) Wells, C.; Vollin-Bringel, O.; Fiegel, V.; Harlepp, S.; Schueren, B. V. der; Bégin-Colin, S.; Bégin, D.; Mertz, D. Engineering of Mesoporous Silica Coated Carbon-Based Materials Optimized for an Ultrahigh Doxorubicin Payload and a Drug Release Activated by PH, T, and NIR-Light. *Adv. Funct. Mater.* **2018**, *28* (17), 1706996.

(25) Li, Z.; Barnes, J. C.; Bosoy, A.; Stoddart, J. F.; Zink, J. I. Mesoporous Silica Nanoparticles in Biomedical Applications. *Chem. Soc. Rev.* **2012**, *41* (7), 2590–2605.
(26) Wu, S.-H.; Mou, C.-Y.; Lin, H.-P. Synthesis of Mesoporous Silica Nanoparticles. *Chem. Soc. Rev.* **2013**, *42* (9), 3862–3875.
(27) Yang, P.; Gai, S.; Lin, J. Functionalized Mesoporous Silica Materials for Controlled Drug Delivery. *Chem. Soc. Rev.* **2012**, *41* (9), 3679–3698.
(28) Knežević, N. Ž.; Durand, J.-O. Large Pore Mesoporous Silica Nanomaterials for Application in Delivery of Biomolecules. *Nanoscale* **2015**, *7* (6), 2199–2209.
(29) Chen, R. J.; Zhang, Y.; Wang, D.; Dai, H. Noncovalent Sidewall Functionalization of Single-Walled Carbon Nanotubes for Protein Immobilization. *J. Am. Chem. Soc.* **2001**, *123* (16), 3838–3839.
(30) Besteman, K.; Lee, J.-O.; Wiertz, F. G.; Heering, H. A.; Dekker, C. Enzyme-Coated Carbon Nanotubes as Single-Molecule Biosensors. *Nano Lett.* **2003**, *3* (6), 727–730.
(31) Vigier-Carrière, C.; Boulmedais, F.; Schaaf, P.; Jierry, L. Surface-Assisted Self-Assembly Strategies Leading to Supramolecular Hydrogels. *Angew. Chem. Int. Ed.* **2018**, *57* (6), 1448–1456.
(32) Conte, M. P.; Sahoo, J. K.; Abul-Haija, Y. M.; Lau, K. H. A.; Ulijn, R. V. Biocatalytic Self-Assembly on Magnetic Nanoparticles. *ACS Appl. Mater. Interfaces* **2018**, *10* (3), 3069–3075.
(33) Wu, C.; Hu, W.; Wei, Q.; Qiao, L.; Gao, Y.; Lv, Y.; Liu, M.; Li, C.; Wang, X.; Wang, Q. Controllable Growth of Core–Shell Nanogels via Esterase-Induced Self-Assembly of Peptides for Drug Delivery. *J. Biomed. Nanotechnol.* **2018**, *14* (2), 354–361.
(34) Criado-Gonzalez, M.; Fores, J. R.; Carvalho, A.; Blanck, C.; Schmutz, M.; Kocgozlu, L.; Schaaf, P.; Jierry, L.; Boulmedais, F. Phase Separation in Supramolecular Hydrogels Based on Peptide Self-Assembly from Enzyme-Coated Nanoparticles. *Langmuir* **2019**, *35* (33), 10838–10845..
(35) Yang, Z.; Gu, H.; Fu, D.; Gao, P.; Lam, J. K.; Xu, B. Enzymatic Formation of Supramolecular Hydrogels. *Adv. Mater.* **2004**, *16* (16), 1440–1444.
(36) Criado-Gonzalez, M.; Iqbal, M. H.; Carvalho, A.; Schmutz, M.; Jierry, L.; Schaaf, P.; Boulmedais, F. Surface Triggered Self-Assembly of Fmoc-Tripeptide as an Antibacterial Coating. *Front. Bioeng. Biotechnol.* **2020**, *8*, 938.
(37) B. Li, M. Criado-Gonzalez, A. Adam, J. Bizeau, C. Mélart, A. Carvalho, S. Bégin, D. Bégin, L. Jierry and D.Mertz, Design of Thermally Drug Releasing Nanocomposite Peptide Hydrogels Assembled from Enzyme Adsorbed Stellate Mesoporous Silica, Submitted to ACSApplied Nano Materials.
(38) Mertz, D.; Affolter-Zbaraszczuk, C.; Barthès, J.; Cui, J.; Caruso, F.; Baumert, T. F.; Voegel, J.-C.; Ogier, J.; Meyer, F. Templated Assembly of Albumin-Based Nanoparticles for Simultaneous Gene Silencing and Magnetic Resonance Imaging. *Nanoscale* **2014**, *6* (20), 11676–11680.
(39) Perton, F.; Harlepp, S.; Follain, G.; Parkhomenko, K.; Goetz, J. G.; Bégin-Colin, S.; Mertz, D. Wrapped Stellate Silica Nanocomposites as Biocompatible Luminescent Nanoplatforms Assessed in Vivo. *J. Colloid Interface Sci.* **2019**, *542*, 469–482.
(40) Ménard, M.; Meyer, F.; Affolter-Zbaraszczuk, C.; Rabineau, M.; Adam, A.; Ramirez, P. D.; Bégin-Colin, S.; Mertz, D. Design of Hybrid Protein-Coated Magnetic Core-Mesoporous Silica Shell Nanocomposites for MRI and Drug Release Assessed in a 3D Tumor Cell Model. *Nanotechnology* **2019**, *30* (17), 174001.
(41) Fiegel, V.; Harlepp, S.; Begin-Colin, S.; Begin, D.; Mertz, D. Design of Protein-Coated Carbon Nanotubes Loaded with Hydrophobic Drugs through Sacrificial Templating of Mesoporous Silica Shells. *Chem. – Eur. J.* **2018**, *24* (18), 4662–4670.
(42) Mertz, D.; Cui, J.; Yan, Y.; Devlin, G.; Chaubaroux, C.; Dochter, A.; Alles, R.; Lavalle, P.; Voegel, J. C.; Blencowe, A. Protein Capsules Assembled via Isobutyramide Grafts: Sequential Growth, Biofunctionalization, and Cellular Uptake. *ACS Nano* **2012**, *6* (9), 7584–7594.
(43) Mertz, D.; Tan, P.; Wang, Y.; Goh, T. K.; Blencowe, A.; Caruso, F. Bromoisobutyramide as an Intermolecular Surface Binder for the Preparation of Free-Standing Biopolymer Assemblies. *Adv. Mater.* **2011**, *23* (47), 5668–5673.
(44) Vigier-Carrière, C.; Garnier, T.; Wagner, D.; Lavalle, P.; Rabineau, M.; Hemmerlé, J.; Senger, B.; Schaaf, P.; Boulmedais, F.; Jierry, L. Bioactive Seed Layer for Surface-Confined Self-Assembly of Peptides. *Angew. Chem.* **2015**, *127* (35), 10336–10339.
(45) Pearlman, D. A.; Case, D. A.; Caldwell, J. W.; Ross, W. S.; Cheatham, T. E.; DeBolt, S.; Ferguson, D.; Seibel, G.; Kollman, P. AMBER, a Package of Computer Programs for Applying Molecular Mechanics, Normal Mode Analysis, Molecular Dynamics and Free Energy Calculations to Simulate the Structural and Energetic Properties of Molecules. *Comput. Phys. Commun.* **1995**, *91* (1), 1–41.
(46) Maier, J. A.; Martinez, C.; Kasavajhala, K.; Wickstrom, L.; Hauser, K. E.; Simmerling, C. Ff14SB: Improving the Accuracy of Protein Side Chain and Backbone Parameters from Ff99SB. *J. Chem. Theory Comput.* **2015**, *11* (8), 3696–3713.
(47) Wang, J.; Wolf, R. M.; Caldwell, J. W.; Kollman, P. A.; Case, D. A. Development and Testing of a General Amber Force Field. *J. Comput. Chem.* **2004**, *25* (9), 1157–1174.

(48) Joung, I. S.; Cheatham, T. E. Determination of Alkali and Halide Monovalent Ion Parameters for Use in Explicitly Solvated Biomolecular Simulations. *J. Phys. Chem. B* **2008**, *112* (30), 9020–9041.
(49) Bayly, C. I.; Cieplak, P.; Cornell, W.; Kollman, P. A. A well-behaved electrostatic potential based method using charge restraints for deriving atomic charges: the RESP model
(50) Jorgensen, W. L.; Chandrasekhar, J.; Madura, J. D.; Impey, R. W.; Klein, M. L. Comparison of Simple Potential Functions for Simulating Liquid Water. *J. Chem. Phys.* **1983**, *79* (2), 926–935.
(51) Berendsen, H. J. C.; Postma, J. P. M.; van Gunsteren, W. F.; DiNola, A.; Haak, J. R. Molecular Dynamics with Coupling to an External Bath. *J. Chem. Phys.* **1984**, *81* (8), 3684–3690.
(52) Humphrey, W.; Dalke, A.; Schulten, K. VMD: Visual Molecular Dynamics. *J. Mol. Graph.* **1996**, *14* (1), 33–38.
(53) Wu, H.-T.; Li, D.-M.; Zhu, B.-W.; Cheng, J.-H.; Sun, J.-J.; Wang, F.-L.; Yang, Y.; Song, Y.-K.; Yu, C.-X. Purification and Characterization of Alkaline Phosphatase from the Gut of Sea Cucumber Stichopus Japonicus. *Fish. Sci.* **2013**, *79* (3), 477–485.
(54) Lee, D.-H.; Choi, S.-L.; Rha, E.; Kim, S. J.; Yeom, S.-J.; Moon, J.-H.; Lee, S.-G. A Novel Psychrophilic Alkaline Phosphatase from the Metagenome of Tidal Flat Sediments. *BMC Biotechnol.* **2015**, *15* (1), 1.
(55) Mei, L.; Xu, K.; Zhai, Z.; He, S.; Zhu, T.; Zhong, W. Doxorubicin-Reinforced Supramolecular Hydrogels of RGD-Derived Peptide Conjugates for PH-Responsive Drug Delivery. *Org. Biomol. Chem.* **2019**, *17* (15), 3853–3860.
(56) Raza, F.; Zhu, Y.; Chen, L.; You, X.; Zhang, J.; Khan, A.; Khan, M. W.; Hasnat, M.; Zafar, H.; Wu, J.; Ge, L. Paclitaxel-Loaded PH Responsive Hydrogel Based on Self-Assembled Peptides for Tumor Targeting. *Biomater. Sci.* **2019**, *7* (5), 2023–2036.
(57) Nagy-Smith, K.; Yamada, Y.; Schneider, J. P. Protein Release from Highly Charged Peptide Hydrogel Networks. *J. Mater. Chem. B* **2016**, *4* (11), 1999–2007.
(58) Yang, L.; Zhang, C.; Ren, C.; Liu, J.; Zhang, Y.; Wang, J.; Huang, F.; Zhang, L.; Liu, J. Supramolecular Hydrogel Based on Chlorambucil and Peptide Drug for Cancer Combination Therapy. *ACS Appl. Mater. Interfaces* **2019**, *11* (1), 331–339.
(59) Adak, A.; Das, G.; Barman, S.; Mohapatra, S.; Bhunia, D.; Jana, B.; Ghosh, S. Biodegradable Neuro-Compatible Peptide Hydrogel Promotes Neurite Outgrowth, Shows Significant Neuroprotection, and Delivers Anti-Alzheimer Drug. *ACS Appl. Mater. Interfaces* **2017**, *9* (6), 5067–5076.
(60) Karavasili, C.; Komnenou, A.; Katsamenis, O. L.; Charalampidou, G.; Kofidou, E.; Andreadis, D.; Koutsopoulos, S.; Fatouros, D. G. Self-Assembling Peptide Nanofiber Hydrogels for Controlled Ocular Delivery of Timolol Maleate. *ACS Biomater. Sci. Eng.* **2017**, *3* (12), 3386–3394.
(61) Jawad, B.; Poudel, L.; Podgornik, R.; Steinmetz, N. F.; Ching, W.-Y. Molecular Mechanism and Binding Free Energy of Doxorubicin Intercalation in DNA. *Phys. Chem. Chem. Phys.* **2019**, *21* (7), 3877–3893.
(62) Du, X.; Zhou, J.; Shi, J.; Xu, B. Supramolecular Hydrogelators and Hydrogels: From Soft Matter to Molecular Biomaterials. *Chem. Rev.* **2015**, *115* (24), 13165–13307.

Chapter V

Brief statement of collaboration works and technical expertise

Chapter V. Brief statement of collaboration works and technical expertise

In this section, I will mention different scientific works to which I have contributed during my thesis. They allow me to push forward various scientific expertises that I have developed during my PhD and which have contributed to publications in well-renown journals.

These expertise cover the field of:

- Measurements of relaxivities r_1 and r_2
- Calculations of Specific Absorption Rate (SAR) from heating curves of NPs in AMF
- Spectrofluorimetry of different molecular or nano systems
- Synthesis of mesoporous silica NPs for different applications

V.1. Measurements of relaxivities

During my PhD thesis, I had the opportunity to collaborate with different teams of externals laboratories. In particular, I evaluated the performances of magnetic particles as contrast agents for magnetic resonance imaging (MRI) by evaluating r_1 and r_2 relaxivities of these suspensions. The instrument used is a ^{1}H-NMR Brucker Minispec working at 60 MHz and 1.41 T. The device measures the transversal and longitudinal relaxation rates of the protons of water in presence of the species to study. By modifying the relaxation rates of protons, the contrast agents will promote an enhancement or an attenuation of the signal, which allows an easier interpretation of MRI pictures.

A collaboration is in progress with Dr. Maxime Gauberti team from INSERM U1237 Caen, CHU Normandie. One article is currently under revision:

- De Lizarrondo S.-M., Jacqmarcq C., Naveau M., Navarro-Oviedo M., Pedron S., Allouche S., Goux D., Razafindrakoto S., Gazeau F., Freis B., Bégin-Colin S., **Adam A**., Mertz D., Vivien D., Bonnard T., Gauberti M. "Self-assembly of catechol coated nanocrystals into micro-sized probes as ultrasensitive and biodegradable contrast agent for immuno-MRI", ***Advanced Science*** **2022**, in minor revision.

V.2. Measurements of SAR by magnetothermal effect

In the frame of collaborative works, I performed measurements of SAR of different systems containing iron oxides NPs which are able to heat under alternating magnetic field. The device used is a Nanoscale Biomagnetic DM100. The experiment is aimed at evaluating the efficacy of the

magnetothermal effect which can be used for hyperthermia treatment in particular. The device allows to control the field intensity (from 0 to 300 G) and the frequency (between 252 and 796 kHz). The sample is placed in a vacuum-insulated chamber and the coil is cooled down by a thermostatic chiller. A temperature probe is immersed in the sample and the temperature profiles are recorded as a function of time. The data are then plotted and fitted with an appropriate function in order to determine the initial slope of the heating curve. This allows then to calculate the SAR, in watt per gram of studied material. I evaluated the properties of different formulations in the following projects:

- In coll. with Dr. Isabela Janowska and Dr. Anurag Mohanty from Institut de chimie et procédés pour l'énergie, l'environnement et la santé (ICPEES, Strasbourg), we evaluated the SAR of nickel NPs supported on carbon nanofibers.

  Published article: Mohanty, A.; Viet, C. D.; Roger, A.-C.; **Adam, A.**; Mertz, D.; Baaziz, W.; Janowska, I.. "Structural impact of carbon nanofibers/few-layer-graphene substrate decorated with Ni for CO2 methanation via inductive heating". ***Applied Catalysis B: Environmental*** **2021**, 298, 120589.
- In coll. with Dr. Charlotte Vichery and Dr. Jean-Marie Nédelec, we studied the heating properties of γ-Fe_2O_3@SiO_2-CaO heterostructures as biomaterials to fill bone defect.

  Published article: Kesse, X.; **Adam, A.**; Begin-Colin, S.; Mertz, D.; Larquet, E.; Gacoin, T.; Maurin, I.; Vichery, C.; Nedelec, J.-M. "Elaboration of Superparamagnetic and Bioactive Multicore–Shell Nanoparticles (γ-Fe2O3@SiO2-CaO): A Promising Material for Bone Cancer Treatment"**.** ***ACS Appl. Mater. Interfaces*****, 2020**, 12, 47820–47830.
- In coll. with Dr. Halima Alem-Marchand from Institut Jean Lamour, Nancy, we evaluated the magnetothermal properties of several formulations containing polymer grafted with iron oxide NPs for hyperthermia applications. One article is in preparation.

V.3. Spectrofluorimetry

During my thesis, I have also been led to perform fluorescence measurements for different projects in collaboration with other PhD works on molecular systems but also on nanoparticles suspensions. In one published work, I participated to a fluorescence study in the following article with the aim to evaluate the DOX fluorescence emission and its degradation at the surface of NPs in specific chemical environment:

Published article: Ménard, M.; Meyer, F.; Affolter-Zbaraszczuk, C.; Rabineau, M.; **Adam, A.**; Ramirez, P. D.; Bégin-Colin, S.; Mertz, D. "Design of Hybrid Protein-Coated Magnetic Core-Mesoporous Silica Shell Nanocomposites for MRI and Drug Release Assessed in a 3D Tumor Cell Model"**.** **Nanotechnology** ***2019***, 30 (17), 174001.

V.4. Synthesis of mesoporous silica NPs

Finally, thanks to the expertise I developed in the synthesis of different mesoporous silica NPs, I participated to collaborations that aimed at using mesoporous silica NPs for other applications. In our team, I worked with other PhD students who studied MS NPs for biomedical applications:

- With Joëlle Bizeau, we worked together on the coating and release of proteins using IBAM-grafted STMS NPs. An article is published and another is under submission.

  Published article: Bizeau J., **Adam A.,** Bégin S., Mertz D., "Serum Albumin Antifouling Effects of Hydroxypropyl-cellulose and Pluronic F127 Adsorbed on Isobutyramide-grafted Stellate Silica Nanoparticles", ***Eur. J. Inorg. Chem*. 2021**, 2021, 4799.

  Submitted article: Bizeau J., **Adam A**., Nadal C., Francius G., Siniscalco D., Pauly M., Bégin-Colin S., Mertz D. **"**Protein sustained release from isobutyramide-grafted stellate mesoporous silica nanoparticles, **submitted** to ***Coll. and Surf. B.: Biointerfaces***
- With Dr. Bing Li, we studied the formation of peptide hydrogels from STMS NPs coated with an appropriate enzyme able to trigger the self-assembly of the peptide. One article is published:

  Published article: Li B., Criado-Gonzalez M., **Adam A**., Bizeau J., Mélart C., Carvhalo A., Bégin-Colin S., Bégin D., Jierry L., Mertz D. " Peptide Hydrogels Assembled from Enzyme-Adsorbed Mesoporous Silica Nanostructures for Thermoresponsive Doxorubicin Release "***ACS Appl. Nano Mater.* 2022,** 5, 1, 120–125.

General Conclusion

General Conclusion

The objectives of my PhD work were to use the combination of mesoporous silica with magnetic and light responsive materials to produce smart core-shell nanoplatforms for a multimodal therapy of cancer. After reviewing the existing systems from the literature, a set of specifications that these nanoplatforms had to meet was established:

i) By an appropriate choice of the core material, the nanomaterials should generate heat under application of AMF, NIR light or both.

ii) By an optimized engineering of the silica shell, the nanocomposites should be able to carry and release high amount of antitumor drugs.

iii) By an appropriate formulation, the developed nanoplatforms should be usable as an injectable or implantable treatment.

For this, we have focused first on the synthesis of core-shell silica@iron oxide NPs (**Chapter 2**). Starting from IO NPs synthesized by thermal decomposition as core material, we succeeded in the production of various silica shells of different thicknesses and morphologies. To create pores in the silica shell, the use of a suitable surfactant is the most reported route. We demonstrated that by tuning the temperature of the reaction, we were able to control the micelle organization and the silica condensation and therefore to orient the pore morphology (size and spatial arrangement). Moreover, by modulating the reactants and the synthesis methods, we showed that the presence of mesopores or not and their size, have an influence on both MRI relaxivities and magnetothermal properties. With a thicker and denser silica shell coating IO core, the heat transfer is more damped and thus the temperature elevation upon AMF is attenuated. For an optimal heat transfer to the outside of the NP, the silica pore should be wide open and the shell relatively thin. In order to evaluate the variation of the heat transfer as a function of the silica shell, nanothermometry experiments have been implemented. These are still in progress as some optimizations of the set-up are required.

Then, we went further in the use of IO@STMS NPs for hyperthermia treatment but, as an original alternative to MHT, the focus was put on their features as photothermal therapy agents (**Chapter 3**). Indeed, this core-shell NP showed very good conversion of NIR light into heat making them suitable for PTT. Afterwards, the drug (doxorubicin) loading and release behavior of this system has been studied. IO@STMS was chosen because of the large pore openings and the high surface area, favorable for PTT and therapeutics loading. We explained how the pH is crucial when DOX is used as antitumor drug. A pH slightly above 7 improved drastically the amount of drug loaded due to favorable DOX-silica and DOX-DOX interactions. Concerning the drug release, the surface chemistry and the pH appeared to be both important to minimize the unwanted drug leaking and to maximize the drug delivery when needed. For this, IBAM functionalization showed the best results (suitable delivery with limited

leaking). Thus, we synthesized a core-shell NP which can be used for dual-therapy of cancer. Preliminary biological characterizations were carried out to demonstrate the potential of this formulation: IO@STMS@IBAM@DOX@HSA. *In vitro* tests indicated that the DOX release could be triggered by NIR irradiation. Moreover, the synergetic dual antitumor action was pointed out by the effective death of melanoma cancer cells when exposed to NIR light. *In vivo* tests in ZF embryos showed no major toxicity on fish vital signs when no NIR light trigger was activated and the nanoformulation seemed to accumulate around or within tumor aggregates in very preliminary experiments. These results are very encouraging to decipher the efficacy of the developed nanoformulations as antitumor treatments by dual PTT and drug delivery.

In a last chapter, we added a supplementary organization level of the core-shell nanocomposites by incorporating them into a hydrogel (**Chapter 4**). One of the major limitations to the use of hydrogel for biomedical applications is their mechanical resistance which can be very low compared to other implantable matrixes. Thus the nanoparticle was designed such that its incorporation in a gel should bring improved mechanical stability and, in addition, to be remotely activated for therapy. That is why CNTs was chosen as core material. Then a large pore silica shell was synthesized around it to build CNTs@LPMS. Hence, we took advantage of the porosity and the immobilization capacity of IBAM-grafted silica to load an enzyme on it which was able to trigger the self-assembly of a tripeptide into a hydrogel. Therefore, CNTs@LPMS acted as cross-linking points for the hydrogel assembly allowing to maintain the gel stability and prevent any nanoparticle dissemination. Additionally, the gel was loaded with DOX and we demonstrated that the DOX release from the gel could be triggered by NIR light stimulation. This innovative strategy is expected to result in the development of a new generation of smart drug delivery systems.

To conclude, several potential perspectives of these works can be envisioned:

- **In chapter 2**, we pushed forward the understanding of the silica shell influence around IO NPs. However, how the heat front really dissipates inside the shell and the surrounding environment remains unclear. Nanothermometry is a big hope for deciphering this but the experimental set-up needs to be refined to eliminate interfering signals. Future thermal mapping simulation experiments could also help to quantify and visualize the heat transfer even if the complex pore structure makes the modelling quite challenging.
- **In chapter 3**, we managed to control the drug loading by functionalizing the silica surface with IBAM groups and by using an adapted buffer at optimized pH. However, the drug/silica and drug/IBAM interactions as a function of temperature and pH are not fully unraveled and advanced characterizations should be carried out. Atomic force microscopy (AFM), detailed Fourier-transform infrared spectroscopy (FTIR), isothermal titration calorimetry (ITC) are examples of methods that could potentially decipher how such high drug loadings are obtained by identifying and quantifying the bonds involved. Moreover,

works are still ongoing to determine a suitable aqueous buffer for stabilizing the drug-loaded and protein-coated nanoplatform by mimicking a cellular environment. Complementary biological studies are being performed at the moment to evaluate the potential for PTT. *In vitro* analyses on different melanoma cell lines would allow us to define the most appropriate NPs concentration for efficient antitumor action without spurious cytotoxicity when the NP are not exposed to NIR light. *In vivo* studies in ZMEL-1 cells in ZF will also be continued to evaluate the biodistribution and the targeting of the metastatic tumors and their treatment by dual mode therapy.

For further improvement of the nanoplatform, it is also planned to study other functionalization than IBAM. In particular, grafting a polymer such as poly(N-vinyl isobutyramide) (PVIBAm) which has IBAM as side groups is a promising solution to combine the loading capacity of IBAM function with the known thermoresponsiveness of this polymer.

Finally, the fate of the NPs in the body is crucial for clinical approval. They should be eliminated after some time in the organism. Currently, a parallel master project is studying the biodegradability of our nanoplatforms, first in different buffers mimicking physiological pH, ionic force or even cell culture media and later this study will be continued *in vitro* and *in vivo*.

In **Chapter 4**, main perspectives will be the possibility to tune the kind of drugs that could be incorporated into the hydrogels with the aim to develop a versatile system able to load/release any drugs. The second point will be to use suitable peptides able to ensure cell adhesion, proliferation and biocompatibility with the aim to be applied in tissue engineering or to act as a therapeutic implant.

Alexandre ADAM

Nanoplateformes à base de silices mésoporeuses pour l'hyperthermie magnétique, la photothermie et la délivrance d'agents thérapeutiques

Résumé

L'objectif de cette thèse est de développer des nanoplateformes à base de silice, permettant une thérapie multimodale du cancer, administrées par voie injectable ou implantable. Pour cela, les nanoparticules (NPs) de type cœur-coquille sont idéales pour combiner les propriétés de deux matériaux. Les NPs d'oxyde de fer (IO) et les nanotubes de carbone (CNT) sont utilisés en tant que matériaux de cœur pour leurs propriétés magnéto- et photothermiques. Une coquille de silice mésoporeuse est ensuite déposée autour des cœurs par voie sol-gel. Différents types de pores et épaisseurs de silice sont synthétisés puis l'influence de cette couche de silice sur le transfert de la chaleur depuis les NPs cœur-coquille IO@MS sous champ magnétique alternatif est étudié. Les NPs IO@MS sont aussi étudiés en tant qu'agents photothermiques par irradiation sous lumière infrarouge. Le nanocomposite est ensuite chargé en médicaments. Nous avons constaté que le choix de la fonctionnalisation de surface des IO@MS et le pH de la solution médicamenteuse sont déterminants pour avoir de grands taux de chargement. L'irradiation par laser infrarouge du nanocomposite chargé en médicaments induit un échauffement du milieu et une légère baisse du pH de 7.5 à 5.5 permet une bonne libération du médicament. Combinés, ces deux effets montrent une action anticancéreuse synergique efficace lors de tests in vitro sur des cellules du mélanome. Enfin, un nanocomposite CNT@MS est synthétisé pour obtenir un matériau photorépondant capable de charger des enzymes. Par incorporation dans une solution de peptides, l'enzyme déclenche l'auto-assemblage des peptides pour former un hydrogel. En ajoutant un médicament au gel, il est possible d'induire une délivrance contrôlée du médicament par irradiation sous infrarouge.

Mots-clés: Silice mésoporeuse, nanocomposites intelligents, hyperthermie magnétique, thérapie photothermique par infrarouge, délivrance de médicaments

Abstract

The goal of this PhD work is to develop silica-based nanoplatforms for a multimodal therapy of cancer designed for injectable or implantable formulations. Core-shell nanoparticles (NPs) are particularly suited to combine the properties of two materials. Iron oxide (IO) NPs and carbon nanotubes (CNT) were identified as ideal candidates as core materials due to their magneto- and photothermal properties. By sol-gel process, a coating of mesoporous silica (MS) is added to these cores. Different silica morphologies are synthesized and the influence of the silica shell on the heat transfer of IO@MS core-shell NPs to their surroundings upon alternating magnetic field (AMF) is studied. IO@MS are also studied as photothermal agents by using near-infrared (NIR) light laser. The nanocomposite is then loaded with drugs. We found that the surface functionalization of IO@MS and the pH of the drug solution are crucial for a high loading capacity. Irradiation of drug-loaded nanocomposite with NIR laser induces temperature elevation and a moderate decrease of the pH from 7.5 to 5.5 allows an efficient drug release. Combined together, these two effects, show efficient synergistic antitumor action in *in vitro* tests on melanoma cancer cells. Finally, CNT@MS nanocomposite is produced in order to have a photoresponsive material. By loading them with enzymes and by adding it to a peptide solution, the enzyme triggers the peptide self-assembly into a hydrogel. When a drug is added to the gel, it is possible to induce controlled drug delivery by irradiation with NIR light.

Keywords: Mesoporous silica, smart nanocomposites, magnetic hyperthermia, near-infrared photothermal therapy, drug delivery